SMALL-SCALE ELECTRON DENSITY FLUCTUATIONS IN THE HALL THRUSTER, INVESTIGATED BY COLLECTIVE LIGHT SCATTERING

Sedina Tsikata

ÉCOLE POLYTECHNIQUE
ParisTech

Thèse présentée pour obtenir le grade de

DOCTEUR DE L'ÉCOLE POLYTECHNIQUE

Spécialité:

Physique des plasmas

par

Sedina TSIKATA

SMALL-SCALE ELECTRON DENSITY FLUCTUATIONS IN THE HALL THRUSTER, INVESTIGATED BY COLLECTIVE LIGHT SCATTERING

soutenance le 19 novembre 2009 devant le jury composé de:

M. Dominique GRÉSILLON
Directeur de thèse, Directeur de Recherche émérite, École Polytechnique
M. Cyrille HONORÉ
Co-directeur de thèse, Ingénieur de Recherche, École Polytechnique
M. Poul MICHELSEN
Professeur, Risø Technical University of Denmark (Rapporteur)
M. Fabrice DOVEIL
Directeur de Recherche au CNRS, Marseille (Rapporteur)
Mme. Anne HÉRON
Chargée de Recherche au CNRS, École Polytechnique
M. Patrick HUERRE
Professeur, École Polytechnique
M. Jean-Marcel RAX
Professeur, École Polytechnique
M. Stéphane MAZOUFFRE
Chargé de Recherche au CNRS, Orléans
M. Stephan ZURBACH
Ingénieur Snecma (Invité)

Acknowledgements

I was fortunate to be able to interact with some great people during my thesis. I'm very grateful to my thesis advisors especially: Dominique Grésillon, for his kindness, guidance and brilliant suggestions on everything from experiments to thruster physics, and Cyrille Honoré for plenty of help on collective scattering principles and their application. It was a pleasure to work with Messieurs G. and H. and I learned a great deal from them. Nicolas Lemoine's enthusiasm and ideas were very much appreciated.

I'm also grateful to our collaborators Jean-Claude Adam and Anne Héron, whose work inspired these experiments. Their input and interest made for some very lively discussions. Anne's recent work also provided a context for the interpretation of our latest results and it has been truly beneficial to discuss our findings with her.

Last but not least, many thanks to: Pascal Lasgorceix and Sisouk Sayamath, for patiently operating and monitoring the thruster during experiments; Stéphane Mazouffre, for many useful discussions, encouragement and help in organising our experimental campaigns, and Michel Dudeck, for supporting our research in the context of the GDR.

Contents

List of Figures

List of Tables

Introduction

The final frontier

> "If we have learned one thing from the history of invention and discovery, it is that, in the long run - and often in the short one - the most daring prophecies seem laughably conservative."
>
> - Arthur C. Clarke (1917-2008), *The Exploration of Space*, 1951

THE history of artificial satellites began with the launch of Sputnik-1, by the Soviet Union in 1957. Since then, satellites have found a wide range of applications in telecommunications and space exploration. Commercial satellites are used today for relaying communications to ships and planes, telephony and for television and radio broadcasting. Satellites equipped with scientific instruments gather data on the solar system, providing measurements on the Earth's atmosphere, solar wind, cosmic rays, and atmospheric conditions on other planets. Vital to our everyday life, satellites and probes have made it possible to explore environments and worlds beyond our own.

The goals of any satellite mission must be balanced with considerations of mission cost and feasibility. Perhaps the most critical area of the design is the propulsion system. Various technologies exist and are under development, however, the basic limitation on the performance of these techologies is imposed by Tsiolkovsky's rocket equation,

$$m_0 = m_1 \, e^{\frac{\Delta v}{I_{sp} \times g}} \tag{1}$$

in which m_0 is the initial mass (with fuel) of the vehicle, m_1 the final mass of the vehicle, and Δv a measure of the effort required to perform a manœuvre, such as orbital transfer. I_{sp} is the specific impulse and g the acceleration due to gravity; v_e, the fuel exit velocity, is $I_{sp} \times g$.

The exhaust velocities accessible during chemical propulsion are limited by the chemical bond energy, whereas in electric propulsion, the acceleration of the propellant occurs separately from its production. The mass savings in electric propulsion can be considerable because of the higher exhaust velocities which are achievable. Table 1 presents a comparison of I_{sp} values of different thruster types which have been used in flight.

To illustrate the advantages of electric propulsion over chemical propulsion, we may consider two propellant systems, one chemical and another electric (Hall or ion thruster),

both of which require a Δv of 10 km/s. We may assume that the final vehicle mass for both cases will be the same. From Eq. 1, for an exhaust velocity of around 4 km/s in the case of chemical propulsion, and an exhaust velocity of about 35 km/s in the case of ion propulsion, the resulting initial vehicle mass of the electric propulsion system is only 11% of that of the chemical propulsion system; this is without even having taken into account the mass savings on other equipment. For missions requiring a high Δv, chemical propulsion is not feasible because of the large fuel requirements.

Thruster	**Specific impulse (s)**
Chemical (monopropellant)	150-225
Chemical (bipropellant)	300-450
Resistojet	300
Arcjet	500-600
Ion thruster	2500-3600
Hall thrusters	1500-2000
Pulsed plasma thrusters	850-1200

Table 1: Summary of characteristic I_{sp} values for main propulsion methods [27]

Various other propulsion technologies such as nuclear propulsion exist and are being developed. Nuclear systems are massive and require precautions for materials storage. Other concerns, such as the melting temperatures of materials used for reactor cores, must be addressed. However, such systems would deliver even larger exhaust velocities than electric propulsion. Other intriguing options, such antimatter propulsion, could potentially offer exhaust velocities a few orders of magnitude larger than chemical propulsion, but are not yet available.

Electric propulsion has attracted a great deal of industrial and academic interest over the past few decades, as a propulsion technology well-suited to interplanetary missions. Closed electron drift thrusters are a widely-used form of electric propulsion and will be the subject of this introduction.

The development of closed electron drift thrusters

Closed electron drift or Hall effect thrusters (HETs) refer to a class of thrusters in which the electron drift is confined to an azimuthally-circulating cloud at the thruster exit, through which ions are accelerated to provide thrust.

The first ideas for electrostatically accelerating particles for a propulsion system were described by Robert H. Goddard in 1906. From the late 1940s to the 1960s, experiments were carried out to determine the feasibility of ion propulsion by von Braun and Stuhlinger. In parallel, Cleaver, Shepherd and Spitzer performed studies demonstrating the feasibility of using nuclear energy to provide electric power to ion thrusters.

In 1964, the NASA SERT-I program demonstrated that space applications of ion thrusters could match ground test performances, which constituted an important validation of the thruster concept. Under the SERT-II program, the long-term operation of solar-powered ion thrusters in space was successfully tested. The success of these initial tests proved critical for sustaining interest and encouraging further developments in the field.

The fall of the Soviet Union allowed the access of Western scientists to the significant developments made in the USSR on the closed electron drift thruster concept. Two models had been developed: the SPT (Stationary Plasma thruster), by A. I. Morozov, and the TAL (Thruster with Anode Layer), developed by A. V. Zharinov. The key difference between these models is in the length of the acceleration zones and the wall material, however, they operate according to the same basic principles [65]. The first stationary plasma thruster, the SPT-60, was flown in 1972. In 1992, a team of experts evaluated the Russian SPT-100 Hall thruster, whose basic design is still treated as a model for the construction of most Hall thrusters. Its characteristics of high efficiency (exceeding 50%) and high exit velocities (in the range of 20 km/s) encouraged its adoption for use on commercial space vehicles in near-earth orbit, for low-impulse applications such as station keeping and orbit transfer. A competing concept, the more complex gridded ion thruster, has had relatively few applications in space but was successfully flown on NASA's Deep Space 1 (DS1) mission, launched in 1998. A solar-powered Hall thruster, the 1.5 kW PPS®1350-G (Fig. 1) developed by Snecma, was the first to be used for primary propulsion, i.e. responsible for performing major orbital manœuvres. It was flown on ESA's SMART-1 mission to the moon launched in 2003, and established a record for continuous thrust (over 260 hours) and operation in space (5000 hours).

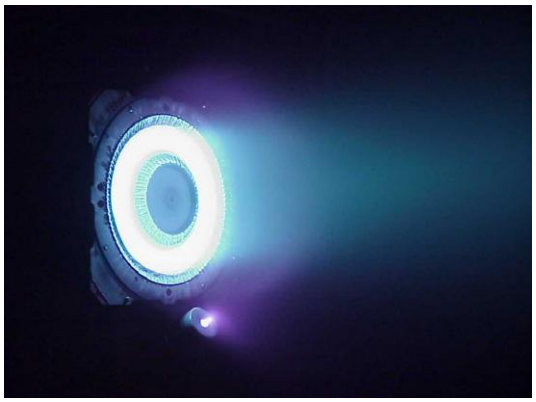

Figure 1: Photo of the PPS®1350-G thruster in operation

The Hall thruster concept has gained increasing attention in recent years because of its suitability for interplanetary missions, due to its simplicity, efficiency, and reliability. New efforts are being made to develop higher-thrust engines, with power in the range of several kW, for use on satellites based on large communications platforms such as Alphabus (planned by Thales Alenia Aerospace and EADS). Research efforts are focused on the understanding of the complex physical phenomena inherent to such thrusters, such as erosion, anomalous electron transport and the origin of a range of oscillations arising spontaneously in the thruster,

all of which have implications on thruster efficiency and lifetime. Such efforts take the form of experimental measurements, theoretical analysis and numerical models.

The Hall thruster

The Hall thruster possesses a simple basic structure. Its annular plasma discharge chamber is formed by the space between two coaxial cylinders (typically ceramic, BN or BN-SiO_2, in contrast to the TAL, whose discharge chamber walls are metallic). It possesses a central magnetic coil and four externally placed coils, which are designed to create a radial magnetic field in discharge chamber. A hollow cathode is situated externally. The anode is at the other end of the discharge chamber, and serves as the gas distributor. A simple schematic side view of the Hall thruster structure is shown in Fig. 2.

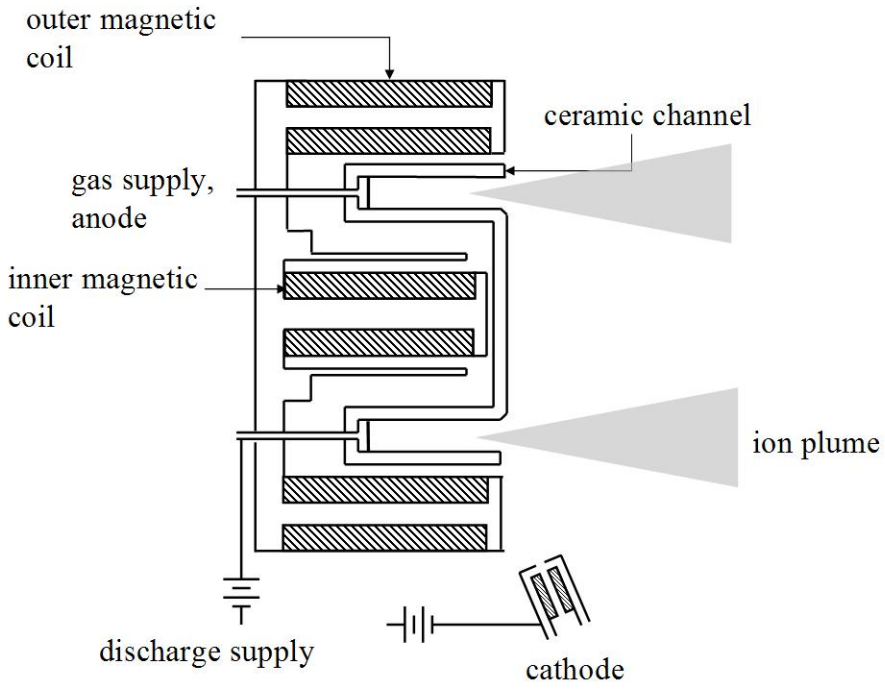

Figure 2: Side view of the Hall thruster structure

Hall thruster operation

Hall thruster operation is based on the interaction of charged particles with orthogonal magnetic and electric fields. A potential difference is imposed between the cathode and anode. The cathode is electrically heated and fed with a supply of Xenon gas, which is subsequently converted to a cathode plasma, which becomes the source of the ejected cathode electrons. Some electrons ejected by the cathode drift in the direction of the anode, while others are directed into the thruster plume.

The confinement of the electrons to a "closed drift" path near the thruster exit, where they circulate azimuthally, is strongly dependent on the magnetic field characteristics. The choice of magnetic field magnitude is designed to give the electrons a small Larmor radius (on the order of 1 mm), constraining them to wrap around the magnetic field lines and remain within the channel (which has a length of 2.5 cm and width of 1.5 cm in the case of the SPT-100). In contrast, the large Larmor radius of the ions (exceeding 1 m) allows them to exit the thruster channel with minimal deviation. The combination of the axial electric field $\vec{E}$ and radial magnetic field $\vec{B}$ produces an azimuthal electron drift of velocity V_d,

$$V_d = \frac{\vec{E} \times \vec{B}}{B^2} \approx \frac{E_x}{B_r} \tag{2}$$

The magnetic field increases to a maximum near the thruster exit and this configuration helps stabilize the electric field distribution [54]. The field lines are also concave, resulting in higher magnetic field strength near the walls than in the centre of the channel; this configuration results in a "magnetic mirror effect", first described in the thruster by Morozov in 1968, which reduces electron-wall losses. This effect influences the electric potential and consequently, the ion acceleration characteristics [38].

Xenon atoms flow into the discharge chamber via the anode and are ionized by the electrons (with ionization rates around 90%), and the ions are accelerated out of the chamber by the electric field. Some electrons ejected by the cathode drift into the plume and neutralize the ions. The majority of the ions are generated inside the thruster channel, in an ionization zone, and accelerated near the exterior of the chamber in a region of high localized electric field, where the electron mobility is small. One of the earliest experimental studies of the effectiveness of the acceleration mechanism and the nature of thruster characteristics such as the electron density distribution in the channel was provided by Bishaev and Kim [7].

The plasma potential is maximum at the anode (equal to the anode potential), where the magnetic field is weak and electron mobility high. It decreases towards the exit, approaching the cathode potential, while the magnetic field increases. This evolution in the magnitude of the potential affects the energy distribution of the accelerated ions. The magnetic and electric field distributions in a typical Hall thruster are shown qualitatively in Fig. 3.

Thrust is imparted to the vehicle via the magnetic field. The azimuthal electron drift and the radial magnetic field produce a force on the electrons equal to the electric field force exerted on the ions (assuming that the number of electrons is equal to the number of ions in the thruster channel). As will be seen in the next section, despite the relatively straightforward mechanism of thrust generation, various phenomena with implications on efficiency and lifetime occur in the Hall thruster.

An overview of Hall thruster phenomena

The physical processes which take place in the Hall thruster are complex, and a number of the most important processes are described below.

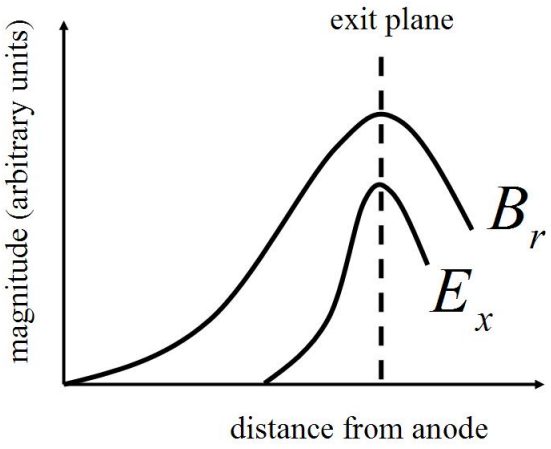

Figure 3: Characteristic magnetic and electric field distributions in a Hall thruster

Thruster erosion

Erosion of the ceramic walls of a Hall thruster is the single most important factor limiting its lifetime. The erosion occurs in two stages. In the first stage, "classical" erosion of the ceramic occurs by ion bombardment, after the first few hundred hours of thruster operation [54, 53]. This erosion causes sharp ridges spaced by about 0.1-0.2 mm to form, and slows as the ceramic wears down to match the ion plume divergence with respect to the thruster axis, which is about 45°. "Anomalous" erosion then begins, in the form of sharp, equally-spaced striations spaced by 1-2 mm and oriented parallel to the ion flux. Anomalous erosion is believed to be due to electron bombardment, however, the mechanisms involved are unclear. Baranov has proposed that the source of such erosion is the formation of a periodic structure at the thruster exit, caused by plasma oscillations [4]. Oscillations of this type may have been observed in the present work.

The thrust and efficiency of the thruster are not affected for several thousand hours despite this wear. However, should the magnetic circuit become exposed, there is a risk of metal deposition on the surfaces of spacecraft elements, such as solar panels. While this has not affected recent Hall thruster missions, it could pose a problem for longer-duration flights.

Anomalous electron transport

Anomalous electron transport is the transport of electrons across the magnetic field, and represents another poorly-understood aspect of Hall thruster operation. The phenomenon manifests as an unusually high electron current towards the anode. Some consequences include reduced thruster efficiency and anomalous erosion. It is commonly attributed to a number of causes:

- Electron-atom collisions in the channel could result in deviations of electrons from their guiding centres. The cumulative effect of many such collisions resembles Brownian motion and results in classical diffusion across the magnetic field. The diffusion

coefficient $D_{\perp c}$ associated with such collisions is derived from an analogy with Fick's law and is written

$$D_{\perp c} \sim \nu_c {\rho_{ce}}^2 = \frac{\eta_{\perp c} n_0 \Sigma k_B T_e}{B^2} \tag{3}$$

where ν_c is the collision frequency, and ρ_{ce} is the electron Larmor radius and the characteristic displacement length per collision. $\eta_{\perp c}$ is the resistivity perpendicular to B, n_0 the plasma density, k_B Boltzmann's constant and T_e the electron temperature [12].

However, Janes and Lowder [36] demonstrated using probe measurements that the actual electron current towards the anode in a device with Hall thruster geometry is much larger (2 to 3 orders greater) than classical diffusion would predict. This important result was an indication that another mechanism plays a role in enhanced transport.

- Electron-wall collisions as a transport mechanism were studied in great detail by Morozov [51, 52], who described the mechanism as "near-wall conductivity". The efficiency of this transport depends on the potential of the plasma sheath at the walls; provided the voltage jump is small enough, electrons can reach the walls and be reflected off them in random directions, contributing to anomalous transport. Experiments performed by Bugrova and colleagues [10] have demonstrated the presence of populations of electrons with enough energy to cross the plasma sheath to cause transport, and secondary effects such as oscillations arising in the plasma sheath are also believed to influence transport [64].

- Plasma oscillations at the thruster exit have been proposed to account for the high electron mobility in this area. While wall collisions go some way to accounting for mobility inside the channel, they are relatively scarce at the thruster exit. Measured mobility at the exit is two orders of magnitude larger than could be produced by collisional diffusion, and the existence of oscillations provoking anomalous transport, or Bohm diffusion, [31] was suggested. The underlying idea of Bohm diffusion is that plasma oscillations cause "drain diffusion" by causing particles to move randomly back and forth, allowing transport across the magnetic field to occur more readily.

  The Bohm diffusion coefficient is written

$$D_{\perp B} \sim \frac{k_B T_e}{16 B e} \tag{4}$$

  where e is the electron charge. The idea that oscillations contribute to axial transport of electrons has led to a large number of studies designed to demonstrate the presence of oscillations and determine their possible contributions to the current.

Secondary electron emission

Electron bombardment of the thruster channel can liberate secondary electrons ("secondary electron emission", or SEE). Secondary electron emission from the wall material lowers the sheath potential, increasing the proportion of electrons with sufficient energy to reach the walls and contribute to axial conductivity. The contribution of SEE to backscattering and axial electron conduction has been demonstrated in a number of numerical and experimental studies ([19, 34, 23]), and the influence of the phenomenon on thruster discharge was discussed in [25].

Spontaneous plasma oscillations

A wide range of oscillations, of different length scales and frequencies, arise in the thruster [14]. Some are generated by thruster processes such as ionization and gas depletion, while others arise because of the relative drift of the electron and ion species, or because of field and density non-uniformities. Their presence has significant consequences on the thruster discharge, stability of operation and lifetime, and is influenced by a wide variety of parameters, including the magnetic field strength, discharge voltage and current, and gas flow rate. The general features and origins of some of the oscillations present are summarized below.

1. Contour and ionization oscillations (frequencies 1-100 kHz): these oscillations are usually related to the time required for an atom to travel the discharge channel and also depend on the discharge circuit. Near the channel exhaust, in the region of high electric field and electron temperature, rapid ionization depletes the neutrals. The neutral front retreats towards the anode, and consequently ionization and electron density at the exit drop. The neutrals then flow back again towards the exit and the cycle is repeated. These oscillations are of very high amplitude and result in large variations in the discharge current and voltage. They are also termed as "breathing modes" and have been measured experimentally at frequencies of a few tens of kHz by several authors ([8, 15, 46, 22]) and have been demonstrated numerically [32, 2].

2. Azimuthally-propagating oscillations (low frequency, 10-100 kHz)): low frequency oscillations linked to the ionization process are seen to propagate in the direction of the azimuthal electron drift. The earliest identifications of the low frequency, rotating "spokes", or density concentrations, were made by Janes and Lowder [36]. Esipchuk and colleagues [20] also observed an isolated ionization wave of low frequency rotating azimuthally. The higher frequency oscillations in this category are due to non-uniformities in the density and magnetic field.

3. Azimuthally-propagating oscillations (high frequency, 1-100 MHz): these oscillations were first observed experimentally in the Hall thruster geometry by Esipchuk and Tilinin [21]. They performed a numerical analysis which revealed the presence of these oscillations in the plasma density, from frequencies of tens of kHz to several tens

of MHz, and measured what they termed "electron drift waves" at frequencies of 2-5 MHz. Various subsequent experiments ([57, 50, 47, 60]) and numerical simulations ([2, 39]) have confirmed the presence of azimuthal high frequency oscillations localized in the vicinity of the thruster exit.

The exact source of the high frequency oscillations in the azimuthal direction is not known. Theoretical analysis by Litvak and Fisch [49] showed that these oscillations could be manifestations of a Rayleigh instability and ascribed to axial gradients in magnetic field, electron density and drift velocity. Other works [2] show that the large drift velocity could be the source of the instability.

4. Ultra high frequency oscillations (several GHz): these oscillations are associated with electron layers and flows of highly energetic electrons parallel and perpendicular to the magnetic field [65]. These oscillations have been identified in very few studies [6].

Background and context of this work

The present work is devoted to the identification and characterization of certain high frequency modes at the thruster exit which are believed to play an important role in anomalous electron transport.

As discussed earlier, there is an increasing need for the development of higher powered Hall thrusters. However, due to the complexity of processes occurring in the thruster, it has been necessary to rely on incremental improvements which must be tested at every stage. This development process is both costly and inefficient. For this reason, a vast research effort is underway to better understand aspects of thruster physics, with the goal of developing predictive models for its operation at different scales and improving thruster efficiency.

The numerical approach to modelling takes a number of forms.

1. Hybrid-PIC (particle-in-cell) approaches model the electrons as a fluid, and the ions and neutrals as particles. Assumptions of quasineutrality require the use of transport equations to determine the electric field, otherwise the field may be deduced from Poisson's equation. Such models, whether one-dimensional (axial coordinate) or two-dimensional (radial and axial coordinates), have proven extremely useful for describing physics of the ion and neutral time scales. Work by Fife [22] as well as Boeuf and colleagues using hybrid-PIC models successfully demonstrated the presence of the thruster breathing mode [8, 5], as well as other oscillations of higher frequency [32]. Various other features of the thruster, such as the relationship between the beam divergence and the oscillations, and the profiles of electric potential, plasma density and ionization rate in the channel have also been calculated. Koo and Boyd have determined parameters such as thrust and specific impulse using this modelling approach [41]. It has been applied not only to discharge characteristics, but to the study of features such as thruster erosion after several thousand hours [40].

   These methods require different electron mobilities inside and outside the thruster channel in order to account for the experimentally-measured discharge current, con-

firming the likely role of instabilities at the thruster exit in enhanced transport. Despite the successes of these codes, they rely on mobilities obtained from experimental data [42], and cannot therefore be fully predictive. In addition, as the electron time scales are much shorter than those of ions, the codes fail to describe the high frequency oscillations which may contribute to transport.

Recent efforts have adapted this approach by assuming from the start the presence of an azimuthal electric field and following electron trajectories in three dimensions; with this approach, it has been determined that turbulence can indeed make electron trajectories chaotic, leading to transport [56].

2. The two-fluid approach models electrons and ions as fluids. This approach has been successfully used in demonstrating wave coupling and the presence of axial and azimuthal high frequency modes [39]. It has also permitted the identification of the Kelvin-Helmholtz shearing instability as a possible mechanism in the perturbation of the potential and velocity.

3. Purely particle-in-cell approaches towards modelling both ions and electrons have also produced important insights into the physics of the discharge. Hirakawa and Arakawa [34] showed that the axial electron flux was best modelled using Bohm mobility, and also that an azimuthal electric field was necessary to explain this flux. Adam, Héron and Laval [2] produced a self-consistent, two-dimensional simulation which predicted the length scales and frequencies for the azimuthal wave responsible for transport. Such PIC simulations require considerable computing power and time in order to model the entire discharge and would therefore not be feasible for industrial development.

4. Additional numerical approaches have been used, including three-dimensional simulation of electron trajectories using experimentally-determined electric and magnetic fields [3, 58].

In summary, a great effort to simulate thruster characteristics has been undertaken using different numerical approaches. The difficulty rests in accurately modelling the different species involved, while taking into account additional effects such as secondary electron emission and sheath dynamics, for which little experimental data is available. A second challenge is to reduce the time and computational expense required for three-dimensional models. Lastly, none of the numerical methods available today can model accurately all the thruster operating regimes.

Theoretical approaches to studying the Hall thruster have proven very useful in accounting for, as well as predicting, certain phenomena. The azimuthal drift wave has received particular attention. Early work by Esipchuk and Tilinin [21] was the first to demonstrate theoretically the presence of such a wave, propagating at the drift velocity and at frequencies on the order of a few MHz. More recently, linear theory has been used to identify dispersion relations of an azimuthal wave and the criteria for which it becomes unstable [2].

Overall, theoretical analyses of the Hall thruster have provided useful interpretations of thruster physics. However, these models require important simplifications (assumptions

on gradients, reduced dimensions, neglect of effects for which little experimental data is available) and can often only explain one particular aspect of thruster operation at a time.

The bulk of experimental measurements on the Hall thruster have focused on the use of probes and antennae (invasive and non-invasive).

Probe measurements have been used since the inception of the Hall thruster concept, first by Janes and Lowder to provide evidence of the role of the azimuthal density variations in anomalous electron diffusion. They have also been used to provide evidence of the existence of electron populations of different energies and their contributions to near wall conductivity [10] and to study the acceleration and ionization zones [7]. Various other probe studies have been able to measure ionization, transit time oscillations and azimuthal oscillations [22, 45, 50]. Uncalibrated antenna measurements have also been used successfully to measure high frequency oscillations [60, 44, 57]. Certain other optical techniques such as optical emission spectroscopy and laser induced fluorescence have been used to characterize ions in the acceleration and ionisation zones, and are suited primarily for studying ion and neutral characteristics such as spatial velocity distributions.

This work draws its inspiration from the work of Adam et. al. in 2004 [2]. This numerical study was the first self-consistent 2D PIC simulation to demonstrate that thruster turbulence could account for anomalous transport. The most significant results from this work were the identification of:

- an azimuthal wave, of wavelength on the order of electron Larmor radius, near the thruster exit and possibly responsible for electron heating and transport,
- a vector component of the wave parallel to $\vec{E}$,
- a wave frequency on the order of a few MHz
- a large-amplitude electric field fluctuation associated with the wave

These predictions have lacked experimental support, because no conventional experimental tools available at the time (or since) could measure fluctuations in the electric field at millimetric length scales, inside the high temperature plasma. The smallest scales measurable via antennae and probes are on the order of a centimetre [47]. A non-invasive collective light scattering diagnostic has the potential of measuring the scales predicted to be significant in transport. This work was therefore dedicated to the construction and exploitation of one such diagnostic, in order to validate key theoretical and numerical predictions.

This work is organized in the following way.

The important principles underlying collective light scattering and heterodyne detection are summarized in Chapter 1. An early collective scattering trial which helped to define the requirements of the new collective light scattering bench, PRAXIS-I, is briefly presented.

Design details and experimental procedures for PRAXIS-I are presented in Chapter 2. Chapter 3 deals with the range of experiments carried out using this bench and the general properties of the observed modes are described. Physical interpretations of the early results are presented and a comparison of the results to the predictions of simple linear theory performed.

The second part of this work deals with a new series of experiments made possible by an upgrade of PRAXIS-I. The necessary improvements to PRAXIS-I and the newly-designed collective scattering bench, PRAXIS-II, are presented in Chapter 4.

Experiments with the goal of localizing the modes and determining the significance of the negative peak frequencies are described in Chapter 5. Chapter 6 focuses on the measurements of the directionality of the observed modes, concluding with a re-calculation of the true density fluctuation level.

Chapter 7 compares the experimental results to the solutions of the 3D theoretical dispersion relation, describing key similarities and differences. A re-evaluation of a proposed electron transport mechanism is performed, using the fluctuating field amplitude deduced from the density fluctuation characteristics.

Chapter 8 deals with the influence of varying thruster parameters on the characteristics of the observed modes, with a focus on the effects of varying flow rate, magnetic field strength and discharge voltage. Observations of low frequency oscillations are also described in this chapter.

Chapter 9 presents a new stability analysis of longitudinal plasma waves, such as are observed experimentally, which takes into account the ion velocity and temperature.

The main text is concluded with a summary of the most important results and a description of future work.

Part I

Chapter 1

Main concepts and preliminaries

Contents

1.1 Collective light scattering as an experimental tool

COLLECTIVE light scattering (CLS) refers to an optical measurement technique whereby the "collective" movements of a medium, due for example to the propagation of waves, are studied using the elastic scattering of incident radiation by a non-uniform spatial distribution of particles. These particles are either atoms (in the case of Rayleigh scattering in a neutral gas), or electrons and ions (in the case of Thomson scattering in a plasma).

Light scattering is a technique which has been used to study the properties of different media for several decades. It has been used for studying large molecules in solution in chemistry, however, studies of characteristics such as thermal fluctuations at the level of constituent particles [55, 30] only became possible with the advent of lasers in the 1960's. Light scattering techniques have been used to study turbulent liquids, via the seeding of the flow with particles [63, 28].

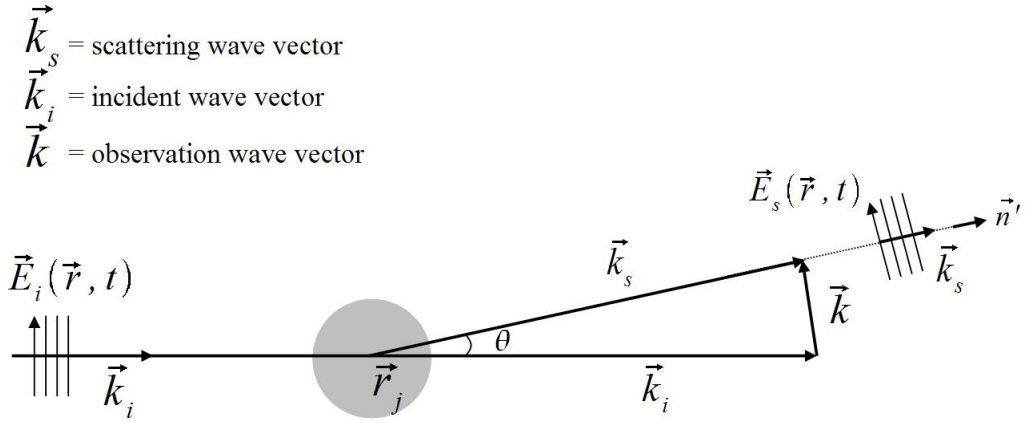

Figure 1.1: Scattering of an incident plane wave by particles

CLS is based on measurements of inhomogeneities inherent to the flow itself, rather than passive scalars which have been introduced into the flow. CLS has been applied to the study of gas flows [29, 9] and in magnetized plasmas to study features such as edge and core turbulence and to determine scaling laws of density fluctuations [62, 16, 33]. The breadth of applications of this technique are proof of its versatility.

Collective light scattering possesses certain advantages over traditional techniques. Unlike many methods (such as probes and hot-wires), it does not induce a perturbation of the medium under investigation and the measurement volume may be situated virtually anywhere in the flow, provided there are no optical obstructions to this. In the majority of thruster studies, probes are inserted into the ceramic wall, but cannot be used directly in the plume without damage due to the high temperature of the plasma. Using particles as passive scalars in a flow is not always possible, and CLS circumvents this default. Exactly how this is done will be explained in the next section.

1.1.1 Basic principles

An electromagnetic wave incident on a charged particle will accelerate it, causing it to re-emit another wave whose properties (frequency, wavenumber) depend on the incident wave, and whose amplitude depends on the particle's distance to the observer. Figure 1.1 illustrates the scattering of an incident plane wave $\vec{E_i}(\vec{r},t)$ by a group of particles situated at $\vec{r_j}$. The incident wave at the position $\vec{r_j}$ is of the form

$$\vec{E_i}(\vec{r},t) = \vec{E_{i0}} e^{i(\vec{k_i}\cdot\vec{r_j}-\omega_i t)} \tag{1.1}$$

The scattered e.m. wave is $\vec{E_s}(\vec{r},t)$. It is observed at an angle θ to the incident wave.

In Fig. 1.1, the observation wave vector is constructed from the vector sum of the scattering and incident wave vectors ($\vec{k} = \vec{k_s} - \vec{k_i}$). This is known as the Bragg relation.

Each electron may be considered as a dipole oscillating in the direction of the electric field of the incident wave, acting as a point source for a spherical wave. With this approximation, the total scattered field may be written as the summation of all the scattered waves,

$$\vec{E_s}(\vec{r'},t) = r_0 \sum_j \frac{e^{ik_i\left|\vec{r'}-\vec{r_j}\right|}}{\vec{r'}-\vec{r_j}} e^{-i(\vec{k_i}\cdot\vec{r_j}-\omega_i t)} \vec{n'} \wedge (\vec{n'} \wedge \vec{E_{i0}}) \tag{1.2}$$

where r_0 is the Thomson scattering radius for free electrons,

$$r_0 = \frac{1}{4\pi\epsilon_0}\frac{{q_e}^2}{m_e c^2} \tag{1.3}$$

Using a far-field approximation (i.e. where $|\vec{r'}| \gg |\vec{r_j}|$ and $|\vec{r'}| \gg \lambda_i$), the scattered field may be simplified to a superposition of plane wave fronts. With the aid of the reasonable assumption that the analysing wavelength $\frac{2\pi}{k}$ is much larger than the particle spacing, the total scattered field from a volume V_s may be written as

$$\vec{E_s}(\vec{r'},t) = r_0 \frac{e^{i\vec{k_s}\cdot\vec{r'}}}{r'} e^{-i\omega_i t} \vec{E_{i0}} \int\int\int_{V_s} e^{-i\vec{k}\cdot\vec{r}} n(\vec{r},t) d^3\vec{r} \tag{1.4}$$

Hence, the magnitude of the scattered field is proportional to the spatial Fourier transform of the density along $\vec{k}$, $\int\int\int_{V_s} e^{-i\vec{k}\cdot\vec{r}} n(\vec{r},t) d^3\vec{r}$.

If the electrons are distributed randomly in space, the sum of their phases, $\Sigma e^{-i\vec{k}\cdot\vec{r}}$, and therefore the scattered signal magnitude, is small. If, instead, the electrons are distributed in regular manner, on planes perpendicular to $\vec{k}$ as in Fig. 1.2, such that

$$\vec{k}\cdot(\vec{r_{j+1}}-\vec{r_j}) = 2\pi, \tag{1.5}$$

the sum of phases is additive and the scattered signal is large. This is equivalent to saying that the projections of the positions $\vec{r_j}$ in the direction $\vec{n_k}$ are spaced a distance $\lambda_0 = \frac{2\pi}{k}$, such that

$$\vec{n_k}\cdot(\vec{r_{j+1}}-\vec{r_j}) = \lambda_0 \tag{1.6}$$

In this way, a longitudinal wave propagating in a plasma may be identified via its periodic density concentrations. In a compressible, turbulent fluid medium, the scattered signal is obtained due to the presence of coherent structures in the flow.

The wave number k is a property of the medium under consideration, which may be related to the incident wave number k_i. $\vec{k_i}$ and $\vec{k_s}$ have the same magnitude, and k may therefore be written

$$k = 2k_i \sin\left(\frac{\theta}{2}\right) \tag{1.7}$$

and λ_0 as

$$\lambda_0 = \frac{1}{2\sin\left(\frac{\theta}{2}\right)}\lambda_i \tag{1.8}$$

Hence the length scales of periodic density concentrations which may be measured by collective scattering, for angles θ of typically few mrad, are several times the incident wavelength.

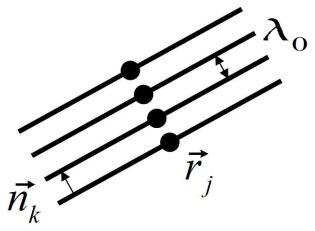

Figure 1.2: Distribution of electrons for a large scattered signal

1.2 Heterodyne detection

1.2.1 Necessity for heterodyne detection

The scattered field may be detected directly by a photodiode. The current produced is proportional to the scattered field intensity on the surface, i.e. the Poynting vector flux across the detector surface D. The detector is placed perpendicular to the direction of propagation of the wave, and the resulting power received on the detector, P_s, is written

$$P_s(t) = \frac{N}{\mu_0 c}\int\int_D \left|\vec{E_s}(\vec{r'},t)\right|^2 d^2\vec{r'} \tag{1.9}$$

using Eq. 1.4, this becomes

$$P_s(t) \propto \left|\int\int\int_{V_s} e^{i\vec{k}\cdot\vec{r}} n(\vec{r'},t) d^3\vec{r}\right|^2 \tag{1.10}$$

This form of P_s is inadequate, for two reasons:

- the scattered power is small and very difficult to detect,
- a complete description of the scattered field requires both the temporal phase information due to convection and the magnitude of the density fluctuation; the former is missing from Eq. 1.10.

Heterodyne detection is therefore used to overcome these disadvantages by providing a signal of sufficient amplitude containing the phase information.

1.2.2 Basic elements

The local oscillator

Heterodyne detection uses the combination of the scattered signal and a reference signal, shifted in frequency but propagating in the same direction, to produce an interference term measurable by the detector.

The reference signal is known as the local oscillator and has frequency ω_{LO}, and the frequency shift is ω_m: $\omega_{LO} = \omega_i + \omega_m$.

ω_m is much smaller than ω_i, allowing the scattered radiation and the local oscillator to remain in phase. ω_m is chosen to be smaller than the passband of the detector (which is around 1 GHz) and larger than the frequency range of the expected signal. The local oscillator amplitude used is as large as is permissible by the detector, in order to maximize the amplitude of the interference term and thus the ease with which it may be detected.

The primary beam

The primary beam is another necessary reference beam, not measured at the detector. It is used to define the direction of the incident wave vector k_i and thus the scattering angle θ, as well as the dimensions of the scattering volume V_s. It is also a high intensity beam - depending on the application, it may typically have an intensity a few orders of magnitude larger than the local oscillator - which enables the emission of a scattered signal of a large amplitude.

Fig. 1.3 shows the arrangement of primary and local oscillator beams.

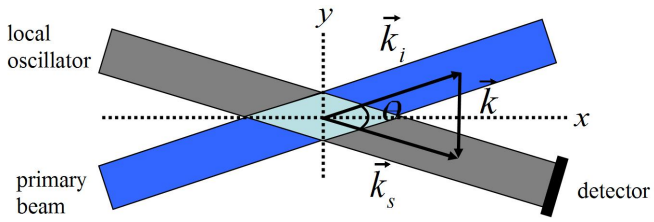

Figure 1.3: Local oscillator and primary beams as used in heterodyne detection. The beams intersect and create a common volume (light blue) centred in the region of interest.

Observation region characteristics

The observation volume obtained from the intersection of two Gaussian beams of waist w is

$$V_s = \frac{\pi^{3/4} w^3}{4\theta} \tag{1.11}$$

The longitudinal integral length, l_l, of V_s (along x in Fig. 1.3) is

$$l_l = \frac{\sqrt{\pi}w}{\theta} \tag{1.12}$$

while the transverse integral length, l_t, is

$$l_t = \frac{\sqrt{\pi}w}{2} \tag{1.13}$$

The longitudinal wave number resolution is given by

$$\delta k_l = \frac{\theta}{w\sqrt{2}} \tag{1.14}$$

while the transverse wave number resolution is

$$\delta k_t = \frac{2\sqrt{2}}{w} \tag{1.15}$$

1.2.3 Measured signal

Interference term

The field arriving at the detector is due to a combination of the scattered wave, $\vec{E_s}(\vec{r'}, t)$ and the local oscillator, $\vec{E_{LO}}(\vec{r'}, t)$. The squared modulus of this total field is

$$\left|\vec{E_s}(\vec{r'}, t) + \vec{E_{LO}}(\vec{r'}, t)\right|^2 = \left|\vec{E_{LO}}(\vec{r'}, t)\right|^2 + 2\vec{E_s}(\vec{r'}, t) \cdot \vec{E_{LO}}(\vec{r'}, t) + \left|\vec{E_s}(\vec{r'}, t)\right|^2 \tag{1.16}$$

The resulting total power on the detector is comprised of three contributions,

$$P_{tot}(t) = P_{LO} + P_b(t) + P_s(t) \tag{1.17}$$

P_{LO} is the constant local oscillator power, $P_b(t)$ the interference term, and P_s the power due to scattered wave alone. The interference term is written

$$P_b(t) = \frac{N}{\mu_0 c} \int\int_D 2\vec{E}_{LO}(\vec{r'}, t) \cdot \vec{E_s}(\vec{r'}, t) d^2\vec{r'} \tag{1.18}$$

The current on the detector resulting from this interference term is

$$i_b(t) \propto \Re e^{i\omega_m t} s(\vec{k}, t) \tag{1.19}$$

where ω_m is the frequency modulations of the scattered signal after interference.

Reconstitution of the scattered signal

The scattered signal is recovered in the following way:

- the current received by the photodiode is split into two parts: a continuous component (due to the constant local oscillator current), and a time-varying component (due to the interference of the fields).
- the time-varying signal is amplified in a low noise amplifier
- the time-varying signal is then split into two parts for demodulation: the first part is multiplied by a signal at frequency ω_m, the second multiplied by another signal of frequency ω_m but in quadrature with the first
- low-pass filters are applied to both parts of the signal to remove the term of frequency $2\omega_m$ arising from the previous step
- both parts of the signal are amplified

The individual contributions of the signal (real and imaginary) are then combined as

$$s(\vec{k}, t) \propto [x_f(t) + iy_f(t)] \tag{1.20}$$

Eq. 1.20 contains all the time-varying characteristics of the scattered signal; the continuous current value is retained for signal normalization.

Absolute measurement of density fluctuation

The measurable component of the scattered signal defined by the scattering volume V_s. Hence the signal received at the detector is not only a function of the density, but also the beam profile $U(r)$ [35], i.e.

$$s(\vec{k}, t) = \int n(r', t)\ U(\vec{r}) e^{i\vec{k}\cdot\vec{r}} dr^3 \tag{1.21}$$

A Fourier transform is performed on this signal to give the spectral density.
The mean square density fluctuation rate, assuming a Gaussian volume profile, is

$$\frac{\langle \tilde{n}^2 \rangle}{n_0^2} = \frac{1}{4\pi^3 \left|r_0^2\right| \lambda^2 {l_s}^2 {n_0}^2} \frac{\hbar w}{\eta P_P} \int_{-\infty}^{+\infty} \frac{I_k(\omega)}{I_n} \frac{d\omega}{2\pi} \tag{1.22}$$

where I_n is the photonic noise spectral density, defined as

$$I_n = e^2 \frac{\eta P_{LO}}{\hbar w} \tag{1.23}$$

n_0 is the mean density of the measurement region. λ is the incident wavelength, l_s the scattering length (much smaller than the dimension l_l of the scattering volume), η the detector efficiency, P_P the power of the primary beam, and w the beam waist in the measurement region. The term $I_k(\omega)$ is the spectral density of the scattered signal at a particular wave number k. A full development of this expression can be found in [29].

1.3 Collective scattering on the Hall thruster: first trial

As mentioned in the introduction, density fluctuations at short length scales, which cannot be measured by other means, can potentially be determined using CLS . It was therefore suggested by G. Laval (CPHT, Ecole Polytechnique) and A. Bouchoule (GREMI, Université d'Orléans) in 2004 that a CLS diagnostic be installed for tests on an SPT-100 thruster. The first attempt with such a diagnostic was undertaken by N. Lemoine and D. Grésillon in 2006. A summary of the main results and conclusions of this first trial will be presented.

Thruster characteristics

The thruster used for this preliminary trial was the SPT-100, an upgraded version of that originally designed by the Russian manufacturer Fakel. Its general characteristics are presented in Table 1.1.

Dimensions	Discharge channel length (cm)	2.5
	External diameter (cm)	10
	Internal diameter (cm)	7
	Cathode distance below axis (cm)	8
Nominal operating parameters	Discharge voltage (V)	300
	Discharge current (A)	4.2
	Flow rate (mg/s)	5
Performances	Thrust (mN)	80
	Specific impulse (s)	1700
	Efficiency (%)	50

Table 1.1: Summary of main SPT-100 thruster characteristics

Plasma parameters

The SPT-100 thruster magnetic field (B_0) and electric field (E_0) strengths used were 0.02 T and 4×10^4 V/m respectively. The plasma density assumed was 5×10^{17} particles per m^3. These parameters are used to determine plasma characteristics, such as an electron cyclotron frequency, ω_{ce},

$$\omega_{ce} = \frac{eB_0}{m_e}$$

The value of ω_{ce} is 3.5×10^9 rad/s. The drift velocity, V_d, is E_0/B_0, a value of 2×10^6 m/s. The ion plasma frequency, ω_{pi}, is

$$\omega_{pi} = \sqrt{\frac{n_0 e^2}{\epsilon_0 m_i}}$$

ω_{pi} is 8.2×10^7 rad/s.

Expectations from theory and simulation

Linear theory predicts that the azimuthal drift instability arises only for certain discrete wave numbers (this will be discussed in more detail in Chapter 3). Simulations show that the excited azimuthally-propagating instability is present within a wave number range of 2600 - 13300 rad/m. The range of wavenumbers accessible during this trial is 3200 - 19200 rad/m.

The predicted intensity of the fluctuations has been determined to be on the order of 8×10^6, while the expected frequency dispersion is 10^7 Hz.

Expectations from existing optical bench

The collective scattering bench used was initially built for turbulent aerodynamics experiments performed twenty years ago [11]. It used a CO_2, 10.6 μm-wavelength, 3 W laser. The beam waist in the convergence zone in front of the thruster was 5 mm.

The bench was installed on the SPT-100 Hall thruster with the local oscillator and primary beams crossing in front of the thruster face at a distance of 10 mm. The thruster was operated at a flow rate of 6 mg/s. The beams, on leaving the bench, entered and exited the thruster vacuum vessel through ZnSe windows. The plasma-scattered radiation and the local oscillator beam were recovered by mirrors and sent to a detector on the bench.

The estimated signal-to-noise ratio was 2.4, which suggested that this optical bench was already sufficiently sensitive for the measurement of the electron density fluctuations. Only minor modifications to the bench optics were made to adapt it to the experiment.

1.3.1 Results from experiment

Low frequency signal

An intense signal at 30 kHz, up to 30 dB above the noise, was observed (Fig. 1.4). The frequency of this signal was independent of the wavenumber, however, its magnitude was largest at small wavenumbers and at higher Xe flow rates and magnetic field values.

Surprisingly, this signal was present even with the detector closed, an indication that the signal measured was not a collective scattering signal, but represented instead a plasma oscillation picked up by the electronics circuit.

Broadband high frequency signal

The expected broadband, high frequency signal was not immediately apparent on the spectra (with frequencies analyzed up to 10 MHz). Repeated aquisitions were made of the plasma signal to increase the number of points (which was limited by the oscilloscope at each acquisition to 200,000) and averaged, and the noise signal treated in the same way. Averaging was performed over 4×10^7 samples. The net signal obtained after subtraction of the photonic

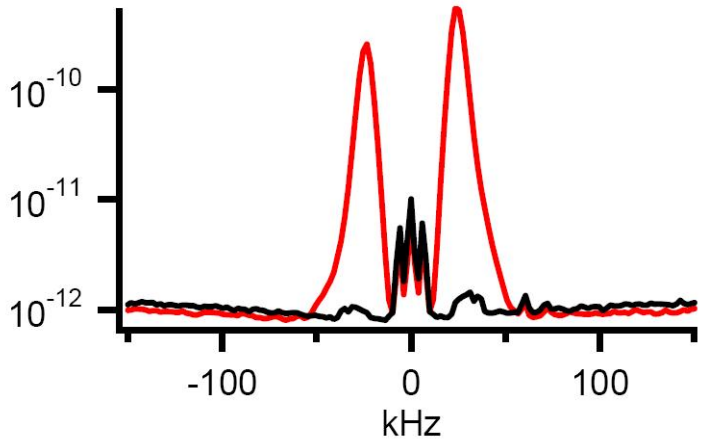

Figure 1.4: 30 kHz frequency peaks. In red - plasma signal, in black - photonic noise. The y-axis is in arbitrary units

noise was very small (5×10^{-16} arbitrary units) but positive, and twice the sensitivity level of the measurement (2×10^{-16}). The photonic noise r.m.s. level was 1.6×10^{-13} in the same units.

The final signal-to-noise ratio corresponding to this experiment was only 3×10^{-3}.

The trial experiment provided some initial evidence as to the presence of a very small collective scattering signal from the plasma at the length scales of interest. It indicated the need to increase the signal-noise ratio by about a factor of about 300 in order for the scattered signals to become readily detectable. This initial evaluation provided the motivation for the creation of a specially-adapted, high-performance optical bench. A number of initial ideas for improving the detection of the signal were proposed at the end of the trial:

- increasing the laser power
- reducing the beam waist in the measurement zone
- implementation of a trigger to eliminate noise records - the signal is believed to be intermittent and a typical sequence contains several periods during which only noise is present. The signal-noise ratio could be increased by recording only the time segments during which the signal is present
- electronics shielding to reduce pickups of stray signals

Chapter 2 will describe measures taken to improve the signal-noise ratio.

Chapter 2

PRAXIS-I

Contents

THE first trial revealed the necessity for dramatically increasing the signal-noise ratio. A number of basic design and construction decisions were made specifically to attain this goal. A new optical bench, known as PRAXIS-I (**PR**opulsion **A**nalysis e**X**periments via **I**nfrared **S**cattering), was constructed. The design decisions for increasing the signal level are described below.

2.1 Main approaches for increasing signal-noise ratio

1. Beam power: The simplest method of increasing the signal-to-noise ratio involved increasing the laser power. A GEM Select 50 W Coherent^{TM} laser (42 W effective power) CO_2 laser, wavelength 10.6 μm, replaced the 3 W laser used in the first trial. The expected gain in the scattered signal was a factor 14.

2. Optics: Losses at the mirror surfaces were reduced. The original bench used highly-polished steel mirrors, with a reflectivity of 95%, however, given the large number of mirrors necessary to direct the beams, the final power losses of both primary and local oscillator beams were significant. Gold-coated copper mirrors (reflectivity 99%) and a large number of treated copper mirrors (reflectivity 99.8%) were therefore used on PRAXIS-I. The expected gain in signal over the previous bench was a factor larger than 2.

3. Beam characteristics: The beam waist in the observation zone was reduced from the original value of 5 mm to 2.5 mm, resulting in a factor 4 increase in the signal.

4. Acquisition: The 8-bit oscilloscope (acquisition rate 25MHz, 200,000 samples per channel) used in the previous trial was replaced with a numerical acquisition module from National Instruments, providing 14-bit resolution and an acquisition rate of up to 100 MS/s (with 6.5 MS per channel being acquired). The advantages of this acquisition module were three-fold:

   - the high resolution allowed the weak signal to be more easily extracted from the background noise
   - the larger number of samples allowed for more sophisticated post-acquisition processing
   - the higher acquisition rate made it possible to record higher frequency signals

   The final gain in signal was expected to exceed a factor of 5.

5. Detection: The detector from the previous bench (quantum efficiency of 0.3) was replaced with another of quantum efficiency of 0.7, providing a gain in the signal level of a factor 2.3

The final resulting gain in signal using PRAXIS-I, over the 2006 trial, was projected to be at least a factor of 1250.

2.2 PRAXIS-I design

The design of PRAXIS-I is presented in this section.

2.2.1 On-bench assembly

The bench design is shown in Fig. 2.1 and a description of certain critical components of the optical bench are briefly presented below. In Fig. 2.1 the optical path of the primary beam is shown in red, the local oscillator path in blue.

In the figure, M and MT are used to denote mirrors, with MT referring only to the large mirrors which are common to both primary and local oscillator beams. L represents the

lenses, BS the beam-splitter, DET the detector and AOD the acousto-optical deflector. TR denotes the translator-rotator and $A1$ an absorber. $A2$ is a diaphragm used in the off-bench assembly.

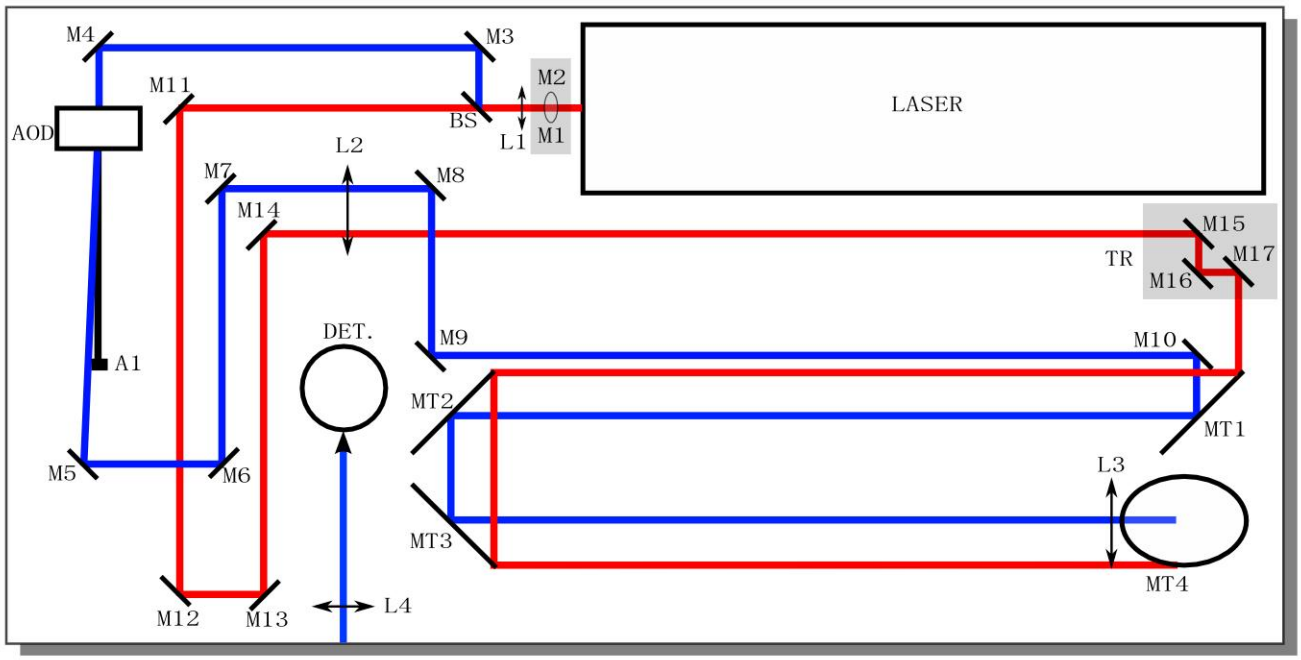

Figure 2.1: Configuration of optical bench elements on PRAXIS-I

- First periscope: the first periscope consists of two mirrors ($M1$, $M2$ in Fig. 2.1) angled at 45°, intended to raise the beam from its initial laser height of 6 cm to the chosen optical height of 15 cm with respect to the table.
- Beamsplitter: a ZnSe beamsplitter is used to divide the initial laser beam into two secondary beams: 0.7% of the laser power to be used to construct the local oscillator, and 99.3% for the primary beam.
- Acousto-optical deflector: the acousto-optical deflector (AOD) is a 1207B-6 model from Isomet. It uses single-crystal Germanium, which is excited at 40 MHz. The crystal is controlled by a piezoelectric element and produces a sound wave which interferes with the (horizontally polarized) incident beam. A fraction of the incident beam is deflected through a Bragg angle of 17.5 mrad and shifted in frequency by 40 MHz. This deflected beam constitutes the local oscillator.
- Translator-rotator: this arrangement of mirrors ($M15$, $M16$ and $M17$) allows the variation of the magnitude of the observation wave vector, as well as its direction. A micrometer positioning system is used to alter the separation of the primary and local oscillator beams (and hence the resulting angle between them in the observation zone), and a rotation stage is used to vary the orientation of the incident wave vector.

- Second periscope: The beams are directed perpendicularly off the bench via $MT4$ in Fig. 2.1, after which they are recovered by a second mirror and directed through the vacuum vessel window and across the thruster face.

According to the configuration shown, the initial laser beam encounters the first periscope, where its optical height is raised. It is then divided into two beams using a beamsplitter. The weaker beam (power 290 mW) is sent to the acousto-optical deflector, where a local oscillator beam is created. The local oscillator beam is conducted using a series of mirrors to $M10$, where together with the primary beam, it defines the orientation and magnitude of the wave vector.

The primary beam travels undeviated across the beamsplitter and is directed to the translator-rotator. Together with the local oscillator it is conducted by a series of large mirrors to the lens $L3$ and encounters the first periscope mirror $MT4$.

2.2.2 Bench configuration

Due to the demanding nature of the experiment, care was taken to ensure beforehand that each component performed as expected. Tests were performed to determine the limitations of different components.

The most critical of the characteristics is the M^2 value of the laser beam. This value, described by the manufacturer as typically inferior to 1.1, was independently determined to be 1.2 (the procedure is described in Appendix A). The bench was originally conceived for a perfect Gaussian beam with an M^2 value of 1, and the elements were situated on the bench such as to respect restrictions on the beam size, e.g. the AOD has a window whose smaller dimension, h_w, measures 6 mm. To avoid diffraction, a beam entering the window must have a waist w restricted to

$$w \leq h_w/4$$

The larger-than-expected divergence meant that this and other such conditions were no longer respected. The bench was therefore redesigned to account for the divergence.

The position of the laser embedded waist was also independently determined and factored into the calculation of the spacing of the bench elements.

The standard relations for Gaussian beam optics were used in determining the propagation of the beam and separation of the elements, with a modification due to the M^2 value. As a function of the propagation distance z from the minimum beam waist w_0, the beam waist is written

$$w(z) = w_0\sqrt{1 + \left(\frac{z}{e_R}\right)^2} \tag{2.1}$$

where the Rayleigh length, e_R, is given by

$$e_R = \frac{\pi {w_0}^2}{M^2\lambda} \tag{2.2}$$

where λ is the laser wavelength. The Rayleigh length (the distance from the minimum beam waist over which the electric field amplitude at the minimum waist is divided by $1/e$) provides a measure of the beam expansion. The minimum beam waists and their corresponding distances on either side of a converging lens of focal length f are determined using the relations

$$d_i = \frac{f\,[d_o(d_o - f) + e^2]}{(d_o - f)^2 + {e_R}^2} \tag{2.3}$$

$$w_i = \sqrt{\frac{{w_o}^2 f^2}{(d_o - f)^2 + {e_R}^2}} \tag{2.4}$$

where d_i is the image distance from the lens, d_o the object distance from the lens, w_i the image waist and w_o the object waist.

The beam waists are chosen according to two main criteria: (i) to prevent the beam from diffracting at critical locations such as the AOD, translator-rotator, and (ii) to fabricate the desired 2.5 mm beam waist in the observation zone in front of the thruster. The most important beam waists are listed in Table 2.1, in which L_w represents the embedded minimum laser waist.

Elements	**Beam waist (mm)**	**Rayleigh length (mm)**
L_w	1.09	291
AOD	1.25	387
TR	3.24	2587
thruster axis	2.50	1544
detector	0.069	1.176

Table 2.1: Summary of key beam waists on PRAXIS-I bench

The lens focal lengths and positions were chosen to produce the key beam waists. Wherever possible, the lenses and positions were chosen to be confocal for the sake of simplicity; the object distance d_o to the lens was set equal to the lens focal length. In this case, as is evident from Eq. 2.3, the image position d_i is also equivalent to the focal length and the ratio w_i to w_o is the ratio of f to the Rayleigh length based on w_0. The lens focal lengths are provided in Table 2.2.

The resulting separations between the most important elements on the bench are summarized in Table 2.3.

The bench components are set up in a compact fashion on an aluminium-honeycomb optical table of dimensions 1.5 m by 0.75 m, equipped with rubber anti-vibration elements between the table and its supporting legs.

Lens	Focal length (mm)
L1	381
L2	1000
L3	2000
L4	190

Table 2.2: Summary of lens focal lengths used on PRAXIS-I

Elements	Separation (mm)
L_w - L1	535
L1 - BS	50
L1 - AOD	590
AOD - L2	1000
L2 - TR	1000
TR - L3	2000

Table 2.3: Summary of key distances on PRAXIS-I

2.2.3 Off-bench configuration

A system of mirrors and aluminium support structures allow the beams to be conducted off the bench, across the plasma, and back to the bench. Fig. 2.2 shows the configuration of the bench and the external chassis on which the off-bench components (mirrors and diaphragm) are mounted.

Fig. 2.3 is shows the beam trajectories after the beams leave the bench.

The local oscillator and primary beams leave the bench together from $MT4$, after which they are reflected by $MT5$ to intersect in front of the thruster exit plane at O. The beams are recovered on $MT6$ on the opposite side of the vacuum vessel and directed towards an anodized aluminium diaphragm, $A2$. The local oscillator passes through a hole 2 cm in diameter in the centre of the diaphragm, while the primary is absorbed on the main plate, which has a diameter of 30 cm. The local oscillator (and the plasma-scattered radiation in the same direction) is then directed by the mirrors $M18$, $M19$, $M20$ and $M21$ towards the bench. The lens $L4$ focuses the beam on the detector.

In the off-bench assembly, one beam waist is critical: the waist at O. The value of 2.5 mm for this waist was chosen based on the resolution and minimum angle.

In the observation zone, a waist of 2.5 mm translates to a resolution δk_t of 1130 rad/m. As will be discussed in more detail later, theoretical results indicate a possible saturation in the mode amplitude in the range of 3000 - 4000 rad/m. One of the goals of this experiment was to achieve minimum wave numbers on the same order. The smallest wave number which can be achieved experimentally must be a few times larger than δk_t, and with the chosen

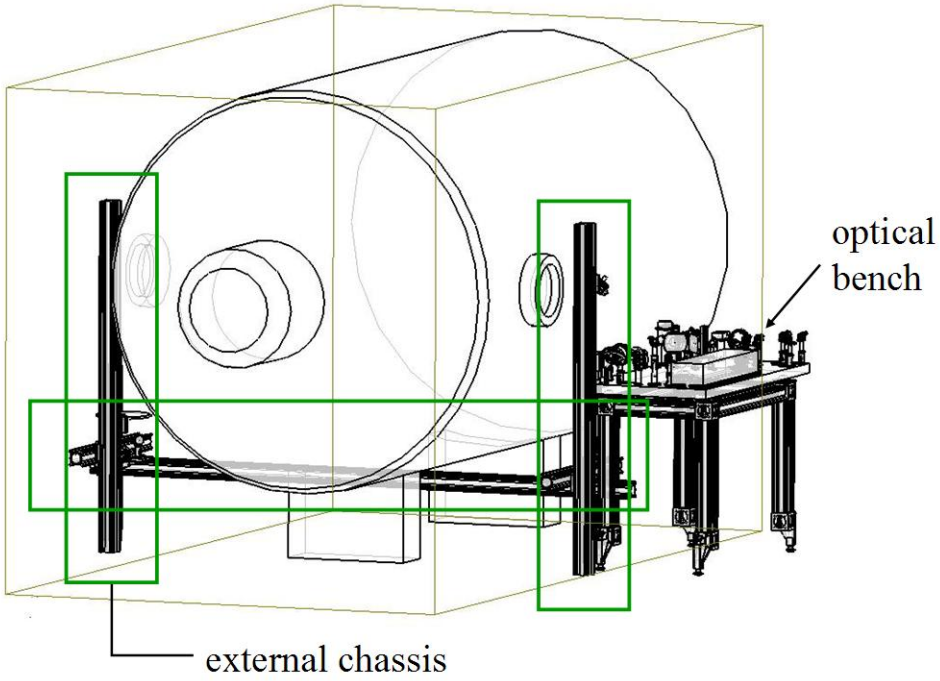

Figure 2.2: Configuration of bench and external chassis around thruster vacuum vessel

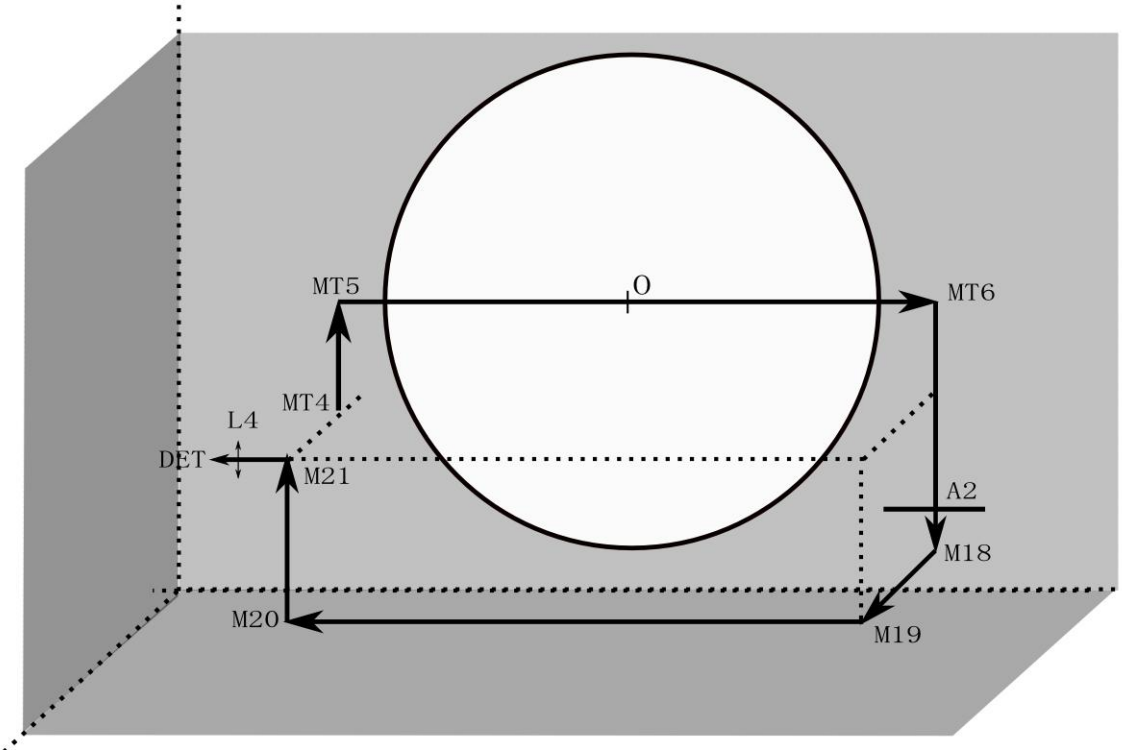

Figure 2.3: Configuration of off-bench optical components on PRAXIS-I

waist, this condition is satisfied.

Larger beam waists, while ensuring better resolution, would result in a signal more difficult to detect, as its measured amplitude scales as $1/w^2$. One design decision for this bench was in fact to reduce the original beam waist from the first trial to 2.5 mm in order to increase the signal amplitude by a factor of four.

The chosen beam waist in the observation zone affects the magnitude of the smallest wave number. The beam waist in the convergence zone fixes the beam waist at the translator-rotator, and consequently, the minimum separation required for the primary and local oscillator beams and therefore the minimum wave number (subsection 2.3.1).

The important distances in the off-bench assembly are shown in Table 2.4. The thruster centre, O, is located 2 m from $L3$ to respect confocality, and the remaining distances (from O to $M21$) are less critical. The distance $MT6$ to $A2$ has been fixed at a value such that the primary and local oscillator beams are sufficiently far from each other at the diaphragm for the primary beam alone to be blocked, while the local oscillator traverses the diaphragm aperture.

Elements	**Separation (mm)**
MT4 - MT5	410
MT5 - O	1450
O - MT6	1450
MT6 - A2	1000
A2 - M18	200
M18 - M19	500
M19 - M20	2800
M20 - M21	790
M21 - L4	150

Table 2.4: Summary of key distances on off-bench assembly.

The remaining distance, from $A2$ to $M21$, is required to conduct the beam across the space at the bottom of the vacuum vessel and return it to the bench. The focal length of $L4$ has been chosen to provide a minimum waist at the detector at a reasonable distance on the bench. The detector has a surface area of 200 μm^2 and the final beam waist on its surface is 69 μm.

2.2.4 Electronics and signal acquisition

Nearly all the electronics used were taken from a previous collective scattering bench (used in works [61, 48]), with the main changes being modifications to the filters and amplifiers. Fig. 2.4 shows the electronic elements, the key elements of which are described below.

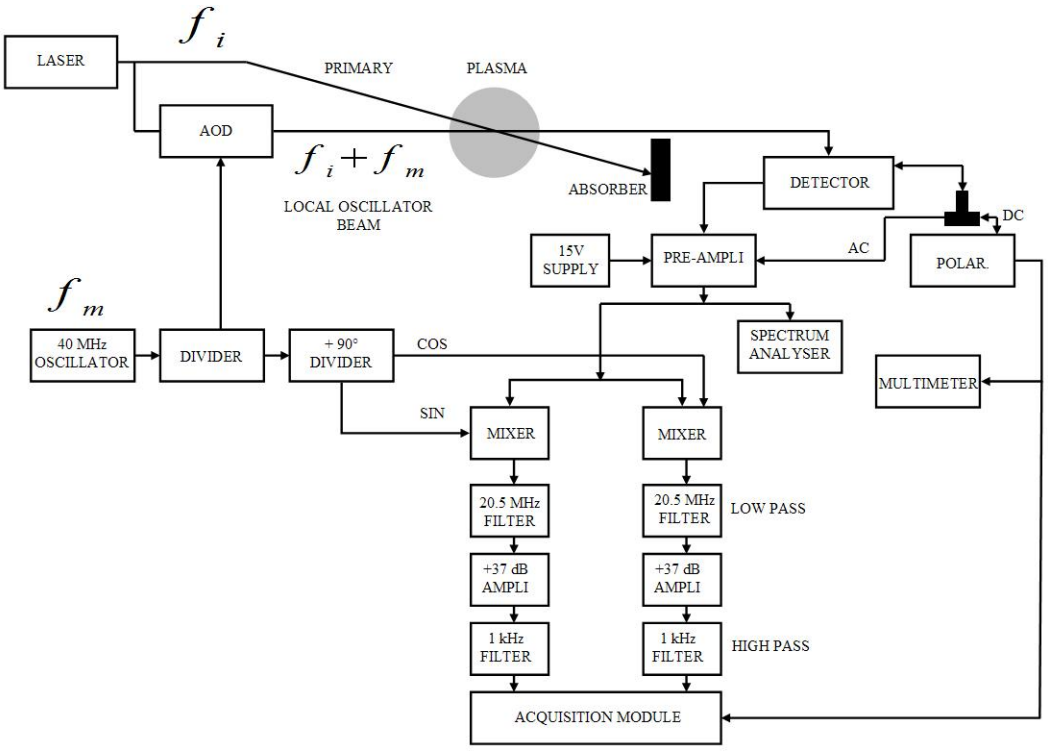

Figure 2.4: Setup of PRAXIS-I electronics

- Detector and polariser: the detector is a photovoltaic diode sensitive to infrared. It requires liquid nitrogen cooling to reduce its own radiation and is installed in a dewar. The detector requires a degree of polarisation (by a few hundred mV) in order to function. The time-varying and constant components of the detector signal are separated using a polarisation T, with the constant part of the signal sent to the polariser as well as to a multimeter for monitoring. The polariser provides a conversion from voltage to current, with 1 V corresponding to 1 mA detector current.

- Pre-amplifier: the time-varying component of the signal is sent to a low-noise pre-amplifier of 30 dB gain. The noise due to the pre-amplifier is necessarily smaller than the photonic noise of the detector. The signal output by the pre-amplifier is sent to mixers and also to a spectrum analyser for monitoring of the frequencies.

- Dividers: a divider is used to split the signal from the quartz oscillator into two components: one which is sent to the acousto-optical deflector to create the local oscillator, and another which is sent to another divider which generates two identical signals at the frequency f_m but in quadrature. Another divider is used to split the time-varying pre-amplifier output into two components which are supplied to separate mixers.

- Mixers: the signals from the phase-shifting divider and the pre-amplifier are multiplied in the mixers.

- High-pass filters: two low-pass 20.5 MHz filters are used on both $\cos$ and $\sin$ output channels to eliminate frequencies outside the expected range of the signal, such as high-frequency laser peaks which could result in a saturation of the amplifiers.
- Amplifiers: two amplifiers (gain of 37.5 dB) are used on both output channels
- Filters: two 1 kHz, high-pass filters are used to remove the original modulation frequency (appearing after demodulation at 0 Hz on the spectra).

The $\sin$, $\cos$ and continuous detector current outputs are sent to a special acquisition device. As before noted, it was necessary to replace the simple numerical oscilloscope used in the first trial because of its insufficient sample depth and resolution.

The new acquisition device is from National Instruments. Acquisition is performed using NI PXI-5122 modules, with three channels active. These modules allow for a high sample depth (up to 100 MS/s) and high resolution (14 bits). The signal input range is from $\pm$ 2 mV to $\pm$ 5 V and the bandwidth 100 MHz. The modules are connected to a laptop using an NI PXI-8360 ExpressCard.

An acquisition program in LabView is used to set the acquisition parameters (50 MHz sample acquisition rate, 6.5 MS/s) and record samples.

2.2.5 Experimental facility and thruster

The experiments are performed in a vacuum chamber at a ground test thruster facility in Orléans, known as PIVOINE-2G (*Propulsion Ionique pour les Vols Orbitaux: Interprétations et Nouvelles Expériences - 2ème Génération*). Fig. 2.5 is a photo of the vacuum vessel.

The vacuum chamber is a cylinder of radius 1.1 m and length 4 m. It is equipped with two-stage primary pumping and cryogenic pumping systems and can evacuate 150,000 litres of Xenon per second, and provide a residual pressure of 3x10^{-5} mbar for a 6 kW thruster operating at a flowrate of 20 mg/s. The thruster is situated at one end of the chamber and typically positioned on the axis of the vessel. Its axial position inside the chamber may be varied.

The chamber is normally fitted with a number of tools for monitoring the thruster performance [43]. These include a thrust balance, gaussmeter, antenna frequency analyser and electrostatic probes. Windows located at various points on the vessel allow the plasma to be accessed by a number of optical diagnostics, such as high-speed cameras and devices for emission spectroscopy, laser-induced fluorescence and IR thermography.

For the collective light scattering experiment, diametrically-opposed ZnSe windows on either side of the vessel, of diameter 100 mm and thickness 5 mm, are used to access the plasma. The windows are treated with an anti-reflective coating.

The thruster used in this study is the PPS®X000-ML model designed by Snecma, a high-powered, 5 kW-class experimental thruster. This thruster was chosen rather than the SPT-100 model used in the first trial partly to test a newer thruster model and partly because the signal amplitude was expected to be larger. The PPS®X000-ML, while possessing a

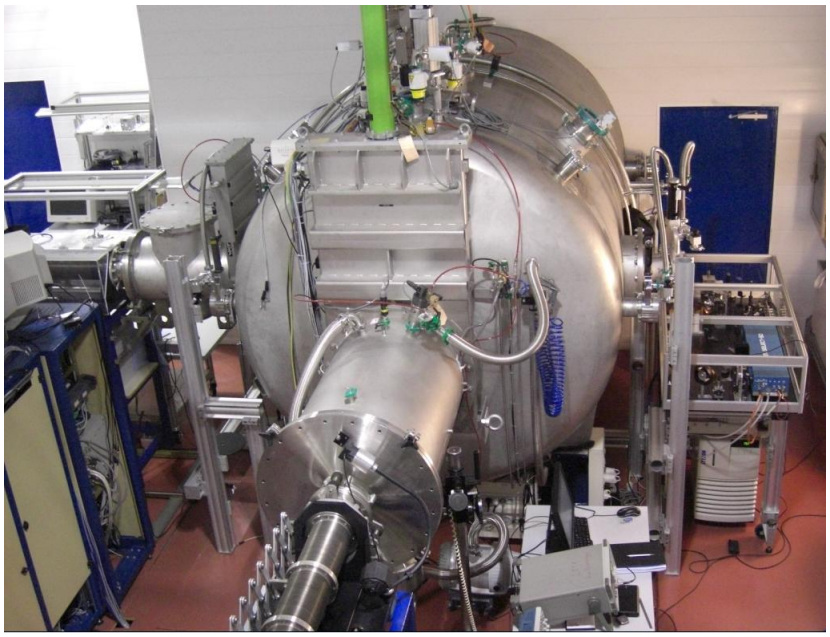

Figure 2.5: Vacuum vessel at PIVOINE ground test facility with optical bench PRAXIS-I

nominal flow rate of 6 mg/s, allows for much larger flow rates to be used (up to 20 mg/s). The thruster dimensions and operating characteristics are summarized in Table 2.5.

Dimensions	Discharge channel length (cm) External diameter (cm) Internal diameter (cm) Cathode distance below axis (cm)	3.17 15 10 11
Nominal operating parameters	Discharge voltage (V) Discharge current (A) Flow rate (mg/s)	500 5.3 6
Performances	Thrust (mN) Specific impulse (s) Efficiency (%)	135 2300 58

Table 2.5: Summary of main PPSX000-ML thruster characteristics

Fig. 2.6(a) shows the thruster extracted from the vacuum chamber. The annular gap through which the plasma is discharged is clearly visible, as is the cathode, situated at the bottom of the thruster. Fig. 2.6(b) shows the thruster in operation.

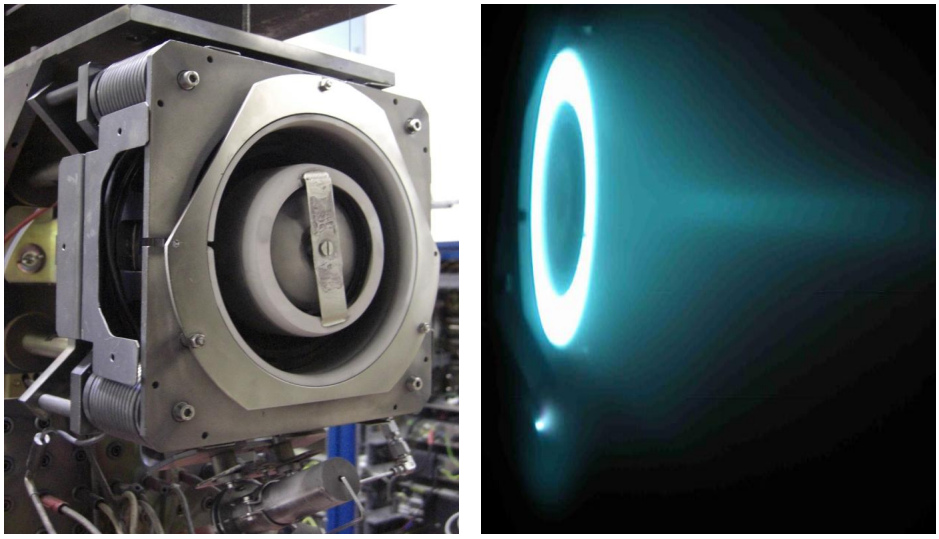

(a) The PPS®X000-ML thruster outside the vacuum chamber

(b) The PPS®X000-ML thruster firing in the vacuum chamber

Figure 2.6: The PPS®X000-ML thruster

2.3 Experimental procedures

Some of the procedures followed for calibration and positioning of the beams are presented briefly in this section.

2.3.1 Beam alignment

The alignment of the beams is complicated by two factors: (i) the beams travel a very long distance - from the locations where the primary and local oscillator are created, each travels a total distance of 6 m to the convergence zone in front of the thruster, and (ii) the volume occupied by the vacuum vessel is inaccessible, and the positioning of the beams in the front of the thruster cannot be directly viewed.

Care is taken to first assure alignment on the bench. In order to define the wave number, on rotation the primary must describe a circle of constant radius r about the local oscillator in the wv plane as shown in Fig. 2.7.

In Fig. 2.7, $M17$ rotates in the wv plane to change the scattering plane in which the observation wave vector is situated; this is done using the rotator element (a goniometer). The distance between $M16$ and $M17$ is changed to alter the magnitude of the observation wave vector; this is done using the translator element (a micrometer vernier).

The radius must not change with the distance to the convergence zone. This is checked by an iterative alignment procedure where the near-field and far-field beam positions are corrected in small steps.

To ensure convergence, a "virtual" focus is created by redirecting the beams to a point away from the vacuum vessel, and checking the convergence there (Fig. 2.8). The redirection

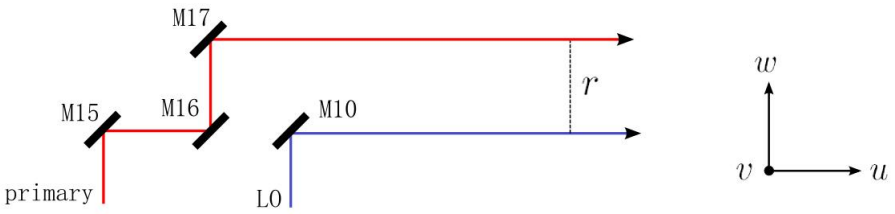

Figure 2.7: Translator-rotator: rotation of primary about local oscillator beam

of the beams is done using a mirror installed temporarily after $MT4$, identified as MR in Fig. 2.8. The distance between $L3$ and the virtual focus plane is 2000 mm. If necessary, additional slight adjustments are made to the orientations of the lenses $M16$, $M17$ and $M10$ such that the primary and local oscillator converge at the same point on the virtual focus plane. Once this is assured, MR is removed and the beams allowed to follow the usual trajectory towards $MT5$.

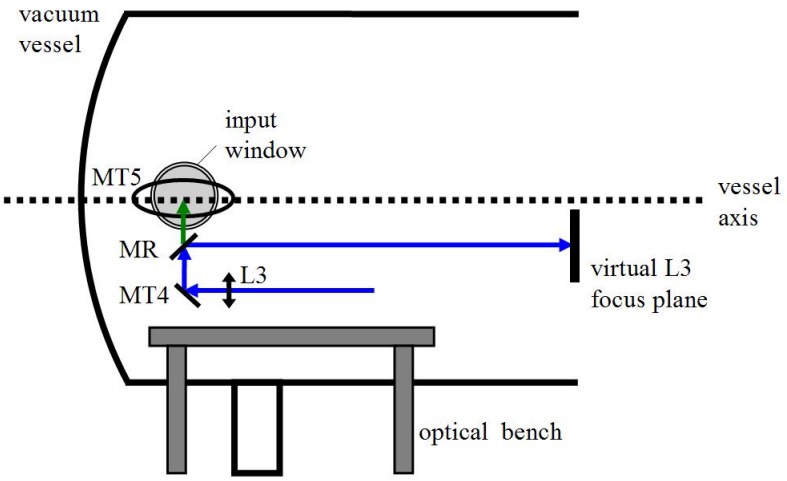

Figure 2.8: Virtual focus for establishing convergence in front of thruster exit

Once the convergence has been checked, the beams are redirected across the vacuum vessel.

2.3.2 Calibration of wave vector

The beam waists at the translator-rotator are imposed by the required beam waist in front of the thruster. This in turn fixes a certain minimum separation distance, r_0, between the beams at the translator-rotator, which is four times the beam waist to avoid diffraction.

The separation distance fixes the angle between the beams in the convergence zone, which in mrad is

$$\theta\,[mrad] = r\,[mm]\,/2 \tag{2.5}$$

since the focal length of $L3$ is 2000 mm.
The wave number k in rad/m is given by

$$k = \frac{2\pi\theta}{\lambda} \tag{2.6}$$

In the present bench configuration, the beam waists at the translator-rotator are 3.24 mm; this translates to an expected minimum angle of 6.48 mrad between the beams in the convergence zone, or a minimum wave number of 3841 rad/m.

The maximum wave number is fixed by the maximum separation allowed at $L3$ between the beams, where the local oscillator is placed in the centre of the lens. Because of restrictions such as the dimensions of the lens holder, the maximum separation of the beams without diffraction is about 48 mm, corresponding to a maximum possible wave number of 14226 rad/m.

The most important bench characteristics have been presented in this chapter. The initial ideas for improving the signal-noise ratio have been taken into account during the conception of PRAXIS-I. The beam trajectories on and off the bench have been carefully chosen and the desired beam waists imposed at the different locations. Unexpected problems, such as the large beam divergence, have been compensated for in the design.

The set of experiments carried out using PRAXIS-I are described in Chapter 3.

Chapter 3

Phase I experiments

Contents

THE experiments carried out using PRAXIS-I will be identified henceforth as Phase I experiments. A range of parameters are varied: the orientation of the scattering plane, the observation wave vector magnitude, the measurement volume position and external parameters such as the thruster discharge voltage.

Fig. 3.1 shows the coordinate system and the positioning of the measurement volume in front of the thruster. The measurement volume, in dark grey, is formed from the intersection of the Gaussian local oscillator and primary beams, and is aligned along the z axis. The observation wave vector $\vec{k}$ forms an angle α with Ox. α is zero when $\vec{k}$ is aligned in the direction of positive Ox and increases in the anti-clockwise direction. Its components k_y and k_y correspond to the projections on Oy and Ox respectively.

The plasma volume contained in the annular volume between the inner and outer ceramic walls is shown in light grey.

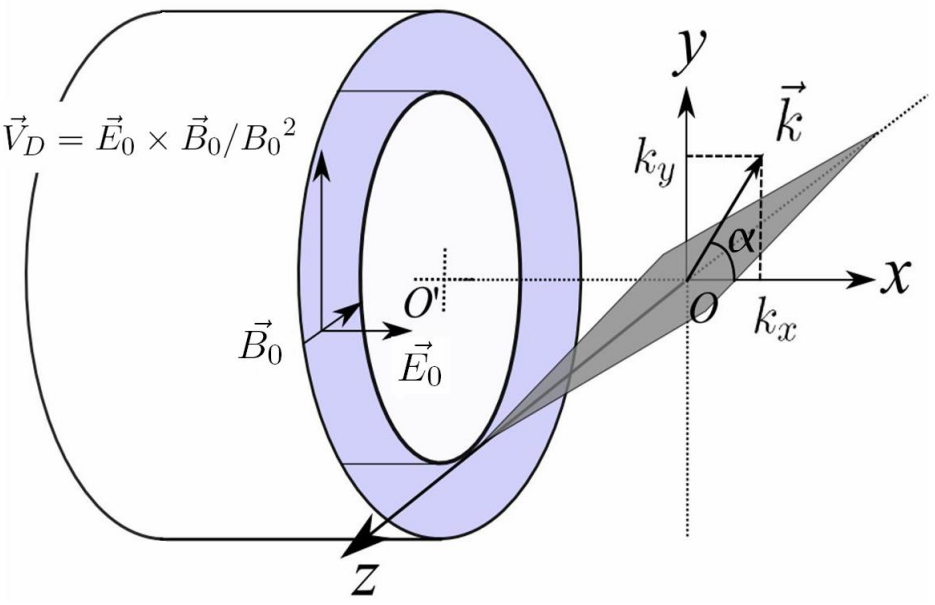

Figure 3.1: Coordinate system and placement of beams in front of thruster

The observation volume centre, O is aligned with the thruster axis $O'x$. The magnetic field, $\vec{B}_0$, is directed radially outwards (anti-parallel to Oz), while the electric field, $\vec{E}_0$, is parallel to Ox. This gives rises to a drift velocity V_D parallel to Oy.

The coordinate system shown in Fig. 3.1 will serve as the reference for experiments described in this chapter.

3.1 Signal acquisition and spectra details

For each acquisition, signals are recorded on three channels: $\cos$, $\sin$, and detector current. The number of samples, N, was set at 6.5×10^6. A high acquisition rate (50 MHz) is chosen to allow the resolution of high frequency oscillations in the signal. The total acquisition duration is 0.13 s.

The spectral density of each signal acquisition requires a Fourier transform of the complex signal, written as

$$f(t) = XA + iXB \tag{3.1}$$

where XA represents the $\cos$ channel output, and XB the $\sin$ channel output, in mV.

The discrete Fourier transform, $\mathcal{F}(\omega)$, is determined in Matlab for the series $f(t)$, of length N, using the algorithm

$$F(\omega) = \sum_{j=1}^{N} f(j) {q_N}^{(j-1)(\omega-1)} \tag{3.2}$$

where

$$q_N = e^{(-2\pi i)/N} \tag{3.3}$$

As will be shown soon, four types of acquisitions are necessary for determining the absolute scattered signal level. These are:

(a) Plasma + primary + local oscillator (to be referred to as **PL+PB+LO**): made with the plasma on, and the local oscillator and primary beams present. The corresponding signal is one which is expected to show evidence of a plasma fluctuation.

(b) Plasma + local oscillator (**PL+LO**): made with the plasma on and only the local oscillator beam present (the primary beam being blocked by an absorber on the bench). No plasma-scattered signal is expected to be present, unless stray radiation from the thruster current pollutes the acquisition channels.

(c) Primary + local oscillator (**PB+LO**): made with the plasma off, but both primary and local oscillator beams present. This acquisition is used to determine the spectral density of the photonic noise.

(d) Detector closed (**D**): made with the detector closed and the thruster running. This acquisition is used to determine the base electronic noise spectral density, due to thermal and amplifier noise.

The spectral density for each acquisition type is determined from the Fourier transform. The spectral density is calculated over a reduced time series of length n (such as 200[1]

[1]Use of a comparable 2^n length for the slice, such as 256, had a negligible effect on the time required for the calculation

points). This procedure was repeated over all the remaining time series of length n from the total N points. A mean spectral density was then obtained from an average of all the spectral densities obtained from N/n segments. The segment length of 200 will be used for subsequent discussions of high frequency signals in this chapter. The corresponding frequency step in a spectrum is 250 kHz.

The use of the average has the advantage of reducing the variance of the signal by a factor of $\sqrt{N/n}$ - for the values used here, a factor of 180.

Fig. 3.1 shows the effect of the averaging procedure. Fig. 3.2(a) shows the spectral densities obtained for three acquisition types, using only one time segment of 200 points. No scattering signal is evident from the noisy $PL + PB + LO$ record. In contrast, when N/n spectral densities are averaged, as is the case in Fig. 3.2(b), a large scattering signal can be observed in the $PL + PB + LO$ record at 5.5 MHz.

3.2 Evidence of high frequency modes

The first important result is the identification of two kinds of high frequency modes. Fig. 3.3 shows the averaged spectral densities for the four acquisition types. The y-axis units are not yet normalized. These signals correspond to an observation wave number of 9630 rad/m (observation wavelength of 0.65 mm), oriented parallel to the $\vec{E} \times \vec{B}$ direction, i.e. in the direction of positive y. The Xe flow rate is 20 mg/s and the observation volume is positioned a distance 7.5 mm from the thruster exit plane.

Fig. 3.3 shows the four acquisition types. A large scattered signal is located near 5 MHz, with a smaller peak near -5 MHz. The sharp, narrow peak at zero is thought to be largely due to stray diffraction, eg. from scratches on the mirror surface or off dust particles crossing the measurement volume. However, it will be shown later that intermittent low frequency oscillations can be also be identified. The narrow signal at -20 MHz, present in all spectra, is due to the RF laser power supply and does not constitute plasma activity. The variation in the level of the signals is due to variations of amplifier gain with frequency.

This first observation of a scattering signal is a sign of wave propagation, of characteristic length scale 0.65 mm and frequency near 5 MHz, perpendicular to the magnetic field.

A different type of high frequency signal is observed when $\vec{k}$ is oriented parallel to Ox. This case is shown in Fig. 3.4, where the wave number is 6520 rad/m. The Xe flow rate is 20 mg/s and the distance OO' is 27.5 mm. This spectrum shows a higher frequency signal located near 20 MHz. Apart from the large peak near 20 MHz, the difference in levels of the spectra is due purely to variations in the detector current between the records (and hence, the corresponding level of the photonic noise). These variations are accounted for during the signal normalization procedure, which will be described shortly.

These observations of two high frequency modes validate the design choices made for PRAXIS-I and represent the first unambiguous identification of plasma oscillations in the thruster using collective light scattering. The characteristics of these modes will be examined in some detail via techniques explained in the next section.

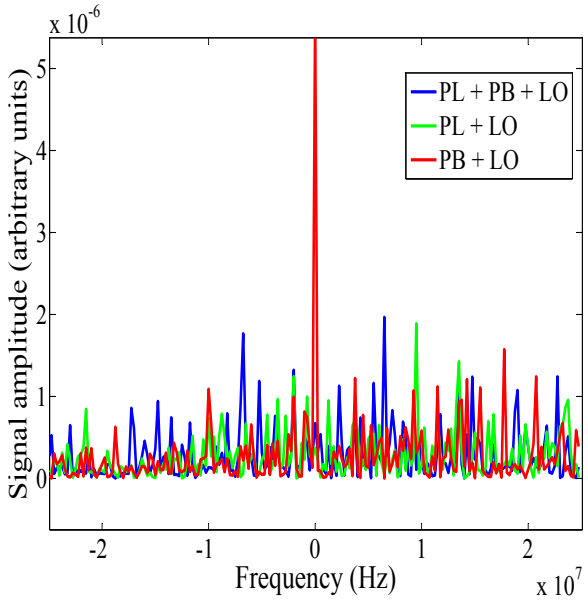

(a) Raw spectra without averaging

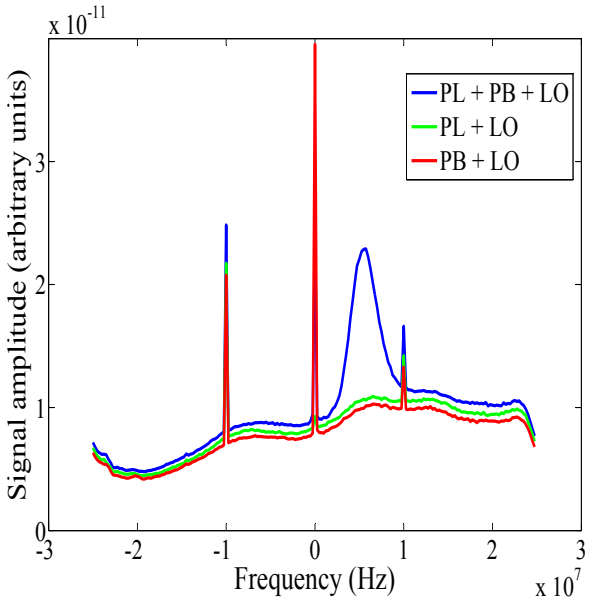

(b) Raw spectra to which averaging procedure has been applied

Figure 3.2: Spectral averaging for the extraction of the plasma-scattered signal from noisy data

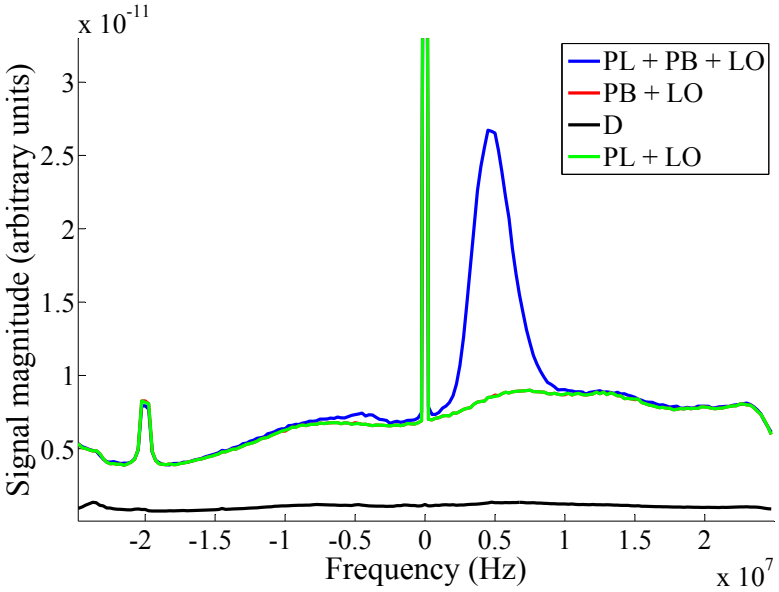

Figure 3.3: Spectral densities obtained for different records for $\vec{k}$ oriented parallel to the $\vec{E} \times \vec{B}$ direction. A scattered signal near 5 MHz (blue line) is clearly visible. A lower-intensity peak, symmetric in frequency, is also visible. The photonic noise spectrum (in red) and the $PL + LO$ spectra (in green) superpose. The background noise is in black. The peaks apparent around 0 MHz and -20 MHz constitute stray signals. The observation wave number is 9630 rad/m.

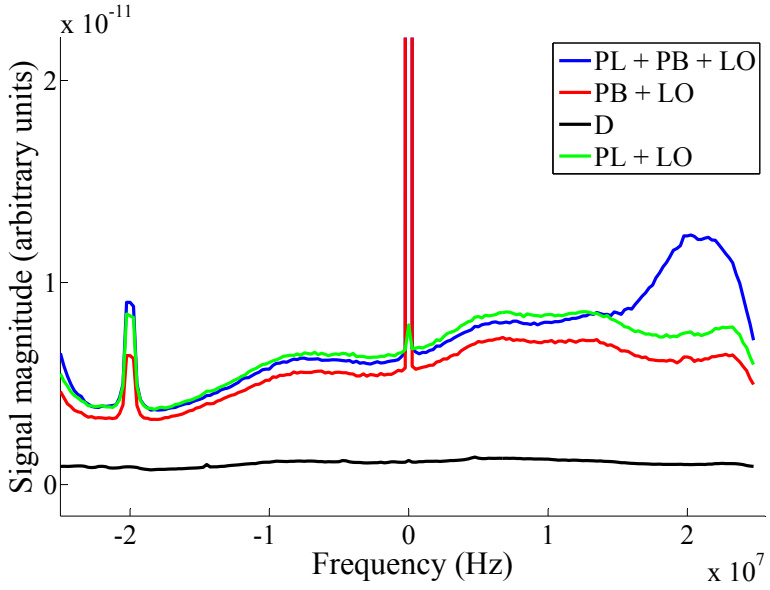

Figure 3.4: Spectral densities obtained for different records for $\vec{k}$ oriented parallel to $\vec{E}$. The presence of a broad, high frequency scattered signal around 20 MHz (blue line) is clear. The peaks apparent around 0 MHz and -20 MHz constitute stray signals. The observation wave number is 6520 rad/m.

3.3 Signal analysis techniques

A number of procedures were adopted to convert the raw signals into physical quantities and determine absolute properties of the fluctuations.

3.3.1 Signal normalization

The goal of the signal normalization is to isolate the collective scattering signal from the noise, while removing artefacts such as variations in the amplifier gain over the frequency range and compensating for variations in the detector current between records.

The signal normalization procedure uses all four acquisition types in the following way.

(a) The spectral density is calculated (arbitrary units) in the same manner for all four types: $PL + PB + LO$, $PB + LO$, $PL + LO$ and D. First, the mean level of the $\cos$ and $\sin$ channels over the full record is adjusted to zero (to eliminate any offsets which might be present), i.e.

$$Xn = Xn - \overline{Xn}$$

where Xn represents the raw voltage reading versus time from either channel.

The level on both channels is divided by a mean value of the detector current, because the signal magnitude is proportional to the magnitude of this current. For the record with the detector closed, the current value is arbitrarily set to 1 mA. Finally, the levels of the $\sin$ ("XB") and $\cos$ ("XA") channels relative to one another are adjusted,

$$XB = XB \times \frac{\sigma_{\mathrm{XA}}}{\sigma_{\mathrm{XB}}}$$

where σ_{Xn} is the standard deviation of the signal level.

The levels of the two channels are expected to be very similar. This adjustment of the signal levels with respect to each other is intended to correct, if they exist, any minor differences in the signal levels caused by differences in the mixers, amplifiers and filters for each channel. After these procedures, the spectral density is calculated as the mean spectral density of N/n segments (6.5×10^6 / 200).

(b) The signal spectral density due only to the plasma scattering, $\Psi(\vec{k},\omega)_{plasma}$ is determined as

$$\Psi(\vec{k},\omega)_{plasma} = (\Psi(\vec{k},\omega)_b \times I_b^2) - (\Psi(\vec{k},\omega)_c \times {I_c}^2)$$

where $\Psi(\vec{k},\omega)$ represents the spectral density and I the mean value of the detector current over the full record. The subscripts b and c denote $PL+PB+LO$ and $PB+LO$ records respectively.

Similarly, the photonic noise signal $\Psi(\vec{k},\omega)_{photonic}$ is determined as

$$\Psi(\vec{k},\omega)_{photonic} = (\Psi(\vec{k},\omega)_a \times {I_a}^2) - (\Psi(\vec{k},\omega)_d \times {I_d}^2)$$

where the subscripts a and d represent $PL + LO$ and D records respectively.

The normalized signal spectral density $\Psi(\vec{k},\omega)_{norm}$ is then obtained from

$$\Psi(\vec{k},\omega)_{norm} = \frac{\Psi(\vec{k},\omega)_{plasma}}{\Psi(\vec{k},\omega)_{photonic}}$$

(c) The normalized signal may now be converted to a physical quantity, the dynamic form factor $S(\vec{k},\omega)$, using the plasma and laser beam characteristics

$$S(\vec{k},\omega) = \left(\frac{h\nu}{\eta P_p}\frac{\pi w^2}{\lambda^2 {r_0}^2}\frac{1}{n_0 l_s}\right)\Psi(\vec{k},\omega)_{norm} \tag{3.4}$$

where h, ν and r_0 represent Planck's constant, the incident wave frequency (2.83×10^{13} Hz), and the Thomson radius (2.8×10^{-15} m), respectively. η, the detector efficiency, is 0.7. The primary beam power, P_p, is 42 W. The beam waist in the measurement zone, w,

is 2.5 mm, and the scattering length l_s is 50 mm (twice the thruster channel width). The electron density n_0 is not precisely known in the measurement zone, but it is on the order of 10^{17} - 10^{18} m^{-3}. The value of 10^{18} m^{-3} will be used.

$S(\vec{k},\omega)$ has units of seconds. The dynamic form factor is a measure of the intensity of the density fluctuations over a range of frequencies. Fig. 3.5 shows the calculated dynamic form factor corresponding to the signal considered in Fig. 3.3. Signal artefacts have been removed and the symmetric scattering signal peaks are clearly distinguishable from the noise.

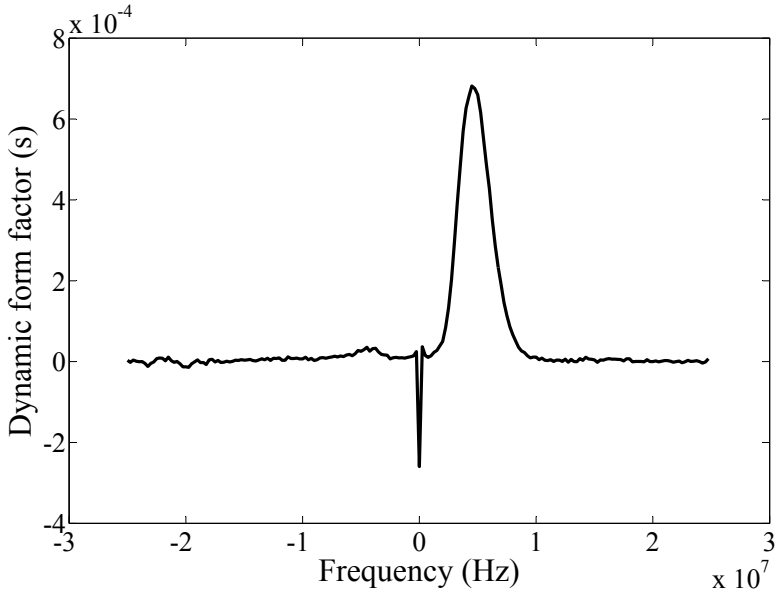

Figure 3.5: The dynamic form factor of the $\vec{E} \times \vec{B}$ mode, corresponding to the data shown in Fig. 3.3, obtained after signal normalization

3.3.2 Static form factor

Once the signal due to plasma scattering has been identified, a more useful form for quantifying the mean square amplitude of the mode, at a particular wave number, is the static form factor $S(\vec{k})$. This is the dynamic form factor integrated over an appropriate frequency range,

$$S(\vec{k}) = \int S(\vec{k},\omega)\frac{d\omega}{2\pi} \tag{3.5}$$

The value of this integral is approximated by limiting it to the frequency limits for which the scattering signal is present. These frequency limits are easy to identify with a large enough signal, after the normalization procedure. For the positive frequency peak in Fig. 3.5, the integration limits are 1 and 10 MHz. The static form factor for the modes identified is

large (for the positive frequency peak in Fig. 3.5, this value is 3.6×10^3; in comparison, the value of $S(\vec{k})$ for a plasma at thermal equilibrium is around 1.

3.3.3 Characteristic frequency of a mode

Each signal peak is associated with a characteristic frequency. With a few rare exceptions, the signal peaks are nearly Gaussian. A Gaussian fit $G(\vec{k},\omega)$ to the peak, of the form

$$G(\vec{k},\omega) = Ae^{-\frac{(\omega-\mu)^2}{2\sigma^2}} \tag{3.6}$$

is made to the dynamic form factor, where A represents the amplitude, ω the frequency, μ the mean frequency value, and σ the standard deviation. The parameters A, μ and σ are the output parameters of a fit optimization procedure which seeks to minimize the variance between the experimental points of the dynamic form factor and the Gaussian fit values. This variance χ_g is defined as

$${\chi_g}^2 = \left[\sum_{\omega\in[\omega_1,\omega_2]} \Big[G(\vec{k},\omega) - S(\vec{k},\omega)\Big]^2\right] / \sum_{\omega\in[\omega_1,\omega_2]} \Big[S(\vec{k},\omega)\Big]^2 \tag{3.7}$$

where $[\omega_1,\omega_2]$ is the frequency range for the fit. The characteristic frequency of the peak is identified as μ and the peak width as σ. For the positive peak in Fig. 3.5, μ is 4.72 MHz and σ is 1.34 MHz.

3.3.4 Error bars on wave number and frequency

The main source of error in the determination of the wave number is from the calibration procedure described in Chapter 2. The separation r between the two beams is generally measured just in front of $L3$, using a burn pattern generated on a piece of paper by the laser, at a particular vernier and angle. The burn spot diameter at this point is between 2 and 5 mm. The beam separation is determined by measuring from the centre of the local oscillator spot (visible only with a liquid crystal sheet) up to the centre of the burn spot of the primary beam. The error in wave number, Δk, is estimated as

$$\Delta k = \frac{2\pi r_s}{\lambda f} \tag{3.8}$$

where r_s is the burn spot radius and f the focal length of $L3$.

The position of the local oscillator spot is determined using a liquid crystal sheet in front of L3 and this also introduces a small error in the determination of the wave vector.

The error in the frequency determination is due to the noisiness of the frequency peak. For large signals, the 250 kHz frequency resolution in the dynamic form factor is sufficient, and the mean value of the frequency is easily identified by a Gaussian fit. For signals which are close to the level of the noise, such as the negative frequency peak in Fig. 3.5, the

noisiness of the peak makes identification of the mean frequency less precise. This fact is used to define a frequency error (Fig.3.6), Δf.

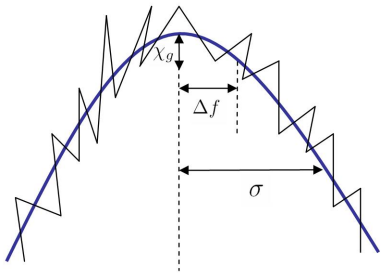

Figure 3.6: Definition of frequency error Δf. The Gaussian fit to the experimental dynamic form factor is in blue.

In Fig. 3.6, the value of χ_g is applied to the frequency axis to estimate to what degree the characteristic peak frequency may be shifted by the noisiness of the peak.

3.4 Dispersion relations

For a fixed value of α (90° for the $\vec{E} \times \vec{B}$ mode, and 0° for the mode propagating along Ox), the characteristic peak frequency is seen to change when the value of the wave number is varied. The variation of frequency with wave number is studied for the $\vec{E} \times \vec{B}$ and axial modes in this section.

3.4.1 Dispersion relations for $\vec{E} \times \vec{B}$ mode

A number of dispersion relations for the $\vec{E} \times \vec{B}$ mode are shown in Fig. 3.7. The experimental conditions for each are identical (20 mg/s flow rate, 300 V discharge voltage, and beams crossing the thruster axis at a distance 7.5 mm from the thruster exit plane). Dispersion relations for the positive frequency peak for slightly different alignments are shown in blue; an example of a negative frequency peak dispersion relation is shown in red (absolute values). A number of observations can be made:

(a) Distinct frequencies of the positive frequency peak are obtained for the same wave number in the three *a priori* identical cases. The frequency difference between the cases is about the same or larger than the error bar. This indicates partial reproductibility of the experiments.

(b) Within the margin of error, the slopes for the positive frequency cases are the same. The slope may be considered as the group velocity of the mode. The mean slope is 3.41×10^3 m/s, with a standard deviation of 778 m/s. Although an ion acoustic mode is not expected to propagate across the magnetic field, it is interesting to note that this group velocity is

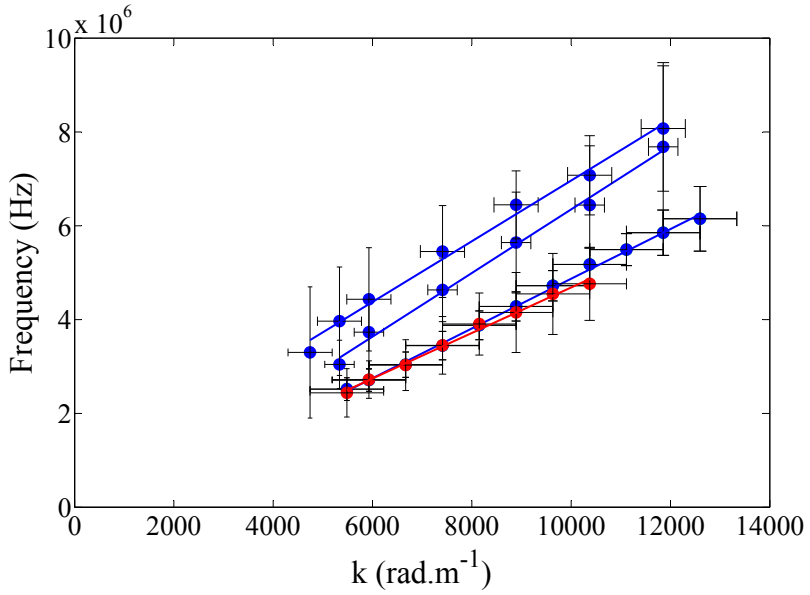

Figure 3.7: Dispersion relations for the $\vec{E} \times \vec{B}$ mode. Dispersion relations for the positive frequency peak, for identical experimental conditions but different alignments, are in blue. The dispersion relation for a negative frequency peak is shown in red (absolute values).

on the same order of magnitude as that of an ion acoustic mode propagating in a plasma with an electron temperature of a few tens of eV.

(c) The near-identical linear slopes of the positive and negative frequency peaks suggest that these symmetric frequency peaks concern the same mode. The large difference in the peak amplitudes, evident in Fig. 3.5, must therefore be accounted for.

(d) Most experiments were conducted at a high Xe flow rate (20 mg/s) because this was seen to provide a large signal amplitude. The effect of different flow rates on the dispersion relation is shown in Fig. 3.8, where flow rates are 6 and 20 mg/s. The larger flow rate corresponds to the larger group velocity.

3.4.2 Dispersion relations for the axial mode

The axial mode has frequencies an order of magnitude larger than the those of the $\vec{E} \times \vec{B}$ mode. A dispersion relation for $\vec{k}$ oriented parallel to the jet axis is shown in Fig. 3.9. The Xe flow rate is 20 mg/s and the discharge voltage 300 V.

The upper range in k for this experiment was limited by practical reasons. The frequency of the peak increases with wavenumber, beyond the range of the filters, and the frequencies can no longer be (accurately) identified, even though the signal is still large. The axial mode presents some interesting features.

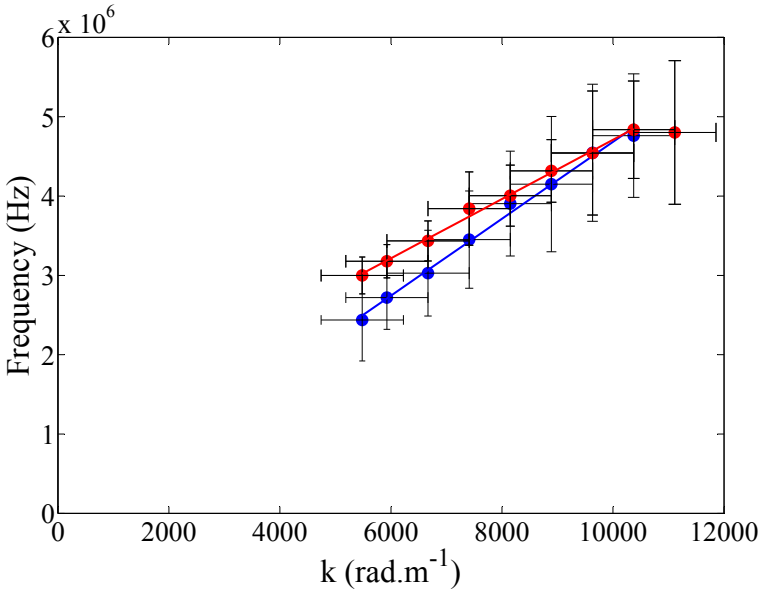

Figure 3.8: Dispersion relations for the $\vec{E} \times \vec{B}$ mode at different flow rates (in blue - 20 mg/s, in red - 6 mg/s)

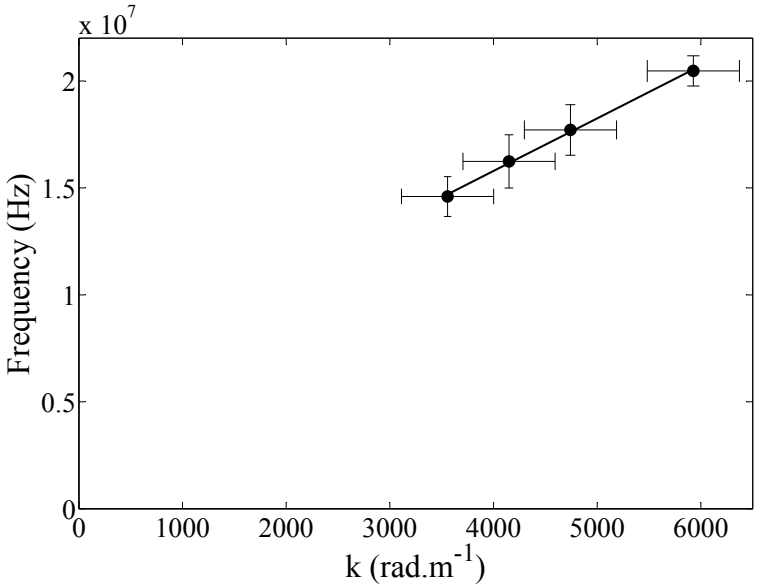

Figure 3.9: Dispersion relation for the axially-propagating mode

(a) The dispersion relation, as for the $\vec{E} \times \vec{B}$ mode, is linear. The group velocity associated with the slope is 15.5×10^3 m/s. This value is, interestingly, close to the ion beam velocity measured using laser-induced fluorescence [26] (a little less than 20×10^3 m/s for similar parameters of the motor used). This axial mode appears to correspond to the sweeping of electrons by ions ejected at the thruster exit.

(b) The sign of the observed peak frequency is positive. This is because the wave vector is oriented in the same direction as the phase velocity of a mode moving in the direction of positive Ox (Fig. 3.1).

(c) The intercept of the line is 0.6×10^7 Hz. Clearly, the relationship between the measured group velocity and the frequency is more complicated than a simple Doppler relation. The value of the frequency intercept is on the order of the ion plasma frequency, which will be discussed later.

3.5 Peak width of the $\vec{E} \times \vec{B}$ mode

A closer examination of the form of the frequency peak reveals interesting features. The signals are not fine spectral lines, but broad peaks. The natural peak width due to the finite resolution of the diagnostic is obtained from

$$\Delta f = \frac{\delta k_t v_g}{2\pi} \tag{3.9}$$

where δk_t is the device wave number resolution (Eq. 1.15). The resulting value of Δf is 307 kHz, much smaller than the peak width determined for Fig. 3.5.

The peak half-widths for an experiment as a function of the wave number (the $\vec{E} \times \vec{B}$ mode, 20 mg/s flow rate, 300 V discharge voltage) are shown in Fig. 3.10.

The peak width increases linearly with wave number, with a slope of 753.5 m/s and a y-intercept of 293 kHz (nearly identical to the computed device resolution Δf, which is what would be expected). Were the peak width due purely to the device resolution, there would be no reason for it to increase with wave number, as is the case in Fig. 3.10.

Clearly, some physical mechanism influences the peak width. Two likely explanations may be proposed. First, electron temperature non-uniformities in the ion acoustic velocity and azimuthal drift velocity V_D would tend to broaden the range of phase velocities contributing to the shape of the peak. The linear increase with wave number would be due to the fact that the frequency width is the product of the spatial dispersion in phase velocity and the wave number.

Secondly, damping effects could broaden the definition of the mean peak frequency. If the mode observed is due to resonance excitation by a background, broadband frequency source, then the expected peak profile $P_k(\omega)$, at a particular wave number, as a resonant function of frequency ω may be written as a Lorentzian of the form

$$P_k(\omega) = P_0 \left[\frac{{\gamma_k}^2}{(\omega - \omega_k)^2 + {\gamma_k}^2} \right] \tag{3.10}$$

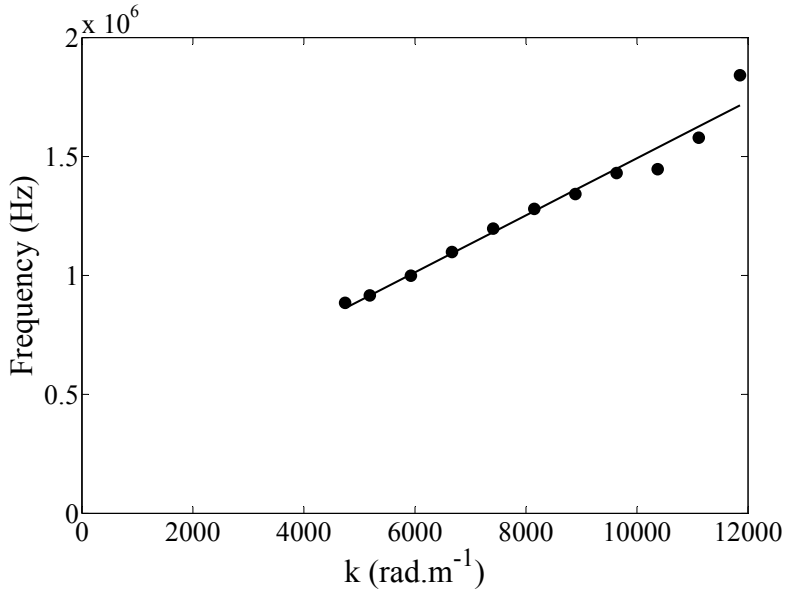

Figure 3.10: Peak half-widths for the $\vec{E} \times \vec{B}$ mode as a function of wave number

where the frequency width at a particular wave number, represented by γ_k, is also the resonance damping rate. The peak mean frequency is ω_k. The actual profile is a convolution of the Lorentzian profile resulting from the resonance and the inherent Gaussian profile of the diagnostic. This convolution produces a Voigt profile, with a Gaussian central portion and Lorentzian wings. The convoluted spectral width, $\Delta\omega_v$ may be estimated from the Gaussian width σ_g and Lorentzian width γ_k,

$$\Delta\omega_v = \sqrt{{\gamma_k}^2 + {\sigma_g}^2} \tag{3.11}$$

Since the observed spectral width $\Delta\omega_v$ is much larger than the Gaussian resolution width, $\Delta\omega_v \approx \gamma_k$. The damping ratio for the convoluted fit can be approximated as γ_k/ω_k, which is a constant value. From Fig. 3.10, the calculated damping ratio γ_k/ω_k is 0.21.

Fig. 3.11 shows a comparison of the Lorentzian and Gaussian fits to the normalized spectrum for the $\vec{E} \times \vec{B}$ mode at large wave number (k = 12600 rad/m), at which damping effects should be more apparent.

The Gaussian fit provides a better fit to the right hand and central portions of the spectrum, but the Lorentzian fits much better to the right hand side of the spectrum. A more accurate investigation of damping can only be done with a Voigt fit to the entire profile. This is, however, impossible given the low amplitude of the spectra at large wave numbers; any long tails in the spectra become difficult to distinguish from the noise.

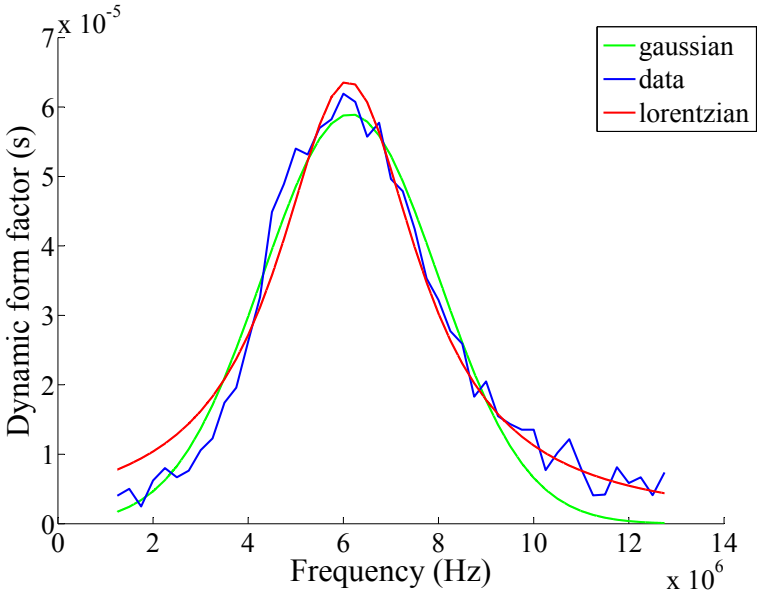

Figure 3.11: Lorentzian and Gaussian fits to the $\vec{E} \times \vec{B}$ mode normalized spectrum

3.6 Energy distribution with length scale

An analysis of the mean square amplitude of the modes at different scales can be performed using the static form factor $S(\vec{k})$.

3.6.1 Form factor dependence on wave number for the $\vec{E} \times \vec{B}$ mode

The variation of the form factor of the mode for different values of wave number is shown on semilog scales in Fig. 3.12.

The form factor of the positive frequency peak, which corresponds to propagations parallel to $\vec{E} \times \vec{B}$, exceeds ten thousand times the equilibrium value at small wave numbers. The negative frequency peak form factor is less intense. There is a clear exponential relationship between $S(\vec{k})$ and the wave number for both modes.

The positive frequency peak shows an e-decrement of 0.37 mm, on the side of the smaller wave numbers. This characteristic length is on the order of the electron cyclotron radius. On the side of the larger wave numbers, the e-decrement is larger (1.3 mm). This larger value is believed to be due to Landau damping which becomes more significant at larger wave numbers; as the frequency increases with wave number and approaches the ion plasma frequency, the ion acoustic wave damping increases rapidly.

Numerical analysis (1D, 2D) [2] shows that the instability should no longer develop for wave number values inferior to about 4000 rad/m. In the present experiment, this cannot be verified because of practical limitations on the smallest wave number attainable (caused by some diffraction due to asymmetry of the laser beam).

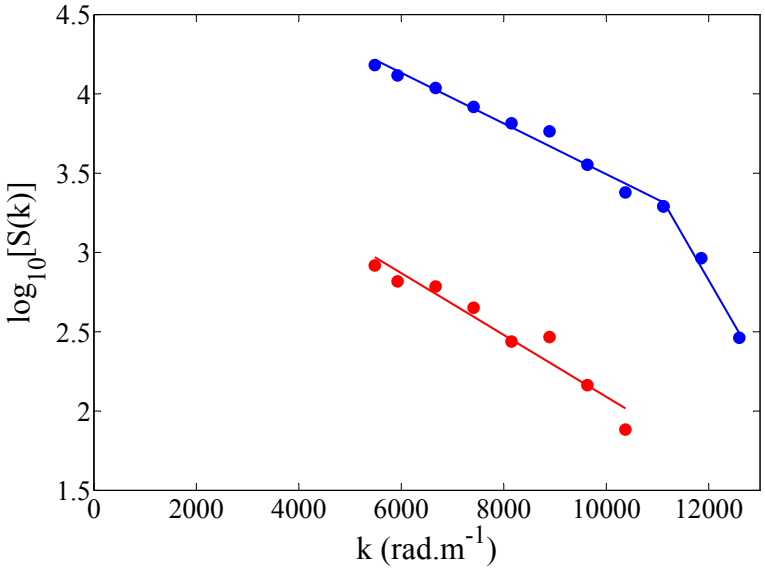

Figure 3.12: Exponential variation of form factor $S(\vec{k})$ with wave number for the $\vec{E} \times \vec{B}$ mode. The positive frequency peak data is in blue, the negative frequency peak in red

The negative frequency peak has an e-decrement of 0.45 mm. The ratio of the positive and negative peak intensities is around 30 and is maintained over the range of wave vector values.

These observations permit additional interpretations about the origins of the negative frequency peak. Certain hypotheses about its origin are proposed and each point is discussed separately below.

(a) The negative frequency peak may be due to "ghosting" in the electronics. If the two mixed channels are not perfectly in quadrature, a small residual image of the positive frequency peak may be present at the negative frequency. In order to determine conclusively if this played a role in the presence of the negative peak, an experiment was conducted in still air to measure the level of an acoustic wave propagating in one direction (corresponding to a positive frequency peak). The resulting signal spectra show a negative peak due to ghosting, at a level 27 dB below the positive frequency peak. In comparison, for the plasma scattering experiment, the level of the negative frequency peak is over 15 dB above this stray peak. Hence the negative frequency signal observed in this and other experiments is indeed due to plasma oscillations.

(b) The presence of the negative frequency peak may be due to oscillations propagating in the opposite direction to the wave vector. Fig. 3.13 will be used here to describe the azimuthal positions on the thruster circumference. The plasma volume is in light blue, the measurement volume in grey.

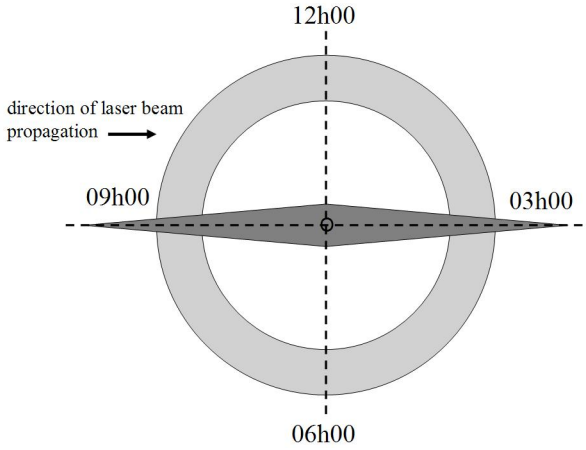

Figure 3.13: Reference for azimuthal positions on thruster (referred to as clock hours). The thruster plume is directed out of the page

At the 09h00 position, $\vec{k}$ is oriented upwards, in the same direction as the $\vec{E} \times \vec{B}$ drift. There are two likely possibilities: (i) a wave may be propagating in the same side of the thruster channel, but in the reverse direction, giving rise to the negative frequency peak, or (ii) the negative frequency peak corresponds to the same wave as the positive frequency peak, but measured in the opposite channel (03h00) where it would now be propagating opposed to $\vec{k}$.

(c) The difference in intensity of the two peaks could be due to the differing sensitivities in the observation volume. The observation volume, a lozenge, has different sensitivities along on its length, due to the Gaussian profiles of the intersecting beams. If the lozenge is not positioned on Oz such that its centre coincides with the thruster axis (Fig. 3.1), the amplitudes of the positive and negative peaks would be different (if these peaks corresponded to fluctuations in opposite sides of the channel). The longitudinal dimension of the observation volume, l_l, has a minimum value of 21 cm (for a maximum experimental angle of 21.25 mrad), and a maximum value of 48 cm (for a minimum experimental angle of 9.3 mrad). In comparison, the outer thruster diameter is 15 cm. The maximum error in the positioning along Oz is between 0 and 20 cm. This corresponds to a sensitivity ratio of between 1 and 0.16. The amplitude ratio of the negative frequency and positive frequency peaks is 0.033, smaller than than five times the smallest sensitivity ratio.

If the negative frequency peak were attributed to fluctuations in the 03h00 side of the channel, the amplitude of this peak would be five times (for O shifted off axis by 20 cm) to thirty times (for O shifted by 0 cm) smaller than the amplitude of the positive frequency peak situated at 09h00. Even taking into account possible sensitivity differences due to the positioning of the measurement volume, if the peaks do indeed correspond to fluctuations on either side of the channel, the fluctuations are not azimuthally symmetric.

3.7 Frequency dependence on position along the thruster axis $0'x$

Thruster characteristics are known to evolve rapidly from inside the channel to the exterior, over a length of a few millimeters. These characteristics include the ion axial velocity profile, the electric field and the magnetic field. For this reason, it is interesting to examine how the $\vec{E} \times \vec{B}$ and axial mode frequencies evolve with distance along $O'x$. For both cases, the observation wave number is fixed at a value of about 6200 rad/m, a relatively small value chosen to provide a large signal amplitude, and sufficiently small for the axial mode frequency to be identifiable within the limits imposed by the filters. There is no reason to suppose that the frequency characteristics observed are wave number-specific.

An experiment to determine the evolution of the frequency and energy of both modes is performed by translating the thruster on its axis (the thruster is attached to a retractable arm which allows its axial position relative to the beams to be varied). The closest approach of the observation volume centre to the thruster exit is 7.5 mm. Some observations about the modes are made below.

3.7.1 Frequency dependence on axial position for the $\vec{E} \times \vec{B}$ mode

The variation of frequency with axial position is shown in Fig. 3.14.

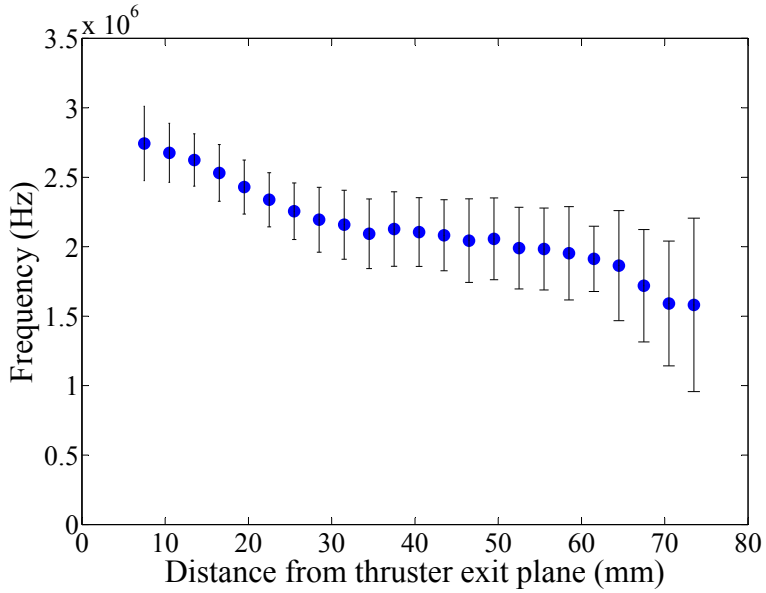

Figure 3.14: Frequency variation with axial distance from the thruster exit plane for the $\vec{E} \times \vec{B}$ mode

The frequency steadily decreases from a value of 2.7 to 1.6 MHz over a distance of about 70 mm from the thruster exit plane. For our thruster operating parameters, the electric

field drops to zero beyond a distance of 20 mm front of the thruster axis. These results show that the $\vec{E} \times \vec{B}$ mode is present far beyond this distance. The presence of this mode beyond the range of the electric field appears to be due to a convection of the electrons by the ions. The drop in frequency may be associated with a reduction in the drift velocity which occurs further away from the thruster exit.

3.7.2 Frequency dependence on axial position for the axial mode

The variation of frequency with axial position for the axially-propagating mode is shown in Fig. 3.15.

The frequency of the axial mode remains close to 20 MHz, with a noticeable decrease at around 15 cm from the thruster exit plane. The axial mode persists for the entire distance accessible in the experiment, above 30 cm from the exit plane. This observation is consistent with the long distance over which the plume is visible (well beyond 30 cm from the exit plane).

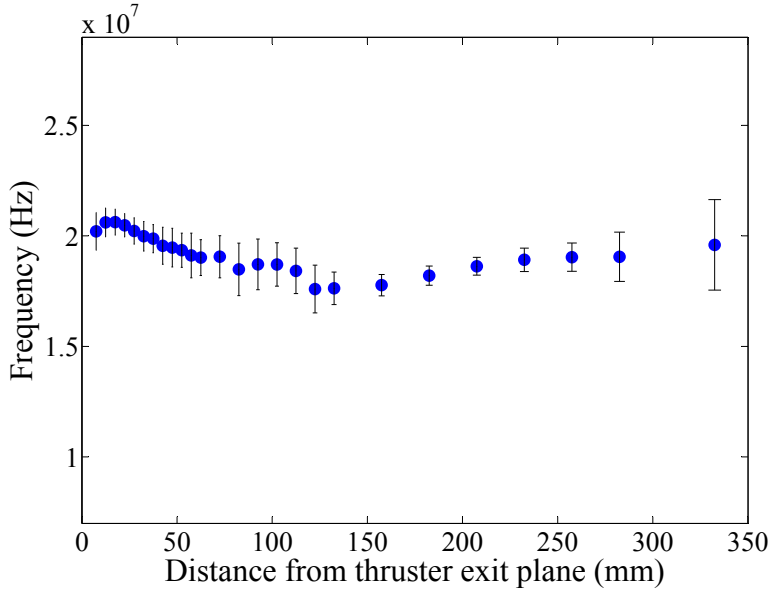

Figure 3.15: Frequency variation with axial distance from the thruster exit plane for the axial mode

3.8 Form factor dependence on position along the thruster axis $0'x$

3.8.1 Form factor dependence on axial position for the $\vec{E} \times \vec{B}$ mode

Fig. 3.16 shows the form factor measured at different distances for the $\vec{E} \times \vec{B}$ mode.

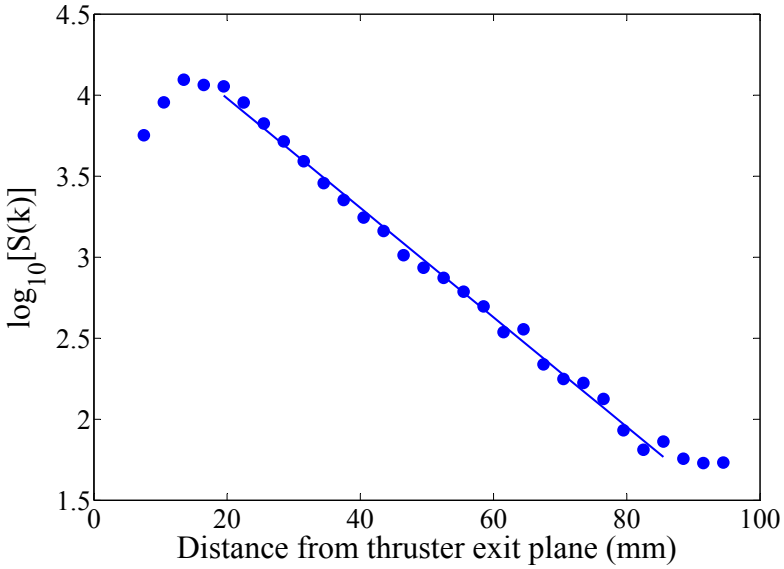

Figure 3.16: Form factor variation with axial distance from the thruster exit plane for the $\vec{E} \times \vec{B}$ mode

The $\vec{E} \times \vec{B}$ mode, which has a short persistence in space, has an exponential energy decrease with distance. The corresponding e-decrement is 12.85 mm. The energy of the mode is increases to a maximum at a distance of 13.5 mm from the thruster exit plane before decreasing. This is in fact consistent with numerical models (e.g. [42]) which show the fluctuation level and the anomalous electron mobility increasing beyond the thruster exit plane.

3.8.2 Form factor dependence on axial position for the axial mode

The form factor variation with distance from the exit plane for the axial mode is shown in Fig. 3.17.

The energy of the axial mode also reaches a maximum at 13.5 mm from the thruster exit, and then decreases. The maximum fluctuation intensity of this mode is only 20% of the maximum fluctuation intensity for the $\vec{E} \times \vec{B}$ mode at a comparable wave number. This pattern of much weaker fluctuations in the axial direction in the vicinity of the thruster exit has been repeatedly observed. The energy of the axial mode increases beyond 100 mm and

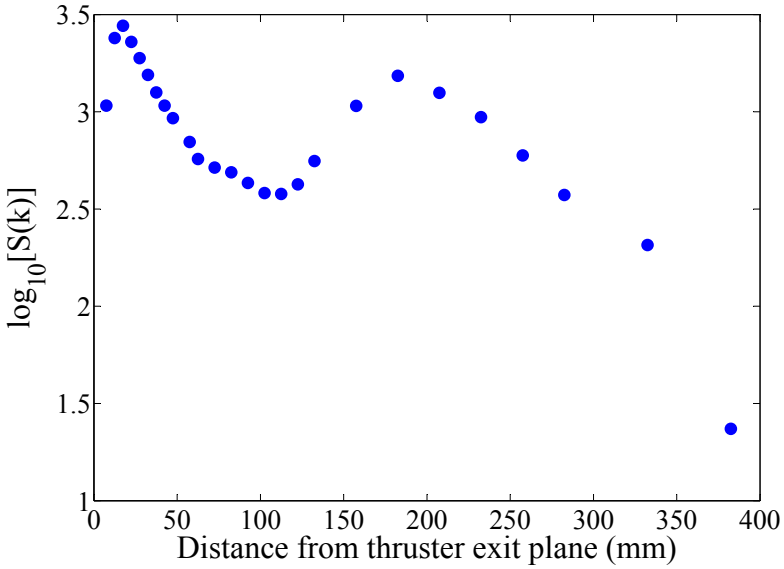

Figure 3.17: Form factor variation with axial distance from the thruster exit plane for the axial mode

reaches a second maximum. The explanation for the appearance of stronger fluctuations at such a large distance is not known. One idea is that it is due to the evolution in shape of the thruster plasma plume, which, after its initial divergence, becomes more focused on the thruster axis. The density fluctuations measured parallel to the axis would then appear larger, and then decrease again as the ion velocity distribution becomes increasingly homogeneous.

3.9 Total density fluctuation rate of the $\vec{E} \times \vec{B}$ mode

In PIC simulations, the observed $\vec{E} \times \vec{B}$ mode accounts for the most intense fluctuations. The density fluctuation rate of this mode is believed to be on the order of several percent, but this value is not precisely known. The density fluctuation rate may be approximately measured by collective light scattering based on a number of assumptions and experimental observations.

(a) The electron mobility parallel to $\vec{B}$ is high, while the electric field component parallel to $\vec{B}$ is very small. The main direction of propagation of the instability is perpendicular to $\vec{B}$. Thus the $\vec{k}$ component along $\vec{B}$, Δk_z, is small and on the order of the inverse of the channel width a,

$$\Delta k_z \approx 2\pi a^{-1}$$

(b) The fluctuations are mainly situated in the plane $(\vec{E} \times \vec{B} - \vec{E})$. An experiment in this campaign during which α (the angle between the wave vector and Ox) was varied was performed and appeared to indicate that as a rough approximation, the fluctuations of the $\vec{E} \times \vec{B}$ mode are situated in an angular opening Ψ of $\pi/2$.

Fig. 3.18 is a depiction of the localization of the fluctuation energy in k-space, based on the two previous assumptions.

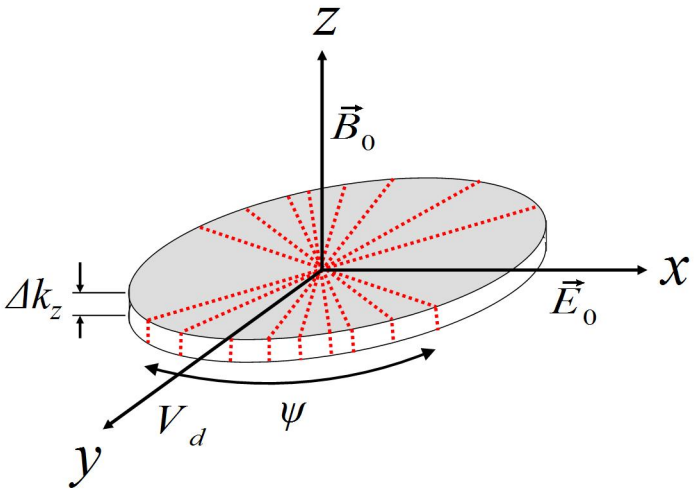

Figure 3.18: Reference frame showing the $\vec{E} \times \vec{B}$ mode propagation

The relationship between the energy of the $\vec{E} \times \vec{B}$ mode and wavenumber is an exponential law, as demonstrated in Fig. 3.12, such that

$$S(k) = S_0 e^{-bk} \tag{3.12}$$

The resulting values for b and S_0 are 3.7×10^{-4} m and 9.4×10^4 respectively.

A value for the fluctuation level may now be deduced. The fluctuation level is related to the form factor as

$$\left\langle \tilde{n}^2 \right\rangle = \frac{n_0}{(2\pi)^3} \int S(\vec{k}) dk^3 \tag{3.13}$$

i.e. , an integration of the form factor in k-space, which is simplified by the previously described assumptions to

$$\int S(\vec{k}) dk^3 \approx S_0 \Delta k_z \Psi \int_0^\infty k e^{-bk} dk \tag{3.14}$$

which is integrated to give

$$\int S(\vec{k}) dk^3 \approx S_0 \Delta k_z \Psi b^{-2} \tag{3.15}$$

The r.m.s density fluctuation level $\langle \tilde{n}^2 \rangle^{1/2}$ thus obtained is 4×10^{14} m^{-3}. The mean plasma density n_0 in Eq. 3.13 is cancelled out by the corresponding mean density used in Eq. 3.4, and therefore this r.m.s density fluctuation is an absolute value. The r.m.s density fluctuation *rate*, obtained using a mean plasma density of 10^{18} m^{-3}, is then

$$\frac{\langle \tilde{n}^2 \rangle^{1/2}}{n_0} \approx 4 \times 10^{-4} \tag{3.16}$$

This value is very small, less than 0.1%. Before interpreting the significance of this level, it is worth bearing in mind a number of points:

(a) The determination of the fluctuation rate depends on a knowledge of the mean plasma density, which was in this case chosen to be 10^{18} m^{-3}, but whose value could easily be an order of magnitude smaller, in which case the fluctuation rate would be 4×10^{-3}. The value used is a typical plasma density in the region of the thruster exit obtained from hybrid models.

(b) It is necessary to measure the angular opening of the mode more accurately. This would allow the fluctuation rate to be integrated over a precise range and account for the wave number component parallel to $\vec{B}$. A better determination of the wave number component parallel to $\vec{B}$ is also necessary.

(c) The optical bench was carefully designed for the measurement of a low level of electron density fluctuations. However, a calibration of the bench will be required to determine if the measured fluctuation level is in some way underestimated due to signal losses, due, for instance, to a poor heterodyning efficiency.

3.10 Further interpretations and analysis

3.10.1 A hypothetical determination of the electron temperature

The dispersion relation of the $\vec{E} \times \vec{B}$ mode shown in Section 3.4.1 provides interesting clues as to the properties of this mode.

Firstly, the mean value of this intercept in Fig. 3.7 is 133.7 kHz, with a standard deviation of 436 kHz. The intercept value is quite close to zero, and considering the linear nature of this mode's dispersion relation, its topology resembles that of an ion acoustic mode, with a group velocity v_g corresponding to the slope. As mentioned earlier, the ion acoustic mode is not expected to propagate strictly perpendicular to $\vec{B}$ for wavelengths on the order of, or larger than, the electron cyclotron radius. However, since the $\vec{B}$ field is not entirely uniform and the wavelength is small, an attempt at comparing the observed mode with the characteristics of an ion acoustic wave appears legitimate. The dispersion relation for such an ion acoustic mode is

$$v_g = \frac{\delta \omega}{\delta k} = \sqrt{\frac{k_B T_e}{m_i}} \tag{3.17}$$

where k_B is Boltzmann's constant and m_i the Xenon ion mass.

Hence an electron temperature may be estimated from the experimental dispersion relation. The resulting value is 16 eV. Later experiments designed to determine the direction of propagation of this mode more precisely are able to show that there is in fact a small k-component parallel to $\vec{B}$.

For now, this estimate of the electron temperature will be used to determine several characteristic velocities and frequencies.

3.10.2 Characteristic velocities, frequencies and length scales for the experiment

For reference, the thruster and plasma parameters are summarized in Table 3.1.

Parameter	Symbol	Value
Electric field	E_0	10^4 V/m
Magnetic field	B_0	15×10^{-3} T
Xe ion mass	m_i	2.175×10^{-25} kg
electron mass	m_e	9.11×10^{-31} kg
Local electron density	n_e	10^{18} /m^3
Local electron temperature	T_e	16 eV

Table 3.1: Thruster and plasma parameters

The resulting velocities, frequencies and length scales are given in Table 3.2.

Taking these values into account, a further commentary on the experimental results can be made.

3.10.3 Interpretations of the frequencies of the $\vec{E} \times \vec{B}$ and axial modes

The frequencies of the dispersion relation of the $\vec{E} \times \vec{B}$ mode (Fig. 3.7) are smaller or on the same order as the ion plasma frequency. This indicates that the ion and electron motions are not strictly identical. One possible consequence of this decoupling is a damping of the mode.

Concerning the axial mode, the non-zero frequency intercept suggests that the axial electron movement can be regarded as a superposition of two motions. There is a convection of electrons caused by the coupled ion species leaving the channel, and in addition, a coupled oscillation of the two species, with a frequency on the order of the ion plasma frequency. A Doppler frequency shift, linearly increasing with wave number, would then account for the observed group velocity.

Parameter	Definition	Value
Azimuthal drift velocity	$V_d = E_0/B_0$	6.67×10^5 m/s
Electron thermal velocity	$v_{the} = \sqrt{kT_e/m_e}$	1.68×10^6 m/s
Ion cyclotron angular frequency	$\omega_{ci} = eB/m_i$	1.09×10^4 rad/s
Ion plasma angular frequency	$\omega_{pi} = \sqrt{n_e e^2/(\epsilon_0 m_i)}$	1.15×10^8 rad/s
Electron cyclotron angular frequency	$\omega_{ce} = eB/m_e$	2.64×10^9 rad/s
Electron plasma angular frequency	$\omega_{pe} = \sqrt{n_e e^2/(\epsilon_0 m_e)}$	5.63×10^{10} rad/s
Ion cyclotron frequency	$\omega_{ci}/2\pi$	1.74×10^3 Hz
Lower hybrid frequency	$f_{LH} \approx \sqrt{f_{ce} f_{ci}}$	8.55×10^5 Hz
Ion plasma frequency	$\omega_{pi}/2\pi$	18×10^6 Hz
Electron cyclotron frequency	$\omega_{ce}/2\pi$	4.20×10^8 Hz
Electron plasma frequency	$\omega_{pe}/2\pi$	8.97×10^9 Hz
Cyclotron drift length	$l_{ce} = 2\pi V_d/\omega_{ce}$	1.59×10^{-3} m
Electron Larmor radius	$\rho_{ce} = v_{the}/\omega_{ce}$	6.36×10^{-4} m
Electron Debye length	$\lambda_D = v_{the}/\omega_{pe}$	2.98×10^{-5} m
Cyclotron drift wave number	$k_c = \omega_{ce}/V_d$	3.93×10^3 rad/m
Larmor wave number	$k_L = {\rho_{ce}}^{-1}$	1.57×10^3 rad/m
Debye wave number	$k_D = {\lambda_D}^{-1}$	3.35×10^4 rad/m
Doppler frequency, motion parallel to $\vec{B}$	$\Delta k_z v_{the}$	6.72×10^7 rad/s
Doppler frequency, $\vec{E}\times\vec{B}$ drift	$k_c V_d = (2\pi l_c)V_d = \omega_{ce}$	2.64×10^9 rad/s

Table 3.2: Characteristic plasma frequency and length scales

3.10.4 Experimental results in the context of linear theory

These experimental results may now be considered in the context of the theoretical predictions of Adam et. al. [2]. The theoretical approach used to determine the conditions for which the azimuthal drift instability arises is discussed.

Basic assumptions in linear theory

The coordinate system adopted places x coincident with the thruster axis, z parallel to the magnetic field, and y coincident with, but opposite in sign to, the azimuthal drift.

- The electric field is constant (E_0) and purely axial; the magnetic field is constant (B_0) and purely radial.
- The drift velocity V_d is sufficiently large that the magnetic field drift velocity and the density gradient drift velocity can be neglected.
- The ions are cold, immobile, and unaffected by the magnetic field.
- The electrons may be described by a shifted Maxwellian distribution function with isotropic temperature, of the form

$$f_0 = n_0 \left(\frac{m_e}{2\pi k_B T_e} \right)^{3/2} \exp \left[-\frac{(\vec{v} - \vec{V_d})^2}{2{v_{the}}^2} \right] \tag{3.18}$$

Theoretical dispersion relations

Fluid equations are used to derive the perturbed ion density as a function of ϕ, and the ion mean velocity and temperature are neglected. The electron velocity distribution is substituted into the Vlasov equation, linearized as a function of the wave potential Φ and integrated to give the perturbed electron density. These densities are substituted into Poisson's equation to yield the dispersion relation, in simplified 2D form (by ignoring perturbations parallel to $\vec{B}$),

$${k_\perp}^2 {\lambda_D}^2 \left(1 - \frac{m_e}{m_i} \frac{{\omega_{pe}}^2}{\omega^2} \right) + \left[1 - I_0(b) e^{-b} + \sum_{n=1}^{n=\infty} \frac{2(\omega - k_y V_d)^2 I_n(b) e^{-b}}{(n\omega_{ce})^2 - (\omega - k_y V_d)^2} \right] = 0 \tag{3.19}$$

where ${k_\perp}^2 = {k_y}^2 + {k_x}^2$. I_0 and I_n are Bessel functions of order zero and n, while $b = (k_\perp v_{the}/\omega_{ce})^2$.

This is further simplified (by neglecting perturbations parallel to the thruster axis, i.e. $k_x = 0$) to give the one dimensional dispersion relation,

$${k_y}^2 {\lambda_D}^2 \left(1 - \frac{m_e}{m_i} \frac{{\omega_{pe}}^2}{\omega^2} \right) + \left[1 - I_0(b) e^{-b} + \sum_{n=1}^{n=\infty} \frac{2(\omega - k_y V_d)^2 I_n(b) e^{-b}}{(n\omega_{ce})^2 - (\omega - k_y V_d)^2} \right] = 0 \tag{3.20}$$

where b is now written as $(k_y v_{the}/\omega_{ce})^2$.

The perturbed electrostatic potential Φ is of the form

$$\Phi = \phi \; e^{i(\vec{k}\cdot\vec{r}-(\omega_r+i\gamma)t)} \tag{3.21}$$

where k is real, and the complex frequency consists of the real ω_r and the instability damping frequency γ. The numerical solutions to these dispersion relations are now considered in the context of our results.

Numerical solution of the one- and two-dimensional dispersion relations

According to Eqs. 3.19 and 3.20, the transitions from stability to instability occur for resonances of $k_y V_d/\omega_{pe}$ with the cyclotron harmonics $n\omega_{ce}/\omega_{pe}$, i.e.

$$k_y V_d \approx n\omega_{ce} \tag{3.22}$$

where n represents integer values.

From Eq. 3.22, the transitions to instability would occur for

$$k_y = 3.956 \times 10^3 n \;\; \text{rad/m} \tag{3.23}$$

The experimental wave number range is 5480 to 12600 rad/m. In the experimental range, the instability would be expected only in the vicinity of 8500 and 12500 rad/m (i.e. n = 2 and n = 3 respectively).

The solution to the two-dimensional dispersion relation is shown in Fig. 3.19. The parameters used to generate this figure have been chosen to cover the range of experimental wavenumbers and plasma parameters: the plasma density used in the code has been set to 10^{18} m^{-3}, the ratio v_{the}/V_d to 2.5, and the ratio ω_{ce}/ω_{pe} to 0.047. The frequencies and growth rates will be presented in Hz to aid direct comparisons to experimental results.

Fig. 3.19 shows the discrete nature of the two-dimensional theoretical dispersion relation; the instability is restricted to the neighbourhood of certain values of k_y only, whereas the experimentally-obtained dispersion relation is continuous.

The imaginary part of the frequency (the growth rate of the instability) is shown in Fig. 3.20.

As is evident from Figs. 3.19 and 3.20, the dependencies of the frequency and growth rate on k_x are negligible. The exact form of the unstable regions as a function of k_y can be examined for a fixed k_x value. k_x is set to zero and the lobes corresponding to the one-dimensional solution are obtained.

Fig. 3.21 shows the comb-like form of the frequency lobes for k_x=0. The frequencies expected experimentally fall between 10 and 20 MHz. The maximum growth rates are similarly localized about certain values of wave number (Fig. 3.22).

The experimental results, while consistent with the frequencies and wave numbers predicted for the instability by linear theory, do not reproduce the discrete nature of the theoretical dispersion relation. The inherent resolution of the diagnostic, for the Gaussian beam waist of 2.5 mm in the measurement zone, is about 570 rad/m. During an experiment, the

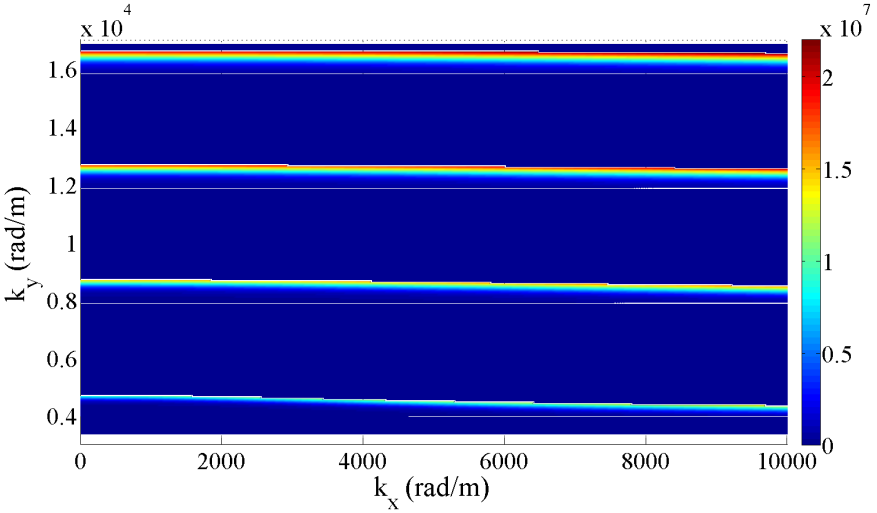

Figure 3.19: Frequency (Hz) as a function of k_y and k_x for the $\vec{E} \times \vec{B}$ mode

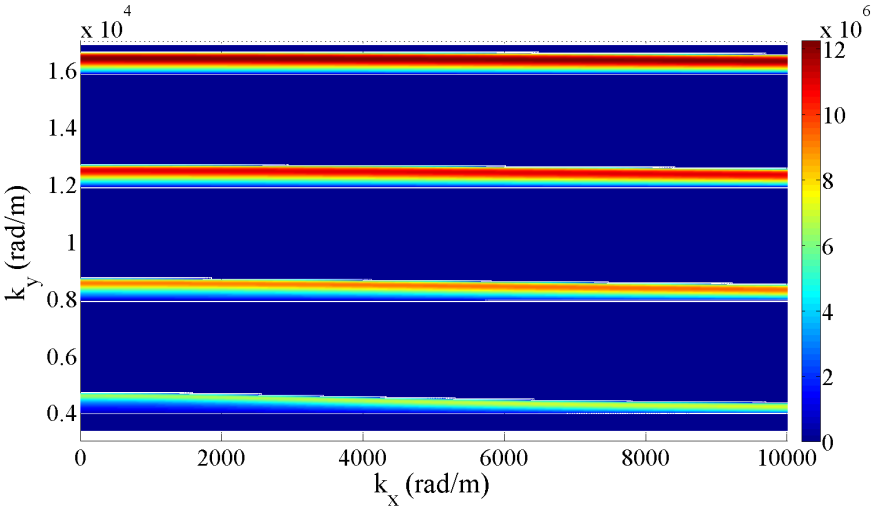

Figure 3.20: Growth rate (Hz) as a function of k_y and k_x for the $\vec{E} \times \vec{B}$ mode

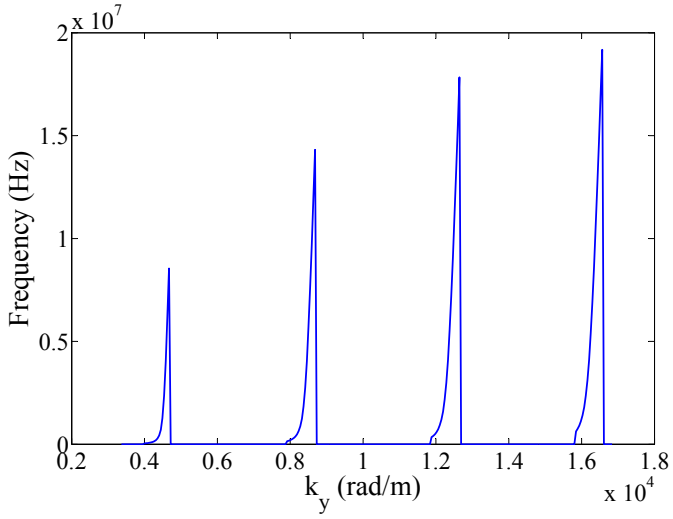

Figure 3.21: Frequency as a function of k_y, for fixed $k_x = 0$.

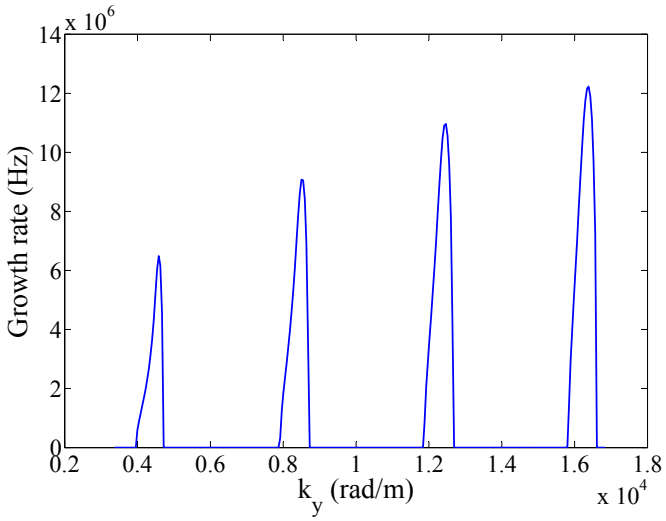

Figure 3.22: Growth rate as a function of k_y, for fixed $k_x = 0$.

wave vector is typically varied in steps of 740 rad/m, which is on the same order as the device resolution. Hence, neither the device resolution nor the experimental wave number step justify missing the unstable lobes, if they do exist.

For k_x = 0, the dependence of frequency and growth rate on k_y may be shown for a very large range of k_y values (of which our range is only a small part). It has already been observed that the dispersion relation resembles a series of comb-like lobes (Figs. 3.21 and 3.22). The maximum of each lobe (for w_r and γ) is now associated with the k_y value for which it appears. The resulting points are plotted over a range of k_y from 0 to 17×10^5 rad/m. Each point therefore represents a particular lobe n. The values obtained for frequency and growth rate are shown in Figs. 3.23 and 3.24.

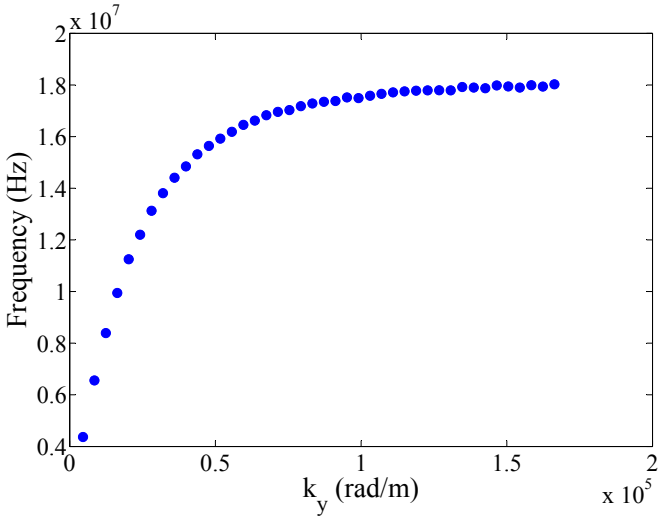

Figure 3.23: Characteristic lobe frequencies as a function of k_y, for k_x = 0.

Certain observations can be made concerning the instability.

The first lobe accessible experimentally (n = 2) at k_y = 8500 rad/m has a frequency associated with the maximum growth rate at 6.6 MHz. The second lobe accessible experimentally (n = 3) at k_y = 12500 rad/m has a frequency associated with the maximum growth rate at 8.4 MHz. Both frequency values are on the order of those seen during the experiment. The range used experimentally is very small compared to that shown in Fig. 3.23, but the linearity seen in the experimental dispersion relation is not inconsistent with the numerical findings at small k_y. For larger k_y values, the frequency reaches the ion plasma frequency, as expected for an ion acoustic wave.

The growth rate characteristics are quite interesting. The lobes attainable experimentally are associated with growth rates of 9.1 MHz (n = 2) and 11.0 MHz (n = 3). These values are inferior to the maximum growth rate (13.4 MHz, seen at lobe n = 7, for which k_y = 28100 rad/m), but still significant. Apparently, the maximum growth rate would only be visible at small length scales of 0.2 mm. The experimentally-observed form factor of these fluctuations is not compatible with this growth rate behaviour, since the form factor is large

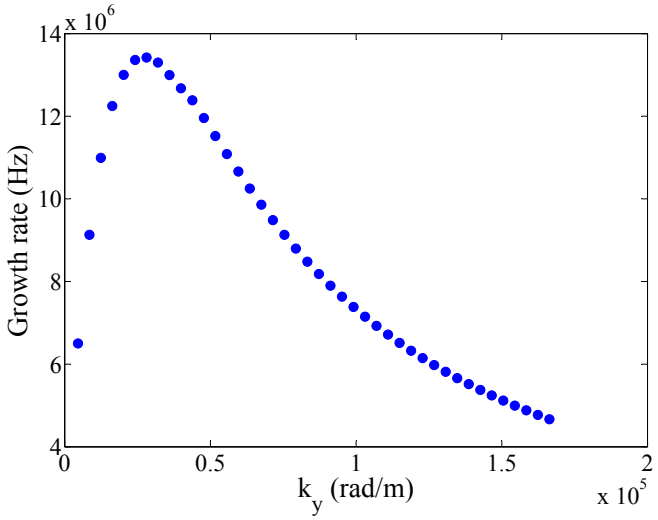

Figure 3.24: Characteristic growth rates as a function of k_y, for k_x = 0.

at larger scales and decays exponentially with wave number.

It is possible the presence of gradients, in the drift velocity, for instance, which are not accounted for in the model, may explain the non-discrete dispersion relation observed experimentally. A radial gradient in V_d would reduce the growth rate, but the instability would spread over the space in k_y, rather than being restricted to narrow lobes. In addition, the electron thermal velocity v_{the} may not be constant. In fact, there are several electron populations of different energies present in the thruster [10] and this could also play a role in expanding the range of the unstable lobes beyond certain limited k_y values.

The main goal of these experiments has been achieved: the small-scale azimuthal instability has been identified experimentally, in addition to an axial mode. The specially-designed collective scattering bench PRAXIS-I has proven capable of measuring the weak density fluctuations associated with this instability.

Apart from the qualitative similarity of the $\vec{E} \times \vec{B}$ mode characteristics and the predictions provided by linear theory, there are quantitative agreements. For similar wave numbers, the frequencies predicted by linear theory and those obtained experimentally are comparable. It has been observed that the component k_x appears to affect only slightly the instability frequency and growth rate, and this will be verified more carefully experimentally.

Linear dispersion relations and the form factor levels with length scale and position along the thruster axis have been obtained for both modes. The differences between the experimental and theoretical dispersion relations may be accounted for by additional effects, such as gradients in drift velocity, a broad distribution of electron temperatures, and the possible presence of a wave vector component parallel to the magnetic field. This will be studied

in more depth in Phase II.

Concerning the theoretical results discussed in this chapter, an important assumption was made during the development of the dispersion relation: that the electron distribution is Maxwellian. This greatly simplifies the solution of the equation, but restricts the validity of the solutions to a limited case. A. Ducrocq [17] studied the effect on the instability when distorted distribution functions were applied. It was observed that the distortion reduced the width of the unstable lobes, and the value of k_y for which the maximum growth rate was seen became smaller. The electron distribution represents a major unknown in the characterization of the modes observed.

Despite the challenges involved in modelling the instability, thanks to these early experiments, a clearer picture of the azimuthal fluctuations is emerging. The second phase of experiments will attempt to resolve a number of new issues arising from the first campaign, such as obtaining a better characterization of the modes, determining their location and directionality, and narrowing the gap between theory and experiment.

Part II

Chapter 4

PRAXIS-II

Contents

4.1 Goals of Phase II experiments

THE main goals of the second phase of experiments may be summarized as follows:

Reduce the minimum wave number : In order to view experimentally a possible saturation in the energy of the $\vec{E} \times \vec{B}$ mode at large scales, it is necessary to reduce the minimum wave number attainable, from 5480 to about 3900 rad/m, as shown in Eq. 3.23. This requires a redesign of the optical bench and an improvement of the laser profile to reduce diffraction.

Determine the significance of the negative frequency $\vec{E} \times \vec{B}$ mode : The question was posed during Phase I experiments as to whether the presence of the negative frequency peak was due to an observation of the far side thruster channel (03h00), or whether the fluctuations occur in the same side as the positive frequency peak (at the 09h00 side). Experiments will be designed to clarify the origin of the negative frequency peak.

Determine the directionality of modes : A determination of how the modes propagate in space requires experiments which can measure three wave vector components: in the

direction of the azimuthal drift, along the ion plume, and parallel to $\vec{B}$. A knowledge of the directionality of the modes would also allow a more accurate estimation of the density fluctuation rate.

Determine the true signal level : To determine if the signal level measured is the absolute signal level, the diagnostic requires calibration, and a determination of possible heterodyning losses.

Explore the possible sources of experiment-theory discrepancies : Experiments to determine the true signal level will verify whether the density fluctuations of this instability are indeed very small, contrary to numerical expectations. They will also determine whether the two-dimensional view of the propagation of the instability is accurate.

Determine the relative level of density fluctuations along $\vec{B}$: The density fluctuations along the magnetic field are expected to be very small, and their Doppler frequency very high, 6.72×10^7 rad/s according to Table 3.2. Experiments designed to measure propagations in this direction will be performed.

Determine effect of varying thruster parameters The influence of thruster parameters such as flow rate, discharge voltage, and magnetic field on the azimuthal instability will be studied.

To attain these goals, several new experiments are required, some of which are beyond the capabilities of PRAXIS-I.

4.2 Changes to PRAXIS-I

For the second phase of experiments an upgraded optical bench with expanded capabilities, PRAXIS-II, is built. Some of the main approaches used to adapt the optical bench are outlined below:

(a) Improvement of the laser profile: on PRAXIS-I, the laser beam was observed to be non-Gaussian, with an asymmetric profile and long tails. To avoid diffraction at the translator-rotator, which would result in a fraction of the primary beam reaching the detector, it was necessary to increase the minimum separation between the primary and local oscillator beams. This in turn increased the minimum wave number; the final minimum value on PRAXIS-I was 5480 rad/m. On PRAXIS-II, in order to achieve smaller wavenumbers, the laser beam is made to pass through a ceramic tube before division into its primary and local oscillator components. This tube, when precisely aligned, absorbs to some extent the low-energy tails of the beam and renders the beam more symmetric.

(b) Expansion of the beam waist: the beam waist in the measurement zone is increased from 2.5 mm to 2.9 mm, by the replacement of the lens $L2$ (focal length 1000 mm) with lenses of focal lengths 625 mm. This reduces the divergence of the beam as well as the

minimum attainable wave number: the k-resolution is now reduced to 975 rad/m, giving a minimum (theoretical) wave number attainable of about 3900 rad/m.

(c) Modifications to the translator-rotator: the range of rotation of the wave vector in the plane xOy was limited to 295° on PRAXIS-I because of the optical supports used for mirror $M8$. The actual experimental range used in Phase I was only 90°. In this second phase of experiments, the optical supports are modified to allow the full 360° range of rotation, of which 320° will be fully explored in the experiments. An angular opening of only 40° is unaccessible due to the modified optical support. This modification is intended to allow a much fuller map of the directionality of the modes.

4.3 PRAXIS-II design

4.3.1 Bench configuration

The modified design of PRAXIS-II is presented in Fig. 4.1. The naming conventions observed in Fig. 2.1 are the same. CR represents the ceramic tube, which is positioned such that the minimum waist created by $L1$ is near the entry of the tube (21 mm in front of it). An additional lens $L2$ is used to fabricate a sufficiently small waist for entry into the AOD window. The tube internal diameter is 4.80 mm, slightly under four times the beam waist (1.25 mm) at this location, and was determined adequate for the absorption of the long tails of the beam. The tube length, 305 mm, is on the same order as the Rayleigh length. The power loss due to the tube, from the initial laser power of 42 W, is about 19%. The recalculated M^2 value post-tube is close to 1, whereas it was determined to be 1.2 on PRAXIS-I.

The spacing of the important elements is given in Table 4.1, while the lens focal lengths are summarized in Table 4.2. The beam waists and associated Rayleigh lengths are summarized in Table 4.3.

Elements	**Separation (mm)**
L_w - L1	589
L1 - entry CR	525
entry CR - L2	375
L2 - BS	75
L2 - AOD	359
AOD - L3	625
L3 - M8	750
L3 - L5	2750
L4 - TR	750
TR - L5	2000

Table 4.1: Summary of key distances on PRAXIS-II

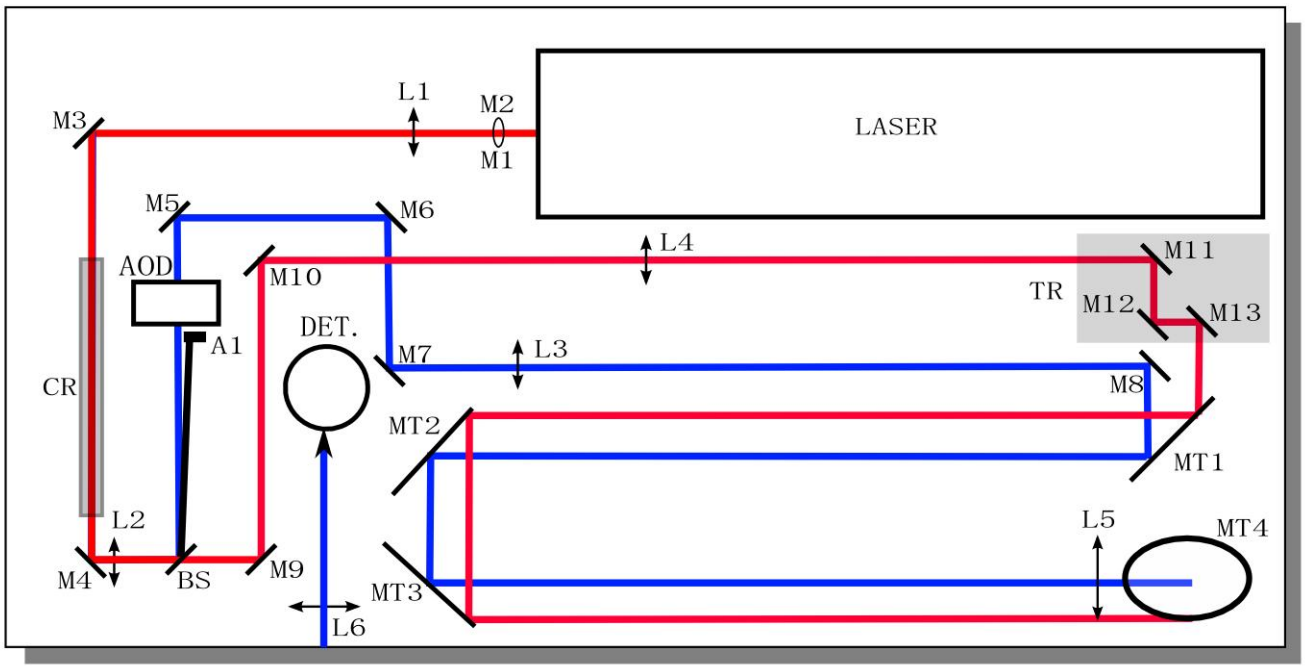

Figure 4.1: Configuration of optical bench elements on PRAXIS-II

Lens	Focal length (mm)
L1	381
L2	508
L3	625
L4	625
L5	2000
L6	190

Table 4.2: Summary of lens focal lengths used on PRAXIS-II

Elements	Beam waist (mm)	Rayleigh length (mm)
L_w	1.09	291
entry CR	1.25	386
AOD	1.32	463
TR	1.60	759
thruster axis	2.90	2493
detector	0.069	1.411

Table 4.3: Summary of key beam waists on PRAXIS-II bench

The addition of the ceramic tube is a major factor in improving the beam quality, however, it should be noted that some diffraction is still observed to occur at the translator-rotator, most noticeably on the horizontal plane (at which observations of the $\vec{E} \times \vec{B}$ mode are made). It is possible to reduce the minimum wave number for the $\vec{E} \times \vec{B}$ mode to 4000 rad/m and no further, falling short of the theoretical value of 3900 rad/m. In contrast, in the vertical plane where the diffraction is minimal, the improved beam profile makes it possible for a smaller scattering angle (6 mrad) and minimum wave number (3550 rad/m) to be achieved.

The original design for PRAXIS-II called for a larger beam waist, close to 4 mm in front of the thruster, in order to reduce the minimum wave number. However, due to unexpected diffraction effects which are not entirely eliminated using the ceramic tube, wave numbers smaller than 4000 rad/m for the observation of the $\vec{E} \times \vec{B}$ were not achievable.

The off-bench assembly remains largely unchanged. The final beam waist on the detector is projected to be 69 μm, compared to a detector element size of 200 μm^2. This is checked by plotting the DC detector current due to the focused local oscillator beam as the focusing lens ($L6$) position is adjusted using two micrometers parallel and perpendicular to the optical table. The current profiles at different positions as the lens is shifted are shown in Fig. 4.3.1. Gaussian profiles are fitted to the right hand and left hand portions of the points shown in Figs. 4.2(a) and 4.2(b) to determine the beam size. The differences between the maximum currents in the horizontal and vertical displacement cases are due simply to an artificially-added beam attenuation. The mean beam waist for the horizontal displacement deduced from the Gaussian fits is 72 μm, while the mean beam waist from the vertical displacement is 75 μm. These values are close to the projected beam waist at the detector of 69 μm.

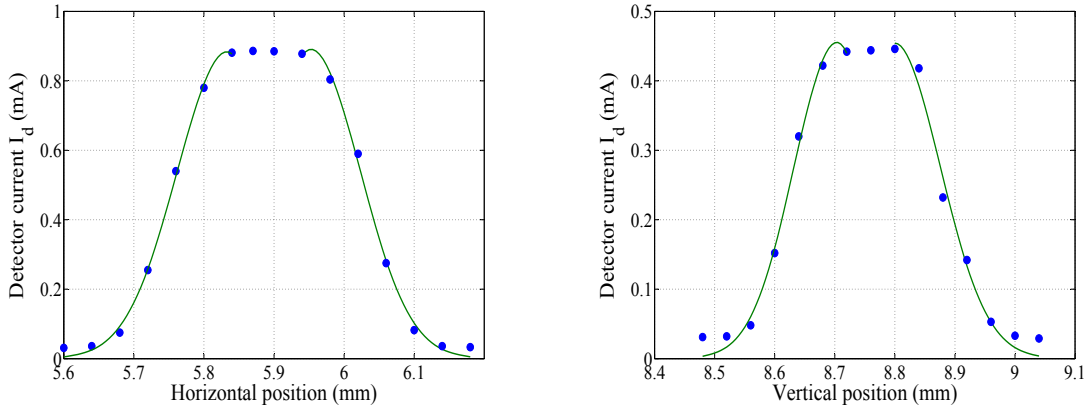

(a) Detector current with lens horizontal position

(b) Detector current with lens vertical position

Figure 4.2: Detector current due to the local oscillator as a function of horizonal and vertical lens positions. Gaussian fits to the left and right hand side profiles are shown in green

The main differences arising from the bench redesign are summarized in Table 4.4.

	PRAXIS-I	PRAXIS-II
Measurement zone waist (mm)	2.50	2.90
Accessible α range (mechanical) ($^\circ$)	295	360
Experimental α range (optical) ($^\circ$)	90	320
Minimum wave number (rad/m), $\vec{E} \times \vec{B}$ mode	5480	4000
Maximum wave number (rad/m), $\vec{E} \times \vec{B}$ mode	12600	13200

Table 4.4: Summary of key differences between PRAXIS-I and PRAXIS-II

4.3.2 Measurement of heterodyne efficiency

The heterodyne efficiency of the optical bench provides one measure of its performance. The usual heterodyning procedure relies on the interference of the plasma-scattered wave and the reference local oscillator on the detector active area. If the wave fronts of the two waves are in phase on the detector surface, the efficiency is maximum and the signal measured is the maximum which can be recovered when integrated over the detector surface. If the waves are out of phase, the interference field amplitude is smaller and the magnitude of the plasma-scattered signal is underestimated.

The efficiency of the heterodyning could theoretically be determined by measuring separately the power on the detector due to the local oscillator and that due to the scattered wave. However, the latter is obviously too weak to be directly measured. Instead, the interference of the local oscillator and another wave of comparable amplitude (an attenuated primary beam) is used. The two beams are superposed in a manner intended to simulate the interference of the scattered wave and the local oscillator during the actual experiment. In this way, the power of the combined beams can be compared with the power from the individual beams and the heterodyning efficiency may be determined.

Principles involved in determining heterodyne efficiency

The power received by the detector is supplied by the Poynting vector, which is formed by the addition of the two waves - an attenuated primary beam wave, and the local oscillator, shifted in frequency by $\Delta\omega$. This power is written as

$$P = \int_A \vec{R}(\vec{r}) \cdot \ \vec{n} dr^2 \tag{4.1}$$

where A is the detector surface area, $\vec{n}$ the normal to this surface, and $\vec{R} = \frac{1}{\mu_0} \left\langle \vec{E} \times \vec{B} \right\rangle_T$.

For each wave j,

$$\vec{B}_j = \frac{\vec{E}_j}{c} \wedge \vec{n_j} \tag{4.2}$$

If the primary ($\vec{E}_P$) and local oscillator ($\vec{E}_{LO}$) fields are parallel to each other, and parallel to the detector surface, the power incident on the detector can be expressed as

$$P = \frac{1}{\mu_0 c}\int \left\langle \left|\vec{E}_P(r) + \vec{E}_{LO}(r)\right|^2_T \right\rangle dr^2 = \varepsilon_0 c \int \left\langle \left|\vec{E}_P(r) + \vec{E}_{LO}(r)\right|^2_T \right\rangle dr^2 \qquad (4.3)$$

where $\vec{E}_P = E_P(\vec{r})\cos(\omega_0 t)$ and $\vec{E}_{LO} = E_{LO}(\vec{r})\cos(\omega_0 t + \Delta\omega)t$.

The time average can be performed if we consider that

$$\left\langle \cos^2\omega_0 t \right\rangle = \frac{1}{2} \quad \text{and} \quad \left\langle \cos^2(\omega_0 + \Delta\omega)t \right\rangle = \frac{1}{2}. \qquad (4.4)$$

Then

$$\langle \cos\omega_0 t \cdot \cos(\omega_0 + \Delta\omega)t\rangle = \left\langle \frac{1}{2}\left[\cos(2\omega_0 + \Delta\omega)t + \cos\Delta\omega t\right] \right\rangle_T \qquad (4.5)$$

The power incident on the detector may then be written as

$$P = \frac{\varepsilon_0 c}{2}\int_A \left[|E_P(\vec{r})|^2 + |E_{LO}(\vec{r})|^2 + E_P(\vec{r})\ E_{LO}(\vec{r})\ \cos\Delta\omega t\right] \qquad (4.6)$$

If the spatial amplitude and phase distributions $w(r)$ of the electric fields on A are the same, i.e.

$$E_P(r) = w(r)E_1 \quad \text{and} \quad E_{LO}(r) = w(r)E_2 \qquad (4.7)$$

then

$$P = \left[\frac{\varepsilon_0 c}{2}\int_A \left|w^2(r)\right| dr^2\right]\left[\left|{E^2}_1\right| + \left|{E^2}_2\right| + E_1 E_2 \cos\Delta\omega_t\right] \qquad (4.8)$$

This electromagnetic power is converted to an electric current with a quantum efficiency η,

$$I = \eta e \frac{P}{h\nu} \qquad (4.9)$$

i.e.

$$I = \frac{\eta e \varepsilon_0 c}{2h\nu}\left[\int_A w^2(r) dr^2\right] \cdot \left[{E_1}^2 + {E_2}^2 + E_1 E_2 \cos\Delta\omega t\right] \qquad (4.10)$$

The current therefore contains three terms:

- a continuous current due to the primary beam, $I_1 = \alpha {E_1}^2$
- a continuous current due to the local oscillator, $I_2 = \alpha {E_2}^2$

- an alternating current at the frequency $\Delta\omega$, $I_{\Delta\omega} = \alpha E_1 E_2$
  with $\alpha = \frac{\eta e \varepsilon_0 c}{2h\nu} \int_A w^2(r) dr^2$, i.e.

$$I_{\Delta\omega} = \sqrt{I_1 I_2}$$

The alternating current is measured in the form of an electric power P_e entering an amplifier of gain G with a resistance R_i of 50Ω,

$$P_e = \frac{1}{2} R_i {I_{\Delta\omega}}^2 \tag{4.11}$$

The total electric power leaving this amplifier is

$$P_s = \frac{G}{2} R_i {I_{\Delta\omega}}^2 \tag{4.12}$$

If the detector heterodyne efficiency is ideal, as in the calculation above, then the ratio between the local oscillator current at the frequency $\Delta\omega$ and the continuous currents I_2 and I_1 is such that

$$\frac{{I_{\Delta\omega}}^2}{I_1 I_2} = 1 \tag{4.13}$$

or

$$\frac{2P_s}{G R_i I_1 I_2} = 1 \tag{4.14}$$

The actual system is not perfect; the profiles $w(r)$ of the primary and local oscillator beams are not the same because the beams are not strictly parallel. Hence the resulting distribution of phases on the detector surface is not the same. The heterodyne efficiency η_H is defined as the ratio between the power of the oscillator at the frequency $\Delta\omega$, measured at the exit of the preamplifier (P_m), and the power which is expected from the oscillator if the local oscillator and primary beam electric fields were identical, i.e.

$$\eta_H = \frac{P_m}{P_s} = \frac{2P_m}{G R_i I_1 I_2} \tag{4.15}$$

Heterodyning efficiency experiment

Fig. 4.3 shows the setup used for determining the heterodyne efficiency.

Mirrors are denoted by M, full (100%) absorbers by A, partial absorbers by a, lenses with L, and beam-splitters by BS. The reflectances of $BS1$ and $BS2$ are 0.44% and 58% respectively. The partial absorbers $a1$, $a2$, $a3$ and $a4$ are CaF_2 windows of thicknesses 3.5, 5, 6 and 3.5 mm respectively, with corresponding transmittances of 28%, 17%, 12% and 28%. The primary beam P (in red) and local oscillator LO (in blue) are first superposed at $BS2$, and the superposition of the beams is maintained over a long distance (6.7 m, on the order of the distance between the translator-rotator and the detector in the plasma experiments)

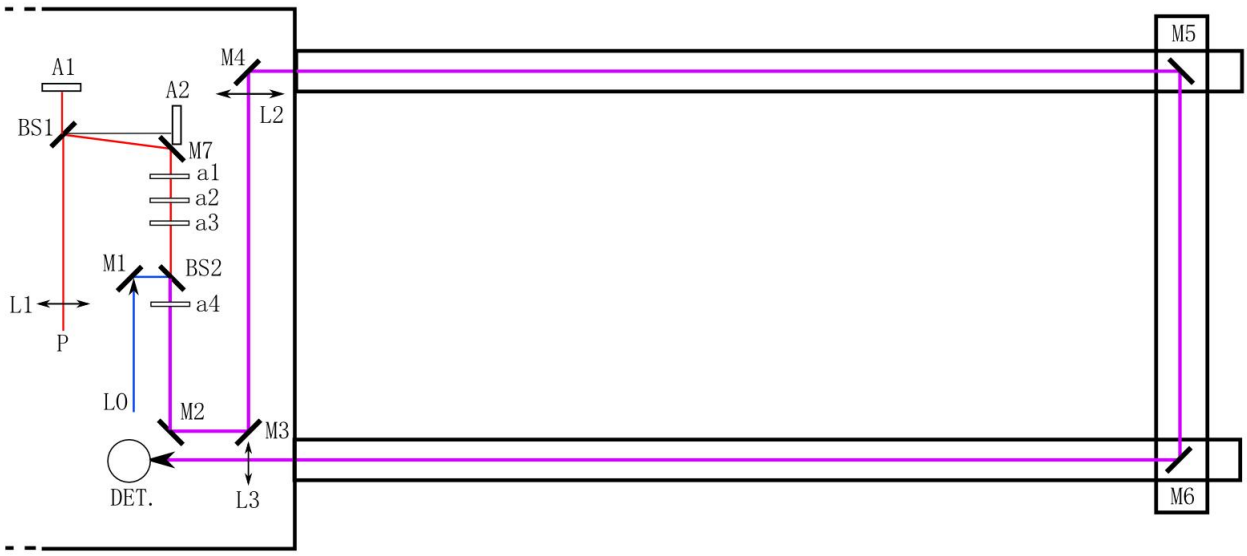

Figure 4.3: Schematic of optical bench setup for determination of heterodyning efficiency

up to the detector, with a detector beam size comparable to that used during the plasma experiments.

The primary beam has an initial power of 35 W; after partial reflection and attenuation by the absorbers, it provides a detector current of 0.243 mA. The local oscillator is reflected by $BS2$ and further attenuated by $a4$; with a reference 5 dB attenuation in the 40 MHz AOD source, it provides a detector current of 0.221 mA. The detector current, when both beams are allowed to arrive at the detector, is 0.432 mA. The thermal noise current present when the detector is closed is 0.029 mA and is subtracted from the beam currents.

The 40 MHz peak, which is seen on the detector and pre-amplifier output, corresponds to the oscillation at the frequency $\Delta\omega$ mentioned above. It has a level of 8.10 dBm, i.e. P_m = 6.46 mW. The preamplifier gain G has been independently measured as 37.22 $\pm$ 0.1 dBm.

Substituting these values into Eq. 4.15,

$$\eta_H = 1.19 \pm 2\% \tag{4.16}$$

This value is close to, but slightly larger than, 1; this is most likely due to slight laser power variations or a slight error in the determination of the preamplifier gain. The heterodyning efficiency of the bench is maximum, which means that the wavefronts along the plasma-scattered field optical path are indeed in phase with those of the local oscillator. Hence no losses in the measured signal are due to the heterodyning procedure.

4.3.3 Verification of signal level

Now that it has been assured that the heterodyning efficiency is good, the signal level output by the bench may be verified. This is done by measuring the density fluctuation of a

signal of known amplitude using the bench and comparing this measured signal level to its expected theoretical level. This calibration may be most easily done using a piezo-electric transducer which excites an acoustic wave.

The bench and off-bench assemblies are set up as for the plasma experiments, with the piezo placed in the position which would normally be occupied by the thruster, with the beams crossing just in front of the transducer face. Fig. 4.4 shows the simplified setup for measurements using an acoustic wave.

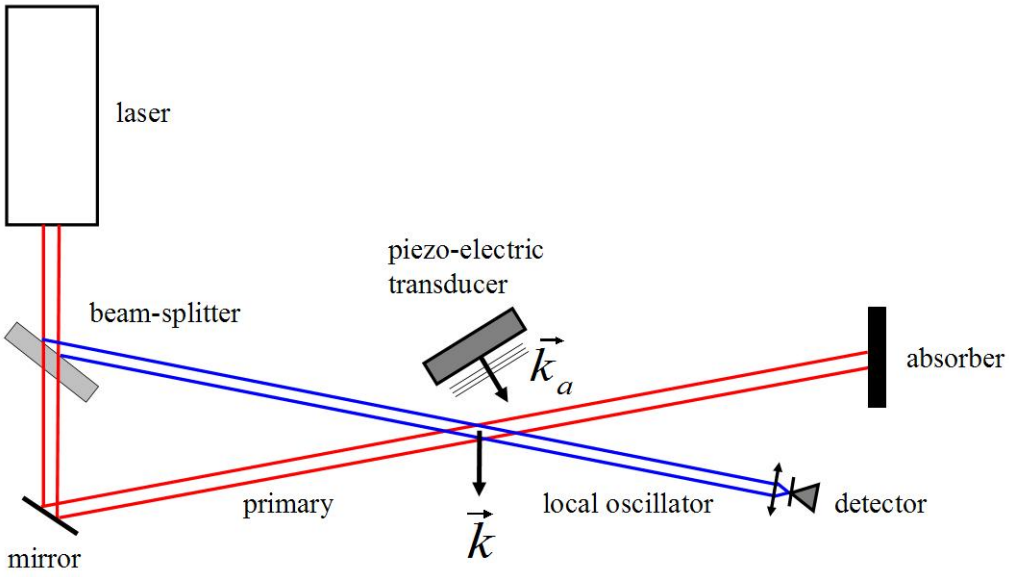

Figure 4.4: Orientation of $\vec{k}$ for calibration using an acoustic wave. The acoustic wave vector is denoted by $\vec{k_a}$, the observation wave vector by $\vec{k}$

The observation wave vector $\vec{k}$ adjusted such that it is oriented in approximately the same direction and parallel to the acoustic wave vector $\vec{k}_a$, and the scattering angle is first set to an arbitrary value of around 13 mrad. The corresponding frequency f at which a sound wave propagating in air at a velocity of c_s would be detected is related to the wave number k by

$$f = \frac{c_s k}{2\pi} \tag{4.17}$$

The value of c_s used is 340 m/s. The transducer is supplied with a sine wave signal (amplitude 2.4 V) via a signal generator, with a frequency close to f. The frequency of the sine wave is then more finely-tuned until the observed scattered signal reaches a peak as observed on a spectrum analyser, at 422 kHz in this case. This frequency is then maintained and used to make finer adjustments of the magnitude of the wave vector. The orientation of the transducer is adjusted to ensure that the acoustic wave vector is parallel to $\vec{k}$; provided this is the case, the signal is maximum.

The displacement characteristic of this transducer is 4.8×10^{-10} m/V, known with an accuracy of 50% [59]. For the supplied sine wave of frequency, the corresponding displacement amplitude, a, is 11.5×10^{-10} m.

The amplitude of this signal, n_1, is given by

$$\frac{n_1}{n_0} = \frac{a\omega}{c_s} \tag{4.18}$$

where n_0 is the density of air (2.68×10^{25} molecules/m^3) and ω the acoustic wave frequency.

The mean squared value of this amplitude is

$$\left\langle {n_1}^2 \right\rangle = \frac{1}{2}\left(\frac{a\omega n_0}{c_s}\right)^2 \tag{4.19}$$

Using the above numerical values, $\langle {n_1}^2\rangle$ = 2.89×10^{40} m^{-6}.

Hence the r.m.s value of the density fluctuation of the excited acoustic wave, $\sqrt{\langle {n_1}^2\rangle}$, is $1.70\times10^{20}\pm50\%$ m^{-3}. For a plane harmonic wave, the r.m.s value of the measured density fluctuation, $\langle {n_a}^2\rangle$, may be obtained from the optical bench characteristics and measurements as

$$\left\langle {n_a}^2 \right\rangle = \frac{2}{(r_R\lambda L)^2}\frac{h\nu}{\eta P_o}\frac{\left\langle i(t)^2\right\rangle}{\left\langle I_{ph}(\omega)^2\right\rangle} \tag{4.20}$$

where $\left\langle i(t)^2\right\rangle$ is the signal mean square value and $\left\langle I_{ph}(\omega)^2\right\rangle$ the spectral density of the photonic noise. r_R is the Rayleigh radius, L the length of the scattering volume (defined here by the transducer diameter, 25 mm). The primary beam power P_p is 35 W.

The spectral density of the photonic noise at the pre-amplifier output is obtained by subtracting the spectral density at a reference frequency, obtained when the detector is closed (P_{DC}), from that obtained when the laser beam is incident on the detector, but the piezo inactive (P_{DO}). P_{DC} = -91 dBm, or 7.94×10^{-10} mW, while P_{DO} = -98 dBm, or 1.58×10^{-10} mW.

The photonic noise spectral density is written

$$\left\langle I_{ph}(\omega)^2\right\rangle = \frac{dP_{ph}(\omega)}{df} \tag{4.21}$$

where $dP_{ph}(\omega)$ is P_{DC} - P_{DO} and df the bandwidth used, 10 kHz. $dP_{ph}(\omega)$ is 6.36×10^{-13} W. Hence the spectral density of the photonic noise is 6.36×10^{-17} W/Hz.

Now, the signal power is obtained from the level of the 422 kHz peak, which is -16.60 dBm, or 2.19×10^{-5} W. Hence

$$\frac{\left\langle i(t)^2\right\rangle}{\left\langle I_{ph}(\omega)^2\right\rangle} = 3.44\times10^{11}\ \text{Hz} \tag{4.22}$$

Substituting this ratio into Eq. 4.20, we obtain

$$\left\langle {n_a}^2 \right\rangle = 2.77 \times 10^{40} \text{ m}^{-6} \tag{4.23}$$

Therefore $\sqrt{\langle {n_a}^2 \rangle} = 1.66 \times 10^{20} \text{ m}^{-3}$.

This value is very close to that predicted for $\sqrt{\langle {n_a}^2 \rangle}$. This indicates that the signal level measured using the bench is indeed representative of the true level of the density fluctuations.

The experiments described in this chapter, aimed at measuring the heterodyning efficiency and verifying the signal level, have revealed that the signal level output by the bench is not subject to important losses or underestimations. This will allow the density fluctuation level to be interpreted later on with greater confidence.

Chapter 5

Phase II experiments: mode localization

Contents

5.1 Phase II experiments: Localization of the $\vec{E} \times \vec{B}$ mode along z

THe negative frequency peaks in the observed signal spectra are consistent with fluctuations propagating at a phase velocity opposed in sign to the wave vector. In Part I, two explanations were proposed for the presence of these peaks: (i) the negative frequency mode may correspond to a measurement of the fluctuation in the 03h00 side of the thruster channel, in which case the relative peak magnitudes are due to differing sensitivities due to the placement of the observation lozenge along z, or (ii) fluctuations are propagating in the direction of V_d and anti-V_d in the same thruster channel side.

The negative peak amplitudes during the first phase of experiments were consistently several orders smaller than the positive peak amplitudes. This could have resulted from the placement of the observation volume, or a difference in the fluctuation intensity in the azimuthal direction.

An experiment to check the origin of negative peak frequencies and different peak amplitudes is performed during the second phase of experiments and is described in this chapter.

5.1.1 Positioning of observation volume centre

The positioning of the observation volume centre depends on the manner of beam convergence in front of the thruster exit plane. Prior to each experiment, the convergence zone of the primary and local oscillator beams is simulated outside the vacuum chamber, as described in Chapter 2. The superposition of each beam is checked by a systematic comparison and adjustment of the beam positions, but some error is inherent in the procedure.

Fig. 5.1(a) shows an error in the superposition of the two laser beams (primary, in red, local oscillator, in blue) in the xOy plane. The typical error involved in such positioning, dy, is on the order of 0.5 mm, and translates to an error in the positioning of the measurement zone (in light blue), shown in an exaggerated view in Fig. 5.1(b).

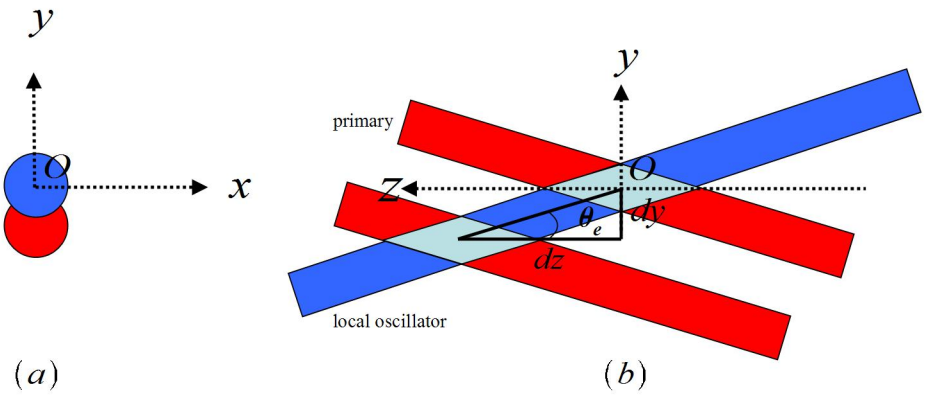

Figure 5.1: Error in positioning of the measurement volume resulting from an imperfect superposition of the primary and local oscillator beams in the plane xOy. (a) shows the situation in the xOy plane and (b) the yOz plane, for an exaggerated superposition error

The corresponding error dz in the horizontal positioning of the volume, is

$$dz = \frac{dy}{\theta_e} \tag{5.1}$$

In the present localization experiment, θ_e = 17.5 mrad, giving a dz value of about 3 cm. This value for θ_e was chosen as a compromise; for small angles, since the corresponding observation volume has a long extension along z it becomes difficult to focus the convergence region on just one side of the thruster at once. On the other hand, the signal intensity has been seen to drop exponentially as θ_e increases, and the frequency peaks become noisier. At 17.5 mrad, the maximum signal intensity is already two orders of magnitude smaller than that which could be obtained at the smallest angles. The observation wave vector is oriented parallel to the $\vec{E} \times \vec{B}$ direction and the observation volume is located 13.5 mm from the thruster exit plane.

In this experiment, the measurement volume is shifted along z to seven different positions, from -30 to $+30$ cm with respect to the thruster axis. This shift in position is performed by means of an adjustment on the optical bench of the virtual intersection position for the two

beams. This adjustment is made by changing the orientation of the mirror $M13$, which is the object-focus of the lens $L5$, with the scattering angle remaining unchanged.

The resulting spectra obtained at the different positions show two peaks (of positive and negative frequency) whose amplitudes change as a function of the position of the measurement volume along z. The positive and negative peak intensities are determined at each position. The results are shown in Fig. 5.2, where the positive peak intensities are shown in blue, the negative peak intensities in red.

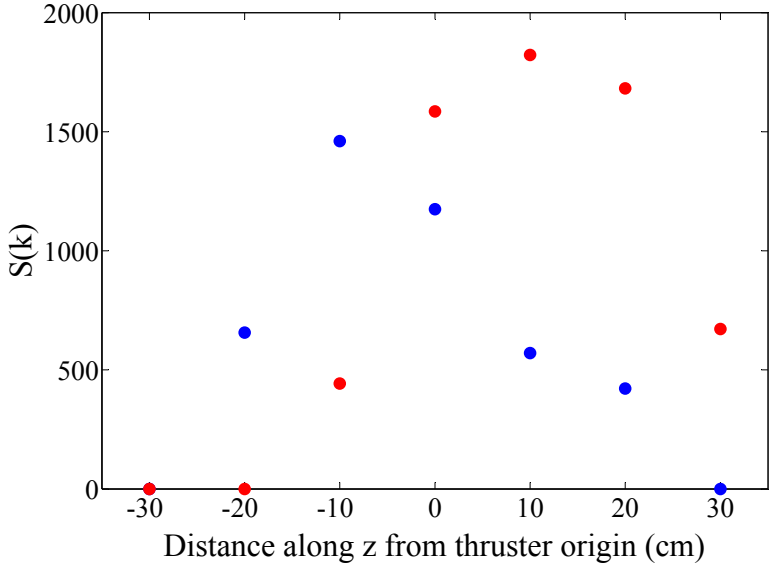

Figure 5.2: Positive (in blue) and negative (in red) frequency peak intensities as a function of the beam intersection position along z

Fig. 5.2 shows that the peak intensities are indeed linked to the position along z. The positive peak dominates when the convergence volume is situated preferentially on the 09h00 side of the thruster, while the negative peak dominates when the volume is shifted to the 03h00 side of the thruster. This first observation confirms that the large difference in positive and negative frequency peak intensities discussed in Part I is due (mainly) to the placement of the observation zone.

The evolution of the peak intensity as a function of position may be studied by considering the intensity which would be measured if the observation volume were centered at a position $\vec{r}_0$. We assume that the mode has a point source of intensity $I_\pm$, situated at $\vec{r}_\pm$, as depicted in Fig. 5.3.

In this case, the measured intensity $I(\vec{r}_0)$ is of the form

$$I(\vec{r}_0) = \int\int\int u(\vec{r} - \vec{r}_0)^2 I_\pm \delta(\vec{r}_\pm) d^3\vec{r} \tag{5.2}$$

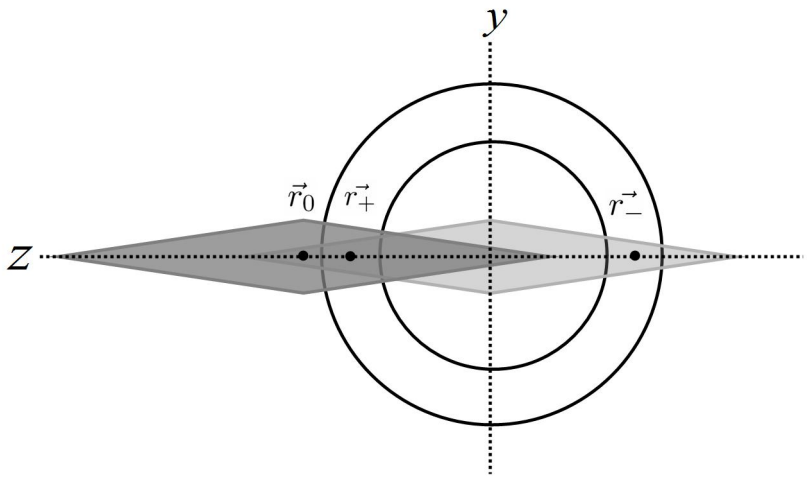

Figure 5.3: Schematic of the observation volume (in light and dark grey) for two positions of the beam intersection centre along z. $\vec{r}_+$ and $\vec{r}_-$ are coincident with the centre of the thruster channel on the 09h00 and 03h00 sides respectively; $\vec{r}_0$ is the position of the observation volume center

where $u^2(\vec{r}-\vec{r}_0)$ is the intensity profile of the observation volume. The profile of the observation volume for the intersection of Gaussian beams of waist w is written as [35]

$$u(x,y,z) = e^{\left[\frac{-z^2{\theta_e}^2}{2w^2} - \frac{2x^2}{w^2} - \frac{2y^2}{w^2}\right]} \tag{5.3}$$

In the geometry used, for $\vec{r} = z_\pm \vec{z}$, the signal intensity is then seen to vary as

$$I(z_0) = I_\pm e^{\left[-(z_0 - z_\pm)^2 {\theta_e}^2 / w^2\right]} \tag{5.4}$$

where the variance $\sigma_\pm$ is written

$$\sigma_\pm = \frac{w}{\theta_e\sqrt{2}} \tag{5.5}$$

Imposing the values of w and θ_e of this experiment (2.9 mm and 17.5 mrad respectively), a Gaussian fit of the form shown in Eq. 5.4 may be made to the data presented in Fig. 5.2, in which the optimized parameters are $I_\pm$ and $z_\pm$. The variance is 11.7 cm. The curves resulting from such an "imposed" fit are shown in Fig. 5.4(a).

The fit parameters corresponding to Fig. 5.4(a) are

$$\begin{aligned} I_- &= 1401, \quad z_- = -5.4 \text{ cm} \\ I_+ &= 2037, \quad z_+ = 10.8 \text{ cm} \end{aligned} \tag{5.6}$$

The fit of Fig. 5.4(a) can be compared with another fit of the form

$$I(z_0) = I_\pm e^{\left[-(z_0 - z_\pm)^2 / 2{\sigma_\pm}^2\right]} \tag{5.7}$$

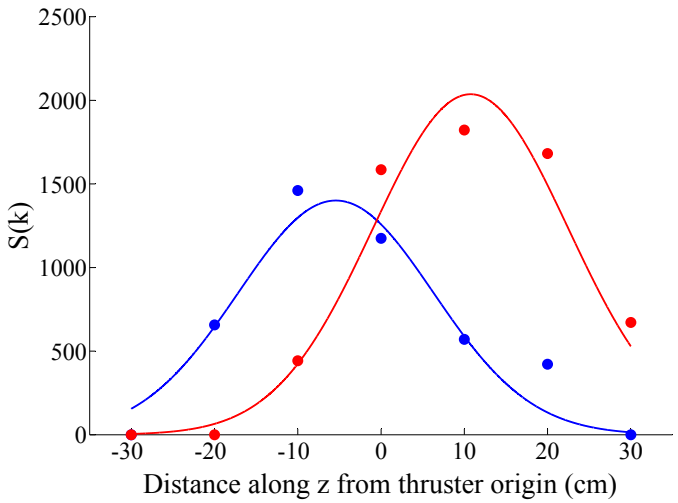

(a) Gaussian fit to peak intensity at different locations, with imposed experimental parameters θ_e of 17.5 mrad and w of 2.9 mm (variance of 11.7 cm)

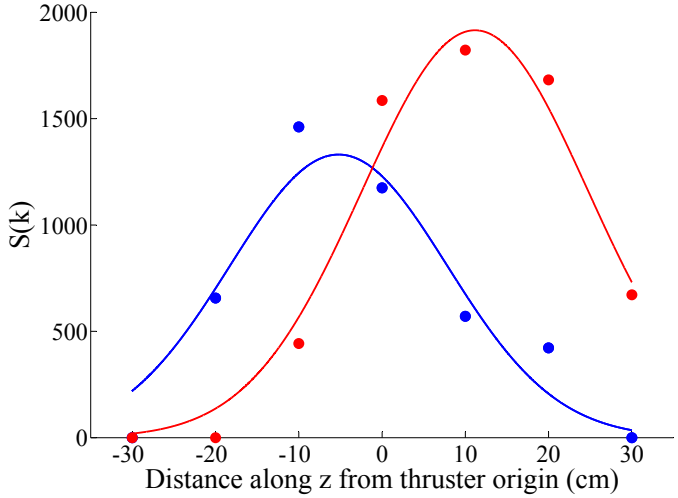

(b) Gaussian fit to peak intensity at different locations, with no imposed parameters

Figure 5.4: Gaussian fits to peak intensities with position along z

for which the experimental parameters are no longer directly imposed. $I_{\pm}$ and σ are optimized. The resulting "free" fit is shown in Fig. 5.4(b) and the corresponding fit parameters are

$$\begin{aligned} I_- &= 1331, \;\; z_- = -5.2 \text{ cm}, \;\; \sigma_- = 13.1 \text{ cm} \\ I_+ &= 1916, \;\; z_+ = 11.2 \text{ cm}, \;\; \sigma_+ = 13.6 \text{ cm} \end{aligned} \tag{5.8}$$

Certain conclusions may be drawn from these fits.

For the imposed fit, the maxima of the positive and negative frequency peaks are separated by 16.2 cm; this separation is larger than the separation of the centre points of the channels, which is only 12.5 cm. This indicates that the fluctuations are most likely situated at the exterior of the thruster channel, near the outer wall. For the free fit, the maxima are spaced by 16.4 cm, providing confirmation of the observation made using the imposed fit.

For both fits, the $z = 0$ position does not coincide with the thruster origin. The $z = 0$ position is situated at 2.7 cm for the imposed fit, and at 3.0 cm for the free fit, on the order of the positioning error which appears during the alignment.

The standard deviation for the imposed fit, $\sigma_{\pm}$, is 11.7 cm. This value is somewhat smaller than σ_+ and σ_- obtained from the free fit.

The main contribution to the amplitude of the positive and negative peak amplitudes is evidently the positioning of the thruster volume along z. However, there is also a possibility that a part of the measured mode intensity, for example, of the negative frequency peak, is due to not only to fluctuations in the 03h00, but also to backwards-propagating (opposed to the drift velocity vector) fluctuations located in the 09h00 side of the thruster channel. This scenario is not the dominant one, but may arise due to a partial reflection of the main mode in the 09h00 side.

How can such an effect be identified? The shape of the experimental points of the positive frequency peak intensities in Fig. 5.2 is one reason to suspect that there might be a contribution of a reflected wave from the 03h00 side of the thruster channel: the right flank is tail-like and non-symmetric with the left flank. A possible better fit to this data is the sum of two Gaussians centered at different locations.

For the positive frequency peak, the new fit may be thus written as

$$I_+(z_0) = I_{+a} e^{\left[-(z_0 - z_+)^2/2\sigma^2\right]} + I_{+b} e^{\left[-(z_0 - z_-)^2/2\sigma^2\right]}, \tag{5.9}$$

a form which now includes a term containing the possible intensity contribution due to propagations in the 03h00 side, $I_{+b} e^{\left[-(z_0 - z_-)^2/2\sigma^2\right]}$. Similarly, for the negative frequency peak, the new fit may be written as

$$I_-(z_0) = I_{-a} e^{\left[-(z_0 - z_-)^2/2\sigma^2\right]} + I_{-b} e^{\left[-(z_0 - z_+)^2/2\sigma^2\right]}, \tag{5.10}$$

The forms shown in Eq. 5.9 and Eq. 5.10 will be referred to as "mixed" fits. The first terms in both equations will be referred to as the "principal" Gaussian, the second as the "secondary" Gaussian.

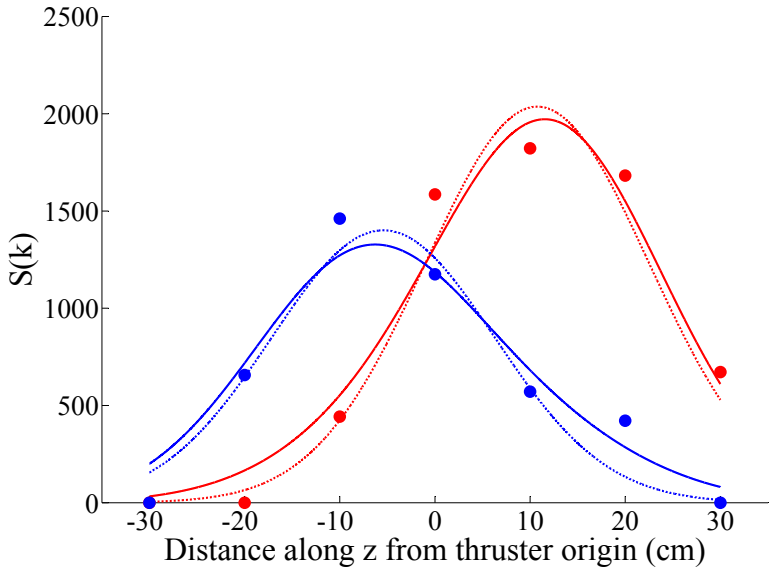

Figure 5.5: Comparison of fits to the intensity data when the mixed fit (full lines) and Gaussian fit (dotted lines) are applied to the positive frequency peaks (in blue) and the negative frequency peaks (in red)

In this new form, two parameters are imposed: (i) the theoretical value of σ, 11.7 cm, and (ii) the location parameter of the secondary Gaussian, z_- in the case of the positive frequency peak, and z_+ for the negative frequency peak. The values of these location parameters are set to the same values as the location parameters of the principal, oppositely-signed frequency peak, obtained from Eq. 5.6. The parameters $I_{\pm a}$, $z_\pm$ and $I_{\pm b}$ are optimized.

Fits to the data using the mixed fit are shown in Fig. 5.5.

The resulting fit parameters when the mixed fits are used are

$$\begin{aligned} I_{-a} &= 1237, \quad z_- = -7.7 \text{ cm}, \quad I_{-b} = 286 \\ I_{+a} &= 1882, \quad z_+ = 12.4 \text{ cm}, \quad I_{+b} = 272 \end{aligned} \tag{5.11}$$

Additionally, a measure of the difference of the goodness of fit may be defined as

$$\chi = \sqrt{\frac{\Sigma(I_{fit} - I_{expt})^2}{\Sigma(I_{expt})^2}} \tag{5.12}$$

where I_{fit} and I_{expt} are the intensity fit values (from the simple Gaussian and mixed fits) and the experimental intensity values, respectively.

We will consider first the fit to the positive frequency values (in blue). The value of χ over all the data points for the simple Gaussian fit is 0.149, compared to 0.0978 when the mixed fit is applied. The mixed fit clearly provides a better description for the right flank of

the experimental values of the positive frequency peak. In the case of the negative frequency peak, the value of χ for the simple Gaussian is 0.120, and 0.101 for the mixed case.

These observations indicate that the hypothesis of partial reflection of the modes is a better estimate of the experimental observations. The mixed fit is a good means of estimating the contribution to the measured signal of fluctuations in the opposite channel. The parameters obtained from the fit can be used to estimate the percentage of energy which is due to fluctuations in the opposite channel.

This rate, τ_R, is defined as

$$\tau_R = \frac{I_{\mp b}}{I_{\pm a}} \tag{5.13}$$

i.e. this rate is determined through a comparison of the amplitude of the secondary Gaussian (obtained from the mixed fit) to the amplitude of the principal Gaussian due to the oppositely-signed frequency peak.

Hence τ_R for the positive frequency peak is 15%, i.e. 15% of the positive peak energy is due to a reflection of the wave propagating in the opposite channel. The reflection rate for the negative frequency peak is 22%.

This reflection sets up standing waves. The periodicity of the standing wave amplitude is half the propagating wavelength. Our observation on the form factor distribution with length scale shows that the largest fluctuation amplitude occurs at wavelengths equal to, or longer than, 1.6 mm. Thus the observed standing wave energy periodicity is equal to, or longer than, 0.8 mm. These waves might account for the presence of the periodic erosion pattern which appears on the thruster ceramic; in particular, the periodicity of these grooves is on the order of a 1 or 2 mm. There is a possibility that the modes we observe near these length scales play some role in the erosion.

This is a point which underscores the usefulness of the thruster plasma experiments which can be performed using collective light scattering: apart from enabling the study of a variety of instabilities, it is also possible to identify the source of other phenomena which affect thruster performance and lifetime.

5.2 Physical hypotheses concerning the localization of the $\vec{E} \times \vec{B}$ mode

The observations on the localization of the $\vec{E} \times \vec{B}$ mode along z_1 may be explained in terms of possible physical mechanisms which are at the origin of the instability. The most intense modes are likely to be located on the periphery of the outer ceramic, rather than near the centre of the thruster channel. This scenario can be explained by considering the radial distribution of the magnetic and electric fields.

The electron cyclotron drift length, l_{ce}, is written as

$$l_{ce} = \frac{2\pi m_e E}{q_e B^2} \tag{5.14}$$

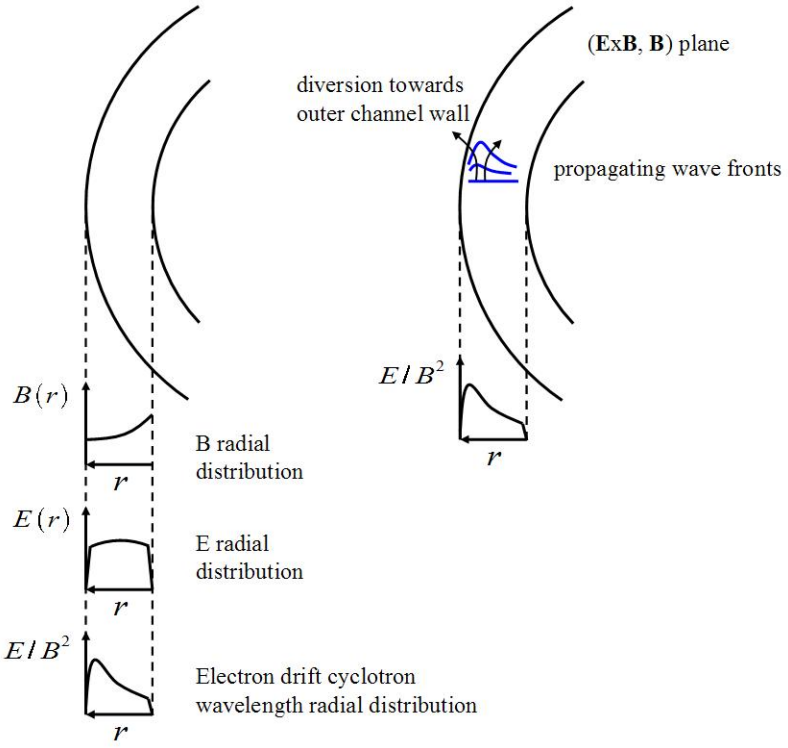

Figure 5.6: Variation of electron cyclotron drift length l_{ce} with radial position (left) and a schematic of wavefront deformation in the direction of propagation (right)

This length scale corresponds to the length scale of the instability, on the order of a mm. l_{ce} evolves with the radial position as shown qualitatively in Fig. 5.6.

l_{ce} is maximum near the outer channel and smaller near the interior; this non-uniformity would generally mean that no particular length scale of instability, and hence no particular mode, is favoured to develop. If, however, the value of l_{ce} were maintained over a sufficient radial distance, a particular mode could grow, mainly parallel to $\vec{E}\times\vec{B}$. This mode propagates from a region where the wavefront is aligned with the thruster radius. As the wavefront moves azimuthally, the distance of the wavefront to the previous, 2π-delayed front, is shorter on the inner and outer locations of the thruster channel where l_{ce} is shorter. Thus the wavefront is bent to a convex shape. The local wave vector, normal to this surface, is oriented outwards at the major channel radius, and inwards at the minor radius, as depicted in Fig. 5.6. The main direction of propagation diverges from the $\vec{E} \times \vec{B}$ direction and this could account for the observation of the most intense modes near the outer channel wall. The divergence from the $\vec{E} \times \vec{B}$ direction will be revisited in Chapter 6.

The experiments described in this chapter have been successfully used to account for the negative frequency peak seen on typical $\vec{E}\times\vec{B}$ spectra, through a localization of the mode

along z. The possibility of reflected modes and the consequences on the peak intensity have also been considered. Additional aspects concerning the nature of the mode propagation will be considered in the next chapter.

Chapter 6

Phase II experiments: low wave number characteristics and mode directionality

Contents

6.1 Mode energy saturation at low wave numbers

An experiment is performed in which the dispersion relation and form factor evolution with wave number for the $\vec{E} \times \vec{B}$ mode are determined. The goals of this experiment in Phase II are to confirm the characteristics of the previously observed dispersion relation, and also examine the behaviour of the $\vec{E} \times \vec{B}$ mode at the longer length scales which are now achievable.

The magnitude of the wave vector is systematically varied between 4000 and 12600 rad/m, while the orientation of the wave vector is maintained parallel to the $\vec{E} \times \vec{B}$ direction (α = 90°). The experiment is performed with a flow rate of 18 mg/s and the beams are positioned at a distance of 12 mm from the thruster exit plane, a location chosen to provide the maximum signal level, as based on observations in the Phase I experiments.

The first unstable mode predicted by linear theory appears for $k_y V_d/\omega_{ce}$ = 1. The corresponding value of k_y associated with this mode is 3956 rad/m, as was shown in Part I. The minimum value of 4000 rad/m attainable by PRAXIS-II is very close to this value, but an exploration below this value requires a number of modifications to the bench which are beyond the scope of the present experimental campaign.

The dispersion relation for the given experimental conditions is shown in Fig. 6.1. The group velocity is 4.21×10^3 m/s and the y-intercept -17.9 kHz, not significantly different from zero.

Of more interest is the trend in form factor, shown in Fig. 6.2. The e-decrement in Fig. 6.2 is 0.5 mm.

Surprisingly, the form factor does not show the marked slope change at large wave number which was shown in Part I. The reason for this inconsistency is not yet clear. The form factor exhibits an exponential dependence on wave number. At the smallest wavenumbers, there is no evidence that the energy of the mode has reached its maximum value, and it may very well continue to increase as the wave number decreases. A saturation in the mode amplitude at the first cyclotron harmonic can therefore not be confirmed at present.

In order to describe azimuthally-propagating fluctuations, poloidal coordinates will be adopted in this chapter. Fig. 6.3 shows the configuration which will be used to describe the experiments in this chapter. The laser beam crosses the thruster axis along z_1. The wave vector is oriented at an angle α to the direction x_1, and has components k_θ and k_x of variable magnitudes. k_θ is oriented in the opposite direction to the electron drift velocity, while k_x is

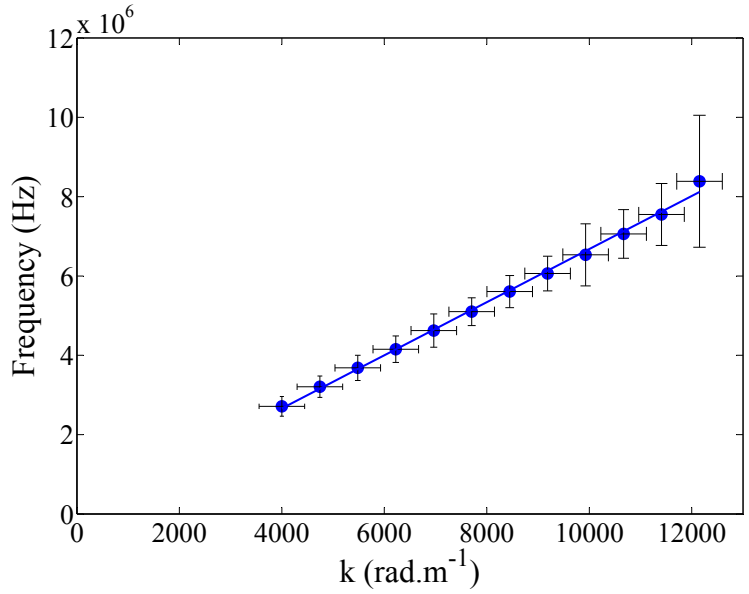

Figure 6.1: Dispersion relation for the $\vec{E} \times \vec{B}$ mode, for an experiment featuring the minimum wave number

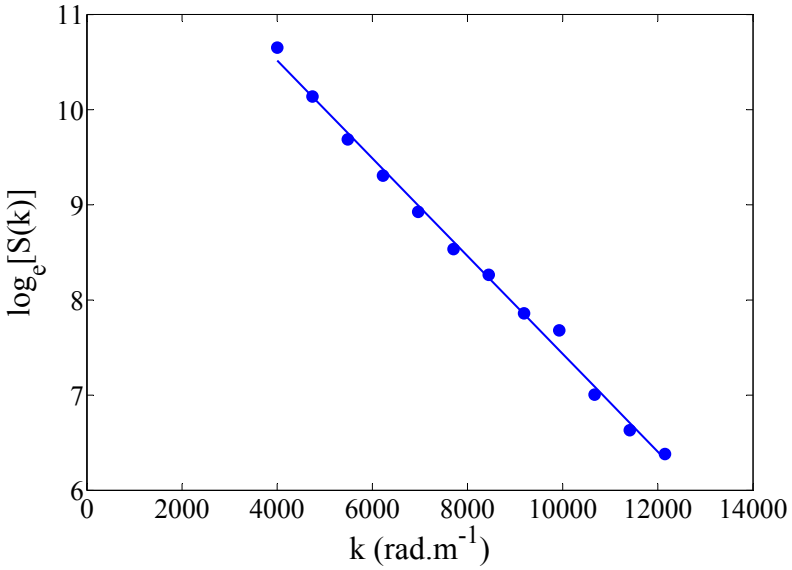

Figure 6.2: Form factor variation with wave number, for an experiment featuring the minimum wave number

in the direction of the electric field. k_r is oriented in the opposite direction to the magnetic field. In the orientation shown in Fig. 6.3, the k_r component of the wave vector is zero.

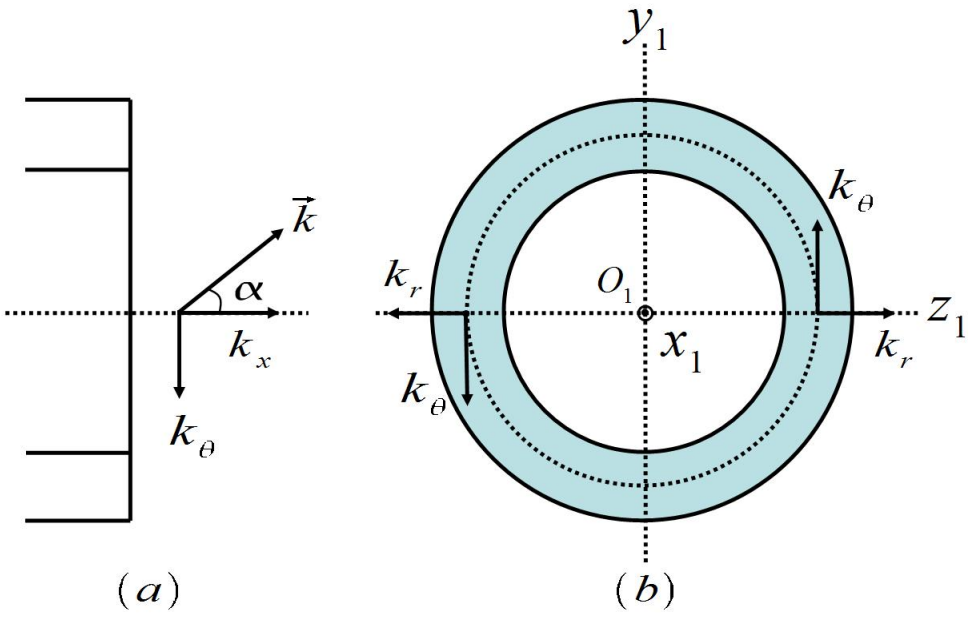

Figure 6.3: Poloidal coordinate system for the examination of the k_θ and k_x components of the wave vector when the laser beam crosses the thruster axis along z_1; (a) shows a side view of the thruster with the reference angle α, which is varied, (b) shows the orientation of the wave vector components as viewed from the thruster face

6.2 Form factor variation in the (k_x, k_θ) plane

The variation of the mean square amplitude of the modes can be examined on PRAXIS-II over an expanded range of 320°.

In these experiments, the magnitude of the wave vector is fixed at the lower end of the range of accessible wave numbers, for two reasons: firstly, to allow a large signal to be obtained and to study its progressive change in level over a sufficiently large range of angles, and secondly, to also allow a visualization of the high frequency axial mode within the 20 MHz frequency range of the experiment.

In the experiment presented here, the gas flow rate is 18 mg/s, and the observation volume is 17 mm from the thruster exit plane. The wave number used is 5928 rad/m.

6.2.1 $\vec{E} \times \vec{B}$ mode directionality in the (k_x, k_θ) plane

Fig. 6.4 shows the form factor variation with α, for the positive and frequency peaks. The $\vec{E} \times \vec{B}$ drift direction corresponds to 90°.

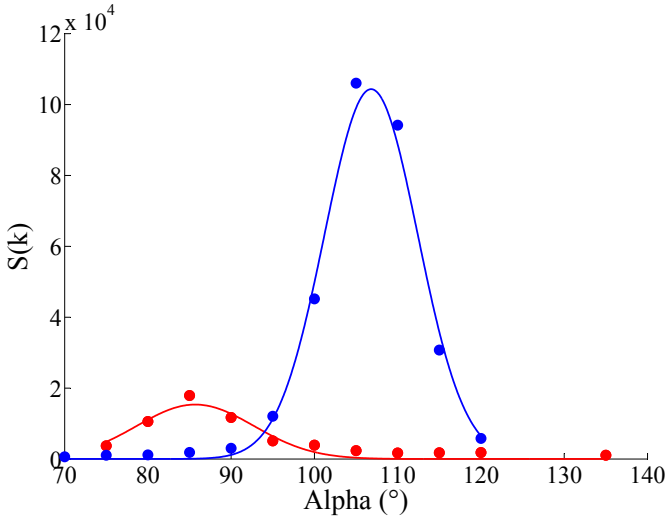

Figure 6.4: Variation of form factor of the $\vec{E} \times \vec{B}$ mode with α in the (k_x, k_θ) plane. The positive frequency peak data is shown in blue, the negative frequency peak data in red

The difference in amplitudes of the peaks is due to the positioning of the observation volume along the direction z_1, as has been shown earlier.

The data points are fitted with Gaussian curves whose parameters are

$$\begin{aligned} A_1 &= 1.04 \times 10^5, \quad \mu_1 = 106.8^\circ, \quad \sigma_1 = 5.60^\circ \\ A_2 &= 1.54 \times 10^4, \quad \mu_2 = 85.7^\circ, \quad \sigma_2 = 7.05^\circ \end{aligned} \tag{6.1}$$

with

$$\begin{aligned} \mu_1 - \mu_2 &= 21.1^\circ \\ \bar{\mu} = (\mu_1 + \mu_2)/2 &= 96.25^\circ \end{aligned} \tag{6.2}$$

where A, μ and σ represent the amplitude, mean value and standard deviation for Gaussian fits to the positive frequency peak data (subscript 1) and the negative frequency peak data (subscript 2).

The first important observation from this experiment is that the maximum in energy of the mode is not obtained at an α of 90° for the positive frequency peak (or 90° for the negative frequency peak), as was expected. From the values in Eq. 6.1, it is evident that the mode does not propagate purely parallel to $\vec{E} \times \vec{B}$, but with an additional inclination of 16.8° towards the thruster for the positive peak, and 4.3° towards the thruster for the negative peak. The reference angle α is not absolute, however, the precision in the determination of the wave vector orientation in the (k_x, k_θ) plane is 2.7±4°. The angular position of the two peaks should be symmetric on either side of the $\vec{E} \times \vec{B}$ drift direction; this is obtained if the

reference angle is shifted by $(\frac{\mu_1+\mu_2}{2} - 90°)$, or 6.25°. This is an acceptable shift, in the range of precision of the measurements. For the symmetric positive and negative frequency peaks, the mean deviation from the $\vec{E} \times \vec{B}$ drift direction is therefore 10.6°.

The second important observation is that the mean angular width σ of the mode is only 6.33° ($\frac{\sigma_1+\sigma_2}{2}$). In the experiments with PRAXIS-I, the angular opening of the mode in the $x_1O_1y_1$ quadrant was greatly overestimated at 45°. In reality, the mode has a much more limited angular extension in this plane, so small, in fact, that it must be considered in the context of the resolution of the diagnostic in order to determine its true extent.

The relation of the angular device resolution σ_d to the wave number k and device wave number resolution is shown in Fig. 6.5.

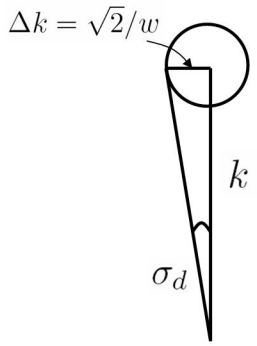

Figure 6.5: Relation between device angular resolution σ_d and wave number resolution Δk

Its r.m.s value is

$$\sigma_d = \frac{\sqrt{2}}{2\pi k w} \cdot \ 360° \tag{6.3}$$

The device resolution is 4.71°. A Gaussian with standard deviation of σ_d and with an amplitude and mean value chosen to be equivalent to the positive frequency peak values is now compared to the experimental data (Fig. 6.6).

The observed angular extension of the mode is broadened by the device resolution; if this effect is excluded, then the true extension of the mode σ is

$$\sigma = \sqrt{{\sigma_1}^2 - {\sigma_d}^2} \tag{6.4}$$

The true angular extension of the mode in this plane is therefore 3.0°.

It should be noted that when $\vec{k}$ is oriented parallel to $\vec{E} \times \vec{B}$, but in the opposite direction to the drift, as is the case when α is around 270°, near-identical observations are made: the only difference is that the negative frequency peak is now the dominant peak (Fig. 6.7).

The Gaussian fit parameters for this symmetric position of $\vec{k}$ are shown in Eq. 6.5.

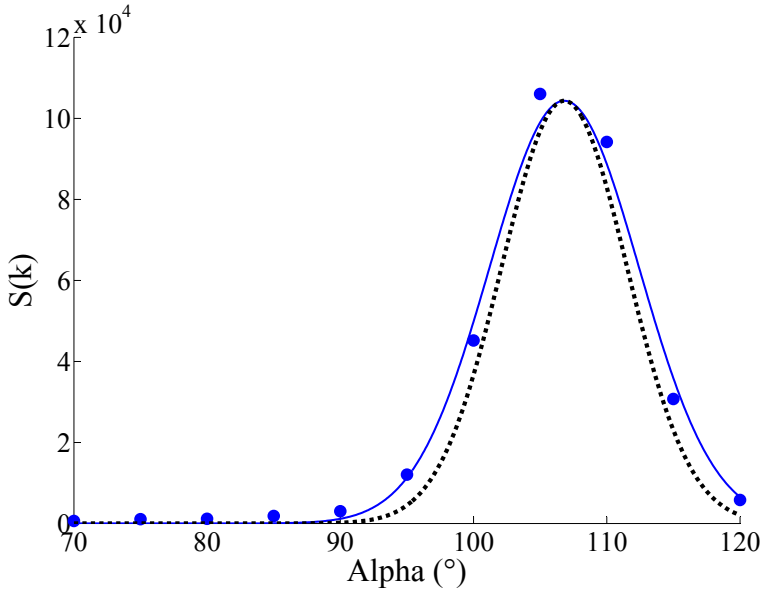

Figure 6.6: Comparison of experimental angular extension of the $\vec{E} \times \vec{B}$ mode in the (k_x, k_θ) plane for the positive frequency peak (in blue) to the natural angular extension resulting from the device resolution (dotted line)

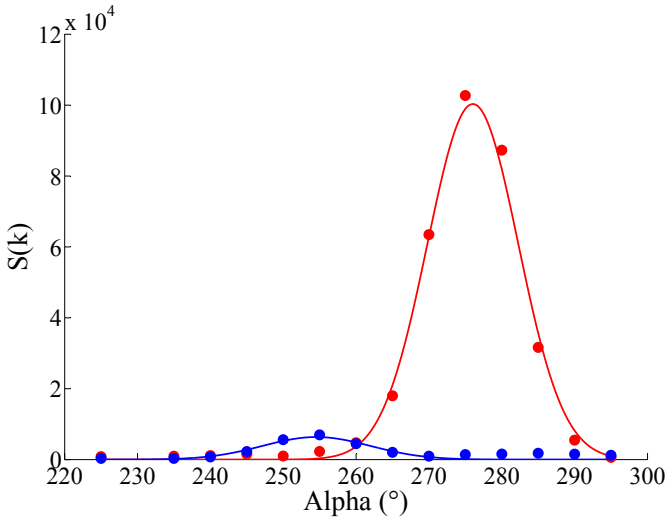

Figure 6.7: Variation of form factor of the $\vec{E} \times \vec{B}$ mode with α in the (k_x, k_θ) plane. The positive frequency peak data is shown in blue, the negative frequency peak data in red

$$\begin{aligned} A_1 &= 6.35 \times 10^3, \;\; \mu_1 = 254.6^\circ, \;\; \sigma_1 = 7.05^\circ \\ A_2 &= 1.00 \times 10^5, \;\; \mu_2 = 276.0^\circ, \;\; \sigma_2 = 6.24^\circ \end{aligned} \tag{6.5}$$

with

$$\begin{aligned} \mu_1 - \mu_2 &= 21.4^\circ \\ \bar{\mu} = (\mu_1 + \mu_2)/2 &= 265.3^\circ \end{aligned} \tag{6.6}$$

The difference in mean angular positions in Eq. 6.6 is the same as in Eq. 6.2 to within 0.3°. The difference in the mean angle $\bar{\mu}$, obtained when the wave vector is oriented at 90° and 270°, is not precisely 180°, but 169°. This indicates a slight irregularity in the mirror rotation used.

In summary,

- the $\vec{E} \times \vec{B}$ mode propagates within a very narrow angular range in the (k_x, k_θ) plane, determined to be 3.0°
- the mode is inclined at 10.6° angle to the vertical, oriented inwards towards the thruster exit plane, and therefore possesses a component anti-parallel to the electric field

The observation that the mode is not aligned purely along the $\vec{E} \times \vec{B}$ drift direction but is directed towards the interior of the thruster has certain consequences which will be examined more closely in future work. For instance, it has already been demonstrated that standing waves can be set up in the thruster which could contribute to the periodic erosion pattern of the ceramic. The inclination of the mode toward the interior would appear to make such erosion likely.

6.2.2 Axial mode directionality in the (k_x, k_θ) plane

The angular extension of the axial mode is studied in the same experiment, albeit at a slightly different wave number, 5631 rad/m. The variation of the form factor of the positive high frequency peak with α (observed when $\vec{k}$ is oriented in about the same direction as the ion beam) is shown in Fig. 6.8.

The Gaussian fit parameters corresponding to Fig. 6.8 are

$$A = 4.37 \times 10^3, \;\; \mu = 8.22^\circ, \;\; \sigma = 24.2^\circ \tag{6.7}$$

The first important observation here is that the angular extension of the axial mode in the (k_x, k_θ) plane is much greater than that of the $\vec{E} \times \vec{B}$ mode. After removing the effect of the device resolution from the peak width, the angular extension of the mode is 23.7°.

The mean angle is not aligned with the x_1 direction, with a deviation of 8° which exceeds the angular resolution. This non-zero angle with respect to x_1 appears to correspond with visual observations which show that the thruster plume is not entirely symmetric about the thruster axis.

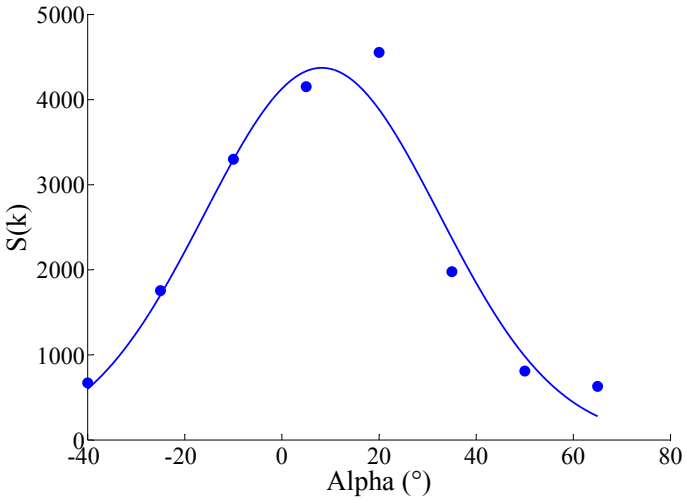

Figure 6.8: Variation of form factor of the axial mode with α in the (k_x, k_θ) plane

6.3 Mode frequency variation in the (k_x, k_θ) plane

6.3.1 Frequency variation with α for the $\vec{E} \times \vec{B}$ mode

The $\vec{E} \times \vec{B}$ mode has been observed to have large amplitudes within a very restricted range of α. We now examine the evolution of the mode frequency within this range.

Fig. 6.9 shows the variation of the $\vec{E} \times \vec{B}$ mode peak frequency with α. The frequencies shown correspond to the peak frequencies of the peaks whose energies are shown in Fig. 6.4. Surprisingly, the frequency changes by a large degree over the range of α values, and also exhibits an unexplained abrupt variation. As the angle is increased from 70° to 85°, the amplitude increases and the frequency decreases to an eventual value of 1.35 MHz. As the angle is increased further, the amplitude continues to increase but the frequency jumps suddenly to a value of 4.43 MHz, at 90°, where $\vec{k}$ is now aligned with the $\vec{E} \times \vec{B}$ drift. While the amplitude increases only until 105° and then decreases, the frequency monotonically decreases as the angle increases.

The reason for the sudden change in frequency is not yet known, pending further analysis of linear kinetic theory. Despite the angular restriction of the mode, the mode frequencies appear to be very sensitive to the angle α.

The dependence of the frequency on α has certain implications for the dispersion relation. The dispersion relations that have been so far investigated for the $\vec{E} \times \vec{B}$ mode have used a wave vector oriented parallel to the $\vec{E} \times \vec{B}$ drift. The maximum mode amplitude is, in reality, obtained at 105°, and the corresponding peak frequency is lower by a factor of 1.6 than the frequency obtained when $\vec{k}$ aligned along $\vec{E} \times \vec{B}$. It must therefore be kept in mind that frequency values of the dispersion relation solutions are descriptive of a particular angle α, even though the group velocity obtained from such dispersion relations may be independent

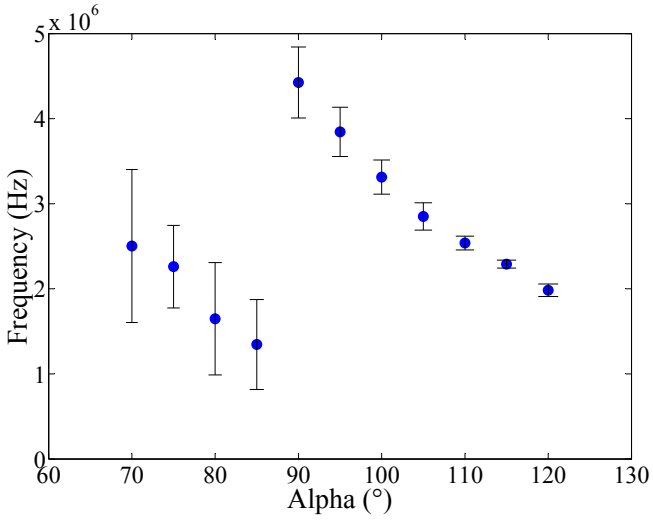

Figure 6.9: Variation of the frequency of the positive frequency peak with α in the (k_x, k_θ) plane, for the $\vec{E} \times \vec{B}$ mode

of α.

6.3.2 Frequency variation with α for the axial mode

The variation in frequency of the axial mode (positive frequency peak) with α is shown in Fig. 6.10. The frequency variation observed is consistent with that expected if the mode frequency were proportional to the projection of wavenumber along the axis x_1. The data is fitted to a curve of the form $f = A\cos(\theta + \phi)$, and the fit parameters obtained are

$$A \;=\; 2.12 \times 10^7 \text{ Hz}, \quad \phi = 1.80^\circ \tag{6.8}$$

Interestingly, a fit of this form (in red in Fig. 6.10) fails to match the data, particularly for angles outside the range -40° $< \alpha <$ +40°, where the frequencies are higher than would be expected. It therefore appears that the idea of simple projection of the wave number (and velocity) may not be accurate. Instead, a modified fit of the form $f = A\cos(n\theta+\phi)$ is applied (in blue in Fig. 6.10), for which the fit parameters are now

$$A \;=\; 2.06 \times 10^7 \text{ Hz}, \quad n = 0.75, \quad \phi = 9.83^\circ \tag{6.9}$$

This modified fit is clearly superior. This seems consistent with the previous observation that the dispersion relation for the axial mode is not a simple Doppler relation.

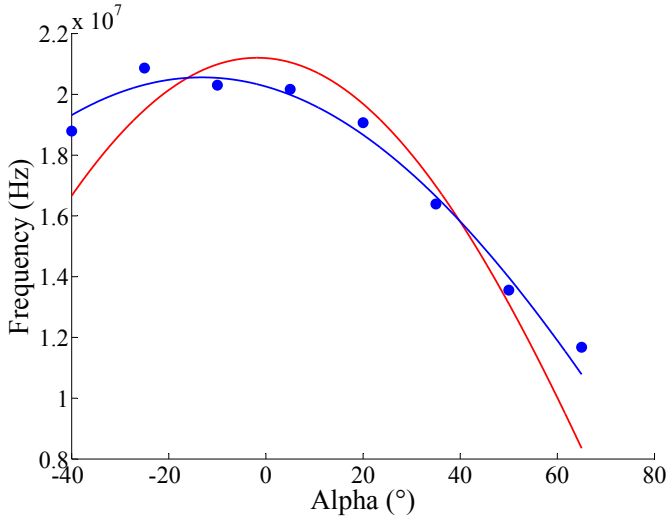

Figure 6.10: Variation of frequency of the axial mode with α in the (k_x, k_θ) plane, with two fits applied: a simple cosine law (in red), and a modified cosine law (in blue)

6.4 Form factor variation in the (k_x, k_r) plane

In the configuration discussed in the previous section, in which the beams were aligned along the z_1 direction and parallel to the radial $\vec{B}$ field, the k_r component was on the order of its smallest possible value (the inverse channel dimension, or 250 rad/m). The early numerical simulations of the wave performed by Adam et. al. [2] were based solely on k_θ and k_x components (with k_r = 0).

However, the influence of a wave vector component parallel to $\vec{B}$ cannot be neglected. For instance, as was mentioned after the first phase of experiments, the presence of a non-negligible k_r could be sufficient to explain why the experimental dispersion relations, unlike those derived from linear theory using k_r = 0, are continuous. For this reason, and also to complete the study of directionality of the modes, it was decided to perform experiments with different, known k_r components.

New numerical solutions to the dispersion relation taking into account a non-negligible k_r component have been recently performed by A. Héron (Centre de Physique Théorique, Ecole Polytechnique) and these results will be discussed in the context of experimental data in a subsequent chapter.

6.4.1 Comparison of fluctuations perpendicular and parallel to $\vec{B}$

The first experiment involving the addition of a k_r component aims to compare the mode amplitudes perpendicular to $\vec{B}$ and parallel to $\vec{B}$. In the configuration shown in Fig. 6.3, whatever the orientation of $\vec{k}$ in the (k_x, k_θ) plane, it is necessarily perpendicular to $\vec{B}$. The sole configuration which permits an orientation of the wave vector purely parallel to $\vec{B}$

(for a certain α) is the placement of the observation volume at the top or bottom thruster channel.

Fig. 6.11 shows the configuration adopted for one such experiment. To make this experiment possible, the thruster is raised by 47 mm inside the vacuum chamber, and the observation volume lowered by 20 mm. The observation volume is finally situated a distance h (67 mm) below the thruster axis. For measurements of the top thruster channel, the measurement volume is situated 60 mm above the thruster axis.

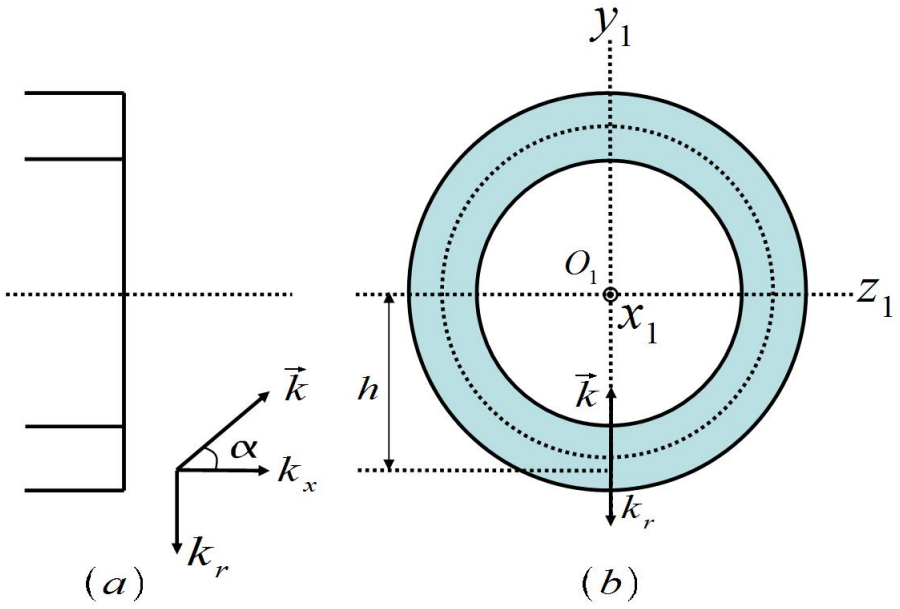

Figure 6.11: Configuration for the measurement of $\vec{k}$ aligned along $\vec{B}$; (a) shows a side view for the variation of α, (b) shows the orientation in which $\vec{k}$ may be aligned parallel to $\vec{B}$, corresponding to $\alpha = 90°$

An angular exploration in α is carried out at the lower thruster channel to determine how the mode amplitudes change as $\vec{k}$ becomes progressively more aligned with $\vec{B}$. The value of wave number is fixed at 5780 rad/m. The thruster exit plane is 17 mm from the observation volume center, and the flow rate is 18 mg/s. The mean square amplitudes of the modes are presented in Fig. 6.12.

In Fig. 6.12, peaks pertaining to the axial mode, at α from -45° to 45°, are present with relatively high form factors. The form factor reaches a maximum of over 17000. Consistent with earlier observations for this axial mode, this maximum in energy is not observed at 0°, but a few degrees inclined with respect to the x_1 axis. The Gaussian fit parameters obtained for this range of data are: A = 1.63×10^4, μ = -17.3°, and σ = 24.5°. The significance of the negative μ value will be discussed shortly.

In the range $100° < \alpha < 150°$, signals corresponding to the axial mode are measured. This is possible because as the angle continues to increase, $\vec{k}$ becomes progressively more oriented in the direction opposite to that of the the axial mode propagation. The $\vec{E} \times \vec{B}$ mode,

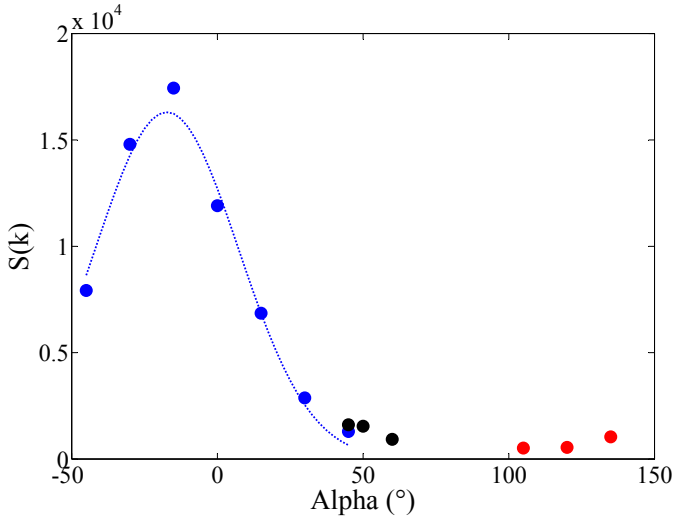

Figure 6.12: Variation in form factor of modes with α in the plane (k_x, k_r), for the observation volume situated at the lower thruster channel (06h00). Points pertaining to the axial mode positive frequency peak are in blue; points pertaining to the axial mode negative frequency peak are in red; points identified as the "cathode mode" are in black. A Gaussian curve (dotted line) is shown superposed on the axial mode positive frequency peak data

on the other hand, cannot be seen in this experimental configuration because $\vec{k}$ is always located in the (k_x, k_r) plane, and therefore perpendicular to $\vec{E} \times \vec{B}$.

No signal is seen when $\alpha = 90°$, the angular value for which the wave vector is aligned parallel to $\vec{B}$ (and anti-parallel to k_r).

A similar angular exploration is performed at the top thruster channel. The corresponding form factor trend is shown in Fig. 6.13.

As in the case of the lower channel, no signal is seen when $\alpha = 90°$, or at the symmetric position of $\alpha = 270°$. These experiments confirm that the neglect of density fluctuations parallel to $\vec{B}$ in comparison with fluctuations perpendicular to $\vec{B}$ is indeed justified.

6.4.2 The "cathode" mode

Fig. 6.12 shows a number of points which correspond neither to the $\vec{E} \times \vec{B}$ mode frequencies nor to the axial mode. These correspond to low-frequency, non-Gaussian peaks which appear between 45 and 60°. In the present work, this new mode has been named the "cathode mode" because it is seen during observations of the lower thruster channel only, the channel position closest to where the cathode is located. The possible link of this mode to the cathode has been confirmed by an angular exploration in the (k_x, k_r) plane performed at the top thruster channel. The observations of the axial mode positive and negative high frequency peaks were repeated, however, the cathode mode was absent at the top thruster channel.

At $\alpha = 45°$, both cathode and axial modes can be identified. Fig. 6.14 shows the

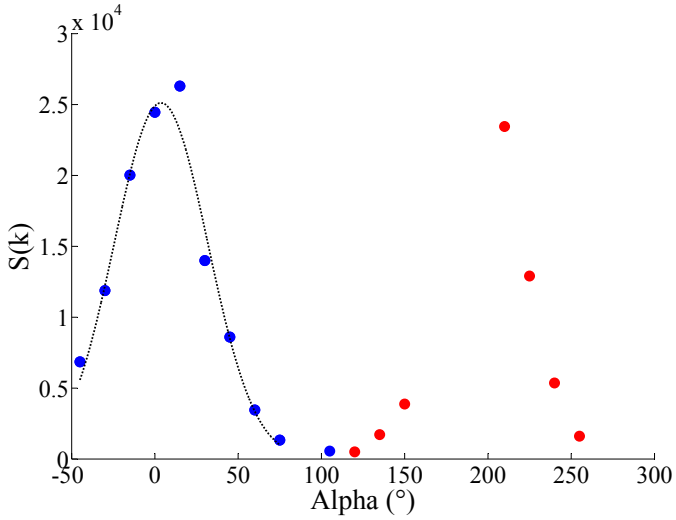

Figure 6.13: Variation in form factor of modes with α in the plane (k_x, k_r), for the observation volume situated at the upper thruster channel (12h00). Points pertaining to the axial mode positive frequency peak are in blue; points pertaining to the axial mode negative frequency peak are in red. The cathode mode is absent. A Gaussian curve (dotted line) is shown superposed on the axial mode positive frequency peak data

frequency spectrum corresponding to this angle. The form factor of the cathode mode is nearly identical to that of the axial mode at this angle and appears to change little with α.

6.4.3 Axial mode width and mean angle in the (k_x, k_r) plane

It is interesting to consider how the axial mode mean angle and width in the (k_x, k_r) plane change when the observation volume is situated at the top and bottom thruster channels. Apart from the observation of the cathode mode at the lower channel, are the 12h00 and 06h00 positions on the azimuth otherwise symmetric? Fig. 6.15(a) and Fig. 6.15(b) show the variation in form factor over α for the lower and upper thruster channels (positive frequency peaks of the axial mode), for an angular exploration around $\alpha = 0°$.

The Gaussian fit parameters for the bottom thruster channel form factors are

$$A = 1.63 \times 10^4, \quad \mu = -17.4°, \quad \sigma = 24.6° \tag{6.10}$$

while for the top thruster channel the parameters are

$$A = 2.51 \times 10^4, \quad \mu = 3.70°, \quad \sigma = 28.1° \tag{6.11}$$

The angular widths are comparable to the on-axis case, and quite similar to each other. However, it is interesting to observe here that the mean angle μ is very different at

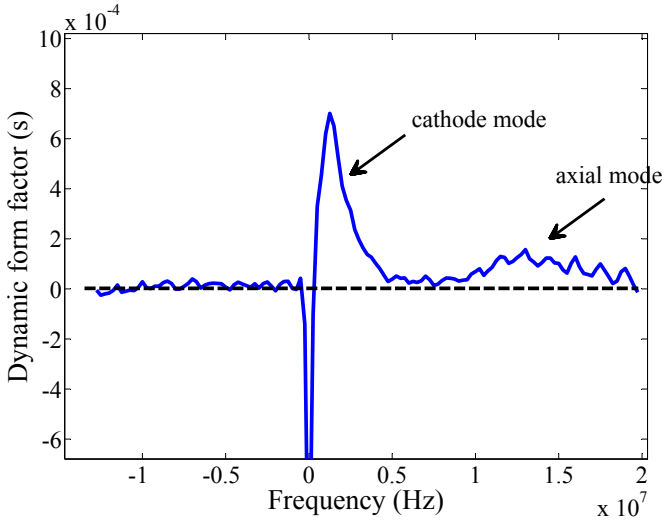

Figure 6.14: Dynamic form factor versus frequency for the case in which axial and "cathode" modes coexist ($\alpha = 45°$), observation in the (k_x, k_r) plane

the top and bottom thruster channels. At the top thruster channel, the mean angle is positive and the mode propagates with an upward deviation with respect to x_1. On the other hand, at the bottom thruster channel, the same mode now propagates with a significant downward deviation with respect to x_1. This observation is a confirmation of the asymmetry of the 12h00 and 06h00 thruster positions.

6.5 Mode frequency variation in the (k_x, k_r) plane

The variation in frequency of the axial and cathode modes is examined for the lower and upper thruster channels.

In Fig. 6.16, the frequencies of the axial (and cathode) mode are shown as a function of α, where the observation volume is situated at the bottom thruster channel. A cosine profile of the form $f = A\cos(n\theta + \phi)$ is fitted to axial mode frequency data. The corresponding fit parameters are

$$A \;=\; 1.84 \times 10^7 \text{ Hz}, \quad n = 1.1, \quad \phi = 2.00° \tag{6.12}$$

The negative frequency mode is symmetric with the positive frequency mode.

The frequencies of the cathode mode with α are presented in Fig. 6.16. One interesting feature is that the frequency of the cathode mode remains constant at 1 MHz, independent of the angle. The precise mechanism by which the cathode mode is produced is not clear. It may be related to the electron source issuing from the cathode. The asymmetry between the fluctuations at the lower and upper thruster channels may be due to the fact that the cathode is located only at the 06h00 position on the azimuth.

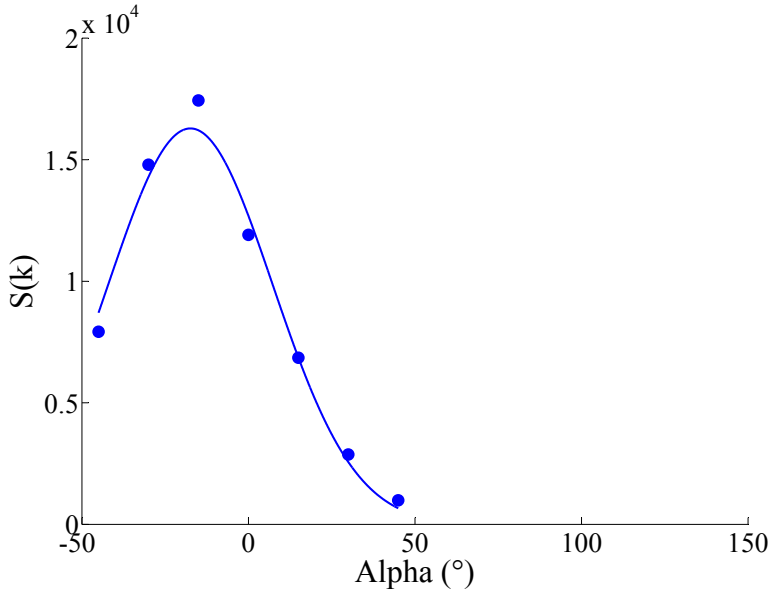

(a) Form factor variation with α, bottom thruster channel

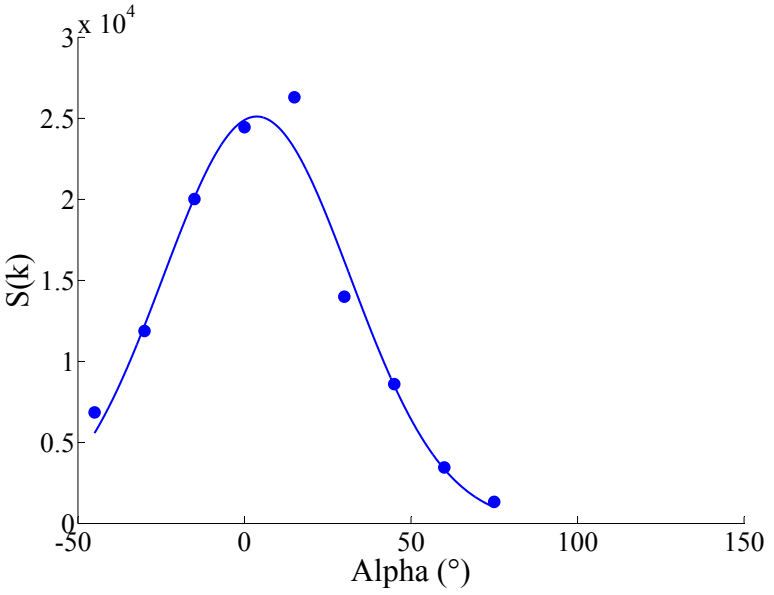

(b) Form factor variation with α, top thruster channel

Figure 6.15: Angular extension of axial mode at bottom and top thruster channels

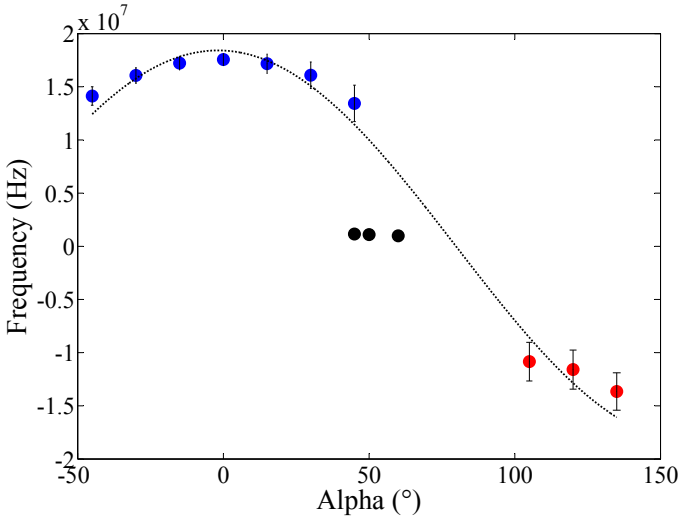

Figure 6.16: Variation in frequency of modes with α in the plane (k_x, k_r), for the observation volume situated at the lower thruster channel (06h00). Points pertaining to the axial mode positive frequency peak are in blue; points pertaining to the axial mode negative frequency peak are in red; points identified as the "cathode mode" are in black. A cosine fit (dotted line) is shown applied to the axial mode positive and negative frequency peak data

The frequency observations at the top thruster channel, concerning the axial mode, are shown in Fig. 6.17. The cosine law fit parameters corresponding to a fit to the entire range of angles are

$$A \;=\; 1.85 \times 10^7 \text{ Hz}, \quad n = 1.0, \quad \phi = -12.0^\circ \tag{6.13}$$

However, a separate fit to the frequency data in the region of -40° $< \alpha <$ +40° may be made in order to compare these observations to those made in the (k_x, k_θ) plane, where the thruster was on-axis. In this case as well, a fit using a simple cosine law is not adequate, as demonstrated in Fig. 6.18. The n value from the modified cosine fit is 0.82.

The results presented in this section on the axial mode reveal some interesting asymmetries between the upper and lower channels. The study of the directionality of the $\vec{E} \times \vec{B}$ mode is resumed in the next section, where an exploration in the (k_θ, k_r) plane is described.

6.6 Form factor variation in the (k_θ, k_r) plane

The method used for varying the magnitude of k_r is a systematic shift of the measurement volume position with respect to the axis. The wave vector is maintained at the same orientation in the (k_x, k_θ) plane (at α = 100°, and not at α = 90°, in order to approach the maximum in the $\vec{E} \times \vec{B}$ mode amplitude, as observed in the (k_x, k_θ) plane).

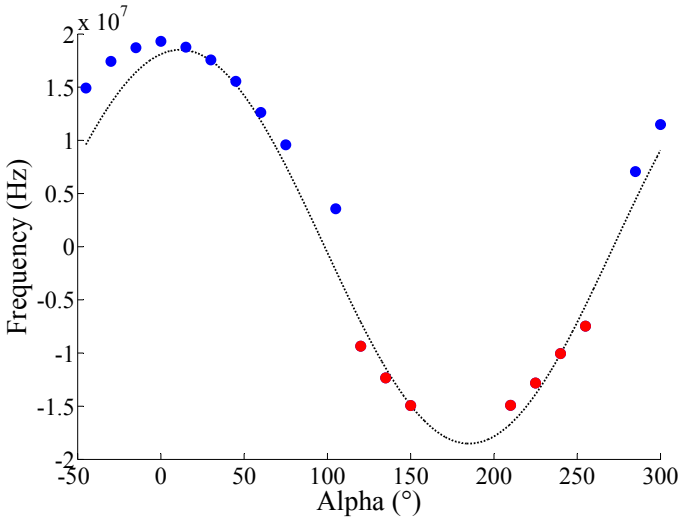

Figure 6.17: Variation in frequency of modes with α in the plane (k_x, k_r), for the observation volume situated at the upper thruster channel (12h00). Points pertaining to the axial mode positive frequency peak are in blue; points pertaining to the axial mode negative frequency peak are in red. A cosine fit (dotted line) is shown applied to the axial mode positive and negative frequency peak data

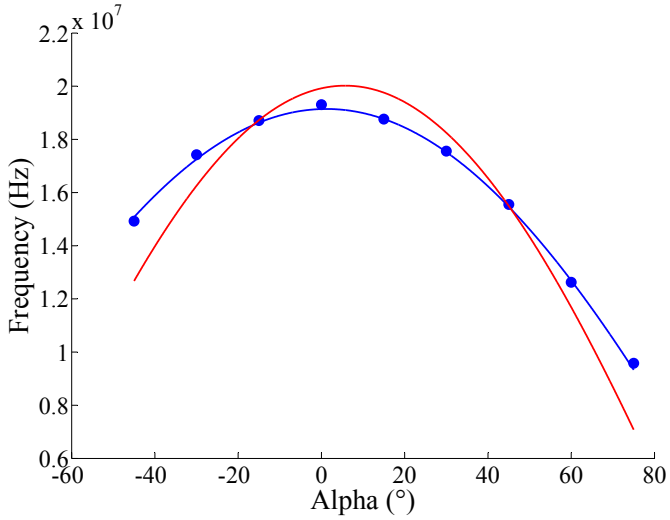

Figure 6.18: Variation of frequency of the axial mode with α in the (k_x, k_θ) plane, with two fits applied: a simple cosine law (in red), and a modified cosine law (in blue). The observation volume is at the upper thruster channel

The goal of these experiments is to study how the energy of the $\vec{E} \times \vec{B}$ mode changes with k_r. The configuration used in the experiments is shown in Fig. 6.19, where the magnitude of the k_r component is changed by displacing the measurement volume to different heights h with respect to the axis.

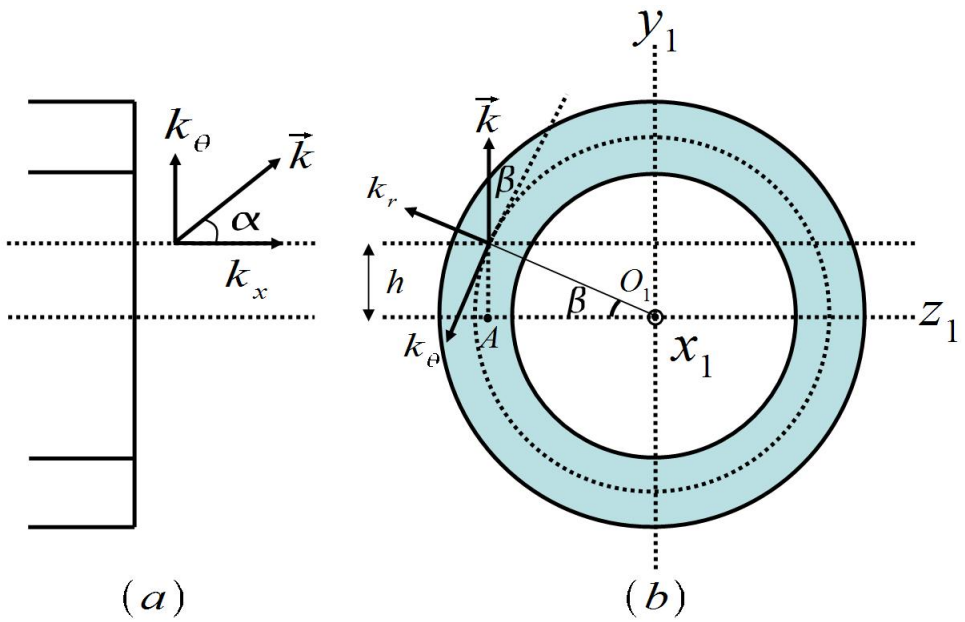

Figure 6.19: Configuration for the variation of the k_r component of the observation wave vector. Beams are positioned at a height h relative to the thruster axis as shown in the side view (a) and front view (b)

The relationship between the observation wave number and k_r is given by

$$k_r = k \sin\beta \tag{6.14}$$

with β obtained from

$$\tan\beta = h/R \tag{6.15}$$

R (corresponding to the distance 0_1A in Fig. 6.19) is a mean distance of 62.5 mm, the distance from O_1 to the middle of the channel, and $R \gg h$. It has been observed previously that the $\vec{E} \times \vec{B}$ modes measured at the 09h00 and 03h00 positions appear to be located near the exterior of the channel. However, given the degree of uncertainty of that previous experiment, for simplicity in this analysis the modes are assumed to be located in the centre of the channels.

For this experiment, only two values of α are used: to study the $\vec{E} \times \vec{B}$ mode, α is set to 100°, while for the axial mode, α is set to 0°. The beams are positioned at a distance of 17 mm from the thruster exit plane, and the flow rate used is 18 mg/s. The wave number value is set to 5187 rad/m. h is varied in 2 mm steps, from -5 to 15 mm.

6.6.1 $\vec{E} \times \vec{B}$ mode directionality in the (k_θ, k_r) plane

The form factors of the $\vec{E} \times \vec{B}$ mode are determined for the different h values. The form factors as a function of β are shown in Fig. 6.20.

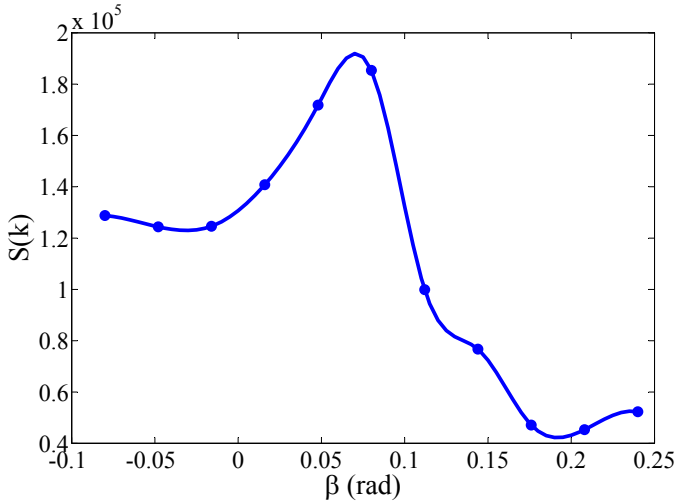

Figure 6.20: Variation of form factor of the $\vec{E} \times \vec{B}$ mode with β (positive frequency peak)

The variation of form factor with β for this mode exhibits some surprising characteristics. The first observation of note is that the form factor of the mode is not maximum for $\beta = 0$, the angle corresponding to the placement of the measurement volume along z_1. Instead, the form factor reaches a maximum in energy (a very high level, 18.5×10^4) at β = 0.08 rad, or h = 5 mm. This is an indication that the mode is inclined in the plane $y_1 O_1 z_1$, i.e. the $(\vec{E} \times \vec{B}) - \vec{B}$ plane. This inclination from the $\vec{E} \times \vec{B}$ drift direction is 4.58°.

To determine the width of the form factor in β due to the device resolution, the formula for the longitudinal resolution, given by Eq. 1.14, is applied. In this case, the corresponding $\delta\beta$ is written

$$\delta\beta = \frac{\lambda}{2\pi\sqrt{2}w} \tag{6.16}$$

The corresponding value of $\delta\beta$ is 4.11×10^{-4} rad. This value is sufficiently small to be considered negligible in comparison with the peak width shown in Fig. 6.20.

The form factor distribution is also non-symmetric around its maximum. It is interesting to consider the distribution in the context of the negative frequency peak form factor, corresponding to observations in the other channel. The form factor distribution for this peak is shown in Fig. 6.21.

In Fig. 6.21, the observed form factor values are several orders of magnitude smaller than those of the positive frequency peak; this is due to the fact that the particular value of angle α used in this experiment (100°) was chosen to obtain the maximum signal amplitude

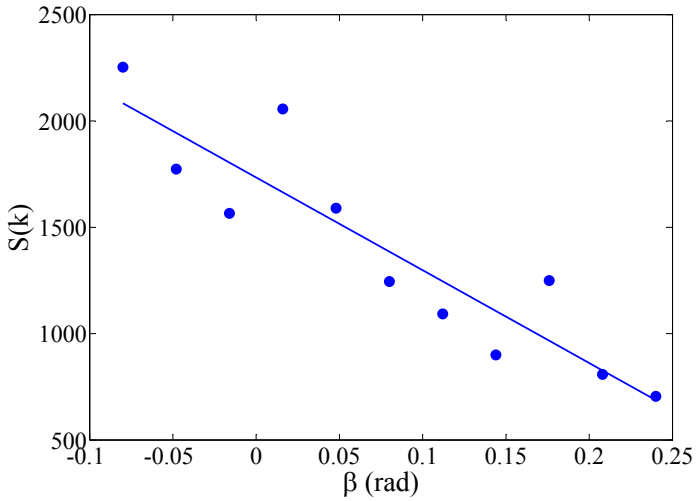

Figure 6.21: Variation of form factor of the $\vec{E} \times \vec{B}$ mode with β (negative frequency peak)

for the positive frequency peak. It should be recalled that, based on the results of the angular exploration in the plane (k_x, k_θ), the maximum in the negative frequency peak would be situated around 80°.

Fig. 6.21 shows an almost uniform decrease in form factor with β, a different distribution from that of Fig. 6.20. The differing distributions are most easily explained using another figure (Fig. 6.22).

Fig. 6.22 illustrates the difference between the positive and negative frequency peak cases. V_p is introduced as the projection of the drift velocity in the direction of the observation wave vector. For the positive frequency peak, this velocity projection is directed in the direction of positive k_r. On the other hand, for the negative frequency peak on the other channel side, the velocity projection is in the direction of negative k_r. The difference in the form factor distributions is accounted for by these projections and their relation to k_r.

What is clear at this point is that there is indeed a non-negligible k_r component to this mode, as seen by the high form factor level for β = 0.08. This indicates that the two-dimensional instability analysis, where the k_r component is neglected, is inaccurate.

6.6.2 Axial mode directionality in the (k_θ, k_r) plane

The variation of the form factors of the axial mode with β is determined for the same range of h values. The distribution is shown in Fig. 6.23.

The axial mode is seen to propagate with the similar intensities at different heights with respect to the thruster axis. Unlike the $\vec{E} \times \vec{B}$ mode, the dependency on k_r is weak for the range of β values considered and no privileged direction with respect to the plane $\vec{E} \times \vec{B} - \vec{B}$ can be identified.

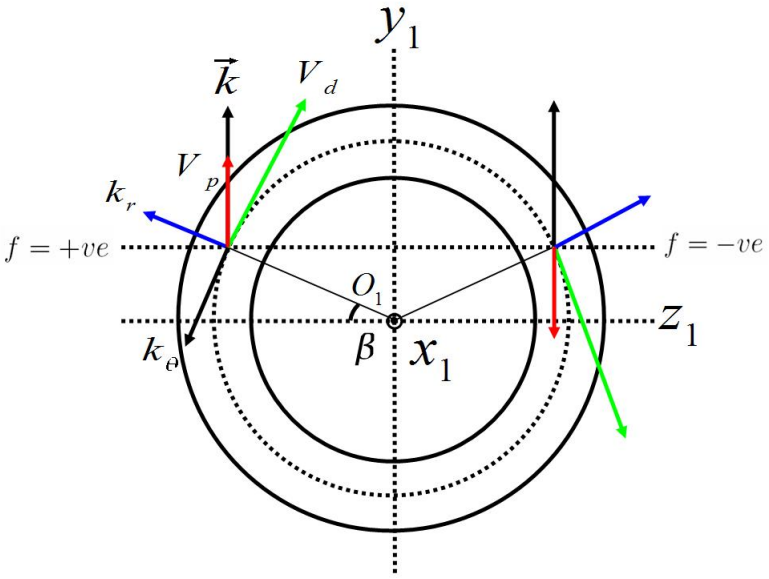

Figure 6.22: Configurations for k_r (in blue), k (in black), V_d (in green) and V_p (in red) for the observation of the positive and negative frequency peaks of the $\vec{E} \times \vec{B}$ mode

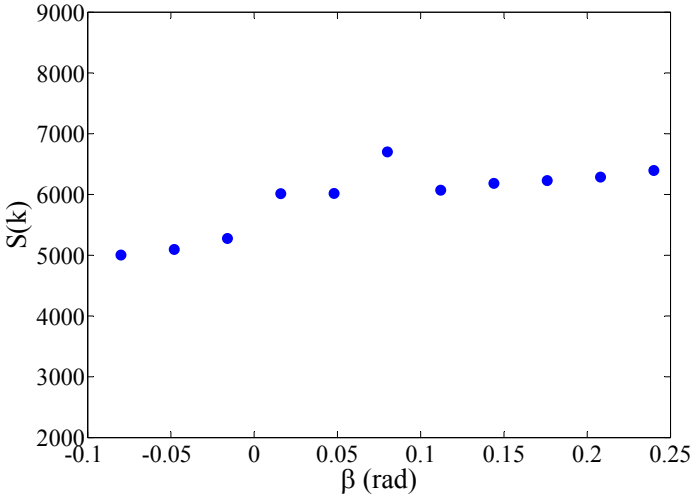

Figure 6.23: Variation of form factor of the axial mode with β (positive frequency peak)

6.7 Mode frequency variation in the (k_θ, k_r) plane

As was observed earlier during an exploration of the (k_x, k_θ) plane, the $\vec{E} \times \vec{B}$ mode shows an abrupt and unexplained frequency change when α is varied. It is interesting to examine whether these frequency discontinuities are evident in the (k_θ, k_r) plane as well. The frequency dependency on β is now examined for both the $\vec{E} \times \vec{B}$ and axial modes.

6.7.1 Frequency variation with β for the $\vec{E} \times \vec{B}$ mode

The variation of the frequency of the $\vec{E} \times \vec{B}$ mode positive frequency peak with β is shown in Fig. 6.24.

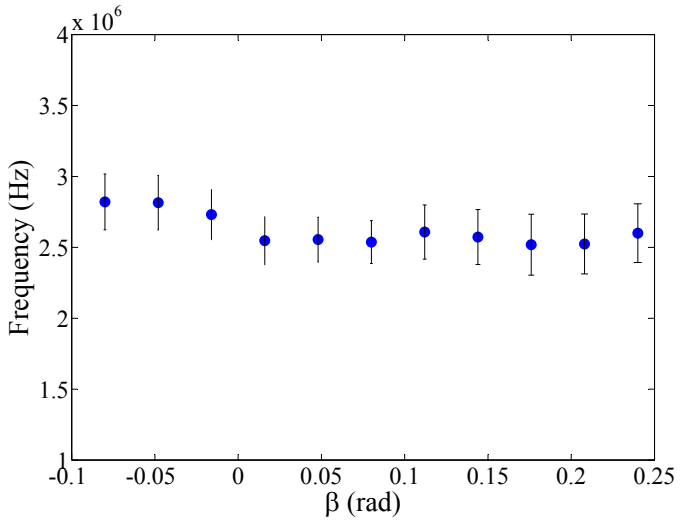

Figure 6.24: Variation of frequency for the $\vec{E} \times \vec{B}$ mode with β (positive frequency peak)

The frequency remains practically constant for various values of k_r, suggesting that the observation is of a single mode despite the differing positions of the measurement volume with respect to the axis. The frequency rupture observed during the variation of α is not evident here.

6.7.2 Frequency variation with β for the axial mode

Fig. 6.25 shows the frequency variation with β for the axial mode. As in the case of the $\vec{E} \times \vec{B}$ mode, the frequency remains constant for different heights with respect to the thruster axis.

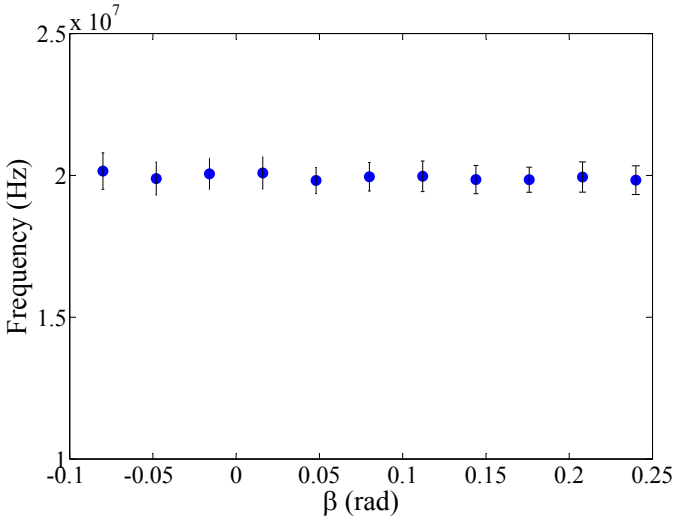

Figure 6.25: Variation of frequency for the axial mode with β (positive frequency peak)

6.8 Form factor of the $\vec{E} \times \vec{B}$ at three reference values of β with varying α

To complete the study of directionality of the $\vec{E} \times \vec{B}$ mode, an exploration in α is carried out for three different values of h. The earlier observations about the mode's angular opening in the plane (k_x, k_θ) were made with the observation volume on the thruster axis, with $h = 0$. It is useful to determine whether these previous findings are dependent on the magnitude of the k_r component present.

For this experiment, the three values of h used are -5, 5 and 15 mm (corresponding to β of -0.08, 0.08 and 0.24). An α exploration is carried out between 75 and 130° to follow the evolution in form factor of the positive frequency peak of the mode.

The experimental conditions (18 mg/s flow rate, 17 mm separation between beams and thruster exit plane) are maintained. The results of the exploration are shown in Fig. 6.26.

Standard Gaussian fits are applied to each set of points to obtain the amplitude, mean and peak widths. The results of these optimizations are given in Eq. 6.17. The values for β = -0.08, 0.08 and 0.24 have subscripts of 1, 2 and 3 respectively.

$$\begin{aligned} A_1 &= 1.69 \times 10^5, \ \mu_1 = 105.1^\circ, \ \sigma_1 = 6.28^\circ \\ A_2 &= 2.06 \times 10^5, \ \mu_2 = 103.9^\circ, \ \sigma_2 = 6.37^\circ \\ A_3 &= 0.877 \times 10^5, \ \mu_3 = 104.0^\circ, \ \sigma_3 = 6.19^\circ \end{aligned} \tag{6.17}$$

It is interesting to note that, although the mode amplitude changes, the maximum in the amplitude is attained at the same value of α for all three values of β. The values of mean angle and standard deviation are very close for the three cases, and are very close to

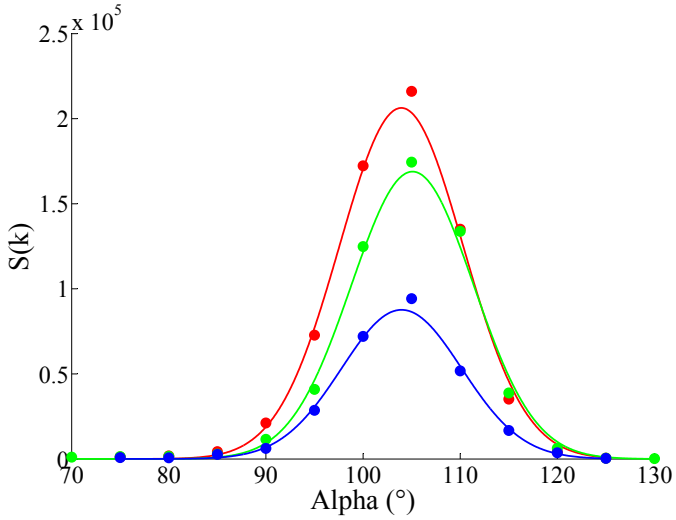

Figure 6.26: Variation in form factor with α for the $\vec{E} \times \vec{B}$ mode (positive frequency peak), for different β values: β = -0.08 (in green), β = 0.08 (in red), and β = 0.24 (in blue)

those obtained for the on-axis measurement for β = 0. This confirms the universality of the properties of the mode extension in α and mode localization within a few degrees which were described earlier. The directionality observed in the (k_x, k_θ) plane is the same whatever the magnitude of k_r.

6.9 Frequency of the $\vec{E} \times \vec{B}$ at three reference values of β with varying α

The variation in frequency for these reference values of β are shown in Fig. 6.27.

The rapid frequency change in the vicinity of the $\vec{E} \times \vec{B}$ drift direction first seen in the on-axis experiment is observed also for $k_r \neq 0$. It should be noted that a frequency rupture for only one case (β = -0.08) is shown. This is because the frequencies are not easily resolved in the other cases (due to a low signal level and very broad peak). However, the sudden change in frequency is observed in all three cases.

The three β values show similar frequency trends with α. While the frequency values observed in a (k, ω) dispersion relation are dependent on the particular value of α, they are independent of the magnitude of the k_r component, at least in the range of values considered.

6.10 Visualization of mode directionalities

Based on the experimental results outlined above, the directionalities of the $\vec{E} \times \vec{B}$ and axial modes may be represented in three dimensions using appropriate diagrams.

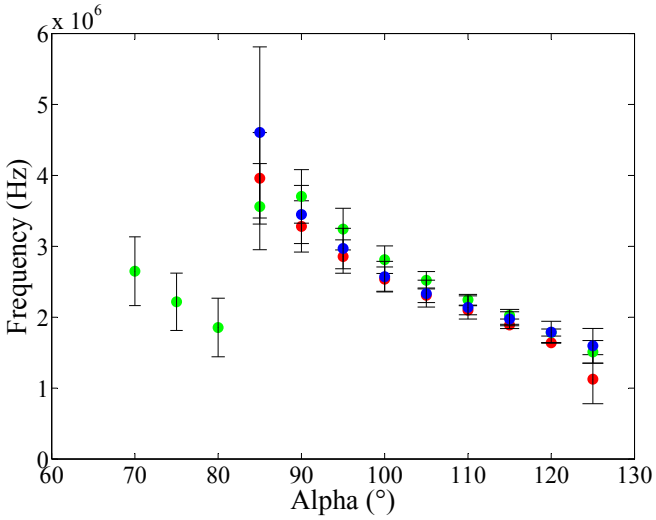

Figure 6.27: Variation in frequency with α for the $\vec{E} \times \vec{B}$ mode (positive frequency peak), for different β values: β = -0.08 (in green), β = 0.08 (in red), and β = 0.24 (in blue)

6.10.1 $\vec{E} \times \vec{B}$ directionality

Fig. 6.28 shows the propagation orientation of the main $\vec{E} \times \vec{B}$ mode, identified by wave vector $\vec{k}_m$. The angles α (90 + 10.6°) and β (4.58°) for the positive frequency peak shown in the figure are exaggerated for purposes of illustration.

A useful visualization is the form factor of the mode, based on its dependencies on α and β determined in this chapter. Fig. 6.29(a) provides such a visualization of the mode amplitude, with the contribution of the device resolution removed.

Fig. 6.29(b) shows a projection of the mode amplitude as a function of α and β which corresponds to the 3D view in Fig. 6.29(a). The thick horizontal line shows the absolute reference for β = 0 rad, the angle for which the observation volume is situated on-axis.

The thick vertical line on the projection indicates the reference angle which corresponds to the position of the axis Oy in the plane (k_x, k_θ). This angle, which would ideally be $90°$, is corrected to take into account the indetermination of the positioning. The corrected reference angle used is 96.25°, as mentioned earlier in Eq. 6.2.

6.10.2 Axial mode directionality

The main direction of propagation of the axial mode is shown in Fig. 6.30, with an angle α determined to be 8.22°.

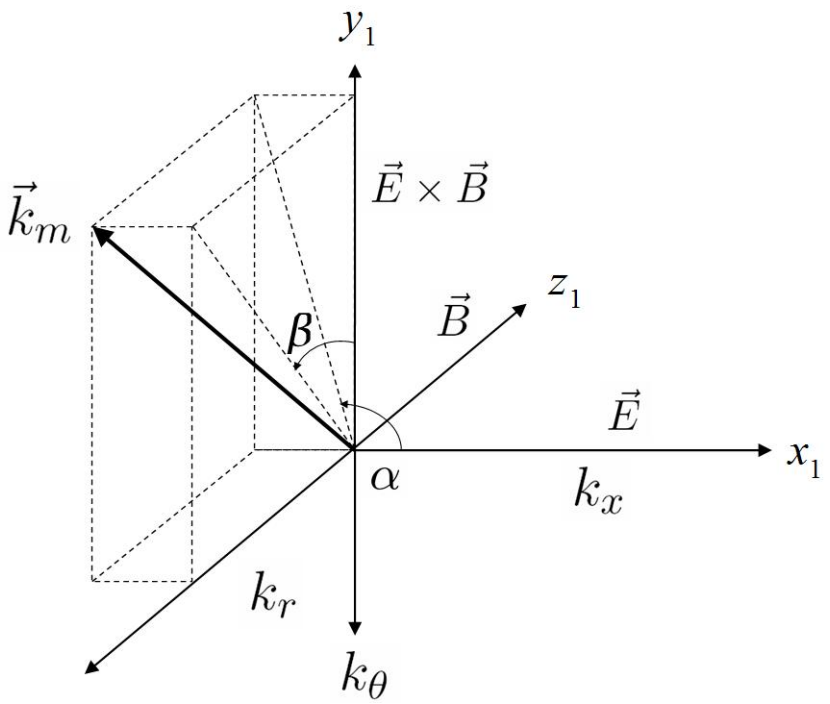

Figure 6.28: Directionality of most intense $\vec{E} \times \vec{B}$ mode, with a wave vector denoted by $\vec{k}_m$. Collective scattering observations have shown that α = 90 + 10.6° and β = 4.58°

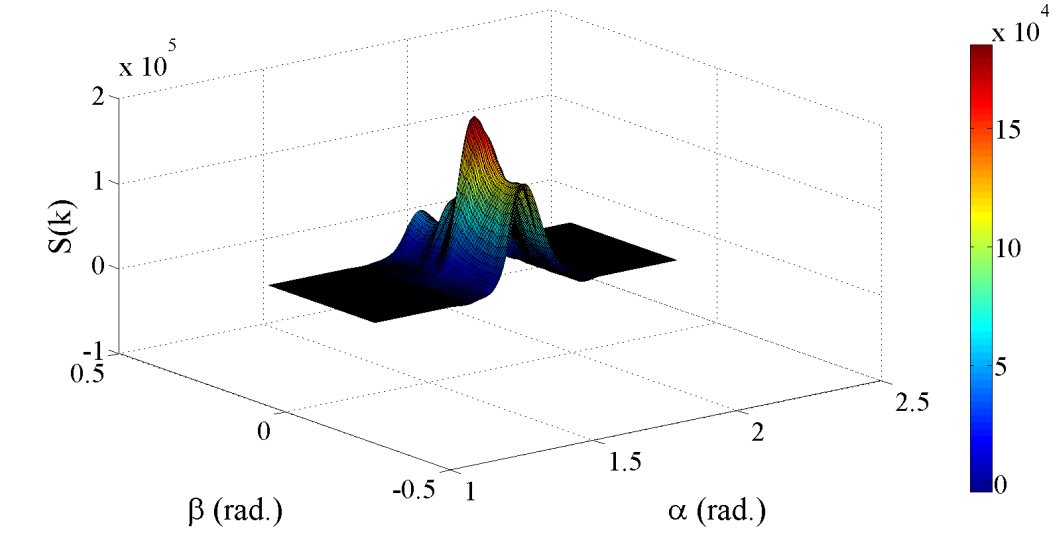

(a) 3D view of the form factor of the $\vec{E} \times \vec{B}$ mode as a function of α and β

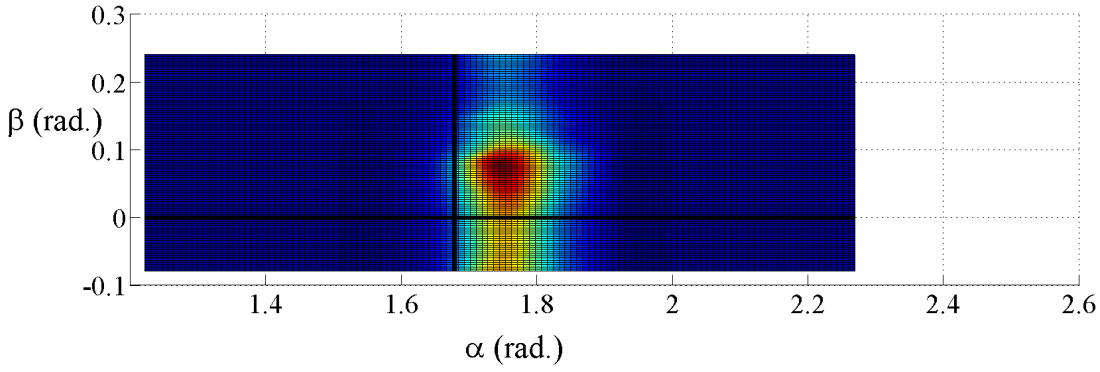

(b) Projection of the form factor of the $\vec{E} \times \vec{B}$ mode as a function of α and β

Figure 6.29: Visualizations of $\vec{E} \times \vec{B}$ mode amplitude as a function of α and β

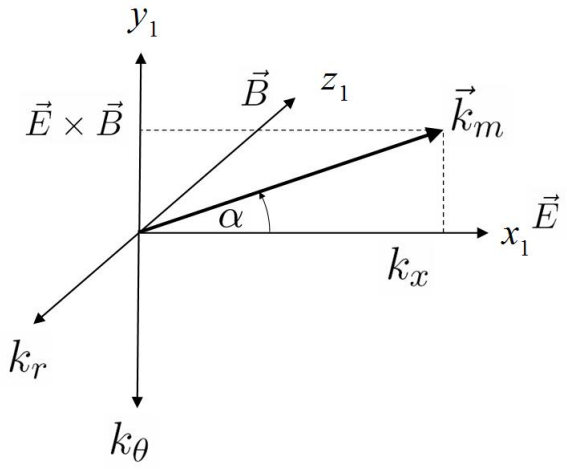

Figure 6.30: Directionality of most intense axial mode on-axis, with a wave vector denoted by $\vec{k}_m$. Collective scattering observations have shown that α = 8.22° on-axis

6.11 Physical hypotheses concerning the directionality of the $\vec{E} \times \vec{B}$ mode

In Chapter 5, the radial non-uniformity in the electron cyclotron drift length was proposed to account for the apparent localization of the $\vec{E} \times \vec{B}$ mode near the outer channel wall. This non-uniformity may be at the origin of the inclination observed with respect to the $\vec{E} \times \vec{B}$ drift observed in this chapter, and in particular, the presence of a non-negligible k_r component.

However, this is only a hypothesis. To explore its validity, an extension must be made of the linear kinetic theory of the instability to a non-uniform plasma. The variation of the form factor with k_r, with the angle of maximum emission β discovered experimentally, should also be compared with the linear growth rate obtained from linear kinetic theory and the dependence of this growth rate on k_r.

Another hypothesis, concerning the inclination of the $\vec{E}\times\vec{B}$ mode towards the thruster face in the (k_x, k_θ) plane, may be proposed. It is quite intriguing that the angle α made by the principal axial mode with the x_1, 8°, is on the same order as the angle made by the main $\vec{E} \times \vec{B}$ mode with the $\vec{E} \times \vec{B}$ drift direction, 10.6°. The two modes have little in common beyond this particular characteristic.

Fig. 6.31 illustrates the situation described above, with $\vec{k}_a$ denoting the main direction of propagation of the axial mode in the plane (k_x, k_θ). $\vec{k}_e$ shows the main direction of propagation of the $\vec{E} \times \vec{B}$ mode.

The axial mode has been identified as resulting from the convection of electrons by the exiting ions, and it provides an indirect means by which the effect of the ion propagation on the $\vec{E} \times \vec{B}$ mode may be characterized. The ions have a damping effect on the electron motion, and the inclination of the $\vec{E} \times \vec{B}$ mode could very easily result from the fact that this is a required angle for the $\vec{E} \times \vec{B}$ mode to avoid damping by the ion velocity. With this

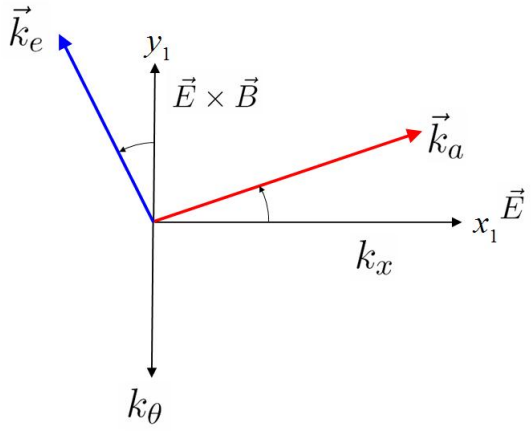

Figure 6.31: Near-orthogonal propagation directions of the main $\vec{E} \times \vec{B}$ and axial modes in the (k_x, k_θ) plane. $\vec{k}_a$ represents the axial wave vector, $\vec{k}_e$ the wave vector of the $\vec{E} \times \vec{B}$ mode

inclination, the most intense axial and $\vec{E} \times \vec{B}$ modes are separated by about 90°. Away from this angle, the $\vec{E} \times \vec{B}$ is quickly subject to damping and its range is therefore restricted, which also accounts for its narrow region of propagation (3.0°) in this plane.

6.12 Redetermination of the density fluctuation rate

With these more precise characterizations of the $\vec{E} \times \vec{B}$ mode, and the certitude that the signal registered is not subject to losses due to heterodyning, the density fluctuation rate may now be more accurately estimated.

The form factor dependency on wavenumber has been shown to be an exponential: $S(k) = S_0 e^{-bk}$. In an earlier experiment during this campaign in which the maximum value of $S(k)$ was observed, the parameters of the exponential were

$$S_0 \;=\; 4.64 \times 10^6, \;\; b = 6.78 \times 10^{-4} \text{ m} \tag{6.18}$$

A further adjustment to S_0 is obtained from the observations made of the variation of $S(k)$ with β. As has been shown, the maximum amplitude of the $\vec{E} \times \vec{B}$ mode is obtained not for β = 0 (with the beams on-axis), but with β = 0.08 rad (with the beams positioned 5 mm above the thruster axis). The value of S_0 in Eq. 6.18 was obtained in an experiment for which $\beta = 0$. To estimate the true maximum value which would be expected at $\beta = 0.08$, S_0 is scaled using the relative mode amplitudes in Fig. 6.20. The scaling factor is 1.4. Consequently, the adjusted S_0 value is 6.5×10^6.

The main idea here is that the optical bench is capable of measuring (and does) a signal level which is representative of the true energy level of the fluctuation. The density fluctuation rate must therefore be determined using the maximum signal level obtained experimentally.

From the α exploration for this mode, it was determined that the angular opening of the mode in the (k_x, k_θ) plane is 3.0°, or 0.05 rad. This value will be identified here as σ_α; the value of the location of the most intense mode (90 + 10.6°) will be identified here as μ_α. The β value is 0.08 rad and the peak width $\Delta\beta$ is estimated at about 0.15 rad.

One key assumption in the first phase of experiments was that the $\vec{k}$ component parallel to $\vec{B}$ was small, on the order of the inverse channel width, and constant; this has been proven in this chapter to be false. The re-evaluated mean square density fluctuation expression is written

$$\left\langle \tilde{n}^2 \right\rangle \approx \frac{S_0 n_0}{(2\pi)^3} \int_0^\infty e^{-kb} dk \int k e^{-\frac{(\alpha-\mu_\alpha)^2}{2{\sigma_\alpha}^2}} d\alpha k \Delta\beta \tag{6.19}$$

This integral reduces to

$$\left\langle \tilde{n}^2 \right\rangle \approx \frac{\alpha_\sigma \Delta\beta}{2^{3/2}\pi^{5/2} b^3} n_0 L \tag{6.20}$$

in which L is the total channel length which coincides with the scattering volume, i.e. for a channel width of 25 mm, L is 50 mm because the measurement volume always traverses the entire thruster diameter.

The mean square density fluctuation is

$$\left\langle \tilde{n}^2 \right\rangle \approx 0.76 \times 10^{31} \text{ m}^{-6} \tag{6.21}$$

The corresponding r.m.s density fluctuation value is 2.76×10^{15} m^{-3}. Once again, the density fluctuation rate is obtained using a mean density of 10^{18} m^{-3},

$$\frac{\sqrt{\langle \tilde{n}^2 \rangle}}{n_0} = 2.8 \times 10^{-3} \tag{6.22}$$

This density fluctuation rate is a factor 7 larger than that calculated from the experiments and assumptions from Part I, but remains very low, only 0.3%.

The results described in this chapter provide new information on the directionality of both the axial and $\vec{E} \times \vec{B}$ modes. The directionality studies have revealed the propagation of the $\vec{E} \times \vec{B}$ mode in three dimensions, contrary to the original simplified 2D view proposed in Part I, and that adopted in linear kinetic theory. The newly-evaluated density fluctuation level is low and now must be interpreted in terms of the possible transport mechanism.

Chapter 7

Detailed comparisons between linear kinetic theory and experiment

Contents

7.1 Introduction

In Chapter 3, a first comparison of the experimental results to the 1D (k_y) and 2D (k_y, k_x) theoretical dispersion relations was made. The predicted theoretical frequency and

wave number ranges were obtained experimentally, however, the experimental and theoretical dispersion relations differed in nature. The numerical solution to the theoretical dispersion relation exhibited discontinuities in the unstable regions which were not seen in experiments.

There are a large number of possible reasons for such differences, not all of which are easily verifiable. For example, the form of the electron distribution function is still unknown, but has been assumed to be Maxwellian for simplicity's sake. For non-Maxwellian distributions, the evolution of the instability would have to be studied using numerical integration. Other physical factors, such as the radial evolution of properties such as electron density and drift velocity, lead to complex kinetic equations which must also be solved numerically.

The simplest factor to consider in order to explain the difference between the experimental and theoretical dispersion relation is the presence of a k_z component. In experiments, a k_z component, whose smallest possible value is on the order of the inverse channel width, is present but is set to zero in the 1D and 2D theoretical dispersion relations. The directionality experiments described in Chapter 6 have revealed that the most intense mode has k_x, k_y and k_z components. This provides a convincing argument for a closer study of the 3D dispersion relation.

In recent months, A. Héron of the CPHT, Ecole Polytechnique, has calculated solutions to the 3D dispersion relation in an effort to determine the influence of k_z. This chapter discusses our experimental results in the context of the newly-evaluated 3D dispersion relation results supplied by Héron.

7.2 The three dimensional dispersion relation

In the geometry considered here and in Chapter 3, x corresponds to the thruster axis, y to the drift direction and z to the radial direction.

The three dimensional dispersion relation is written [17]

$$k^2{\lambda_D}^2\left(1-\frac{m_e}{m_i}\frac{\omega_{pe}}{\omega^2}\right)+1+\frac{\xi^+ + \xi^-}{2}\left\{Z\left(\frac{\xi^+ + \xi^-}{2}\right)I_0(b)e^{-b}+\sum_{n=1}^{n=\infty}I_n(b)e^{-b}(Z(\xi^+)+Z(\xi^-))\right\}=0 \tag{7.1}$$

where

$$\xi^+ = \omega - k_y V_d + n\omega_{ce}/k_z v_{the}\sqrt{2} \tag{7.2}$$

$$\xi^- = \omega - k_y V_d - n\omega_{ce}/k_z v_{the}\sqrt{2} \tag{7.3}$$

Parameters such as magnetic and electric field strengths have been chosen to match those used during experiments, and can be found in Tables 3.1 and 3.2.

The values of k_x used here range from 0 to 10000 rad/m; k_y ranges from 3000 to 17000 rad/m. k_z values are chosen from 0 to 1000 rad/m; experimentally, k_z (or k_r in the convention used for describing the experiments of Chapter 6) varied between 500 to 1500 rad/m. Cartesian coordinates have been used in the three dimensional relation throughout because of the relative simplicity of the resulting analytical form.

7.3 The influence of k_z on the dispersion relation

In Chapter 3, the unstable regions were limited to comb-like lobes. The case is dramatically different when a k_z component is included: from k_z = 230 rad/m onwards, the unstable modes become continuous and the instability is present over the entire range of k_y values. This section describes the effect of the presence of a non-negligible k_z on the dispersion relation. Here, k_z is set to 470 rad/m.

This value of k_z is chosen as representative of the lower limit of k_z during the explorations in the (k_θ, k_r) plane. During these experiments, for an observation wave number of about 6000 rad/m, k_z was varied from 480 - 1440 rad/m.

Two cases are now considered: (i) a low electron temperature (v_{the}/V_d = 1.8), and (ii) an electron temperature corresponding to that determined from the experimental dispersion relation (16 eV), i.e. v_{the}/V_d = 2.5. The value of 16 eV was determined by considering the wave (reasonably) as an ion acoustic wave, however, no direct measure of the electron temperature for the wave is available.

The frequency and growth rates will be given in Hz to facilitate comparison to the experimental results.

7.3.1 The dispersion relation for v_{the}/V_d = 1.8

The dispersion relation is numerically solved to give the frequency of the instability ω_r and its growth rate γ as defined in Chapter 3 for v_{the}/V_d = 1.8. Fig. 7.1 shows dispersion relation frequency as a function of k_x and k_y.

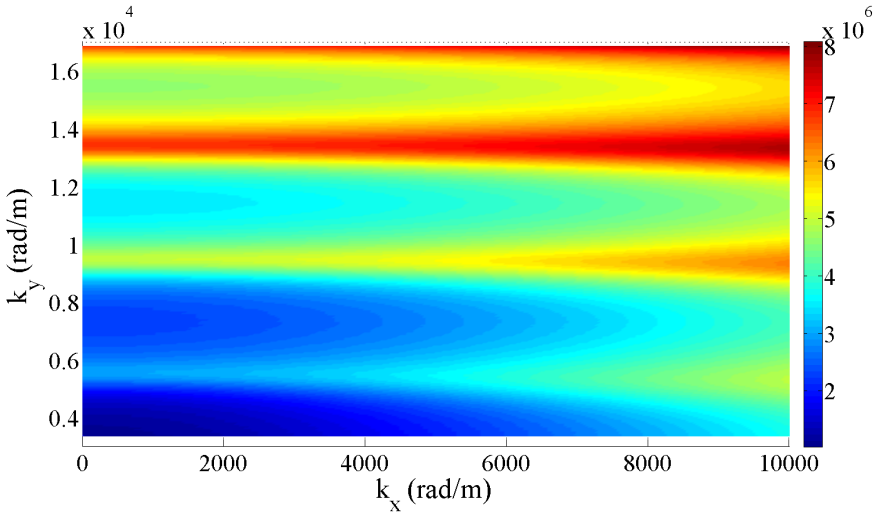

Figure 7.1: Frequency (Hz) as a function of k_y and k_x, for k_z = 470 rad/m and v_{the}/V_d = 1.8

The discontinuity visible in the 2D case has disappeared. The unstable regions have broadened significantly and some form of instability is visible at all values of k_y. This broadening in the unstable region is accompanied by a reduction in the growth rate of the instability,

shown in Fig. 7.2. As was observed in the 2D case, for the same value of k_y, the dependence of the growth rate on k_x is weak. However, a slight dependence of the frequency on k_x appears.

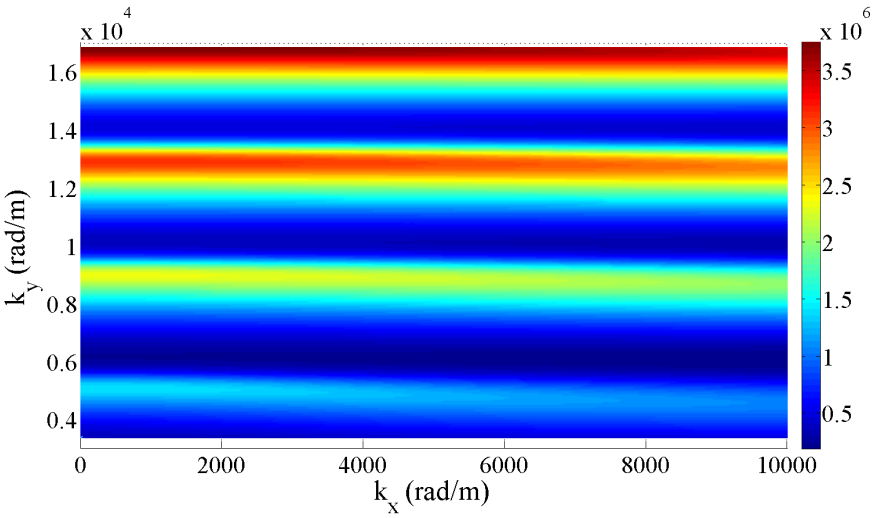

Figure 7.2: Growth rate (Hz) as a function of k_y and k_x, for k_z = 470 rad/m and v_{the}/V_d = 1.8

To examine the lobes more closely, we set k_x to zero (a fairly representative case) and plot the frequency and growth rate as a function of k_y.

Fig. 7.3 shows the frequency as a function of k_y. The broadening of the lobes is clear, and the frequencies observed remain on the same order as those observed experimentally.

Fig. 7.4 shows the growth rate as a function of k_y; the lobes are no longer completely distinct from each other.

7.3.2 The dispersion relation for v_{the}/V_d = 2.5

The electron temperature has an important influence on the form of the unstable lobes and the growth rate of the instability. In this case we consider electron temperatures closer to the experimental scenario. Fig. 7.5 shows the frequency as a function of k_x and k_y, this time for v_{the}/V_{th} = 2.5. k_z is maintained at 470 rad/m.

The lobes have disappeared entirely and the dependence of the frequency on k_x for the same value of k_y is now more marked. The growth rate lobes persist somewhat but are no longer distinct (Fig. 7.6) and the dependence on k_x is weak.

As before, we may plot the frequency and growth rate evolution as a function of k_y at k_x = 0.

Compared with the 2D case, the addition of a k_z component has the effect of slightly shifting the maximum growth rate of a particular lobe to a higher value of k_y, and reducing this maximum growth rate. We may consider the case of the lobe n = 2 in Fig. 7.8, where k_z has been taken into account, to the same n = 2 lobe observed in the 2D case discussed in Chapter 3. The maximum growth rate of the lobe in the 3D case is seen at k_y = 8700 rad/m,

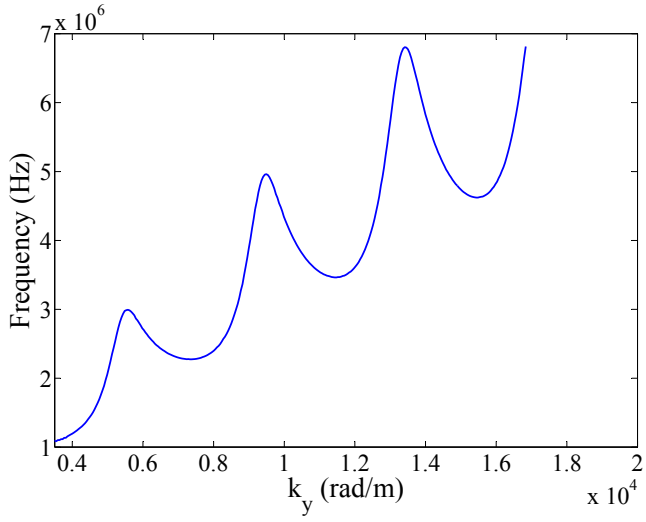

Figure 7.3: Frequency as a function of k_y, for k_x = 0, k_z = 470 rad/m and v_{the}/V_d = 1.8

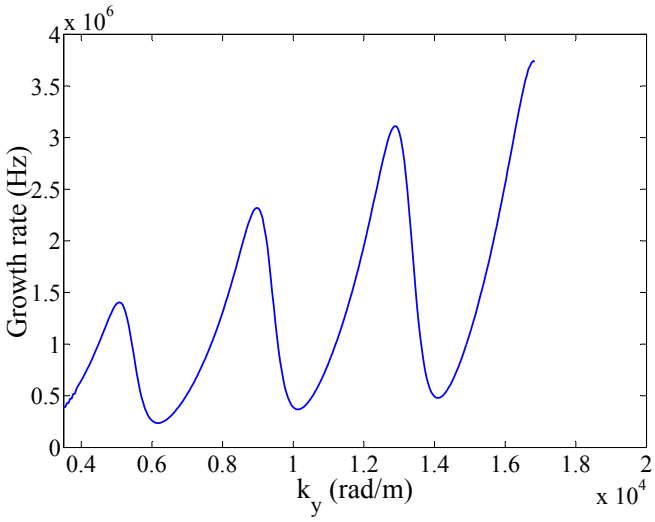

Figure 7.4: Growth rate as a function of k_y, for k_x = 0, k_z = 470 rad/m and v_{the}/V_d = 1.8

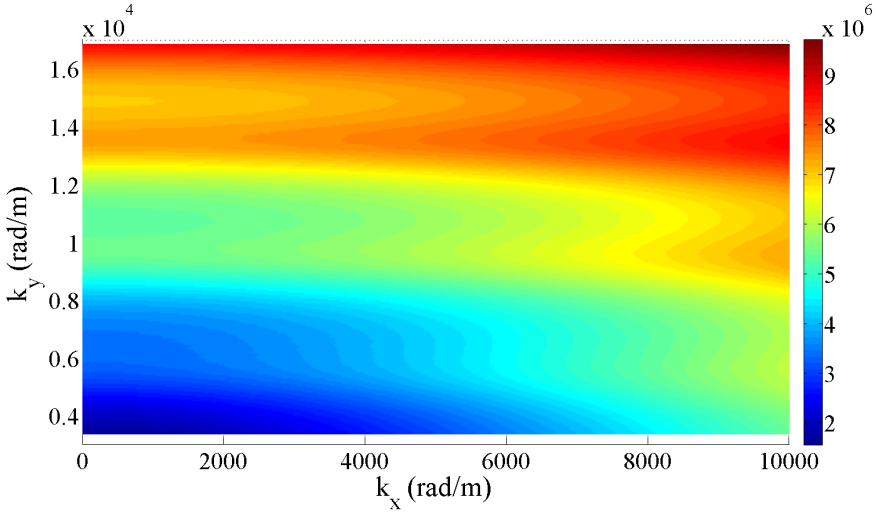

Figure 7.5: Frequency as a function of k_y and k_x, for k_z = 470 rad/m and v_{the}/V_d = 2.5

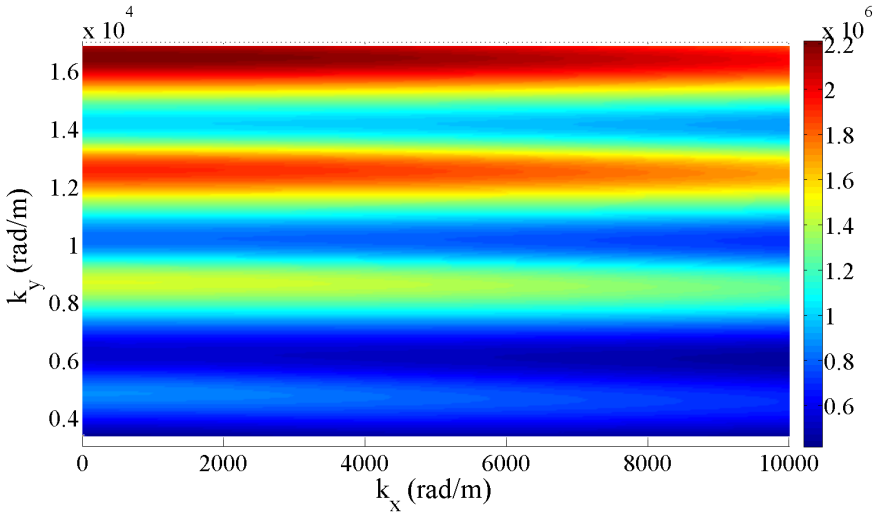

Figure 7.6: Growth rate as a function of k_y and k_x, for k_z = 470 rad/m and v_{the}/V_d = 2.5

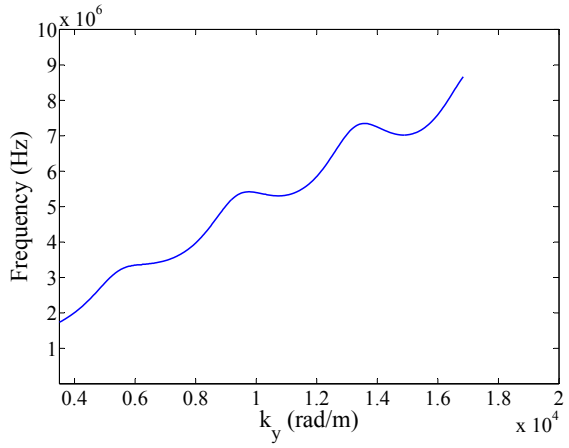

Figure 7.7: Frequency as a function of k_y, for k_x = 0, k_z = 470 rad/m and v_{the}/V_d = 2.5

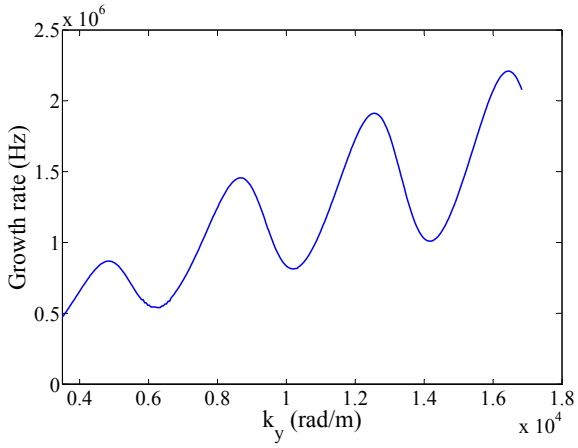

Figure 7.8: Growth rate as a function of k_y, for k_x = 0, k_z = 470 rad/m and v_{the}/V_d = 2.5

while it is seen at k_y = 8500 rad/m in the 2D case. The maximum growth rate for this lobe in the 3D case is 1.5×10^6 Hz in the 3D case, and 9.1×10^6 Hz in the 2D case.

7.3.3 Effect on dispersion relation of increasing k_z

The effect of increasing k_z from 470 to 1000 rad/m is studied in this section. 1000 rad/m is in the upper range of k_z values used experimentally.

The frequency and growth rates as a function of k_y and k_x for k_z = 1000 rad/m are shown in Fig. 7.9 and Fig. 7.10.

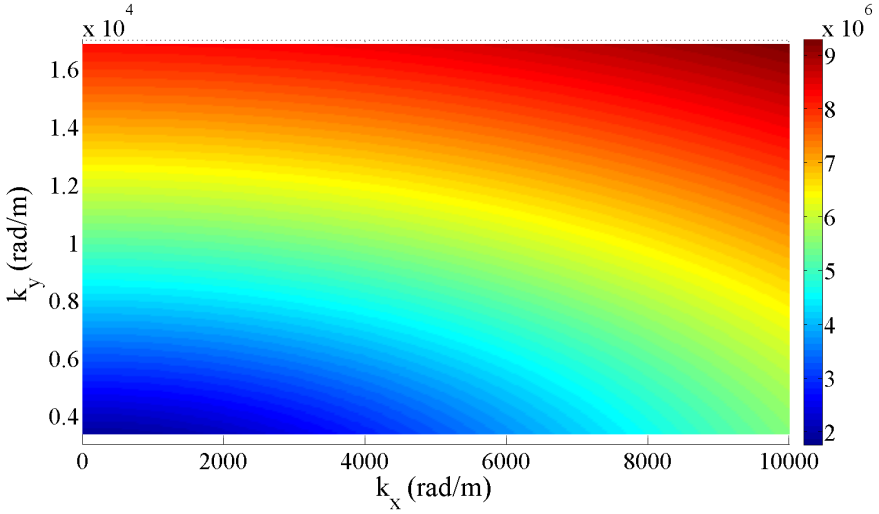

Figure 7.9: Frequency as a function of k_y and k_x, for k_z = 1000 rad/m and v_{the}/V_d = 2.5

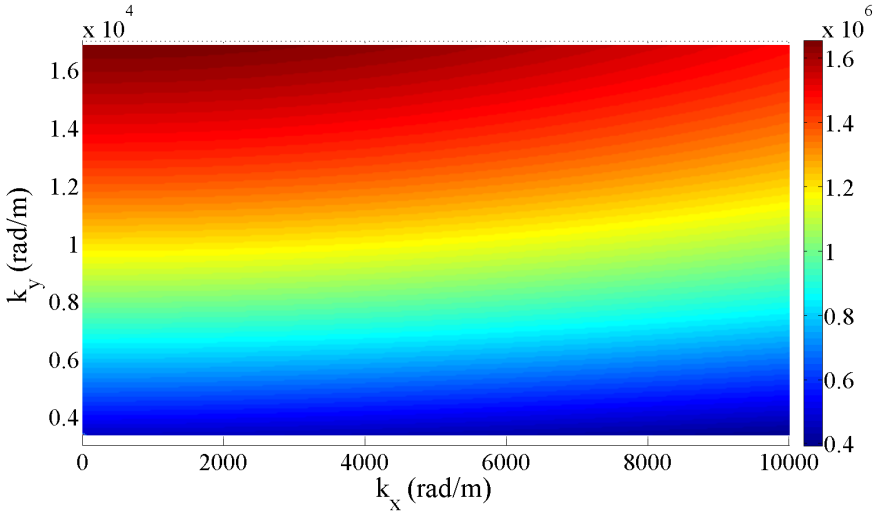

Figure 7.10: Growth rate as a function of k_y and k_x, for k_z = 1000 rad/m and v_{the}/V_d = 2.5

Apart from the complete absence of lobes, an interesting dependence on k_x is also apparent. The frequency increases with both k_y and k_x. The growth rate dependence on k_x is still, however, small. The dispersion relation and growth rate for k_x = 0 are shown in Fig. 7.11 and Fig. 7.12.

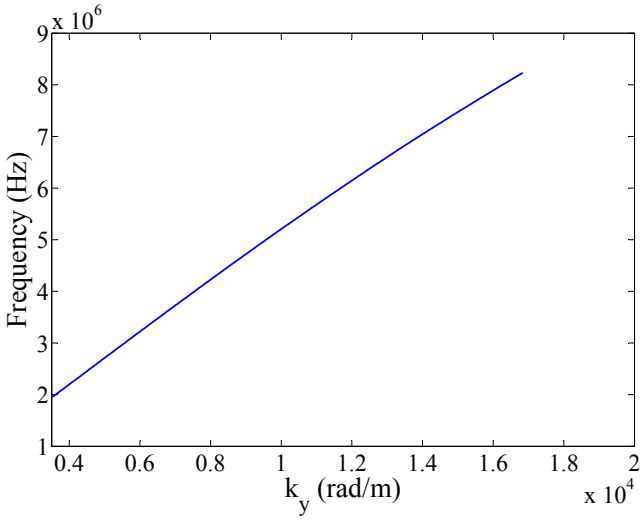

Figure 7.11: Frequency as a function of k_y, for k_x = 0, k_z = 1000 rad/m and v_{the}/V_d = 2.5

The dispersion relation shown in Fig. 7.11 has a slope of 3.0×10^3 m/s, on the same order as the experimentally-obtained slopes (between 3 and 4 $\times10^3$ m/s). The growth rate no longer exhibits lobes and while its value is smaller than in the case for k_z = 470 rad/m, it is still significant.

The results of this section demonstrate that the presence of a k_z component is sufficient to make the dispersion relation non-discrete, even without taking into account additional effects such as gradients and radial variations of plasma properties. This represents a major rapprochement between linear theory and the collective scattering experiments. The effect of the electron temperature has also been investigated here, and it has been observed that higher electron temperatures broaden the lobes, while reducing the growth rate of the instability. Increasing the k_z component leads to a dispersion relation which strongly resembles those obtained experimentally and to lower growth rates than in the 2D case.

The reduction in growth rates associated with the presence of a non-negligible k_z component is likely due to Landau damping effects, but the values of growth rate remain large in all cases.

An important difference between theory and experiments has been resolved. We may proceed to examining other dependencies not previously discussed in theory which have been discovered experimentally.

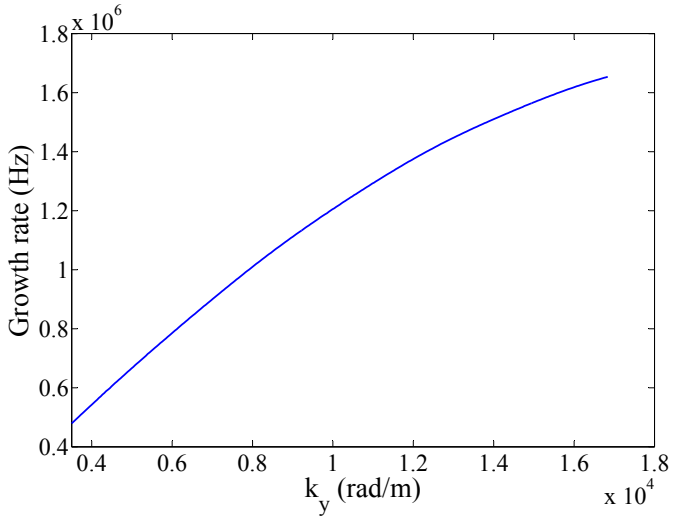

Figure 7.12: Growth rate as a function of k_y, for k_x = 0, k_z = 1000 rad/m and v_{the}/V_d = 2.5

7.4 Variation of frequency with α

For the $\vec{E} \times \vec{B}$ mode it was observed that a variation of α produced a large variation in frequency and a rapid frequency change associated with the position at which $\vec{k}$ is aligned with V_d. It is interesting to determine if this frequency variation and rupture appear in theory when the three dimensional dispersion relation is applied. Two wave numbers will be considered: k = 6400 rad/m and 8800 rad/m. The conditions used in this section are v_{the}/V_d = 1.8, and k_z is once again fixed at 470 rad/m. The values of α shown here are focused around the angular values in the (k_x, k_θ) plane where the largest amplitude of the $\vec{E} \times \vec{B}$ mode positive frequency peak was seen experimentally.

7.4.1 Frequency variation with α for k = 6400 rad/m

Fig. 7.13 shows the variation of frequency with α at a wave number k of 6400 rad/m. The growth rate is shown in Fig. 7.14.

A clear frequency variation with α is observable which shows similarities to the experimental trend. The frequency increases rapidly on the right hand side of the peak in a manner resembling the experimental discontinuity.

The position of the maximum growth rate in Fig. 7.14 seems to be near to the transition. If the growth rate is correlated with the mode amplitude, this trend is different from the experimental observations, where the maximum amplitude of the fluctuations is obtained at a value of α where the frequency variation is minimum.

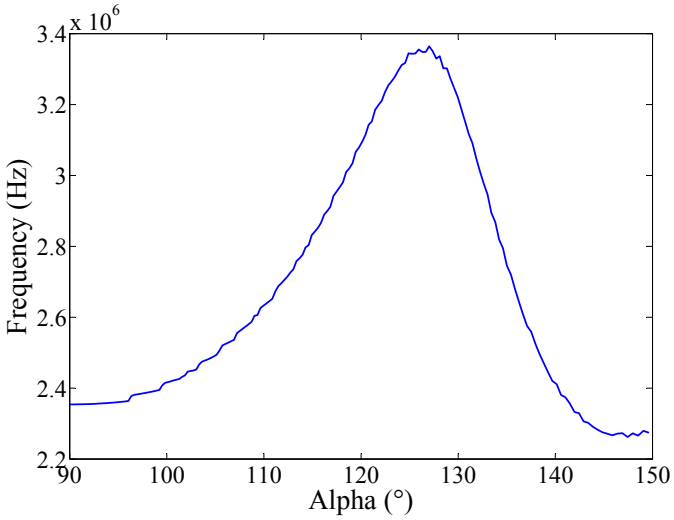

Figure 7.13: Frequency as a function of α, for k = 6400 rad/m

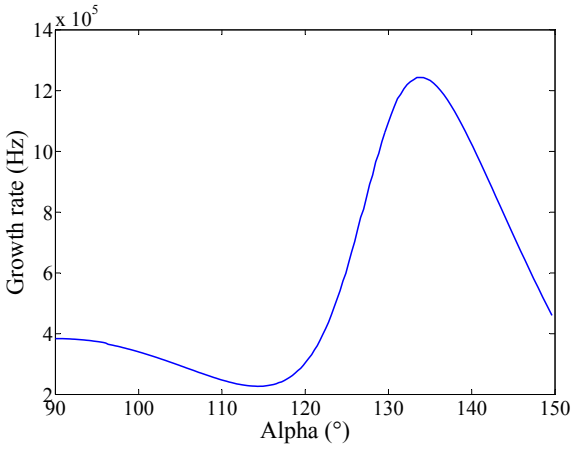

Figure 7.14: Growth rate as a function of α, for k = 6400 rad/m

7.4.2 Frequency variation with α for k = 8800 rad/m

The second case of a larger wave number is now considered. The frequency and growth rate variations with α are presented in Fig. 7.15 and Fig. 7.16.

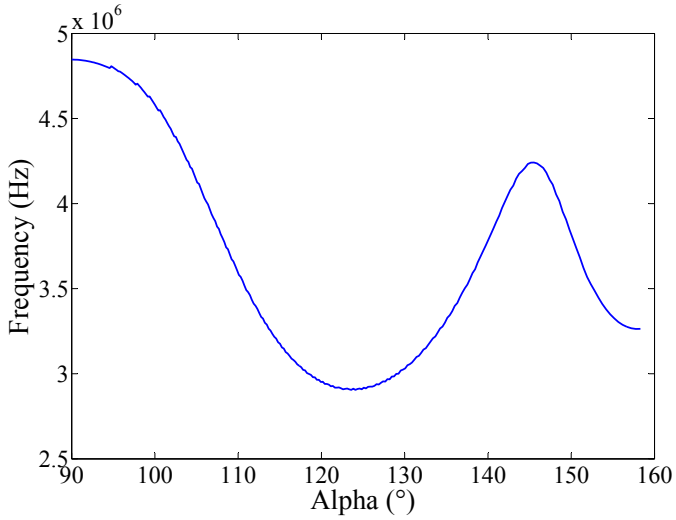

Figure 7.15: Frequency as a function of α, for k = 8800 rad/m

At a different wave number, the trends observed in frequency and wave number are completely different from the lower wave number case, which is unexpected. The experimental frequency variation with α has been seen to have the same form for different wave numbers, which is not the case here. It is therefore impossible to argue for a similarity between the experimental and theoretical results in this specific instance.

7.5 Variation of k_z component

Experimentally, it has been observed that the frequency is independent of the k_z component, for values of k_z between 480 and 1440 rad/m. This interesting property may be examined theoretically. In this example, α is fixed at a value of 100° (i.e. near the α value for which the maximum amplitude of the $\vec{E} \times \vec{B}$ mode (positive frequency peak) was observed).

Two representative cases are considered: k = 6000 and 8000 rad/m, with v_{the}/V_d = 2.5.

7.5.1 Variation of k_z for k = 6000 rad/m

The k = 6000 rad/m results are shown in Fig. 7.17 and Fig. 7.18.

The frequency remains constant with k_z for values of k_z above 750 rad/m, a result which is in accord with experimental observations, where the frequency remained constant in the explored k_z range of 480 - 1440 rad/m. Interestingly, the growth rate of the instability

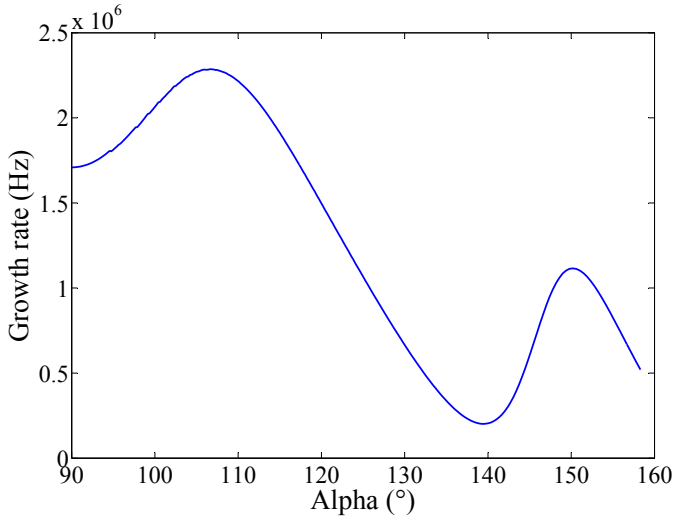

Figure 7.16: Growth rate as a function of α, for k = 8800 rad/m

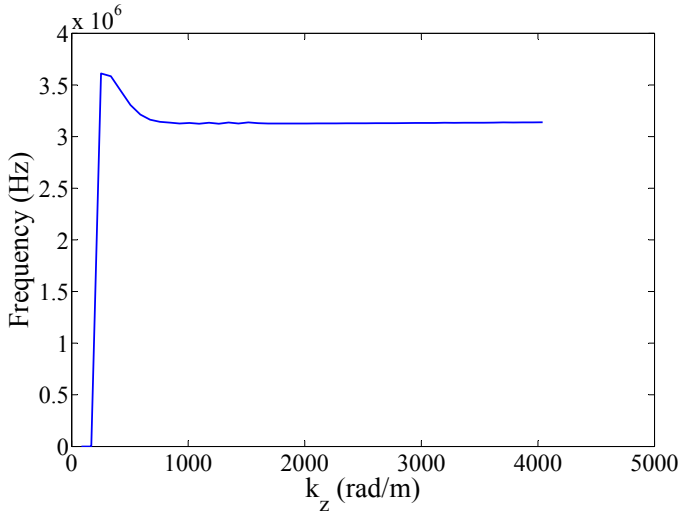

Figure 7.17: Frequency as a function of k_z, for k = 6000 rad/m

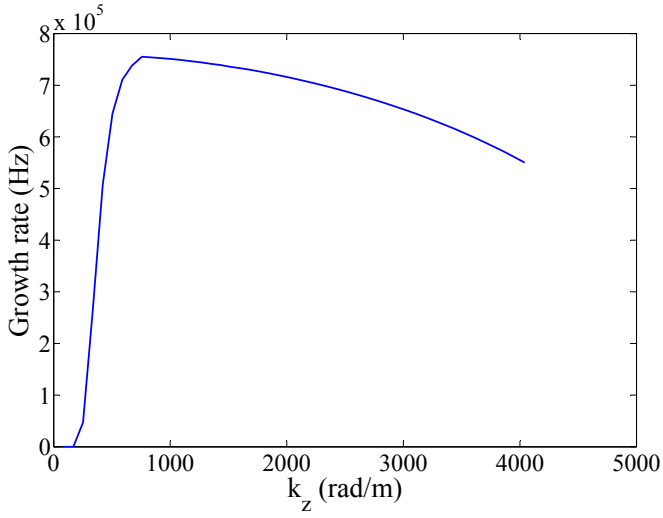

Figure 7.18: Growth rate as a function of k_z, for k = 6000 rad/m

is maximum when $k_z \neq 0$. In addition, the growth rate varies less with k_z than it does with α. In experiments, the mode amplitude was seen to vary more markedly with α than with the angle β, and there may be a connection between this observation and the growth rate.

7.5.2 Variation of k_z for k = 8000 rad/m

When the wave number is changed, a similar trend in frequency is observed which agrees with the experimental observations.

The trend in growth rate is different from that observed in the k = 6000 rad/m case, and the reason for this is not clear. For a value of α different from 100°, for instance, 90°, where $\vec{k}$ is now parallel to the $\vec{E} \times \vec{B}$ drift direction, very similar results are obtained.

The numerical results so far discussed demonstrate some interesting agreements between the experimental and theoretical dispersion relations when k_z is taken into account. Certain other features such as the frequency dependency on k_z are the same in the experimental and theoretical cases. The influence of the electron density has also been studied (but not described in this work) and it has been seen to have a negligible effect on the instability.

It is now worth re-evaluating electron transport in the context of the experimental results. The question at stake here is whether electron transport across field lines can occur under the actual experimental conditions due to the presence of the wave whose characteristics have been measured experimentally.

7.6 Resonance conditions and stochasticity

The experiments described in this work have revealed the presence of an azimuthal wave with characteristics predicted by Adam et. al [2]. The link between this wave and axial

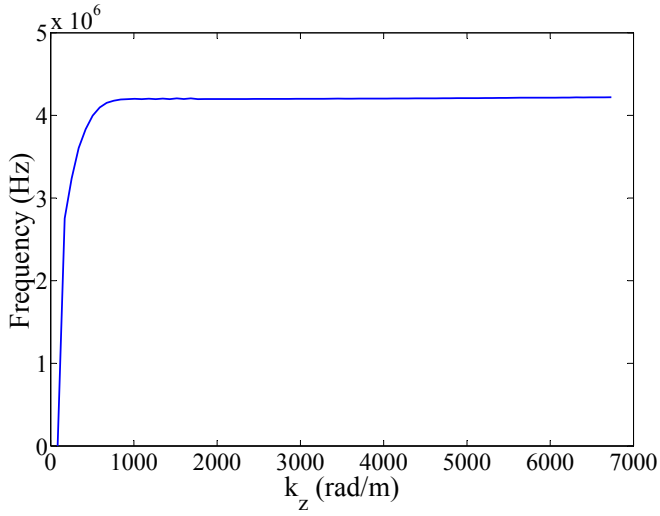

Figure 7.19: Frequency as a function of k_z, for k = 8000 rad/m

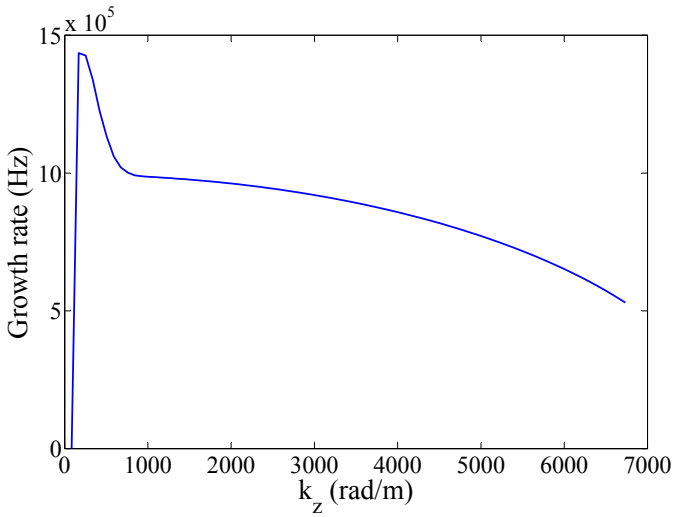

Figure 7.20: Growth rate as a function of k_z, for k = 8000 rad/m

electron transport may be provided by a particle-heating mechanism first described in detail by C. F. F. Karney [37] for a crossed electric and magnetic field configuration.

C. F. F. Karney proposed that lower hybrid waves (waves of frequencies on the order of the lower hybrid frequency) could be used to stochastically heat ions. His pioneering work has been applied to radiofrequency heating in tokamaks.

The mechanism for particle heating is as follows. We consider a charged particle travelling in a cyclotron orbit, subject to a constant magnetic field and a fluctuating electric field, $\vec{B}$ and $\vec{E}$ respectively, of the forms

$$\vec{B} = B_0 \hat{y} \tag{7.4}$$

$$\vec{E} = E_v \cos(ky - \omega t)\hat{x} \tag{7.5}$$

Provided that at some point in its orbit, the particle has a velocity component in the direction of propagation of the wave which is equal to the wave phase velocity, there is a large energy transfer from the wave to the particle. This is the wave-particle resonance condition, i.e.

$$\omega = \vec{k} \cdot \vec{v} \tag{7.6}$$

Such a condition may be satisfied if the wave is of the lower hybrid type, where

$$\omega \gg \omega_{ci} \quad \text{and} \quad k_\perp \gg k_{||} \tag{7.7}$$

For the case of a lower hybrid wave, the wave frequency is sufficiently large that the particle is obliged to undergo multiple energy transfers and can accumulate sufficient energy to escape its cyclotron orbit. The amount of energy transferred at each resonance is related to the amplitude of the electric field. Karney proposed a stochasticity limit - a minimum value of the electric field amplitude necessary for a particle to behave as if liberated from its orbit. This condition is written

$$\frac{E_v}{B_0} = \frac{1}{4}\left(\frac{\omega_{ci}}{\omega}\right)^{1/3}\frac{\omega}{k} \tag{7.8}$$

7.7 Applications to the Hall thruster

A. Ducrocq described in his thesis [17] a similar particle heating scheme which could contribute to anomalous electron transport seen in the thruster. This section discusses his extension of Karney's work to electron heating in the thruster. The stochasticity analysis he undertook is revisited using our experimental results.

In the thruster, three orthogonal fields must be considered: the constant, radial magnetic field $\vec{B}$, the fluctuating field $\vec{E_v}$, and the constant, axial imposed accelerating field, which we shall call $\vec{E_a}$ in this section. The presence of the fluctuating field (whose existence was simply assumed in Ducrocq's analysis) has been confirmed by our observations of density fluctuations.

The presence of the perpendicular fields $\vec{E_a}$ and $\vec{B}$ is the source of the electron drift velocity, which gives an "apparent" frequency to the electrons which is sufficiently high for the following frequency condition to be satisfied,

$$\omega \gg \omega_{ce} \tag{7.9}$$

This condition is analogous to that in Eq. 7.7. The apparent electron frequency, ω_s, Doppler shifted by the drift velocity, is given by

$$\omega_s = \omega - k_y V_d \tag{7.10}$$

In determining the value of $k_y V_d$, we shall use the smallest value of k_y used experimentally (4000 rad/m) as this corresponds to fluctuations of the largest amplitude observed. The maximum length scale at which the wave amplitude is seen to saturate has not yet been observed experimentally. The resulting value of $k_y V_d$ is 2.67×10^9 rad/s.

The frequency of the electrostatic wave observed experimentally is on the order of 3×10^7 rad/s; the value of ω_s is therefore on the order of 2.6×10^9 rad/s.

In the thruster, $V_d = E_a / B_0$. Replacing B_0 in Eq. 7.8 gives

$$\frac{E_f}{E_a} = \frac{1}{4} \left(\frac{\omega_{ce}}{k_y V_d} \right)^{1/3} \tag{7.11}$$

or

$$\frac{E_f}{E_a} \approx 0.3 \tag{7.12}$$

The stochasticity limit thus requires that the amplitude E_f be 30% of the accelerating electric field amplitude.

We may now attempt to link the experimentally-obtained density fluctuation rate to E_f in order to determine if this stochasticity threshold is indeed achieved.

If we consider that the mode observed is an ion acoustic wave, then the density fluctuation is related to the potential as

$$\frac{\tilde{n}}{n_0} = \frac{e\tilde{\phi}}{k_B T_e} \tag{7.13}$$

where $\tilde{n}$ and $\tilde{\phi}$ are root-mean-square values.

$\tilde{n}/n_0$ is on the order of 0.3% (or 3% for a mean plasma density of 10^{17} m^{-3}).

Using a value of electron temperature from Table 3.2[1], the electrostatic potential deduced is

$$\tilde{\phi} = 0.48 \ V$$

For an electrostatic wave, $E_f = -\nabla\phi$. For a potential expressed $\phi = \phi_0 \ e^{i(\vec{k}\cdot\vec{r} - \omega t)}$

[1] A slightly higher electron temperature of about 24 eV was determined for Phase II experiments

$$E_f = k\phi \tag{7.14}$$

The maximum amplitude of such a wave is expected at k = 3958 rad/m (the wave number corresponding to the first resonance). The resulting value obtained for the electrostatic wave amplitude is

$$E_f = 302.4\ V/m$$

For an accelerating field value of 10^4 V/m, the ratio E_f/E_a is 0.03. This value is a factor ten below the stochasticity limit. However, as mentioned before, there is an indetermination concerning the mean density which should be considered. For $\tilde{n}/n_0$ of 3%, the stochasticity limit is reached.

The above analysis confirms to some degree the importance of the mode observed experimentally in contributing to transport via the mechanism described by Ducrocq. Despite a density fluctuation level which appears low, the resulting electrostatic wave amplitude may be just sufficient for transport.

Ducrocq also considers the case of a wave in two dimensions (x and y). The wave observed experimentally has been determined from the directionality experiments to have a component $k_y \gg k_x$; the result of this is that the stochasticity limit for the 1D and 2D cases are virtually identical.

The presence of a k_z component of the wave may have implications on the expected transport. In fact, with a k_z component present, the electrons may be expected to rapidly lose coherence with the wave and circulate around the field lines without the small "kicks" to their trajectories which occur during resonance. Transport is therefore less likely; in this case the mechanism by which the observed wave may contribute to transport is still to be explained. Future work will study more carefully the role played by the k_z component and whether the transport mechanisms described above remain feasible or must be completely reconsidered.

This chapter has shown the interesting agreements between theory and experiments which arise as a consequence of the inclusion of a wave vector component along the magnetic field. The previously calculated density fluctuation level has been correlated with a fluctuating electric field amplitude, and found to be of a sufficient level to provoke transport by an electron heating mechanism which is at the origin of stochasticity. While electron transport is most probably due to a combination of interacting modes at different length and time scales, it is encouraging to observe that the particular mode identified experimentally can also play a role.

Chapter 8

Phase II experiments: Influence of thruster parameters and low frequency characteristics

Contents

THE experiments discussed in the previous chapter have focused on exploring a range of k_x, k_θ and k_r components in order to better characterize the directionality of the observed high frequency modes. The results described in this chapter detail the effects of some external influences, specifically, the main thruster operating parameters, on the modes identified. The influences of Xenon flow rate, discharge voltage and magnetic field strength on the mode form factors and frequencies are described. Such a study of the response of the modes to a variation of the thruster parameters may provide an idea of which operating conditions are most conducive to anomalous transport.

8.1 Effect of Xe flow rate on the $\vec{E} \times \vec{B}$ and axial modes

During the first phase of experiments, a correlation between the flow rate and the amplitude of the $\vec{E} \times \vec{B}$ mode was qualitatively observed. To increase the signal level, the thruster is operated at the highest flow rates permissible. Using high flow rates ensures that signals of sufficient amplitudes may be observed for the entire range of wave numbers used during the experiments. A more careful study of the effect of varying the flow rate is discussed here.

In this experiment, the thruster flow rate is varied from 6 to 18 mg/s, while the discharge voltage is maintained at 300 V. Every time the flow rate is changed, the thruster discharge current is allowed to stabilize.

8.1.1 $\vec{E} \times \vec{B}$ mode form factor and frequency

The form factor and characteristic peak frequencies are determined for the $\vec{E} \times \vec{B}$ mode at different flow rates. The observation wave number is maintained at 5928 rad/m in this experiment and α is maintained at 90°, parallel to the drift velocity direction. The variation in form factor with flow rate for both positive and negative frequency peaks is presented in Fig. 8.1.

This experiment represents one of the rare cases in which the negative frequency peak form factor measurements are not qualitatively identical to those of the positive frequency peak. The positive frequency peak in Fig. 8.1 shows a saturation in amplitude between 15 and 18 mg/s followed by a decrease, while the amplitude of the negative frequency peak continues increases monotonically.

The increase in form factor with flow rate indicates that the oscillations are more pronounced at larger flow rates. However, the form factor as calculated depends on the mean plasma density, which has been assumed throughout to be 10^{18} m^{-3}. An increase in flow rate may also be associated with an increase in the mean plasma density, in which case the actual form factor will be decreasing more rapidly at the highest flow rates than is shown in Fig. 8.1.

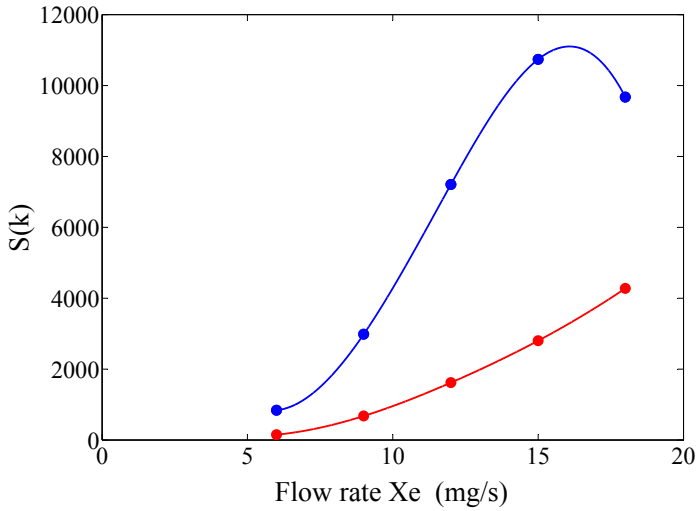

Figure 8.1: Form factor at different flow rates for the $\vec{E} \times \vec{B}$ mode, for the positive frequency peak (in blue) and negative frequency peak (in red)

The fluctuation level may be linked with the alignment of the fluctuations. The emission angle of the fluctuations, as determined from the directionality experiments, is restricted to a very narrow opening. This emission angle may change with flow rate.

It should also be noted that as the flow rate increases with constant discharge voltage, the discharge current also increases and so does the thruster power. This change in level may also influence the measured fluctuation level.

Aside from the increase in amplitude with flow rate, the ratio of the amplitudes of the positive and negative peaks is seen to decrease with increasing flow rate (Fig. 8.2). These peaks have already been determined to be representative of the same mode, measured at different thruster positions, hence the difference in behaviour is not easily explained.

The amplitudes of the modes measured in the 09h00 and 03h00 locations on the thruster azimuth might not be identical because the mode amplitude may evolve with the azimuthal position. This is difficult to measure, but if it were the case, it is possible that at the higher flow rates the plasma becomes more homogenous in the azimuthal direction and the amplitudes measured in opposite sides of the thruster channel become more comparable. This would account for the decrease in the form factor ratio with flow rate evident in Fig. 8.2.

The frequency variation of the mode with flow rate for the positive frequency peak is shown in Fig. 8.3. The frequency is practically invariant with flow rate for both the positive and negative frequency peaks.

8.1.2 The axial mode form factor and frequency

The variation of the axial mode form factor with flow rate is shown in Fig. 8.4. As is the case for the $\vec{E} \times \vec{B}$ mode, the wave number is maintained at 5928 rad/m and α is set to

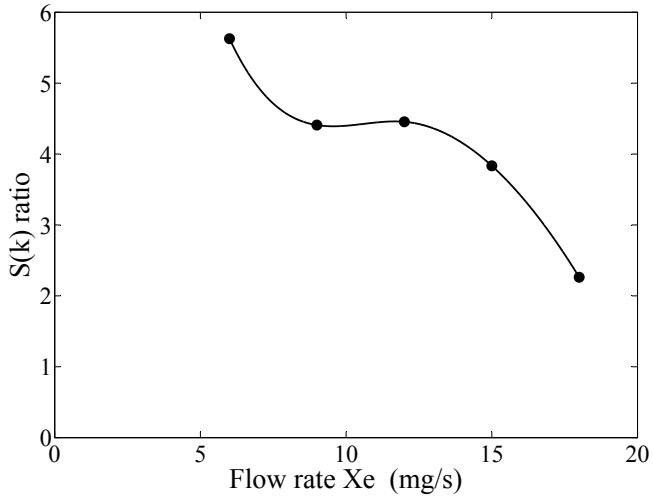

Figure 8.2: Form factor ratio of positive frequency peak to the negative frequency peak at different flow rates for the $\vec{E} \times \vec{B}$ mode

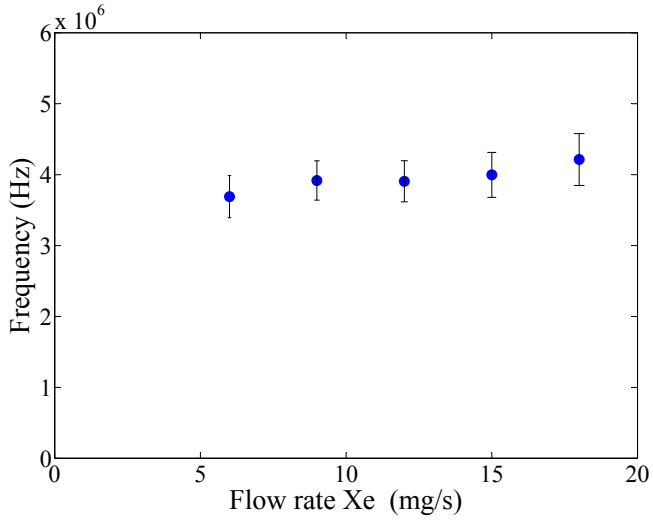

Figure 8.3: Frequency of the $\vec{E} \times \vec{B}$ mode with flow rate (positive frequency peak)

5°.

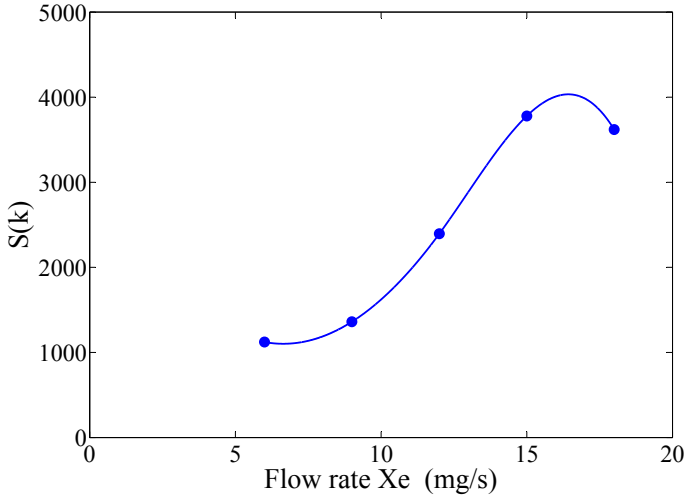

Figure 8.4: Form factor at different flow rates for the axial mode

The axial mode amplitude variation with flow rate resembles the trend observed for the positive frequency peak of $\vec{E} \times \vec{B}$ mode: an increase with flow rate, followed by a saturation and then a decrease. Again, some caution must be exercised in the interpretation of the form factor amplitude because the mean density may change with flow rate.

One difference with the $\vec{E} \times \vec{B}$ mode is that the opening of the emission angle of the axially-propagating fluctuations is large. Thus a change in the main emission angle is unlikely to explain the decrease in amplitude at the largest flow rates for this mode. The decrease in form factor observed for both the axial and $\vec{E} \times \vec{B}$ modes at the largest flow rates is likely to have a common origin.

The frequency of the axial mode is also independent of flow rate as illustrated in Fig. 8.5.

8.2 Effect of discharge voltage on the $\vec{E} \times \vec{B}$ and axial modes

In order to systematically vary the discharge voltage between 200 and 800 V without exceeding the maximum allowed power of 2 kW, it is necessary to maintain the flow rate at 6 mg/s. In this experiment the wave number is maintained at 6670 rad/m and the discharge current at 5 A.

8.2.1 The $\vec{E} \times \vec{B}$ mode form factor and frequency

The $\vec{E} \times \vec{B}$ mode is present at only four of the voltages used - 200, 300, 400 and 500 V. The signal apparently disappears at higher voltages. The form factor has a maximum at

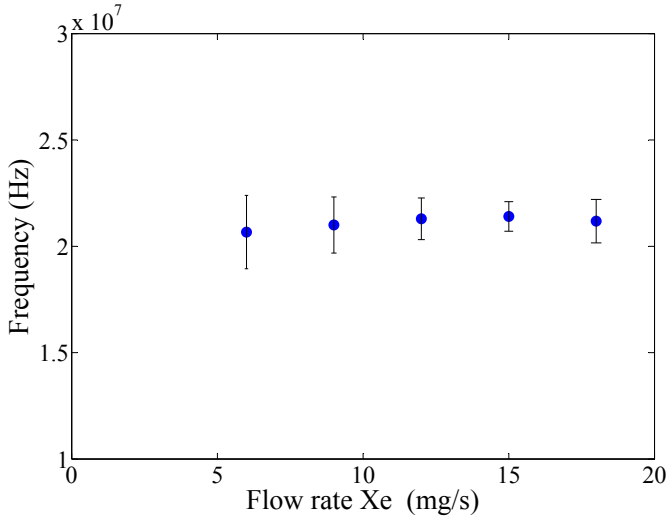

Figure 8.5: Frequency of the axial mode with flow rate

200 V but no clear dependence on the discharge voltage, as is evident from Fig. 8.6.

These observations of form factor with discharge voltage are likely due to a change in the emission angle of the mode with discharge voltage. There is no evident reason for the mode to disappear at higher voltages. It is more likely that the emission angle changes, whereas the observation angle α for this experiment is maintained at 90° at all voltages. A clearer picture of the mode amplitude dependence on discharge voltage would therefore require an exploration of the mode amplitude over a range of α values at each different discharge voltage used.

The frequency of the $\vec{E} \times \vec{B}$ mode is affected only slightly by the discharge voltage, as shown by Fig. 8.7.

8.2.2 General observations concerning the axial mode

Increasing the discharge voltage increases the acceleration of the ions, resulting in higher exit velocities. The axial mode, identified as originating from a coupled ion and electron axial motion, provides evidence of this increased velocity: the peak frequency is seen to increase with the discharge voltage. However, as the peak frequency of the axial mode is already on the order of some tens of MHz, it is difficult to follow the complete evolution of frequency and form factor over the 200 - 800 V range, because the frequency peaks rapidly attain frequencies outside the range of the filters.

8.3 Effect of magnetic field direction on the $\vec{E} \times \vec{B}$ mode

All experiments discussed until now have featured a magnetic field directed radially inwards. A visual observation of the thruster plume confirms that the plasma does not behave

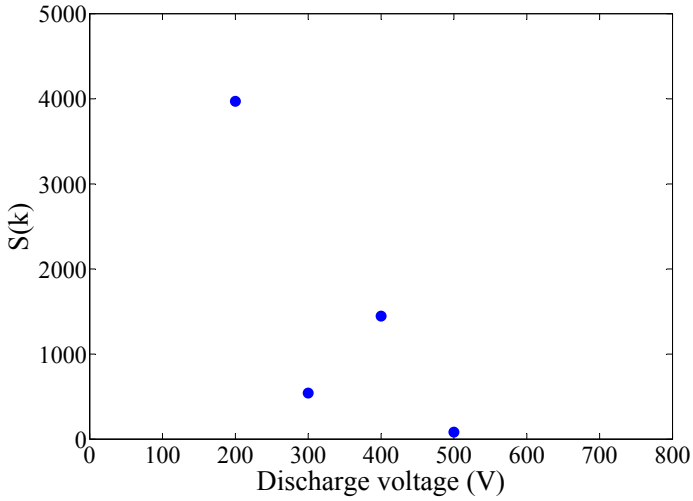

Figure 8.6: Form factor of the $\vec{E} \times \vec{B}$ mode with discharge voltage (positive frequency peak)

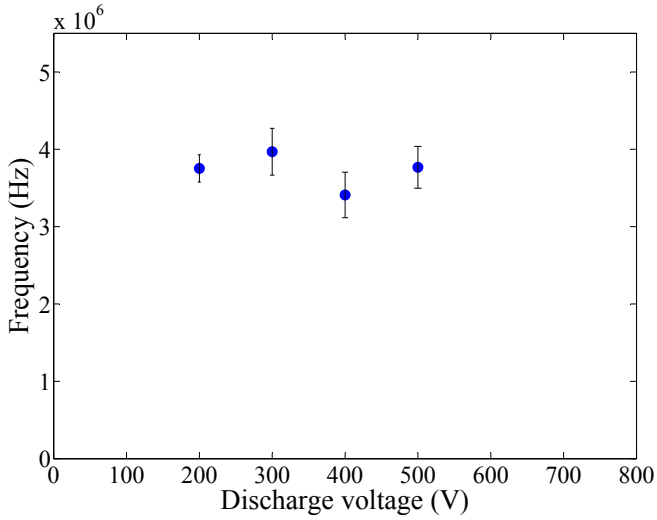

Figure 8.7: Frequency of the $\vec{E} \times \vec{B}$ mode with discharge voltage (positive frequency peak)

in the same manner when the magnetic field is instead directed radially outwards. In the former configuration, the plume appears to contain a tight, distinct beam directed along the thruster axis. In the latter configuration, this beam appears to be split into two diverging streams within the plume. It has also been observed that a maximum Xe flow rate of 20 mg/s is permissible in the radially-outwards B configuration, while the maximum flow rate is limited to 18 mg/s when B is directed radially inwards. Care has been taken to eliminate hysteresis effects (this has been done by rapidly changing the current direction over a large number of cycles) and these curious characteristics appear stable. In general, it appears that the two magnetic field configurations are not identical.

This raises the issue of the effect the field orientation has on the azimuthal instability. To determine this, a new experiment is performed, with the magnetic field directed radially outward (and the direction of the drift velocity therefore naturally reversed).

The dispersion relation for the $\vec{E} \times \vec{B}$ mode corresponding to this situation is shown in Fig. 8.8. The flow rate is 20 mg/s, the discharge current 17 A (nominal value), and α is set to 90°.

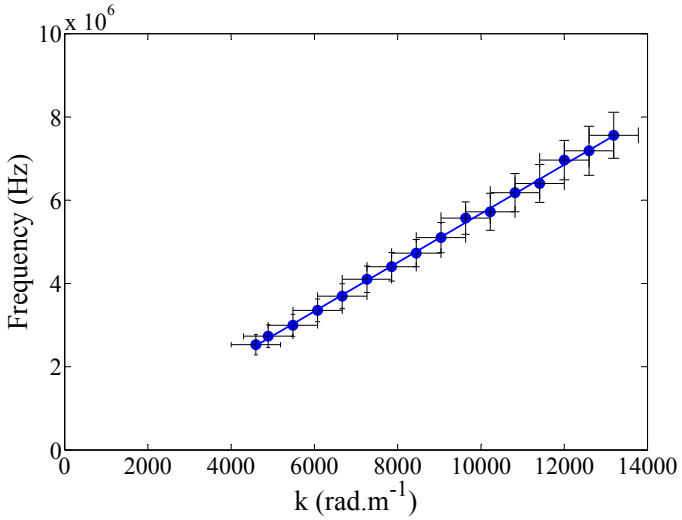

Figure 8.8: Dispersion relation of the $\vec{E} \times \vec{B}$ mode with the magnetic field directed radially outwards (positive frequency peak)

The slope in Fig. 8.8 is 3.69×10^3 m/s, while the y-intercept -1.88×10^5 Hz. The observed values are very similar to those obtained when the magnetic field is oriented radially inwards, and it is clear that the dispersion relation for the mode is unaffected by the orientation of the magnetic field.

It is interesting to check how the mode amplitude is affected by the direction of the magnetic field. The variation of form factor with wave number is shown in Fig. 8.9.

This result shown in Fig. 8.9 differs in a few ways from the typical form factor-wave number plot:

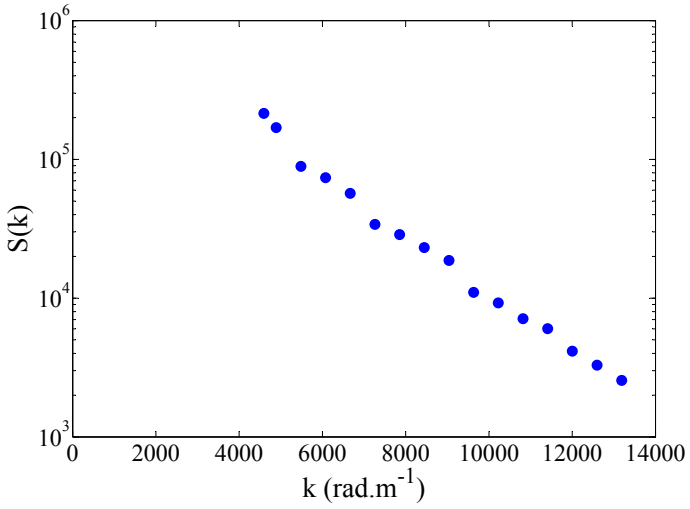

Figure 8.9: Form factor of the $\vec{E} \times \vec{B}$ mode with the magnetic field directed radially outwards (positive frequency peak)

- as the wave number is decreases, the mode amplitude shows significant jumps, rather than a smooth increase; the magnitude of these jumps is well above the uncertainty in the determination of $S(k)$
- at the smallest wave numbers (4594, 4890 rad/m), the mode amplitude increases at a faster rate than the expected exponential form

The differences between the form factor characteristics of this mode for the two field orientations serve as a reminder that the two orientations cannot be assumed to be perfectly symmetric.

8.4 Effect of varying magnetic field strength on the $\vec{E} \times \vec{B}$ and axial modes

The magnetic field strength is changed by varying the current in the internal and external magnetic coils, with the discharge voltage and the discharge current kept constant. The nominal value used for the magnetic coil current during the experiments at 18 mg/s is 17 A. In the region where measurements are carried out (17 mm from the thruster exit plane) a current of 17 A in the coils corresponds to a field strength of about 15 mT.

Variation of the field strength has certain clear consequences. The electron drift velocity is inversely proportional to B. During the discussion of the theoretical results for the azimuthal instability in Chapter 7, it was shown that higher values of v_{the}/V_d are associated with a broadening of the unstable lobes and a reduction in the growth rate of the instability.

Additionally, it was observed that above a certain small value of k_z, the theoretical dispersion relation is continuous. Increasing B, thereby reducing the drift velocity V_d, would have the effect of lowering this limit on k_z further; in other words, the conditions for observing an instability which is non-discrete in k become even more favourable. The prediction of the reduced growth rate does not, however, provide direct information on the expected mode amplitude.

Increasing the magnetic field strength will also reduce the electron and ion Larmor radii. One likely consequence of this is reduced axial transport by electron-neutral collisions, at least inside the channel where the population of neutrals is significant.

An experiment is performed to determine the effects on the $\vec{E} \times \vec{B}$ and axial modes of varying magnetic coil currents. The magnetic field is restored to its habitual orientation (directed radially inwards).

8.4.1 The $\vec{E} \times \vec{B}$ mode form factor and frequency

Dispersion relations at different values of coil current

The first analysis of the influence of the magnetic field concerns the dispersion relation. Three values of magnetic coil current I are chosen: 10, 17 and 24 A. The dispersion relations are determined for each coil current with conditions of 6 mg/s Xe flow rate, 300 V discharge voltage and 5 A discharge current. 10 A is an operational limit below which the plasma is rapidly extinguished, while 17 A is the nominal current. 24 A is chosen to be a good upper limit, sufficiently different from the nominal current.

The three dispersion relations are shown in Fig. 8.10.

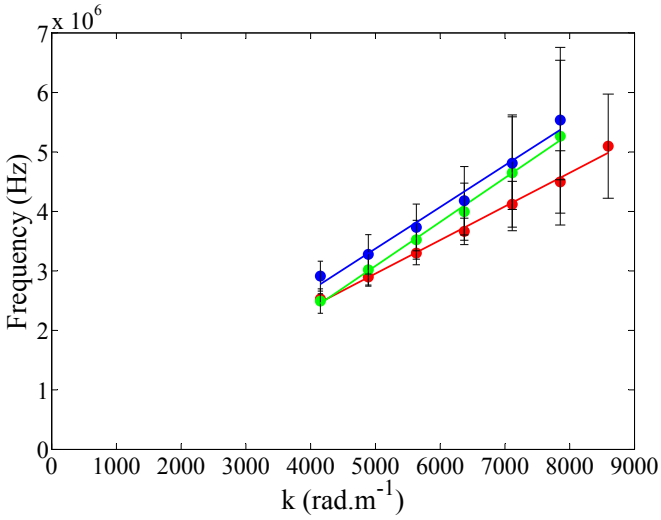

Figure 8.10: Comparison of dispersion relations of the $\vec{E} \times \vec{B}$ mode (positive frequency peak) for different magnetic field strengths: 10 A (in red), 17 A (in green), and 24 A (in blue)

The fit parameters of the dispersion relations are shown in Eq. 8.1, where m represents the slope (velocity) and c the frequency intercept.

$$\begin{aligned} I &= 10 \text{ A}, \quad m = 3.55 \times 10^3 \text{ m/s}, \quad c = 1.29 \times 10^5 \text{ Hz} \\ I &= 17 \text{ A}, \quad m = 4.66 \times 10^3 \text{ m/s}, \quad c = -6.22 \times 10^5 \text{ Hz} \\ I &= 24 \text{ A}, \quad m = 4.40 \times 10^3 \text{ m/s}, \quad c = -1.29 \times 10^5 \text{ Hz} \end{aligned} \tag{8.1}$$

There appears to be a minimal effect of the magnetic field on the frequency and dispersion relation. It was necessary to operate at a low flow rate to cover this range of currents and hence the signal is relatively weak and the error bars on the frequency are quite large.

These three dispersion relations of similar slopes indicate that the $\vec{E} \times \vec{B}$ mode, although related to the $\vec{E} \times \vec{B}$ drift, does not propagate at a velocity which is proportional to the drift velocity E/B.

Form factor with wave number at different values of coil current

A comparison of the mode amplitudes with wave number for the three different coil currents is presented in Fig. 8.11. The usual exponential relationship between the energy and wave number is observed at all three currents. There is a slight variation of the overall mode amplitude with coil current at the same value of wave number. The parameters for an exponential fit of the form $S(k) = Ae^{bk}$ are given in Eq. 8.2.

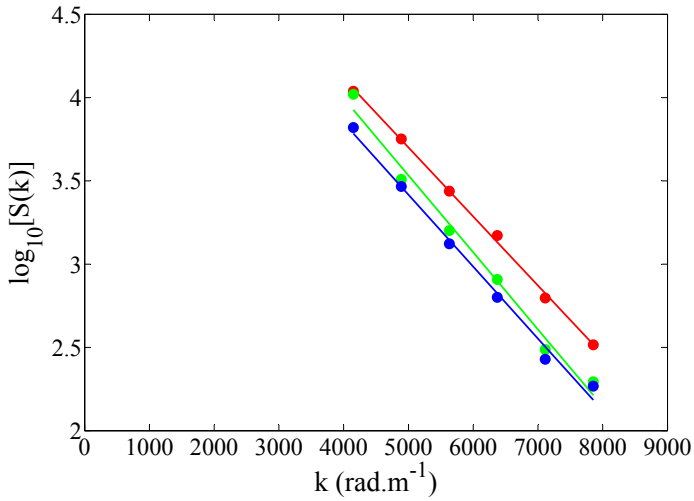

Figure 8.11: Variation of form factor with wave number of the $\vec{E} \times \vec{B}$ mode (positive frequency peak) for different magnetic field strengths: 10 A (in red), 17 A (in green), and 24 A (in blue)

$$
\begin{aligned}
I &= 10 \text{ A}, \quad b = -0.95 \text{ mm}, \quad A = 5.93 \times 10^5 \\
I &= 17 \text{ A}, \quad b = -1.06 \text{ mm}, \quad A = 7.00 \times 10^5 \\
I &= 24 \text{ A}, \quad b = -0.99 \text{ mm}, \quad A = 3.77 \times 10^5
\end{aligned}
\tag{8.2}
$$

No strong dependence of form factor on these values of coil current is evident. This shows that the characteristic decay length of the form factor with wave number is not proportional to a cyclotron radius, although it is of the same order of magnitude. Proportionality of the decay length to the cyclotron radius would mean that the decay length would change as $1/B$. A more systematic variation of coil current at a fixed value of wave number will now be discussed.

Variation of mode frequency with coil current at fixed wave number

The coil current is now varied between 7 and 24 A with the wave number fixed at 4890 rad/m. For this exploration, the flow rate is maintained at 6 mg/s, discharge voltage at 300 V and discharge current at 5 A. α is set to 90°. The frequency variation with coil current is shown in Fig. 8.12; the peak frequency varies only slightly and remains at a value close to 3 MHz.

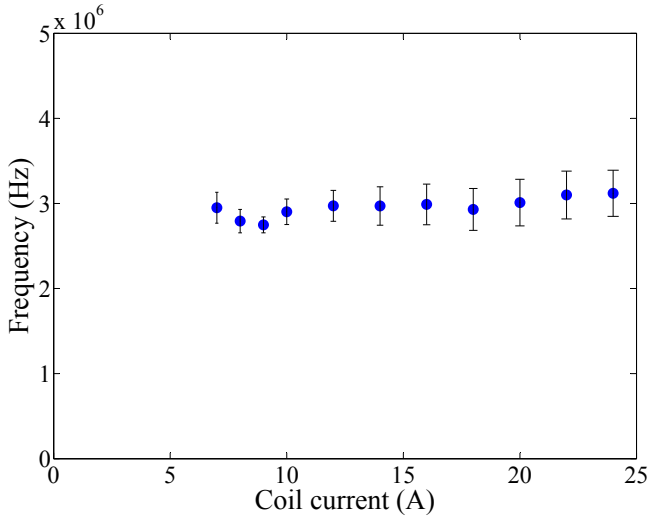

Figure 8.12: Variation of peak frequency with coil current for the $\vec{E} \times \vec{B}$ mode at k = 4890 rad/m (positive frequency peak)

Variation of mode amplitude with coil current at fixed wave number

The variation of the form factor with coil current shows some unusual characteristics. There is a pronounced maximum in amplitude for a coil current of 9 A, followed by a drop and apparent saturation in energy (Fig. 8.13). The significance of the 9 A value of coil current is unknown at this stage.

It should be noted that the magnetic field amplitude does not in fact increase linearly with the magnetic coil current. Above 17 A, a saturation in the field amplitude starts to develop and becomes increasingly marked as the current increases, a fact which may account for the plateau in amplitude visible in Fig. 8.13. This saturation may also explain why a clear dependence of the dispersion relation (Fig. 8.10) and form factor (Fig. 8.11) on the value of coil current is not easily identified.

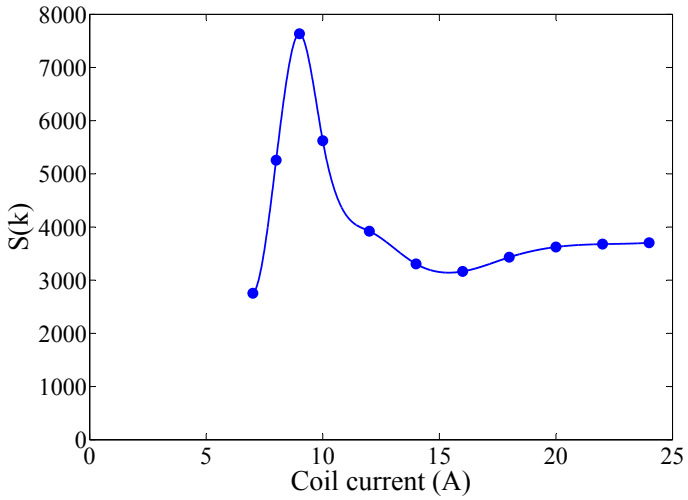

Figure 8.13: Variation of form factor with coil current for the $\vec{E} \times \vec{B}$ mode at k = 4890 rad/m (positive frequency peak)

8.4.2 The axial mode form factor and frequency

The variation of form factor and amplitude of the axial mode are studied for a limited range of magnetic coil currents (16 - 21 A), necessarily at high flow rate (18 mg/s), because of its comparatively low energy. The wave number is set to 4150 rad/m, and α to 5°. The discharge voltage is fixed at 300 V and the discharge current is 17 A.

The frequency of this mode does not vary with the coil current, as seen in Fig. 8.14, but remains around a value of 16 MHz. Intuitively, the only factor which should influence (and is seen to influence) the frequency of the axial mode is one which modifies the ejection velocity of the ions. The discharge voltage is held constant and the magnetic field does not have such an effect.

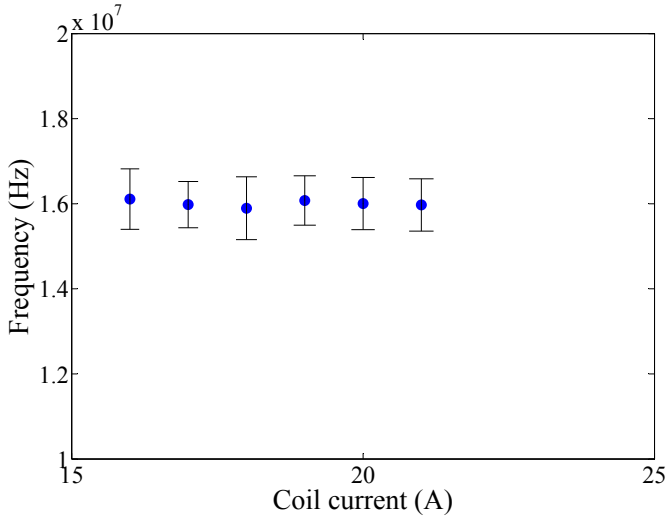

Figure 8.14: Variation of frequency with coil current for the axial mode at k = 4150 rad/m

The form factor does show some variation with coil current, increasing gradually but non-linearly with the coil current, as shown in Fig. 8.15.

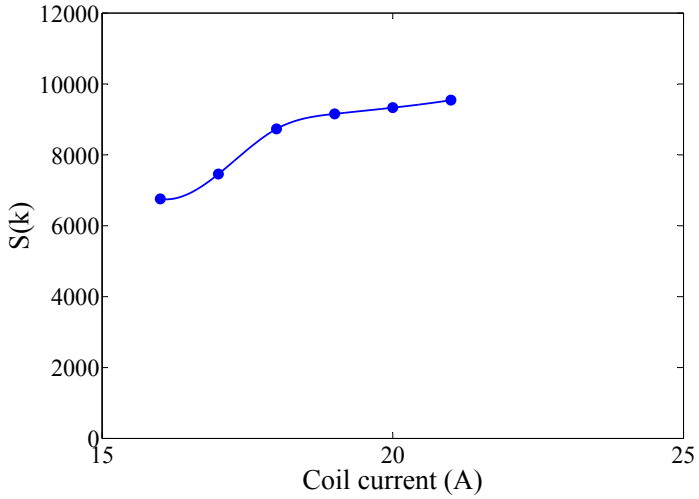

Figure 8.15: Variation of form factor with coil current for the axial mode at k = 4150 rad/m

In general, the frequency of the $\vec{E} \times \vec{B}$ mode is robust and independent of the thruster parameters explored in this chapter. The amplitude of this mode, however, varies quite significantly with the different parameters. Based on the observations of this chapter, if anomalous electron transport is proportional to the $\vec{E} \times \vec{B}$ mode amplitude, then a reduction of such transport would require that the thruster be operated in a low flow rate (6 to 10 mg/s), high coil current (above 14 A) regime. Such considerations should naturally be balanced with thrust requirements, for example.

The axial mode has a smaller amplitude than the $\vec{E} \times \vec{B}$ mode at a similar wave number and is only weakly influenced by changes in the thruster parameters (save for the accelerating voltage). The influence of the discharge voltage on the $\vec{E} \times \vec{B}$ mode is not easy to interpret and the thruster is known to dramatically change its operating regime outside the nominal operating voltage of around 300 V.

The interplay of all these factors makes any definite recommendations for thruster operation premature. Instead, the relationship between the observed fluctuation characteristics for different thruster operating parameters and electron mobility should be investigated in future dedicated experiments.

8.5 Low frequency signal characteristics

8.5.1 Significance of low frequency modes

The presence of low frequency oscillations (below 1 MHz) in the Hall thruster is a widely-known and discussed phenomenon. A short description of some of the main low frequency oscillations was presented in the introduction. Many of these low frequency oscillations, such as the breathing mode and oscillations resulting from the transit time of the ion species, have been described in detail in the literature. Other low frequency modes, seen as density concentrations travelling azimuthally, have also been identified. What is common to all these studies is that they describe low frequency oscillations of length scales typically on the order of a few cm or several mm. It is interesting to examine low frequency oscillations measured at the much shorter length scales of this collective scattering study (0.48 to 1.57 mm) and determine if and how they are influenced by thruster parameters.

8.5.2 Nature of low frequency signals

The normalization procedure applied to the spectra is particularly important for the identification of low frequency signals originating from the plasma. There are several sources of parasitic low frequency signals in the surroundings. Normalization is necessary to distinguish the low frequency plasma oscillations, which have very low amplitudes, from the noise. On the raw spectra, the low frequency signals seen originate from three principal sources:

- Diffraction: diffraction on a mirror surface causes a signal peak to appear at the carrier frequency (i.e. 0 MHz on the spectra). Such a peak is visible in the $PL + LO$, $PL + PB + LO$ and $PB + LO$ records and is removed or attenuated in the normalized

signal. The width and amplitude of signal peaks due to stray diffraction has been greatly reduced on PRAXIS-II in comparison with PRAXIS-I.

- Background vibrations: weak vibrations in the surroundings occur due to the presence of the vacuum pumps, resulting in low frequency vibrations of the optical bench. The corresponding signals are present in the $PL + LO$, $PL + PB + LO$ and $PB + LO$ records and are removed in the normalized signals.

- Plasma coupling to electronics: some plasma oscillations are strong enough to radiate and be detected directly by the electronics circuit, without the need for collective scattering. This observation was made during the first collective scattering trial (Chapter 1). Such signals are present in both $PL + LO$ and $PL + PB + LO$ records (Fig. 8.16). The net amplitude of this oscillation, as detected by collective scattering only, is obtained after normalization.

- Low amplitude plasma oscillations: these signals appear only in the $PL + PB + LO$ record.

Fig. 8.16 shows the raw spectra obtained which illustrate some of the typical low frequency observations. A signal is detected in both $PL + LO$ and $PL + PB + LO$ records at $\pm$ 26 kHz, due to an oscillation detected by the circuit, and greatly attenuated after normalization. At -61 kHz, a large amplitude signal obtained by collective scattering is evident. The experimental conditions used are a flow rate of 18 mg/s and discharge voltage of 300 V. α is 90° and the wave number is 10373 rad/m.

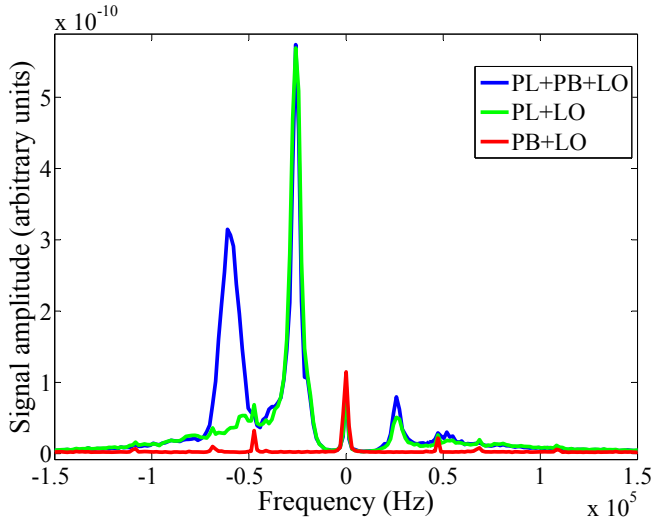

Figure 8.16: Raw low frequency spectra illustrating plasma oscillations detected by the circuit and by collective scattering.

The low frequency signals on the spectra typically have irregular profiles, thus to identify a peak frequency $\langle f \rangle$ for a particular peak, the following form is used

$$\langle f \rangle = \frac{\sum f \cdot S(f)}{\sum S(f)} \tag{8.3}$$

where a weighted frequency value is obtained from the dynamic form factor values from the normalized spectra, $S(f)$, at different frequency values f.

8.5.3 The discharge current

The measured discharge current, I_d, is the sum of the electron current, I_e, and ion current, I_i, flowing to the anode. The ion current flowing towards the anode is considered negligible,

$$I_d \approx I_e \tag{8.4}$$

I_e is formed from two contributions: electrons which are emitted by the cathode and flow directly to the anode, and secondary electrons which are released after ionization. The electron current due to the secondary electrons is naturally equal to the ion beam current.

Hence I_d may be expressed as the sum of the primary electron current flowing to the anode and the ion beam current.

A portion of the time-varying discharge current signal recorded at the same time as the signals shown in Fig. 8.16 is shown in Fig. 8.17. A 24 kHz oscillation is present in the discharge current. This oscillation is associated with the breathing mode.

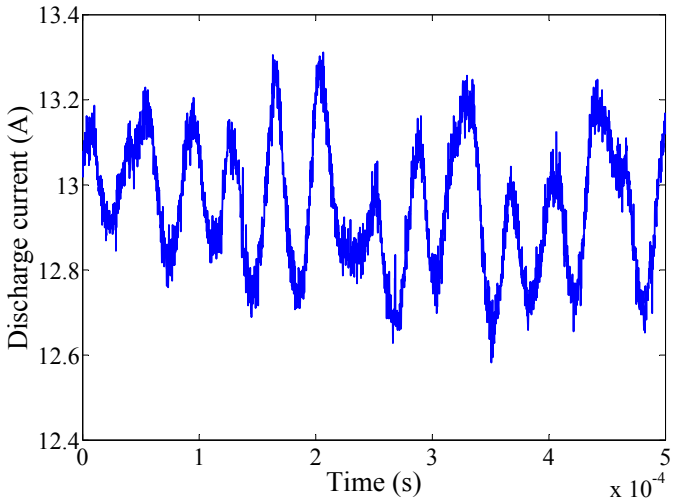

Figure 8.17: Discharge current oscillations for a 0.5 ms duration (from a total acquisition duration of 0.13 s)

8.5.4 Random appearance of low frequency signals

The low frequency signals usually vary from record to record. That is to say, even for identical experimental and thruster conditions, low frequency peaks of different frequencies and amplitudes are seen. Fig. 8.18(a) and Fig. 8.18(b) illustrate the random appearance and character of low frequency peaks. In the experiment shown, $\alpha = 90°$, the Xe flow rate 18 mg/s and the wave number 10373 rad/m, for both cases. The discharge voltage is 300 V. The only difference between the two cases is that the two records were made several minutes apart. Only the $\pm$ 200 kHz range is shown for both figures as all important low frequency signals tended to fall in this range.

The main frequency peaks in Fig. 8.18(a) are at -169 and -61 kHz; in contrast, the low frequency peaks in Fig. 8.18(b) are located at -88, 25 and 21 kHz (with a resolution of 1.5 kHz). In addition, the amplitudes of the observed peaks are much larger in the second case (the maximum dynamic form factor in Fig. 8.18(a) is only 3×10^{-3} s, while in Fig. 8.18(b), in which the maximum is not shown, the maximum amplitude is 0.4 s.

The apparent random nature of the signals complicates analysis of low frequency trends. As the frequencies and amplitudes are seen to vary for identical conditions, it is often unclear whether when one parameter is varied, the peak observed is a shift of the same mode from an original frequency or the spontaneous appearance of another type of oscillation.

8.5.5 Low frequency trends

Some attempts have been made to determine if key dependencies exist, despite the erratic nature of the low frequency signals.

Dispersion relations

No clear dispersion relations have yet been identified for the low frequency modes seen in this chapter. Fig. 8.19 shows the normalized superposed spectra for several values of wave number, for which the flow rate is 6 mg/s, α = 90°, discharge voltage 300 V and magnetic coil current 17 A.

The largest low frequency signal (in red) is seen at the smallest wave number, 4149 rad/m. The characteristic peak frequency is 30 kHz. The other superposed spectra correspond to successively higher values of wave number and their signal amplitudes are lower. The amplitudes are probably too small to be significant, but it appears that the frequency remains the same for different values of wave number. At higher values of wave number, exceeding 7854 rad/m (spectra not shown), no low frequency signals are apparent at the same frequency.

Effect of flow rate

A comparison of the low frequency normalized spectra at different flow rates, from 6 to 18 mg/s, is shown in Fig. 8.20. In this example, α = 90°, with the wave number fixed at 5928 rad/m. The discharge voltage is 300 V.

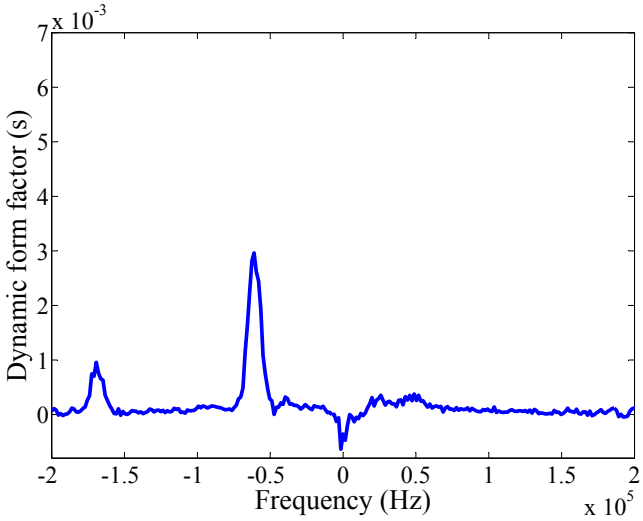

(a) Low frequency spectra, case 1

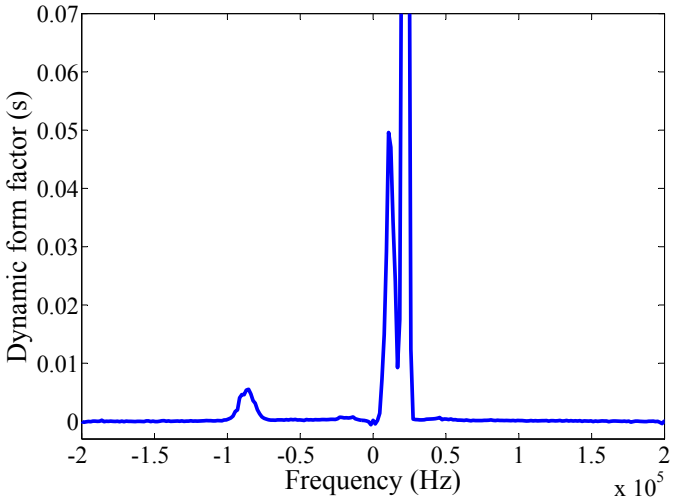

(b) Low frequency spectra, case 2

Figure 8.18: Non-identical low frequency spectra obtained for identical experimental conditions and thruster parameters

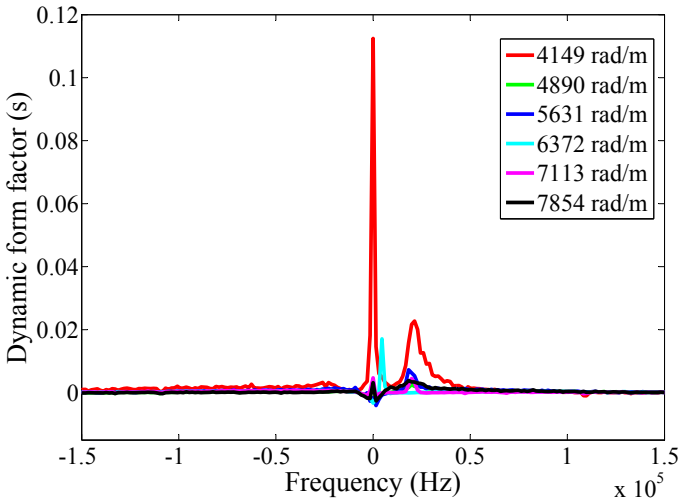

Figure 8.19: Low frequency normalized spectra at different wave numbers, with α=90°

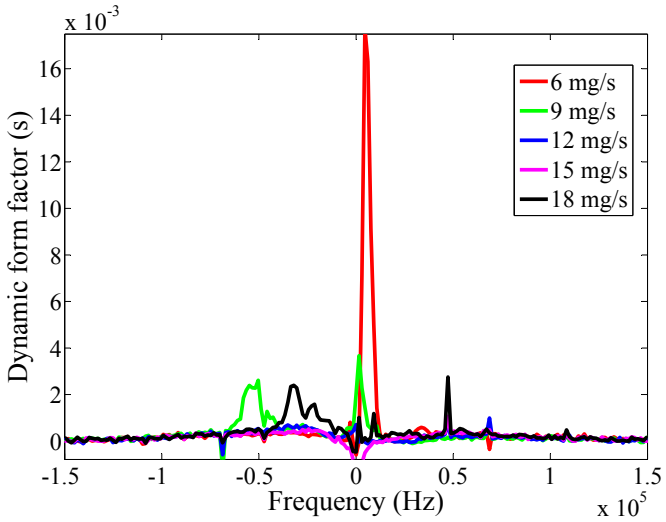

Figure 8.20: Low frequency normalized spectra at different flow rates, with α=90° and k = 5928 rad/m

As is evident from Fig. 8.20, no clear trend in either frequency or form factor is identifiable with flow rate. The large peak apparent at very low frequency (6 kHz) is most likely a diffraction residue which was not removed after normalization. The maximum static form factor is about 80 for this mode.

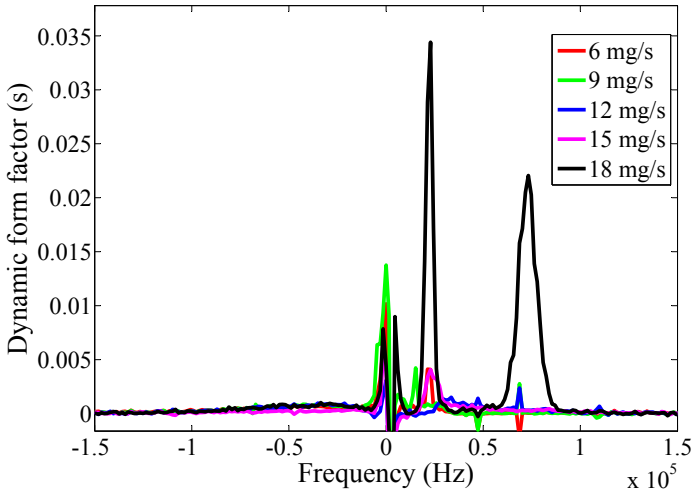

Figure 8.21: Low frequency normalized spectra at different flow rates, with α=0°

A qualitative comparison of these results may be made with the case for which the wave vector is oriented nearly parallel to the thruster axis. Fig. 8.21 shows the low frequency spectra obtained at different flow rates when $\alpha = 5°$. The flow rate is 18 mg/s and the discharge voltage 300 V. Some low frequency signals are observed in this case at frequencies of 23 kHz and 73 kHz, with respective static form factor values of about 170 and 270 respectively.

Effect of magnetic field strength

In this experiment, $\vec{k}$ is oriented parallel to $\vec{E} \times \vec{B}$ and the flow rate is maintained at 6 mg/s, with the wave number fixed at 4890 rad/m. The magnetic field strength is varied by varying the coil current from values of 7 to 24 A.

At high values of magnetic field coil current (20 to 24 A), no low frequency signal is present, apart from the usual diffraction peak at 0 Hz (Fig. 8.22(a)). At lower values of coil current, some low frequency peaks begin to appear (Fig. 8.22(b)). At the lowest values of the coil current (7 to 14 A), a stable and unambiguous low frequency peak is observed, with a frequency and amplitude which appear to evolve with coil current (Fig. 8.22(c)).

This experiment is a case in which some influence of the thruster parameters on the low frequency behaviour may exist. The frequency variation with coil current between 7 and 14 A is shown in Fig. 8.23. The frequency (absolute value) of the low frequency peak is seen

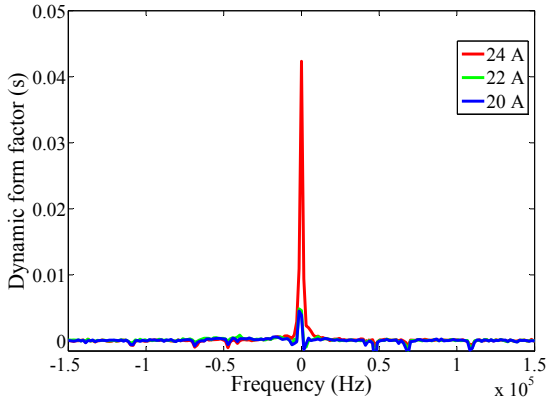

(a) Low frequency spectra for high values of magnetic coil current (20 - 24 A)

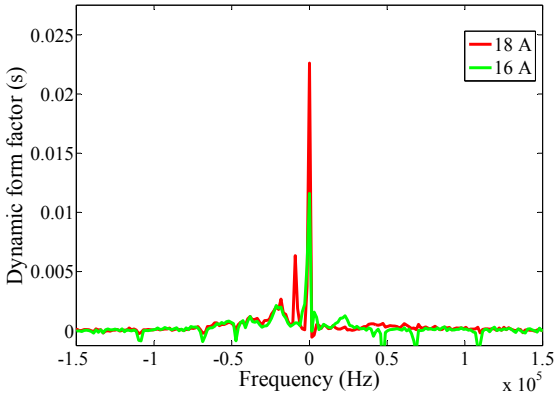

(b) Low frequency spectra for intermediate values of magnetic coil current (16 and 18 A)

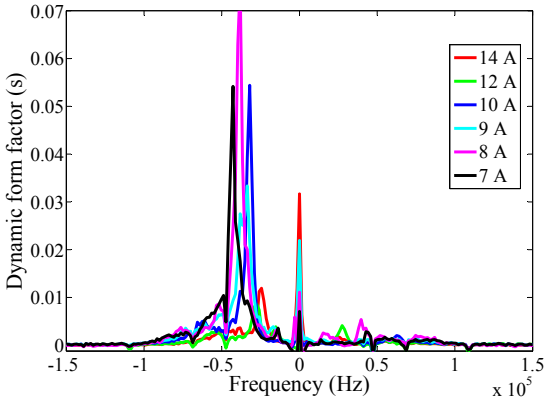

(c) Low frequency spectra for low values of magnetic coil current (7 - 14 A)

Figure 8.22: Behaviour of low frequencies for varying magnetic coil currents

to increase as the coil current decreases. The gradual evolution and the sustained presence of the peak seem to support the idea that it pertains to a particular mode.

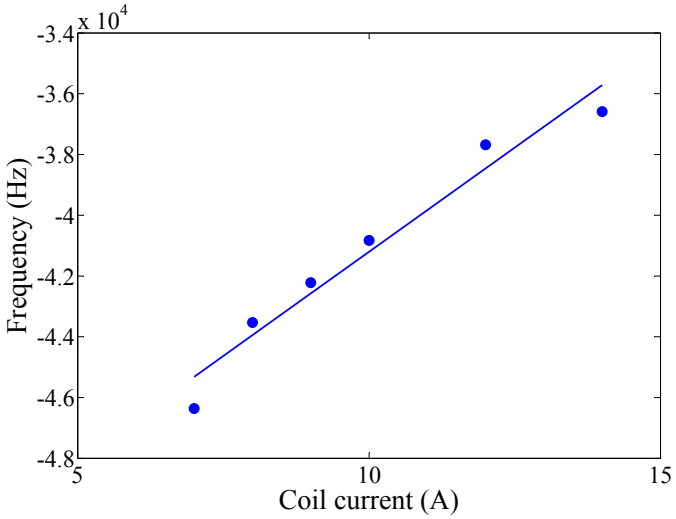

Figure 8.23: Frequency variation with coil current for α = 90° and k = 4890 rad/m

The frequencies, observed around -40 kHz for a wave number of 4890 rad/m, would correspond to velocities on the order of 500 m/s. This velocity is so small that it is not clear what thruster phenomena could produce these oscillations.

The corresponding form factor variation with coil current for the frequency peaks of Fig. 8.23 is shown in Fig. 8.24. The form factor has unusually high values (for low frequencies) at small coil currents, with a maximum around 8 A followed by a decrease as the coil current increases.

8.5.6 Discussion

The form factors of the low frequency signals are typically very small, very seldom exceeding 500. This places their maximum amplitude levels three orders of magnitude smaller than the maximum amplitude of the high frequency oscillations studied in this thesis.

It is important to note that the low frequency observations described here are not necessarily comparable to those mentioned in other works, even though the frequencies are similar. The length scales accessible in our experiments do not correspond to the length scales of the low frequency oscillations commonly described in the literature and so no direct correlation between the breathing mode and transit time oscillations can be described. In the azimuthal direction, for instance, low frequency oscillations have been measured with wavelengths on the order of the thruster circumference [13], a spatial scale well beyond that which is measurable by this diagnostic.

The mechanisms by which electrons are transported to the anode appear to occur over a wide range of spatial and temporal scales. On the one hand, our results concerning the high

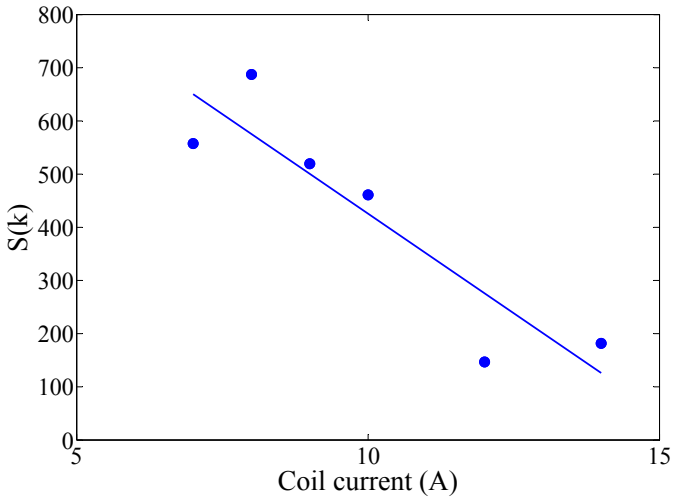

Figure 8.24: Form factor variation with coil current for α = 90° and k = 4890 rad/m. Form factor values correspond to frequency peaks of Fig. 8.23

frequencies at millimetric scales show that these excited modes have very large amplitudes. On the other hand, our low frequency results show that at the same scales, the low frequency oscillations are comparatively very weak.

The influence of the thruster parameters on the high frequency and low frequency oscillations at the millimetric scale has been considered in this chapter. Some interesting dependencies are evident for the high frequency oscillations, but the low frequencies tend to be generally erratic and have very low amplitudes with no clear dependency on the thruster parameters.

Chapter 9

Stability analysis of longitudinal plasma waves

Contents

THE plasma in a Hall thruster may be approximated as a collisionless plasma, subjected to a uniform magnetic field $\vec{B}_0$ parallel to the z axis and a uniform electric field $\vec{E}_0$ parallel to the x axis, in a slab geometry as shown in Fig. 9.1.

The magnetic pressure associated with the magnetic field ($B^2/2\mu_0$) is much larger than the kinetic plasma pressure (nk_BT). The electrons, with a small Larmor radius in comparison to the plasma dimensions, are magnetized, while the ions are not. This chapter is

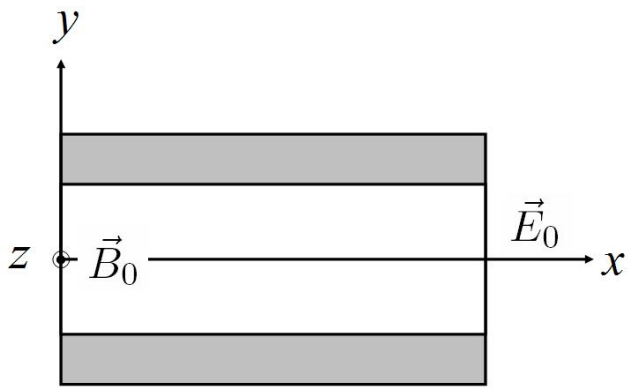

Figure 9.1: Slab geometry of Hall thruster (plasma indicated in grey). The uniform magnetic field $\vec{B}_0$ is directed out of the plane of the page along z, with the uniform electric field $\vec{E}_0$ parallel to x

concerned with determining the stability of the plasma on spatial and temporal scales which are small compared to the plasma dimension and its collective movements. This analysis is intended to account for the modes which have been seen experimentally.

Longitudinal space-charge waves, which will be studied here, are readily produced by the coupling between the electric field and the particle trajectories. The waves seen experimentally are most likely space-charge waves and the linear theory which forms the basis for the analytic studies of Adam et. al. [2] and Ducrocq et. al. [18] demonstrates that the sole condition for the formation of the unstable azimuthal mode is the azimuthal electron drift.

9.1 Evolution of the electron distribution

9.1.1 Vlasov equation

The interaction between a travelling wave and the charged particles depends on the particle velocity. It is therefore necessary to distinguish between the particles according to their velocity distribution. The appropriate description of the particle-wave interaction is obtained from kinetic theory and the Vlasov equation.

The electron density in position and velocity space is defined by a distribution function $f(\vec{r}, \vec{v}, t)$. When the electrons are located in an electromagnetic field, the function f evolves in time in a manner such that the number of electrons in a volume element of the phase space ($\vec{r}$, $\vec{v}$) (which deforms according to the movement) is constant. This property is formalised in the Vlasov equation,

$$\frac{\partial f}{\partial t} + \vec{v} \cdot \frac{\partial f}{\partial \vec{r}} + \frac{q_e}{m_e}(\vec{E} + \vec{v} \times \vec{B}) \cdot \frac{\partial f}{\partial \vec{v}} = 0 \tag{9.1}$$

This is a non-linear differential equation, by way of the third term which is formed

from the product of an electromagnetic field function and f, both of which depend on position and time. To solve this equation, perturbative methods are applied.

The functions f and $\vec{E}$ are developed by orders, i.e.

$$f(\vec{r},\vec{v},t) = f_o(\vec{v}) + f_1(\vec{r},\vec{v},t) \tag{9.2}$$

$$\vec{E}(\vec{r},t) = \vec{E}_o + \vec{E}_1(\vec{r},t) \tag{9.3}$$

We consider space-charge fluctuations, which are decoupled from transverse electromagnetic fluctuations such as magnetic field fluctuations. Thus the magnetic field contains only the zeroth order term, $\vec{B}_0$. These expansions are substituted into the Vlasov equation, which must then be satisfied at every order.

The resulting equations are

$$(\vec{E}_0 + \vec{v}\times\vec{B}_0)\cdot\frac{\partial f_0}{\partial\vec{v}} = 0 \tag{9.4}$$

$$\frac{\partial f_1}{\partial t} + \vec{v}\cdot\frac{\partial f_1}{\partial\vec{r}} + \frac{q_e}{m_e}(\vec{E}_0 + \vec{v}\times\vec{B}_0)\cdot\frac{\partial f_1}{\partial\vec{v}} = -\frac{q_e}{m_e}\vec{E}_1\cdot\frac{\partial f_0}{\partial\vec{v}} \tag{9.5}$$

9.1.2 Zeroth order solution: uniform steady-state motion

The solution to Eq. 9.4 is obtained via a change of variables,

$$\vec{v} = \frac{\vec{E}\times\vec{B}}{{B_0}^2} + \vec{u} \tag{9.6}$$

from which Eq. 9.4 becomes

$$\vec{u}\times\vec{B}\cdot\frac{\partial f_0}{\partial\vec{u}} = 0 \tag{9.7}$$

This equation is satisfied if the function $f_0(\vec{u})$ is isotropic about the axis of $\vec{B}_0$. This condition is fulfilled if in the crossed $\vec{E}$ and $\vec{B}$ configuration of the thruster, the electrons move with a drift velocity $\vec{V}_d$ (Fig. 9.2),

$$\vec{V}_d = \frac{\vec{E}\times\vec{B}}{{B_0}^2} \tag{9.8}$$

and if the distribution function of the electrons at the zeroth order is isotropic in the reference frame moving at the velocity $\vec{V}_d$ in the direction Oy.

f_0 may be written as a shifted Maxwellian distribution

$$f_o(\vec{v}) = n_o \exp\left[-\frac{v_x^2 + (v_y - V_d)^2 + v_z^2}{2v_{the}^2}\right] \tag{9.9}$$

where

$$v_{the} = \sqrt{\frac{k_B T_e}{m_e}} \tag{9.10}$$

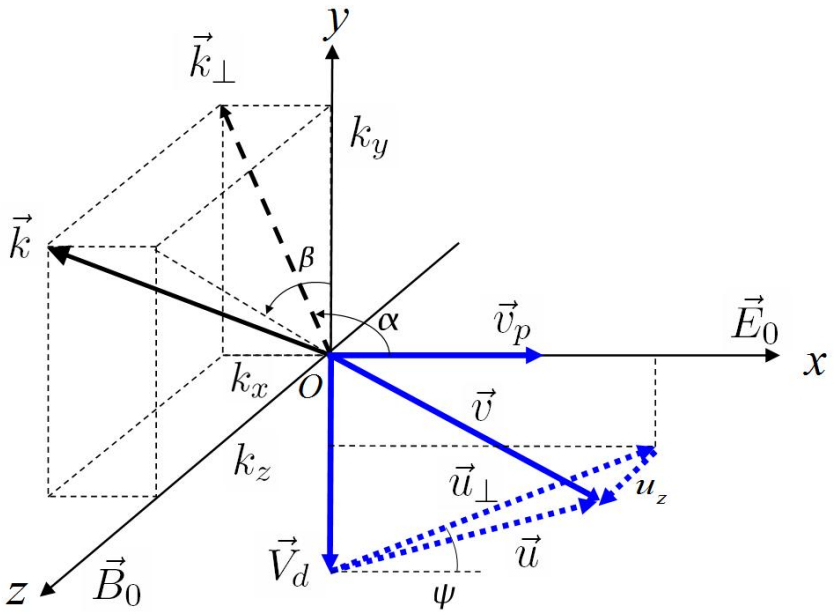

Figure 9.2: Geometry of the Hall thruster. The wave vector $\vec{k}$ is shown with its projections along all three axes; $\vec{k}_\perp$ is the projected wave vector in the xOy plane. The coordinates of the velocity of an electron in the lab reference frame, $\vec{v}$, and in the particle reference frame moving at the drift velocity, $\vec{u} = \vec{v} - \vec{V}_d$, are shown. The angle Ψ is formed between $u_\perp$ and the x axis. The angles α and β shown on the figure are consistent with the definitions used during experiments, and the geometry shown would correspond to observations of a negative frequency peak of the $\vec{E} \times \vec{B}$ mode (in the 03h00 thruster channel side)

9.1.3 Solution to the linearized Vlasov equation: the homogeneous equation

Eq. 9.5 contains two parts. The first member is a homogeneous differential equation involving f_1, while the second is formed by the source terms for the function f_1. The homogeneous and complete solutions are obtained using a property of the Vlasov equation, according to which the function f is constant along the trajectory of an electron. The homogeneous equation is therefore satisfied by every function of $(\vec{r'}, \vec{v'}, t)$ whose arguments $(\vec{r'}, \vec{v'})$ are time-dependent functions of the form $\vec{r'} = \vec{r'}(t)$, $\vec{v'} = \vec{v'}(t)$, which describe the motion of an electron in the presence of the uniform, crossed fields $\vec{E}_0$ and $\vec{B}_0$. To solve the homogeneous equation, we situate ourselves in the reference frame moving at the drift velocity $\vec{V}_d$ (Eq. 9.8). The velocity $\vec{u}$ and the coordinates $\vec{r}_1$ in this reference frame are defined by

$$\vec{v} = \vec{V}_d + \vec{u} \tag{9.11}$$
$$\vec{r} = \vec{V}_d t + \vec{r}_1 \tag{9.12}$$

With these coordinates, the first member of Eq. 9.5 gives the following homogeneous equation:

$$\frac{\partial f_1(\vec{r}_1, \vec{u}, t)}{\partial t} + \vec{u} \cdot \frac{\partial f_1(\vec{r}_1, \vec{u}, t)}{\partial \vec{r}_1} + \frac{q_e}{m_e}\, \vec{u} \times \vec{B}_0 \cdot \frac{\partial f_1(\vec{r}_1, \vec{u}, t)}{\partial \vec{u}} = 0 \tag{9.13}$$

This equation pertains to the distribution function in a uniform and steady magnetic field. The motion of electrons in this reference frame is the cyclotron motion. Let an electron be characterised at time t by a velocity $\vec{u}$, whose component $\vec{u}_\perp$ on the plane perpendicular to $\vec{B}_0$ makes an angle Ψ with the axis Ox, and by a position $\vec{r}_1 = (x_1, y_1, z_1)$. The magnitude of the velocity $\vec{u}_\perp$ is constant, and the angle Ψ rotates in time at the electron cyclotron frequency $\omega_{ce} = eB_0/m_e$. The velocity and the position of the electron at time $t' < t$ are $\vec{u}(t')$ and $\vec{r}_1(t')$ respectively, such that

$$u_x(t') = u_\perp \cos\left[\omega_{ce}(t' - t) + \psi\right] \tag{9.14}$$
$$u_y(t') = u_\perp \sin\left[\omega_{ce}(t' - t) + \psi\right] \tag{9.15}$$
$$u_z(t') = u_z \tag{9.16}$$

and

$$r_{1x}(t') = \frac{u_\perp}{\omega_{ce}}[\sin\left[\omega_{ce}(t' - t) + \psi\right] - \sin\psi] + x_1 \tag{9.17}$$
$$r_{1y}(t') = \frac{u_\perp}{\omega_{ce}}[\cos\psi - \cos\left[\omega_{ce}(t' - t) + \psi\right] + y_1 \tag{9.18}$$
$$r_{1z}(t') = u_z(t' - t) + z_1 \tag{9.19}$$

The velocities in the lab reference frame are obtained using Eq. 9.11,

$$v_x(t') = u_\perp \cos\left[\omega_{ce}(t' - t) + \psi\right] \tag{9.20}$$
$$v_y(t') = u_\perp \sin\left[\omega_{ce}(t' - t) + \psi\right] + V_d \tag{9.21}$$
$$v_z(t') = v_z = u_z \tag{9.22}$$

where $u_\perp$ is defined as

$$u_\perp = \sqrt{{v_x}^2 + (v_y - V_d)^2} \tag{9.23}$$

and the trajectories, obtained from Eq. 9.12, are written

$$x(t') = \frac{u_\perp}{\omega_{ce}}[\sin[\omega_{ce}(t'-t)+\psi] - \sin\psi] + x \tag{9.24}$$

$$y(t') = \frac{u_\perp}{\omega_{ce}}[\cos\psi - \cos[\omega_{ce}(t'-t)+\psi] + y + V_d(t'-t) \tag{9.25}$$

$$z(t') = v_z(t'-t) + z \tag{9.26}$$

9.1.4 Solution to the linearized Vlasov equation: the complete equation

Each function $f(\vec{r},\vec{v},t)$ whose arguments are the trajectories given by Eq. 9.22 and Eq. 9.25, is a solution of the homogeneous equation. The complete solution of Eq. 9.5 is obtained by the integration of the source terms over the trajectories,

$$f_{e1}(\vec{r},\vec{v},t) = -\frac{q_e}{m_e}\int_{-\infty}^{t} \vec{E}_1(\vec{r}(t'),t')\cdot\frac{\partial f_o(\vec{v}(t'))}{\partial\vec{v}}dt' \tag{9.27}$$

Two additional properties will be used: first, the fact that the electric field is a space-charge field, and is therefore derivable from a potential ϕ

$$\vec{E}_1(\vec{r},t) = -\nabla\phi(\vec{r},t) \tag{9.28}$$

and second, the assumption that sinusoidal functions form the basis of the solutions to the linear differential equations. Hence

$$\phi(\vec{r},t) = \tilde{\phi}\, e^{i(\vec{k}\cdot\vec{r}-\omega t)} \tag{9.29}$$

Thus Eq. 9.27 becomes

$$f_{e1}(\vec{r},\vec{v},t) = i\frac{q_e}{m_e}\tilde{\phi}\int_{-\infty}^{t}\vec{k}\cdot\frac{\partial f_o(\vec{v}(t'))}{\partial\vec{v}}e^{i(\vec{k}\cdot\vec{r}(t')-\omega t')}dt' \tag{9.30}$$

9.1.5 The integrand

Integration over the trajectory produces a projection of the gradient (in velocity space) of the distribution function $f_0(\vec{v}(t'))$ at the zeroth order, at time t', over the wave vector $\vec{k}$. $f_0(\vec{v})$ depends only on the modulus of the velocity component perpendicular to the magnetic field (in the moving reference frame), $u_\perp$, and the velocity component parallel to $\vec{B}_0$, v_z. Thus, according to Eq. 9.9,

$$\frac{\partial f_o}{\partial v_x}(t') = -\frac{v_x(t')}{v_{the}^2}f_o(u_\perp,v_z) \tag{9.31}$$

$$\frac{\partial f_o}{\partial v_y}(t') = -\frac{v_y(t')-V_d}{v_{the}^2}f_o(u_\perp,v_z) \tag{9.32}$$

$$\frac{\partial f_o}{\partial v_z}(t') = -\frac{v_z(t')}{v_{the}^2}f_o(u_\perp,v_z) \tag{9.33}$$

Eq. 9.30 may be written by substituting the components of velocity with the velocity definitions from Eq. 9.20 to Eq. 9.21, and the displacement expressions from Eq. 9.24 to Eq. 9.26 into the argument of the exponential. The resulting expression is

$$f_{e1}(\vec{r},\vec{v},t) = -i\frac{q_e}{k_B T_e}\tilde{\phi} f_o(u_\perp, v_z)\int_{-\infty}^{t} dt' \times$$
$$\{k_x u_\perp \cos[\omega_{ce}[t'-t]+\psi] + k_y u_\perp \sin[\omega_{ce}[t'-t]+\psi] + k_z v_z\} \times$$
$$\exp i\{\frac{k_x u_\perp}{\omega_{ce}}[\sin[\omega_{ce}(t'-t)+\psi] - \sin\psi] + k_x x +$$
$$\frac{k_y u_\perp}{\omega_{ce}}[\cos\psi - \cos[\omega_{ce}(t'-t)+\psi]] + k_y V_d(t'-t) + k_y y +$$
$$k_z v_z(t'-t) + k_z z - \omega t'\} \tag{9.34}$$

In the following, polar coordinates $(k_\perp, \theta, k_z)$ are used for the wave vector $\vec{k}$: $k_x = k_\perp \cos\theta$, $k_y = k_\perp \sin\theta$. In Eq. 9.34, it may be observed that the function constituting a projection of velocity on $\vec{k}$, which appears before the exponential, is the time derivative of a part of the function constituting a projection of the position on $\vec{k}$, which appears in the argument of the exponential. Thus, if the function of the position is represented by $g(t)$, then

$$g(t') = i\frac{k_\perp u_\perp}{\omega_{ce}}\{\cos\theta\sin[\omega_{ce}(t'-t)+\psi] - \sin\theta\cos[\omega_{ce}(t'-t)+\psi] + k_z v_z(t'-t)\} \tag{9.35}$$

which may be written

$$g(t') = i\left\{\frac{k_\perp u_\perp}{\omega_{ce}}\sin[\omega_{ce}(t'-t)+\psi-\theta] + k_z v_z(t'-t)\right\} \tag{9.36}$$

Hence

$$f_{e1}(\vec{r},\vec{v},t) = -\frac{q_e}{k_B T_e}\, f_o(u_\perp, v_z)\, \tilde{\phi} e^{i(\vec{k}\cdot\vec{r}-\omega t)} e^{i\frac{k_\perp u_\perp}{\omega_{ce}}\sin(\theta-\psi)} \int_{-\infty}^{t} \frac{\partial g(t')}{\partial t'} e^{g(t')} e^{-i(\omega-\vec{k}\cdot\vec{V}_d)(t'-t)} dt' \tag{9.37}$$

This form of the integrand facilitates an integration by parts.

9.2 The first order electron distribution function

In the coefficient of the integral, an exponential of the form $e^{i(\vec{k}\cdot\vec{r}-\omega t)}$ appears; the function f_1, like the function ϕ, may be written in the form of a plane wave,

$$f_{e1}(\vec{r},\vec{v},t) = \tilde{f}_e\, e^{i(\vec{k}\cdot\vec{r}-\omega t)} \tag{9.38}$$

A change of variable is made in the integrand, $t_1 = t' - t$, and $g_1(t_1) = g(t') = g(t+t_1)$. Consequently, it becomes possible to perform an integration by parts,

$$\tilde{f}_e = -\frac{q_e}{k_B T_e}\, f_o(u_\perp, v_z)\, \tilde{\phi} e^{i\frac{k_\perp u_\perp}{\omega_{ce}} sin(\theta-\psi)} \times$$
$$\left[\left| e^{g_1(t_1) - i(\omega - \vec{k}\cdot\vec{V}_d)t_1} \right|_{-\infty}^{0} + i(\omega - \vec{k}\cdot\vec{V}_d) \int_{-\infty}^{0} e^{g_1(t_1) - i(\omega-\vec{k}\cdot\vec{V}_d)t_1} dt_1 \right] \tag{9.39}$$

Taking into consideration the boundary conditions,

$$g_1(t_1 \to -\infty) \to 0 \tag{9.40}$$

$$g_1(t_1 = 0) = -i\frac{k_\perp u_\perp}{\omega_{ce}} \sin(\theta - \psi) \tag{9.41}$$

The expression for $\tilde{f}_e$ is written as

$$\tilde{f}_e = -\frac{q_e}{k_B T_e} f_o(u_\perp, v_z)\tilde{\phi} \times$$
$$\left[1 + i(\omega - \vec{k}\cdot\vec{V}_d) e^{i\frac{k_\perp u_\perp}{\omega_{ce}} sin(\theta-\psi)} \int_{-\infty}^{0} dt_1 e^{i\frac{k_\perp u_\perp}{\omega_{ce}} \sin(\omega_{ce}t_1 + \psi - \theta) - i(\omega - \vec{k}\cdot\vec{V}_d - k_z v_z)t_1} \right] \tag{9.42}$$

Under this form, the integral of the time-dependent function in $e^{(ic\sin(\omega_{ce}t_1))}$ is not directly calculable. A development using Bessel functions is possible, however, where

$$e^{iz\sin\phi} = \sum_{m=-\infty}^{\infty} e^{im\phi} J_m(z) \tag{9.43}$$

where m is an integer. Using this expression, $\tilde{f}_e$ may be written

$$\tilde{f}_e = -\frac{q_e}{k_B T_e} f_o(u_\perp, v_z)\tilde{\phi} \times \left[1 + (\omega - k_y V_d) e^{i\frac{k_\perp u_\perp}{\omega_{ce}} \sin(\theta-\psi)} \sum_{m}^{\infty} \frac{e^{im(\psi-\theta)} J_m(\frac{k_\perp u_\perp}{\omega_c})}{m\omega_{ce} - \omega + k_y V_d + k_z v_z} \right] \tag{9.44}$$

This equation, with Eq. 9.38, gives the expression for the perturbation of the electron distribution function, at the velocity $\vec{v}(v_\perp, \theta, v_z)$, as a function of time, in the presence of a longitudinal wave characterized by wave vector $\vec{k}(k_\perp, \theta, k_z)$, with a potential of amplitude $\tilde{\phi}$.

In order to facilitate future integrations over the angle Ψ, another expansion using a Bessel function in the form $e^{(ic\sin(\theta-\Psi))}$ is used, such that

$$\tilde{f}_e = -\frac{q_e}{k_B T_e} f_o(u_\perp, v_z)\tilde{\phi} \left[1 + (\omega - k_y V_d) \sum_{l}^{\infty} \sum_{m}^{\infty} \frac{e^{i(m-l)(\psi-\theta)} J_l(\frac{k_\perp u_\perp}{\omega_{ce}}) J_m(\frac{k_\perp u_\perp}{\omega_{ce}})}{m\omega_{ce} - \omega + k_y V_d + k_z v_z} \right] \tag{9.45}$$

This expression is very similar to that obtained by Gary and Sanderson [24] during their development of the dispersion relation for shock waves propagating perpendicular to $\vec{B}$.

9.3 Electron density

9.3.1 Integration of f_1 over velocity components perpendicular to $\vec{B}$

The electron density is obtained via integration over the velocities of the distribution function of Eq. 9.45,

$$\tilde{n}_e = \int_{-\infty}^{+\infty} dv_z \int_0^{\infty} u_\perp du_\perp \int_0^{2\pi} \tilde{f}_e d\psi \tag{9.46}$$

The distribution at the zeroth order is that of Eq. 9.9 with the definition of $u_\perp$ given by Eq. 9.23.

The integration of Eq. 9.46 is first performed over Ψ from 0 to 2π. Due to the cylindrical symmetry of f_0, only the diagonal terms ($l = m$) of the double summation are non-zero,

$$\int_0^{2\pi} \tilde{f}_e d\psi = -\frac{2\pi n_o q_e}{k_B T_e}\ f_o(u_\perp, v_z)\ \tilde{\phi} \left[1 + (\omega - k_y V_d) \sum_m^{\infty} \frac{J_m^2(\frac{k_\perp u_\perp}{\omega_{ce}})}{m\omega_{ce} - \omega + k_y V_d + k_z v_z}\right] \tag{9.47}$$

The next step is the integration over the perpendicular velocity $u_\perp$. The following relation between between Bessel functions of the first type, $J_m(x)$, and the modified Bessel functions $I_n(x)$, is used:

$$\int_0^{\infty} u e^{-\frac{u^2}{2}} J_m^2(xu) du = e^{-x^2} I_m(x^2) \tag{9.48}$$

thus

$$\int_0^{\infty} u_\perp du_\perp \int_0^{2\pi} \tilde{f}_e d\psi = -\frac{n_o q_e}{k_B T_e}\ \tilde{\phi}\ \frac{1}{\sqrt{2\pi} v_{the}} e^{-\frac{v_z^2}{2v_{the}^2}} \times \left[1 + (\omega - k_y V_d) \sum_{m=-\infty}^{+\infty} \frac{e^{-\gamma} I_m(\gamma)}{m\omega_{ce} - \omega + k_y V_d + k_z v_z}\right] \tag{9.49}$$

where the argument γ is a normalization of the perpendicular wave number $k_\perp$ by the mean electron Larmor radius $\rho_{ce} = v_{the}/\omega_{ce}$,

$$\gamma = \left(\frac{k_\perp v_{the}}{\omega_{ce}}\right)^2 \tag{9.50}$$

An equivalent expression may be obtained from Eq. 9.47 and using the identity

$$\sum_{m=-\infty}^{+\infty} J_m^2(x) = 1 \tag{9.51}$$

Thus

$$\int_0^\infty u_\perp du_\perp \int_0^{2\pi} \tilde{f}_e d\psi = -\frac{n_o q_e}{k_B T_e} \tilde{\phi}\, \frac{1}{\sqrt{2\pi} v_{the}} e^{-\frac{v_z^2}{2v_{the}^2}} \sum_{m=-\infty}^{+\infty} \frac{m\omega_{ce} + k_z v_z}{m\omega_{ce} - \omega + k_y V_d + k_z v_z} e^{-\gamma} I_m(\gamma) \tag{9.52}$$

9.3.2 Expansions and developments in the limit of zero magnetic field

When the intensity of the magnetic field tends towards zero, it should be possible to find the expression corresponding to the electron response in an unmagnetized plasma. It may also be desirable to obtain a development of this response at higher orders of B.

Some properties of modified Bessel functions

Before we proceed with the expansion, some properties of Bessel functions useful for the analysis, taken from the handbook by Abramowitz and Stegun [1], are given below.

When B tends toward zero, the argument γ of functions I_m diverge as B^{-2}. It is therefore worth noting the asymptotic expansion of the modified Bessel function,

$$I_m(z) \approx \frac{e^z}{\sqrt{2\pi z}} \left[1 - \frac{4m^2 - 1}{8z} + O\left(\frac{1}{z^2}\right) \right] \tag{9.53}$$

i.e.

$$e^{-\gamma} I_m(\gamma) \approx (2\pi)^{-1/2} \frac{\omega_c e}{k_\perp v_{the}} \left[1 - \frac{4m^2 - 1}{8} (\frac{\omega_c e}{k_\perp v_{the}})^2 + ... \right] \tag{9.54}$$

The following other properties of modified Bessel functions and their sums will prove useful,

$$I_{-m}(z) = I_m(z) \tag{9.55}$$

$$e^{-z} \sum_{m=-\infty}^{+\infty} I_m(z) = 1 \tag{9.56}$$

$$e^{-z} \sum_{m=-\infty}^{+\infty} m I_m(z) = 0 \tag{9.57}$$

$$e^{-z} \sum_{m=-\infty}^{+\infty} m^2 I_m(z) = 1 + z \tag{9.58}$$

where z is real and m is an integer, and hence $I_m(z) \geq 0$.

The parity of modified Bessel functions with respect to their index m allows the summation over the second member of Eq. 9.52 to be rewritten,

$$\sum_{m=-\infty}^{+\infty} \frac{m\omega_{ce} + k_z v_z}{m\omega_{ce} - \omega + k_y V_d + k_z v_z} e^{-\gamma} I_m(\gamma) =$$

$$\frac{k_z v_z}{k_z v_z + k_y V_d - \omega}\, e^{-\gamma} I_0(\gamma) + 2 \sum_{m=1}^{+\infty} \frac{k_z v_z (k_z v_z + k_y V_d - \omega) - m^2 \omega_{ce}^2}{(k_y V_d + k_z v_z - \omega)^2 - m^2 \omega_{ce}^2}\, e^{-\gamma} I_m(\gamma) \tag{9.59}$$

The limit $B \to 0$ with a constant drift velocity

In the limit $B \to 0$, it is necessary to define what becomes of the drift velocity $V_d = E_0/B$. If the electric field is left constant, V_d diverges as B^{-1} and the situation tends towards a non-magnetized plasma, but with an infinite drift velocity, which is not the boundary condition we would expect to obtain. The assumption will therefore be made that E_0 tends towards zero at the same time as B, maintaining a constant drift velocity.

In this case, the summation of the second member of Eq. 9.52 is

$$\sum_{m=-\infty}^{+\infty} \frac{m\omega_{ce} + k_z v_z}{m\omega_{ce} - \omega + k_y V_d + k_z v_z} e^{-\gamma} I_m(\gamma) \to$$

$$\frac{k_z v_z}{k_y V_d + k_z v_z - \omega} \sum_{m=-\infty}^{+\infty} e^{-\gamma} I_m(\gamma) = \frac{k_z v_z}{k_y V_d + k_z v_z - \omega} \tag{9.60}$$

We obtain exactly the expected response in the absence of a magnetic field, with a drift velocity.

9.3.3 Integration over velocities parallel to $\vec{B}$

To obtain the electron density from the function f_1 (Eq. 9.46), all that remains is the integration of the velocities v_z parallel to B,

$$\tilde{n}_e = \int_{-\infty}^{\infty} dv_z \int_0^{\infty} du_\perp u_\perp \int_0^{2\pi} d\psi \tilde{f}_e =$$

$$-\frac{n_o q_e}{k_B T_e}\, \tilde{\phi}\, e^{-\gamma} \sum_{m=-\infty}^{+\infty} I_m(\gamma) \int_{-\infty}^{\infty} \frac{dv_z}{\sqrt{2\pi} v_{the}} \frac{m\omega_{ce} + k_z v_z}{m\omega_{ce} - \omega + k_y V_d + k_z v_z} e^{-\frac{v_z^2}{2v_{the}^2}} \tag{9.61}$$

A normalised variable ζ_m is defined for the frequency ω,

$$\zeta_m = \frac{\omega - k_y V_d - m\omega_{ce}}{k_z v_{the}\sqrt{2}} \tag{9.62}$$

and a variable ξ for the velocity v_z

$$\xi = \frac{v_z}{v_{the}\sqrt{2}} \tag{9.63}$$

from which

$$\frac{m\omega_{ce} + k_z v_z}{m\omega_{ce} - \omega + k_y V_d + k_z v_z} = 1 + \frac{\omega - k_y V_d}{k_z v_{the}\sqrt{2}} \frac{1}{\xi - \zeta_m} \tag{9.64}$$

The plasma dispersion function will be used,

$$Z(\zeta) = \frac{1}{\sqrt{\pi}} \int_{-\infty}^{\infty} d\xi \frac{e^{-\xi^2}}{\xi - \zeta} \tag{9.65}$$

With these definitions and the property from Eq. 9.56, Eq. 9.61 becomes

$$\tilde{n}_e = -\frac{n_o q_e}{k_B T_e} \tilde{\phi} \left[1 + \frac{\omega - k_y V_d}{k_z v_{the}\sqrt{2}} e^{-\gamma} \sum_{m=-\infty}^{+\infty} Z(\zeta_m) I_m(\gamma) \right] \tag{9.66}$$

This form may also be used to write the longitudinal electron susceptibility,

$$\chi_{e//} = \frac{1}{k^2} \vec{k} \cdot \overline{\overline{\chi}}_e \cdot \vec{k} = -\frac{q_e}{\epsilon_o k^2} \frac{\tilde{n}_e}{\tilde{\phi}} \tag{9.67}$$

or

$$\chi_{e//} = \frac{1}{k^2 \lambda_D^2} \left[1 + \frac{\omega - k_y V_d}{k_z v_{the}\sqrt{2}} e^{-\gamma} \sum_{m=-\infty}^{+\infty} Z(\zeta_m) I_m(\gamma) \right] \tag{9.68}$$

where λ_D is the Debye length,

$$\lambda_D = \sqrt{\frac{\epsilon_o k_B T_e}{n_o q_e^2}} \tag{9.69}$$

For the case of propagation purely perpendicular to B, the parallel wave vector is zero ($k_z = 0$). Eq. 9.61 and the symmetry of the terms $-m$ and $+m$ of the summation are used to obtain

$$\tilde{n}_e(k_z = 0) = -2 \frac{n_o q_e}{k_B T_e} \tilde{\phi}\, e^{-\gamma} \sum_{m=1}^{\infty} I_m(\gamma) \frac{m^2}{(\frac{\omega - k_y V_d}{\omega_{ce}})^2 - m^2} \tag{9.70}$$

This expression shows the electron cyclotron resonances with each of the harmonics of ω_{ce}, shifted by a frequency $-k_y V_d$.

It should be noted that the function $Z(\zeta)$ takes values around $\zeta \approx 0$ in an interval $\Delta\zeta \approx 1$, outside of which the function decreases as ζ^{-1}.

The argument ζ_m is close to zero if $\omega \approx k_z V_d + m\omega_{ce}$. The frequency width of the Z function is $\Delta\omega \approx k_z v_{the}$. When the direction of propagation becomes close to perpendicular to B, the frequency width $\Delta\omega$ tends to zero. It is useful to compare this width to the separation ω_{ce} between two cyclotron resonances: if $k_z v_{the} < \omega_{ce}$, the successive resonances at frequencies $\omega - k_z V_d = m\omega_{ce}$ are very distinct. If, in addition, this $\Delta\omega$ interval is on the same order as the ion plasma frequency, a large ion response is expected, of the ion acoustic wave

type. This is the case for cyclotron waves in the thruster: each physical condition corresponds to a different series development of Eq. 9.66 or Eq. 9.68.

9.4 The ion density

The intensity of the magnetic field in the thruster is such that the electron Larmor radius is very small, while that of the ions is large in comparison with the thruster size. For this reason, the ion dynamics are described using kinetic theory in the absence of a magnetic field. The field $\vec{E}_0$ accelerates ions along the axis Ox. The zeroth order Vlasov equation must take into account a velocity which depends on the x position. This spatial variation complicates the solution.

Taking into account the fact that the acceleration zone is short (on the order of 1 cm), the equation will not be solved in this region, but in the region immediately downstream. We will therefore assume that the ions move with a uniform velocity $\vec{v}_p$ and parallel to Ox. The evolution of the corresponding distribution function is dictated by the linearized Vlasov equation. The longitudinal ion susceptibility is therefore

$$\chi_{i//} = -\frac{1}{2k^2\lambda_{Di^2}} Z'(\frac{\omega - k_x v_p}{k v_{thi}}) \tag{9.71}$$

where

$$\lambda_{Di} = \sqrt{\frac{\epsilon_o k_B T_i}{n_{oi} q_i^2}} \tag{9.72}$$

and $Z'(z)$ is the derivative of the plasma dispersion function. λ_{Di}, v_{thi} and n_{0i} are the ion Debye length, ion thermal velocity and the ion density respectively.

9.5 The dispersion relation

The dispersion is obtained when the total space charge density

$$\rho = \tilde{n}_e q_e + \tilde{n}_i q_i \tag{9.73}$$

satisfies Poisson's equation, $k^2\tilde{\phi} = \rho/\epsilon_o$. Since $\tilde{n_e}$ and $\tilde{n_i}$ were obtained as a function of the potential $\tilde{\phi}$, the necessary condition between the wave vector and frequency is obtained. This condition is written

$$1 + \chi_{e//} + \chi_{i//} = 0 \tag{9.74}$$

That is,

$$1 + \frac{1}{k^2\lambda_D^2}\left[1 + \frac{\omega - k_y V_d}{k_z v_{the}\sqrt{2}}\, e^{-\gamma} \sum_{m=-\infty}^{+\infty} Z(\zeta_m) I_m(\gamma)\right] - \frac{1}{2k^2\lambda_{Di}^2} Z'(\frac{\omega - k_x v_p}{k v_{thi}}) = 0 \tag{9.75}$$

where ζ_m and γ are as previously defined.

9.6 Discussion

A comparison may be made between the dispersion relation developed by Adam et. al. [2] and whose solutions were discussed in Chapter 3 and Chapter 7, and the dispersion relation developed here.

The dispersion relations are similar in all respects, save for the inclusion of an ion kinetic susceptibility and ion beam velocity v_p in our description, which differs from a treatment of ions as cold and immobile. This is the source of the last term in Eq. 9.75.

Because the ions originate from different positions within the channel, the longitudinal dispersion of their velocities is large. Since, in addition, the angular opening of the ion beam is large, the transverse dispersion of ion velocities is also large. This results in an equivalent large-temperature ion population which might induce significant changes in the instability growth rate and instability threshold. Such an investigation of Eq. 9.75 will be completed in future work.

Reflections

Experimental diagnostics provide key information on ion and electron behaviour in the thruster, and are indispensable for understanding phenomena such as anomalous transport. They provide a means of improving thruster modelling efforts and identifying the ideal regimes of thruster operation. There is a need for novel diagnostics which could provide complementary information to that obtained via conventional probe methods. This work represents the first application of a collective light scattering diagnostic for the study of high frequency plasma oscillations in the Hall thruster.

The initial goals of this work were to demonstrate experimentally the presence of millimetric, MHz oscillations at the thruster exit which were predicted to have a role in anomalous electron transport. The observation of such a class of oscillations is beyond the reach of conventional diagnostics, and validation of linear kinetic theory required a completely different approach. A high-performance collective scattering diagnostic, PRAXIS-I, was designed, built and tested for thruster studies in 2008 and provided convincing experimental evidence that the predictions from linear kinetic theory had validity. Two different MHz-frequency modes were identified at the thruster exit: an azimuthally-propagating mode with the predicted general characteristics, and a new, axially-propagating mode. Some interesting differences with theory, such as continuous dispersion relations, were also observed.

Based on the initial collective scattering results, a second phase of experiments was performed in 2009 with an upgraded optical bench, PRAXIS-II. The new bench enabled a number of new investigations of the previously identified modes. In particular, localizations of the modes and fine determinations of their directionality were performed. The azimuthal mode was discovered to propagate in three dimensions with an angular opening of only a few degrees, while the axially propagating mode was discovered to have an angular opening on the order of the beam divergence angle. These new directionality experiments not only provided new information on the features of the azimuthal mode, but also provided the impetus for a re-evaluation of the three-dimensional theoretical dispersion relation. It was discovered that the inclusion of a wave vector component parallel to the magnetic field was sufficient to resolve many remaining key differences between linear kinetic theory and experiments.

Despite the quantity of new information and characterizations which have been made available by these experiments, more interesting work remains to be done. From the theoretical standpoint, solutions to the three-dimensional dispersion relation which incorporate the ion velocity and temperature must be obtained. Is it possible to account for features such as the directionality of the azimuthal mode by taking into account the ion dynamics and

damping effects? This modified dispersion relation could provide a better description of the azimuthal mode. In addition, plasma non-uniformities in the radial direction, which have been neglected here for simplicity, must be added to future models. It also remains to be seen whether the azimuthal mode can play a role in thruster erosion, particularly given its length scales and directionality.

From the experimental standpoint, the investigations carried out on PRAXIS-II have provided strong reasons to expand studies of the axially-propagating mode. The next stage of experiments will attempt to increase the experimental frequency and wave number ranges for this mode, and study more closely its link to the azimuthal mode and to the ion beam velocity and velocity dispersion. Finally, work on quantifying anomalous electron transport and electron axial velocities is to be pursued.

Appendix A

Laser profilometry procedures

Laser profilometry has proven to be an indispensable tool for determining the beam quality during various stages of the optical bench construction:

- Initial laser testing: profilometry was necessary to determine the M^2 value of the new laser, a value which was stated to be typically < 1.1 by the manufacturer. In fact, the M^2 value was determined to be 1.2, necessitating important modifications to the initial bench design.
- Determining diffraction reduction: the ceramic tube installed on the path of the laser beam on PRAXIS-II was intended to absorb the long tails of the laser beam which contributed to excess diffraction. Profilometry was performed on the beam after the tube to determine the effectiveness of this installation and determine an exact positioning for the tube.
- Measurement of beam waist: a typical profilometry procedure involves the measurement of the laser beam waist at various locations, such as in the convergence zone in front of the thruster, and at locations where the beam size must be restricted (at the translator-rotator, acousto-optical deflector, etc.)

A.1 Approaches to profilometry

Two main approaches to profilometry were adopted:

- The scanning slit method: this method employs a BeamScan instrument (model 1180-FIR) from Photon Inc. This device uses a slit mounted on a spinning drum head. The laser beam is positioned to be incident on the window and the slit, and the radiation is transmitted to a detector. The magnitude of the transmitted signal is proportional to the laser power and this is used to generate a beam profile. The advantage of this device is that it may be used on the high power initial laser beam (about 40 W) without the necessity for attenuation; the small slit size (18 μm by 9 mm) allows in only a fraction of the total incident power. It is also relatively simple and requires only an

oscilloscope to record the calibrated profile. There are some important disadvantages: the window diameter being only 9 mm, the device could not be used to measure beam waists exceeding 2.25 mm. In addition to this, the profiles are somewhat noisy and the measurement of long laser tails responsible for diffraction impossible. For these reasons, this device was used only in certain limited situations.

- The mobile pyroelectric: this device was set up in the laboratory. It consists of a pyroelectric detector mounted on a potentiometer which translates it across the incident beam in a controlled fashion. The voltage output from both the detector is proportional to the laser power. The advantages of this technique are significant: profilometry of virtually any beam size is possible. The disadvantages are that the beam requires significant attenuation from its initial power (by a factor of a 1000), and several additional devices are required (beam chopper, synchronous detector, power supply, oscilloscope, potentiometer). Despite these disadvantages and complexity, this was the preferred method for determining the beam waists and the presence of tails. Its installation will be described in this appendix.

A.2 The mobile pyroelectric method

The pyroelectric detector has an exposed surface which is limited to a diameter of 0.25 mm by a pinhole placed in front of it, and generally accepts incident power on the order of tens of mW. The initial beam is attenuated by three orders of magnitude using a combination of beam-splitters. The pyroelectric is moved in two directions: along y using a potentiometer (Fig. A.1) controlled by stepper motor, and along z using a vernier adjusted manually in 0.5 mm steps. The profiles generated are therefore in the form of slices.

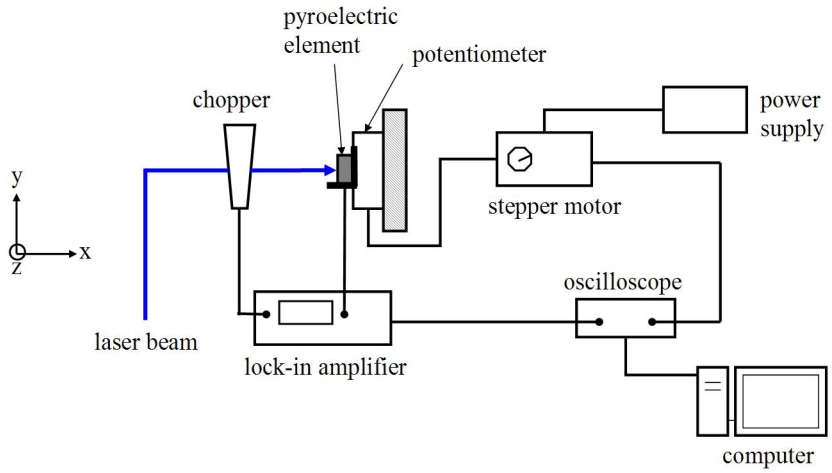

Figure A.1: Setup for the measurement of laser beam profile

In order to follow the small variations in signal intensity as the detector traverses the beam, it is necessary to use a synchronous detector, or lock-in amplifier (EG & G Princeton

Applied Research, Model 5208). The incident beam is sampled at a low frequency (about 1 kHz) using a chopper placed in the beam path, which is connected to the lock-in amplifier and serves as the source of the reference signal. The second input to the lock-in amplifier is the pyroelectric signal itself (a voltage). The lock-in amplifier multiplies the reference and pyroelectric signal, allowing the phase and amplitude of the pyroelectric signal to be obtained after filtering.

The phase of the chopper reference signal is adjusted such that it is matched to the pyroelectric signal; this is necessary for the amplitude of the output signal to be proportional to the pyroelectric signal. To do this, the detector is first moved in y and z to a position which maximizes the output signal, at a random phase, which shall be called p_1. The phase is then changed to $p_2 = p_1 + 90°$. The phase is then finely adjusted around this value such that the signal falls to zero, to a value p_3. Once this signal level is obtained, the phase is changed to $p_3 - 90°$, which should correspond to the value for which the chopper and pyroelectric signals are phase-matched.

The signal is now sent to an oscilloscope, along with the voltage signal from the potentiometer, the latter signal serving to calibrate the displacement through which the pyroelectric moves as it scans the beam.

The result of a profilometry experiment is shown in Fig. A.2.

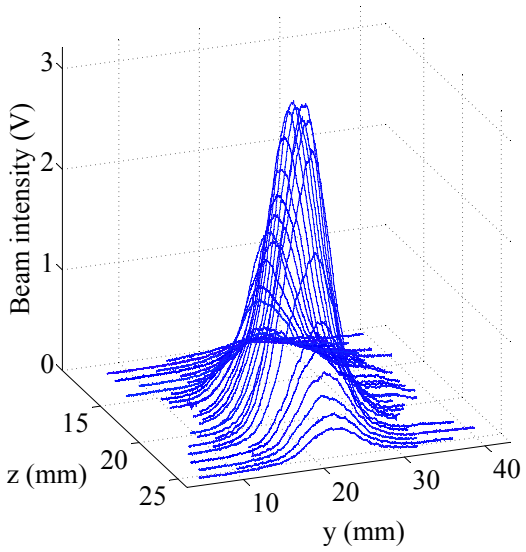

Figure A.2: Reconstitution of laser beam profile; the low noise of the profiles obtained is notable

This profilometry procedure has been used to identify the presence of tails in the laser beam and other irregularities in its profile, and to measure the beam waist at various locations.

A.3 Determination of the M^2 value

Profilometry using the pyroelectric detector has been essential to determining the laser beam quality factor, M^2, which provides a measure of the beam divergence and must be taken into account during the planning of any optical bench. The M^2 value is defined as the ratio of the beam parameter product (BPP) of the laser beam and the BPP of the laser's fundamental transverse mode, identified as TEM_{00}. The beam parameter product is defined as the product of the minimum beam diameter and the beam divergence.

The beam divergence can be determined from a far-field measurement of different beam waists. This cannot be done directly on the initial beam exiting the laser for two reasons: firstly, because the minimum beam waist is located inside the cavity and inaccessible, and secondly, because such a measurement would require determining beam waists over a distance of several metres in order to be accurate.

Instead, an artificial minimum beam waist is constructed using a lens placed at some distance from the laser exit, after the beam has been sufficiently attenuated. The measurements of beam waist are then made in the regions around and far from the minimum beam waist.

In the present example, the separation used between the laser exit and the lens is 1300 mm. It is desirable to to reduce the length of the measurement region necessary by choosing a lens of short focal length. On the other hand, short focal lengths lead to smaller minimum beam waists which are likely to saturate the detector. The lens focal length is 508 mm in the present case and represents a good compromise between these considerations.

Several beam profiles are recorded and fitted to a Gaussian of the form

$$I = I_0 e^{\frac{-(y-\mu)^2}{2w^2}} \tag{A.1}$$

where I_0 is the signal amplitude, y the vertical position of the pyroelectric detector, μ the mean position and w the beam waist. All these parameters are optimized for the best Gaussian fit. A typical profile is shown in Fig. A.3.

The optimized values w for all distances from the lens are determined and plotted as shown in Fig. A.4. These waists are fitted to a curve of the theoretical form for the beam expansion, a hyperbola of the form

$$w(z) = w_0 \sqrt{1 + \left(\frac{z - z_0}{e_R}\right)^2} \tag{A.2}$$

The parameters of the optimized fit - w_0, z_0 and e_R - are determined. In the present example, w_0 is 0.5568 mm, z_0 is 710 mm and e_R 65.31 mm. w_0 represents the minimum beam waist, z_0 the location parameter and e_R the Rayleigh length - the distance from w_0 over which the waist increases to $\sqrt{2}w_0$.

The M^2 value may now be determined.

The M^2 value is calculated as the ratio between the experimentally-determined beam divergence and the theoretical divergence of a perfect Gaussian beam (of M^2 value of 1).

The theoretical divergence is

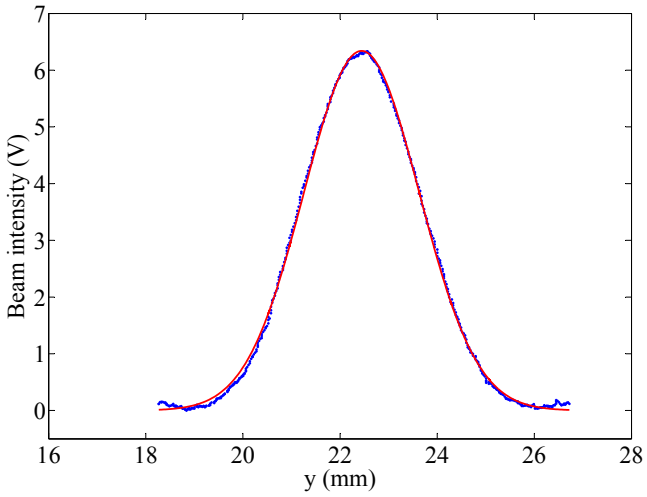

Figure A.3: Beam profile at 267 mm from lens (experimental points in blue, Gaussian fit in red)

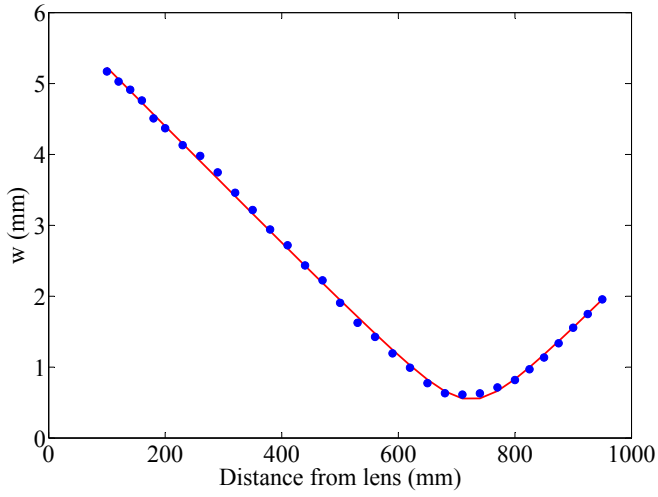

Figure A.4: Beam waists at different distances from the lens

$$\tan(\theta_t) = \frac{\lambda}{\pi w_0} \tag{A.3}$$

where λ is the laser wavelength. $\tan(\theta_t)$ is 6.058×10^{-3}.

The experimental divergence is

$$\tan(\theta_e) = \lim_{z \to \infty} \frac{w - w_0}{z - z_0} = \frac{w_0}{e_R} \tag{A.4}$$

i.e. a value determined in the far-field region, hence the necessity for measures at a large distance from the minimum waist, well beyond the Rayleigh length. The resulting value of $\tan(\theta_e)$ is 8.525×10^{-3}.

The "intermediate" M^2 (subject to a correction) is obtained from

$$M^2 = \frac{\tan(\theta_e)}{\tan(\theta_t)} \tag{A.5}$$

This value is 1.407.

This must be corrected by the size of the pinhole in front of the detector; this pinhole has a diameter of 0.25 mm, compared to the minimum waist of 0.5568 mm, which leads to an overestimation of the waist because of the low resolution. The intermediate M^2 is therefore corrected using a convolution of an "equivalent" Gaussian window based on the pinhole diameter, and the Gaussian beam.

The resulting equivalent waist of pinhole, w_d, is 0.2 mm. The relation between the measured waist w_0 and the corrected waist, w_t, is

$$w_t = w_m \sqrt{1 + \left(\frac{w_d}{w_m}\right)^2} \tag{A.6}$$

The corrected minimum waist 0.520 mm.

Finally, M^2 is deduced from

$$M^2 = \frac{\pi {w_t}^2}{\lambda e_R} \tag{A.7}$$

The value of M^2 in this case is 1.2; this value was applied to the design of PRAXIS-I.

Appendix B

Detector efficiency

The detector used during the experiments is an HgCdTe semiconductor material of area 200 μm^2, sensitive to wavelengths from 8 to 12 μm. It requires liquid nitrogen cooling to lower the inherent thermal noise, which is significant at room temperatures. The quantum efficiency of the detector is one factor in the determination of the absolute signal magnitude and is defined as the ratio of the number of photons which effectively contribute to the measured current, to the total number of photons incident on the detector surface. The detector efficiency is precisely determined and used to determine the signal level.

The detector is rated for a few milliwatts of incident power, and during experiments, this power is kept below 3 mW. This also prevents saturation of the pre-amplifier.

The incident beam power is first attenuated to an acceptable level, and its level is measured at 0.17 mW, using a calorimeter.

The number of incident photons N corresponding to this incident power, P, is

$$N = \frac{P}{h\nu} \tag{B.1}$$

where h is Planck's constant, and ν = 2.83$\times$10^{13} Hz. N is 9.07$\times$10^{15}.

If the detector efficiency is 1, then all the incident photons contribute to the measured current, giving rise to a maximum possible current defined as

$$I_{max} = eN(\eta) \tag{B.2}$$

where e is the electronic charge, and η the detector efficiency. The maximum current expected for this incident power is 1.45 mA.

The actual current, I_m, measured by the detector itself is 0.9 mA. The detector efficiency is then

$$\frac{I_m}{I_{max}} = 0.62 \tag{B.3}$$

This value is applied during calculations of the form factor.

Bibliography

[1] M. Abramowitz and I. A. Stegun. *Handbook of Mathematical Functions with Formulas, Graphs, and Mathematical Tables*. Dover Publications, Inc., 1964.

[2] J. C. Adam, A. Héron, and G. Laval. Study of stationary plasma thrusters using two-dimensional fully kinetic simulations. *Phys. Plasmas*, 11(1), 2004.

[3] D. A. Alman, J. L. Rovey, R. A. Stubbers, and B. E. Jurczyc. Hall thruster electron mobility investigation using full 3D Monte Carlo trajectory simulations. In *30th International Electric Propulsion Conference, Florence, Italy, Sept. 17-20*, 2007.

[4] V. I. Baranov, Yu. S. Nazarenko, V. A. Petrosov, A. I. Vasin, and Yu. M. Yashnov. The mechanism of anomalous erosion in accelerators with closed drift of electrons. In *24th International Electric Propulsion Conference, Moscow, Russia, IEPC-95-43*, 1995.

[5] J. Bareilles. *Modélisation 2D hybride d'un propulseur à effet Hall pour satellites*. PhD thesis, Université Paul Sabatier, Toulouse, 2002.

[6] E. J. Beiting, J. E. Pollard, V. Khayms, and L. Werthman. Electromagnetic emissions to 60 GHz from a BPT-4000 EDM Hall thruster. In *28th International Electric Propulsion Conference, 17-21 March 2003, Toulouse, France (IEPC-03-129)*, 2003.

[7] A. M. Bishaev and V. Kim. Local plasma properties in a Hall-current accelerator with an extended acceleration zone. *Sov. Phys. Tech. Phys.*, 23(9), 1978.

[8] J. P. Boeuf and L. Garrigues. Low frequency oscillations in a stationary plasma thruster. *J. Appl. Phys.*, 84(7), 1998.

[9] J. P. Bonnet, D. Grésillon, B. Cabrit, and V. Frolov. Collective light scattering as non-particle laser velocimetry. *Meas. Sci. Technol.*, 6:620–636, 1995.

[10] A. I. Bugrova, A. V. Desyatskov, and A. I. Morozov. Electron distribution function in a Hall accelerator. *Sov. J. Plasma Phys.*, 18(8), 1992.

[11] B. Cabrit. *Diffusion collective de la lumière par un gaz turbulent: dispersion moléculaire et turbulente*. PhD thesis, Université Paris VI, 1992.

[12] F. F. Chen. *Introduction to plasma physics and controlled fusion*. Plenum Press, New York and London, 1984.

[13] E. Chesta, N. B. Meezan, and M. A. Cappelli. Stability of a magnetized Hall plasma discharge. *J. Appl. Phys.*, 89(6), 2001.

[14] E. Y. Choueiri. Plasma oscillations in Hall thrusters. *Phys. Plasmas*, 8(4), 2001.

[15] F. Darnon, L. Garrigues, J. P. Boeuf, A. Bouchoule, and M. Lyszyk. Spontaneous oscillations in a Hall thruster. *IEEE Transactions on Plasma Science*, 27(1), February 1999.

[16] P. Devynck, X. Garbet, Ph. Ghendrih, J. Gunn, C. Honoré, B. Pégourié, G. Antar, A. Azeroual, P. Beyer, C. Boucher, V. Budaev, H. Capes, F. Gervais, P. Hennequin, T. Loarer, A. Quéméneur, A. Truc, and J.C. Vallet. Edge turbulence during ergodic divertor operation in Tore supra. *Nucl. Fusion*, 42:697–707, 2002.

[17] A. Ducrocq. *Rôle des instabilités électroniques de dérive dans le transport électronique du propulseur à effet Hall*. PhD thesis, Ecole Polytechnique, 2006.

[18] A. Ducrocq, J. C. Adam, A. Héron, and G. Laval. High frequency electron drift instability in the cross-field configuration of Hall thrusters. *Phys. Plasmas*, 13:102111, 2006.

[19] A. Dunaevsky, Y. Raitses, and N. J. Fisch. Secondary electron emission from dielectric materials of a Hall thruster with segmented electrodes. *Phys. Plasmas*, 10(6), 2003.

[20] Yu. B. Esipchuk, A. I. Morozov, G. N. Tilinin, and A. V. Trofimov. Plasma oscillations in closed-drift accelerators with an extended acceleration zone. *Sov. Phys. Tech. Phys.*, 18(7), 1974.

[21] Yu. V. Esipchuk and G. N. Tilinin. Drift instability in a Hall-current plasma accelerator. *Sov. Phys. Tech. Phys.*, 21(4), 1976.

[22] J. M. Fife. *Hybrid-PIC modeling and electrostatic probe survey of Hall thrusters*. PhD thesis, Massachusetts Institute of Technology, 1998.

[23] L. Garrigues, G. J. M. Hagelaar, C. Boniface, and J.-P. Boeuf. Anomalous conductivity and secondary electron emission in Hall effect thrusters. *J. Appl. Phys.*, 100(123301), 2006.

[24] S. P. Gary and J. J. Sanderson. Longitudinal waves in a perpendicular collisionless plasma shock. i. Cold ions. *J. Plasma Phys.*, 4:739–751, 1970.

[25] N. Gascon, M. Dudeck, and S. Barral. Wall material effects in stationary plasma thrusters. i. parametric studies of an SPT-100. *Phys. Plasmas*, 10:4123, 2003.

[26] D. Gawron. *Phénomès de transport ionique dans le plasma d'un propulseur à effet Hall à forte puissance: étude par spectroscopie laser*. PhD thesis, Université d'Orléans, 2007.

[27] D. M. Goebel and I. Katz. *Fundamentals of Electric Propulsion: Ion and Hall Thrusters*. Jet Propulsion Laboratory, California Institute of Technology, 2008.

[28] R. J. Goldstein and W. F. Hagen. Turbulent flow measurements utilizing the Doppler shift of scattered radiation. *Phys. Fluids*, 10:1349–1352, 1967.

[29] D. Grésillon, C. Stern, A. Hémon, A. Truc, T. Lehner, J. Olivain, A. Quémeneur, F. Gervais, and Y. Lapierre. Density fluctuation measurement by far infrared light scattering. *Phys. Scr.*, T2/2:459–466, 1982.

[30] T. J. Greytak and G. B. Benedek. Spectrum of light scattered from thermal fluctuations in gases. *Phys. Rev. Lett.*, 17(4), 1966.

[31] A. Guthrie and R. K. Wakerling, editors. *The Characteristics of Electrical Discharges in Magnetic Fields*. McGraw-Hill Book Company, Inc., 1949.

[32] G. J. M. Hagelaar, J. Bareilles, L. Garrigues, and J. P. Boeuf. Two-dimensional model of a stationary plasma thruster. *J. Appl. Phys.*, 91(9), 2002.

[33] P. Hennequin, R. Sabot, C. Honoré, G. T. Hoang, X. Garbet, A. Truc, C. Fenzi, and A. Quéméneur. Scaling laws of density fluctuations at high-k on Tore Supra. *Plasma Phys. Control. Fusion*, 46:B121–B133, 2004.

[34] M. Hirakawa and Y. Arakawa. Numerical simulation of plasma particle behavior in a Hall thruster. In *32nd AIAA/ASME/SAE/ASEE Joint Propulsion Conference*, Lake Buena Vista, FL, July 1-3 1996.

[35] E. Holzhauer and J. H. Massig. An analysis of optical mixing in plasma scattering experiments. *Plasma Phys.*, 20(9), 1978.

[36] G. S. Janes and R. S. Lowder. Anomalous electron diffusion and ion acceleration in a low-density plasma. *Phys. Fluids*, 9(6), 1966.

[37] C. F. F. Karney. Stochastic ion heating by a lower hybrid wave. *Phys. Fluids*, 21(9), 1978.

[38] M. Keidar and I. D. Boyd. On the magnetic mirror effect in Hall thrusters. *Appl. Phys. Lett.*, 87:121501, 2005.

[39] A. Knoll, N. Gascon, and M. Cappelli. Numerical simulation of high frequency wave coupling within a Hall thruster. In *43rd AIAA/ASME/SAE/ASEE Joint Propulsion Conference and Exhibit, 8-11 July 2007, Cincinnati, OH (AIAA 2007-5266)*, 2004.

[40] H. Koizumi, K. Komurasaki, and Y. Arakawa. Numerical prediction of wall erosion on a Hall thruster. *Vacuum*, 83:67–71, 2009.

[41] J. W. Koo and I. D. Boyd. Computational model of a Hall thruster. *Computer Physics Communications*, 164:442–447, 2004.

[42] J. W. Koo and I. D. Boyd. Modeling of anomalous electron mobility in Hall thrusters. *Phys. Plasmas*, 13:033501, 2006.

[43] P. Lasgorceix, C. Perot, and M. Dudeck. PIVOINE ground test facility for ion thruster testing. In *Proc. Second European Spacecraft Propulsion Conference, 27-29 May*, 1997.

[44] A. Lazurenko, L. Albarède, and A. Bouchoule. Physical characterization of high-frequency instabilities in Hall thrusters. *Phys. Plasmas*, 13:083503, 2006.

[45] A. Lazurenko, G. Coduti, S. Mazouffre, and G. Bonhomme. Dispersion relation of high-frequency plasma oscillations in Hall thrusters. *Phys. Plasmas*, 15:034502, 2008.

[46] A. Lazurenko, T. Dudok de Wit, C. Cavoit, V. Krasnoselskikh, A. Bouchoule, and M. Dudeck. Determination of the electron anomalous mobility through measurements of turbulent magnetic field in Hall thrusters. *Phys. Plasmas*, 14:033504, 2007.

[47] A. Lazurenko, V. Vial, M. Prioul, and A. Bouchoule. Experimental investigation of high-frequency drifting perturbations in Hall thrusters. *Phys. Plasmas*, 12:013501, 2005.

[48] N. Lemoine. *Transport turbulent d'un plasma à travers un champ magnétique: observation par diffusion collective de la lumière*. PhD thesis, Ecole Polytechnique, 2005.

[49] A. A. Litvak and N. J. Fisch. Rayleigh instability in Hall thrusters. *Phys. Plasmas*, 11(4), 2004.

[50] A. A. Litvak, Y. Raitses, and N. J. Fisch. Experimental studies of high-frequency azimuthal drift waves in Hall thrusters. *Phys. Plasmas*, 11(4), 2004.

[51] A. I. Morozov. Conditions for efficient current transport by near-wall conduction. *Sov. Phys. Tech. Phys.*, 32(8), 1987.

[52] A. I. Morozov and V. V. Savel'ev. Theory of the near-wall conductivity. *Plasma Phys. Rep.*, 27(7):570–575, 2001.

[53] A. I. Morozov and V. V. Savelyev. The electron dynamics in SPT-channel and the problem of anomalous erosion. In *24th International Electric Propulsion Conference, Moscow, Russia, IEPC-95-42*, 1995.

[54] A. I. Morozov and V. V. Savelyev. *Fundamentals of Stationary Plasma Thruster Theory*, volume 21 of *Reviews of Plasma Physics*. Kluwer Academic/Plenum Publishers, 2000.

[55] M. Nelkin and S. Yip. Brillouin scattering by gases as a test of the Boltzmann equation. *Phys. Fluids*, 9(2), 1966.

[56] J. Pérez-Luna, G. J. M. Hagelaar, L. Garrigues, N. Dubuit, and J. P. Boeuf. Influence of azimuthal instabilities on electron motion in a Hall effect thruster. In *30th International Electric Propulsion Conference, 17-20 September 2007, Florence, Italy (IEPC-2007-124)*, 2007.

[57] M. Prioul. *Etude expérimentale des propulseurs de type Hall: processus collisionels, comportement dynamique, micro-instabilités et phénomènes de transport*. PhD thesis, Université d'Orléans, 2002.

[58] A. W. Smith and M. A. Cappelli. Investigation of field structure and electron behavior in the near-field of Hall thrusters. In *42rd AIAA/ASME/SAE/ASEE Joint Propulsion Conference and Exhibit, 9-12 July 2006, Sacramento, CA (AIAA 2006-4835)*, 2006.

[59] C. Stern-Forgach. *Diffusion Rayleigh et détection hétérodyne optique. Application aux fluctuations atmosphériques*. PhD thesis, Université Paris 11, 1981.

[60] C. A. Thomas, N. Gascon, and M. A. Cappelli. A study of the azimuthal electron drift in an ExB discharge using a non-invasive antenna array. In *39th AIAA/ASME/SAE/ASEE Joint Propulsion Conference and Exhibit, 20-23 July 2003, Huntsville, AL (AIAA 2003-4854)*, 2003.

[61] B. Tomchuk. *Diffusion des particules transversalement au champ magnétique et diffusion exacerbée des ondes electromagnétiques*. PhD thesis, Ecole Polytechnique, 2000.

[62] A. Truc, A. Quéméneur, P. Hennequin, D. Grésillon, F. Gervais, C. Laviron, J. Olivain, S. K. Saha, and P. Devynck. ALTAIR: An infrared laser scattering diagnostic on the TORE SUPRA tokamak. *Rev. Sci. Instrum.*, 63(7):3716–3724, 1992.

[63] Y. Yeh and H. Z. Cummins. Localized fluid flow measurements with an He-Ne laser spectrometer. *Appl. Phys. Lett.*, 4:176–178, 1964.

[64] D. Yu, H. Li, Z. Wu, and W. Mao. Effect of oscillating sheath on near-wall conductivity in Hall thrusters. *Phys. Plasmas*, 14:064505, 2007.

[65] V. V. Zhurin, H. R. Kaufman, and R. S. Robinson. Physics of closed drift thrusters. *Plasma Sources Sci. Technol.*, 8:R1–R20, 1999.

Abstract

Anomalous electron transport across magnetic field lines in the Hall thruster plasma is believed to be due in part to plasma oscillations. Oscillations of frequencies on the order of a few megahertz and of wavelengths on the order of a millimeter have been shown to be likely to lead to transport. Measurements of fluctuations at these length scales is, however, beyond the reach of conventional thruster diagnostics such as probes. This work describes the first application of a specially-designed collective light scattering diagnostic (PRAXIS) to the measurement of electron density fluctuations and the subsequent identification of unstable modes in the thruster plasma. Two main high frequency modes are identified, propagating azimuthally and axially, of millimetric length scales and megahertz frequencies. The propagation directions and angular openings of the modes are determined. The azimuthally-propagating mode, believed to be responsible for transport, is shown to have wave vector components antiparallel to the magnetic field and parallel to the electric field, and to propagate within an extremely limited region. The axially-propagating mode is shown to have features closely related to the ion beam velocity and divergence. The electron density fluctuation level is calculated and is associated with a high electric field amplitude. The experiments, confirming a number of predictions arising from linear kinetic theory, also provide much additional information permitting the improvement and development of models for both modes.

Résumé

Les oscillations dans le plasma d'un propulseur à effet Hall sont susceptibles de provoquer le transport anormal à travers des lignes du champ magnétique. La théorie cinétique linéaire montre qu'en particulier certaines oscillations, de fréquence de l'ordre du mégahertz et de longueur d'onde millimétrique, peuvent jouer un rôle important dans le transport anormal. Les échelles caractéristiques de ces fluctuations ne sont pas détectables par des outils standards comme les sondes. Ce travail décrit pour la première fois l'utilisation d'un diagnostic de diffusion collective (PRAXIS) conçu pour l'étude du plasma du propulseur, qui a mené à l'identification des modes instables dans le plasma. Deux modes hautes fréquences ont été identifiés, se propageant dans les directions azimutale et axiale, avec des longueurs d'onde millimétriques et des fréquences de l'ordre du mégahertz. Les directions de propagation et les ouvertures angulaires de ces modes ont été déterminées. Le mode azimutal, identifié dans la théorie comme agent principal du transport, possède des composantes anti-parallèles au champ magnétique et parallèles au champ électrique et se propage dans une ouverture angulaire très restreinte. Le mode axial montre des caractéristiques liées à la vitesse et la divergence du faisceau d'ions. Le niveau de fluctuation de la densité est associé à une grande amplitude du champ électrique fluctuant. Les résultats des expériences sont en accord avec les prévisions théoriques et apportent de nouvelles informations, permettant ainsi d'améliorer et de développer des modèles pour les deux modes.